Title
Polymer Surface Modification for Bioengineering Applications

Author
Cheng, Qian

Publication Date
2011

Peer reviewed|Thesis/dissertation

Polymer Surface Modification for Bioengineering Applications

by

Qian Cheng

A dissertation submitted in partial satisfaction of the
requirements for the degree of
Doctor of Philosophy

in

Engineering – Mechanical Engineering

in the

Graduate Division

of the

University of California at Berkeley

Committee in charge:

Professor Kyriakos Komvopoulos, Chair
Professor Lisa A. Pruitt
Professor Song Li

Fall 2011

Abstract

Polymer Surface Modification for Bioengineering Applications

by

Qian Cheng

Doctor of Philosophy in Engineering-Mechanical Engineering

University of California, Berkeley

Professor Kyriakos Komvopoulos, Chair

Polymers are widely used in bioengineering for a wide range of applications, including substrates for *in vitro* cell culture and scaffolds for *in vivo* tissue engineering. Because polymer surfaces are usually non-polar and exhibit low biocompatibility, surface chemical modification must be used to enhance biocompatibility. In this study, biopolymer surfaces were modified by various plasma treatments and the resulting surface properties were characterized in detail by various microanalysis techniques. Although surface chemistry modification of biopolymers is important, modification of the near-surface structure of biopolymers is also critical because it affects cell attachment, proliferation, and infiltration, which is of paramount importance in the fabrication of scaffolds for tissue engineering.

Plasma polymerized fluorocarbon (FC) films grafted onto Ar plasma-treated low-density polyethylene surfaces were shown to increase the surface shear strength while maintaining low friction. These surface characteristics illustrate the potential of FC films as coating materials of bioinstruments, such as catheters used for the treatment of diseased arteries where blood flow is restricted by plaque deposits onto the inner wall of the vessel. In addition to FC film grafting, plasma polymerization with diethylene glycol dimethyl ether monomer was used to graft non-fouling polyethylene glycol (PEG)-like films on various substrates to prevent both protein adsorption and cell attachment, which is of great importance to the fabrication of non-clotting artificial grafts for bypass surgery.

Non-fouling PEG-like films were used to chemically pattern substrate surfaces for single-cell culture. Polystyrene culture dishes coated with a PEG-like film were chemically patterned using a silicon shadow mask or a poly(dimethyl siloxane) (PDMS) membrane mask, fabricated by standard lithography methods, to locally remove the PEG film by Ar plasma etching through the mask windows. Another surface chemical patterning method for long-term single-cell culture was accomplished with polystyrene and parylene C surfaces by taking advantage of the change in surface hydrophilicity induced by plasma treatment. These surface chemical patterning methods were used to regulate the shape and size of smooth muscle cells (SMCs). A strong effect of the shape and size of SMCs on proliferation rate was observed, which was correlated to changes in nuclei shape and volume of the SMCs.

In contrast to solid polymers, plasma surface treatment of fibrous polymer materials to improve biocompatibility has received relatively less attention. Thus, another objective of this dissertation was to explore how plasma surface modification with inert (e.g., Ar) and reactive

(e.g., NH_3) gas plasmas can be used to enhance cell attachment, growth and infiltration into fibrous polymer scaffolds. Poly(L-lactide) (PLLA) microfibrous scaffolds synthesized by electrospinning were plasma treated with Ar and NH_3 gases to improve cell affinity and incorporate functional groups for biomolecule immobilization. Both Ar and NH_3 plasma treatments were shown to improve the cell attachment and growth onto the fabricated microfibrous scaffolds, while surface functional groups produced by NH_3 plasma treatment were also effective in immobilizing biomolecules.

In addition to the surface chemistry, the structure of biopolymer materials also impacts the effectiveness of tissue engineering scaffolds. Using microfabrication technology to produce a patterned PDMS template for electrospinning, patterned PLLA microfibrous scaffolds with different structures were fabricated and their potential for tissue engineering was demonstrated by *in vitro* and *in vivo* cell culture experiments.

The results of this thesis indicate that surface chemistry and structure modification of biopolymers by combining plasma treatment with microfabrication/micropatterning techniques is an effective method of engineering surfaces for single-cell culture and scaffold materials with tailored two- and three-dimensional structures that enhance cell growth and infiltration. The findings of this work have direct application in the development of patterned surfaces for controlled single-cell attachment, which is of particular value to studies of individual cell behavior, and scaffolds for tissue engineering and repair.

Table of Contents

List of Figures

Chapter 1

Chapter 2

Chapter 3

Chapter 4

Chapter 5

Chapter 6

Chapter 7

Chapter 8

Chapter 9

List of Tables

Chapter 1

Chapter 4

Chapter 7

List of Abbreviations

AFM	Atomic force microscopy
Al	Aluminum
ATR	Attenuated total reflectance
BAECs	Bovine aorta endothelial cells
BioMEMS	Biological microelectromechanical systems
BSA	Bovine serum albumin
BSMCs	Bovine smooth muscle cells
CSI	Cell shape index
DAPI	4',6-diamidino-2-phenyindole
Diglyme	Diethylene glycol dimethyl ether
DMEM	Dulbecco's Modified Eagle's Medium
ECM	Extracellular matrix
FBS	Fetal bovine serum
FC	Fluorocarbon
FITC	Fluorescein isothiocyanate
FTIR	Fourier transform infrared spectroscopy
hMSCs	Human mesenchymal stem cells
LDPE	Low density polyethylene
NSI	Nuclei shape index
PC	Polycarbonate
PCL	Polycaprolactone
PDMS	Polydimethylsiloxane
PE	Polyethylene
PEG/PEO	Polyethylene glycol/Polyethylene oxide
PEOT/PBT	Poly(ethylene oxide)terephthalate-co-(butylene)terephthalate
PET	Polyethylene terephthalate
PFA	Paraformaldehyde
PLA	Poly(lactic acid)
PLGA	Poly(lactic- co-glycolic acid)
PLLA	Poly(L-lactide)
PLL-g-PEG	Poly(L-lysine)-g-poly(ethylene glycol)

PMMA	Poly(methyl methacrylate)
PP	Polypropylene
PR	Photoresist
PS	Polystyrene
PTFE	Polytetrafluoroethylene
PU	Polyurethane
PVC	Poly(vinyl chloride)
PVDF	Polyvinylidene fluoride
PVF	Polyvinyl fluoride
RF	Radio frequency
RIE	Reactive ion etch
SEM	Scanning electron microscopy
SFM	Surface force microscopy
Si	Silicon
SMCs	Smooth muscle cells
TCP	Tissue culture plate
UV	Ultra-Violet
XPS	X-ray photoelectron spectroscopy

Acknowledgements

Through the five years of Phd study and research, I felt so grateful to all the people who've provided me support and guidance.

First of all, I'd like to express my deepest thanks to my advisor, Professor Kyriakos Komvopoulos at University of California at Berkeley. I didn't have much background in the area of my research at the first beginning, but his patience and consistent support made me believe in myself and keep exploring new areas that I was not familiar with. His instructions guided me through the intellectual development required for a PhD student and helped me to think on myself. Without his supporting, it's impossible for me to work on such a complicated interdisciplinary project and achieve so much during these years.

A large part of the research work presented in this thesis was conducted in collaboration with Professor Song Li in Department of Bioengineering, University of California at Berkeley. Therefore, I'd like to extend my thanks to Professor Li for all the invaluable support, instructions and discussions over these years.

Professor Lisa A. Pruitt was my qualifying examination chair as well as thesis committee, thanks a lot to her for the precious suggestions on my research projects and thesis.

I'd like to thanks Professor Michael A. Lieberman for being my qualifying examination committee and helpful discussions on plasma system configuration. I'd also like to thanks Professor Van P. Carey and Professor C. K. Hari Dharan for being my qualifying examination committee and helping me moving forward on the PhD study and research.

Part of the thesis work was conducted with the equipment in Molecule Foundry of Lawrence Berkeley National Laboratory and Berkeley Microfibrication Laboratory, so I'd like to express my thanks for their support.

While working in Prof. Song Li's lab, I've met many brilliant and friendly people who helped a lot on developing my bioengineering lab skills, so I'd like to thank all of them for their support over these years: Julia Chu, Ben Lee, Dr. Aijun Wang, Dr. Zhiqiang Yan, Zhenyu Tang, Dr. Randall Raphael R. Janairo, Jeff Henry, etc. I'd also like to thank all the members in S*urface Sciences and Engineering Laboratory* (SSEL) and *Computational Surface Mechanics Laboratory* (CSML) for providing an excellent academic research environment, and for their friendship, support and accompany during these years.

Finally, I owe my deepest gratitude to my parents, my sisters and brother for their unconditional love and invaluable support all over these years.

Chapter 1

Introduction and Background

1.1 Biopolymers and surface modifications

As the largest class of biomaterials, polymers are widely used for numerous bioengineering applications due to their low density, proper mechanical property, chemical stability, processing versatility, as well as biodegradability for some category of polymers. Many biomedical devices are fully made out of different polymers or comprised of polymeric components. For example, polyethylene (PE) and polypropylene (PP) are used for various tubings and total joint replacements, polytetrafluoroethylene (PTFE) is used for vascular graft, and polydimethylsiloxane (PDMS) is used for various implants, etc, as shown in Table 1.1 (Visser et al. (1996). More examples of polymers used in clinical biomedine can be found in Figure 1.1 (Rosato et al. (1983)), including applications for dentures, facial prosthesis, sutures, esophagus/gastrointestinal segments, etc. Both Table 1.1 and Figure 1.1 show the widespread application of polymer materials in biomedical device fields.

The selection of polymer materials for biomedical device applications usually base on the mechanical property, chemical stability, as well as the material surface property. While the mechanical property and chemical stability are usually determined by the bulk material, material surface property modification is usually necessary to fulfill the requirement of 'biocompatibility'. The definition for biocompatibility is kind of vague, but generally speaking, it means that the material used for bio-applications should fulfill their function without causing other unwanted side effects. For example, joint implants should function mechanically without inducing chronic inflammatory response or formation of unusual tissues; invasive catheters should be strong enough to perform functionality but with low surface friction so that surrounding tissue won't be damaged during treatment; vascular grafts should be able to restore blood recirculation without inducing thrombosis; scaffolds for tissue regeneration should be able to promote cell attachment, proliferation, infiltration and tissue formation, etc. Most polymers have surfaces that are relatively hydrophobic, inert and don't meet the specific requirements. For example, the surface of selected biopolymer may not be ideal for cell growth and tissue regeneration when biointegration is critical; it may induce thrombosis when it's unavoidable for the surface to get into contact with blood; it may have high surface friction coefficient when invasive operation will be performed with the device, etc. Therefore, surface chemical modifications of the biopolymers are almost always necessary. In this thesis, research focused plasma assisted biopolymer surface modification will be elaborated, including functional plasma polymer film deposition, plasma treatment for surface chemistry modification, and plasma assisted surface chemical patterning for controlled protein adsorption and cell attachment.

Besides surface chemical property, structure of biopolymers is also critical for some biomedical applications, especially for tissue engineering scaffolds. Since a scaffold is expected to recruit cells, enhance cell growth and form new tissue, both the surface property and scaffold structure are important. While the surface property can be modified similarly as the bulk

biomaterial, the structure of scaffolds is usually modified trying to mimic the porous structure of the extracellular matrix in the body. To achieve this goal, microporous/microfibrous structures can be prepared via different techniques, e.g. self-assembly, phase separation, electrospinning. Among various methods, electrospinning of micro/nanofibrous structure has attracted lots of attention for tissue engineering and drug delivery applications (Huang et al. (2003), Pham et al. (2006), Vasita et al. (2006)) due to their special structures and convenience of preparation. In this thesis, work on preparing microfibrous scaffold with different structures via electrospinning will also be presented.

1.1.1 Surface chemical modification of biopolymers

To modify surface chemistry of biopolymers, there're various methods available (Desmet et al. (2009)). First, the most common and convenient method is wet-chemical methods involving using chemicals to introduce functional groups onto a biopolymer surface, with aminolysis (Zhu et al. (2002) and alkaline acidic hydrolysis (Gao et al. (1998)) as the classical examples. Wet chemical methods tend to increase surface hydrophilicity and roughness as wells as improve cell affinity, the produced chemical groups (e.g. carboxyl end group, primary amine end group) are also really useful for external cell matrix protein (e.g. gelatin) and other bioactive molecules immobilization to further improve cell affinity. The main drawback of wet chemical methods is that the reactions are nonspecific, the degree of surface modification is not well controlled, and the mechanical property of the material is usually affected significantly. Ozone treatment (Gatenholm et al. (1997)), UV- treatment and photografting (Deng et al. (2009)) are another category of methods which create covalent bonds between the molecules of interest and the substrate, usually these methods are combined with wet-chemical methods, or combined with vapor phase grafting, and the whole system can be complicated and always need tedious optimization process. High-energy radiations (e.g. □-radiation and e-beam radiation) are also used to modify biopolymer surface property by creating radical sites and initiating polymerization (Cho et al. (2005)). Then, self-assembly is another well studied method to create specific chemical groups on a surface to realize surface modification. The best known example is the n-alkane thiols self assembles on gold surface, and for biopolymer surfaces usually block-copolymers with an amphiphilic nature are applied as a coating material through hydrophobic interactions (Popelka et al. (2007)). More recently, surface-initiated polymerization (Ranjan et al. (2007)) including atom transfer radical polymerization and reversible addition-fragmentation chain transfer polymerization, and molecular layer deposition (Adarnczyk et al. (2008)) are studied due to possibility of grafting higher density of longer chains or precise control of thickness and conformability.

Finally, in recent years non-thermal plasma treatment has gained more and more attention for biopolymer surface modifications due to its ability to change polymer surface chemistry effectively and with various advantages: one-step simple process, conformal surface modification even for complicated 3D geometry, solvent free and environment friendly, sterile process, etc (Tajima (2006)).

1.1.2 Plasma assisted biopolymer surface chemical modification

Plasma is a partially ionized gas mixture comprised of ions, electrons, uncharged particles (neutrals, atoms, metastables and radicals), and is often called the fourth state of matter. According to the energy states of the different species in plasma, plasmas can be categorized into nonequilibrium plasmas and equilibrium plasmas. For equilibrium plasmas, the temperature of all species are the same, which is true only when the plasma is produces by heating gases to really high temperature, typically ranging from 4000 K for easy-to-ionize elements such as cesium to 20,000 K for hard-to-ionize elements like helium, with stars and fusion plasmas as the example. These kinds of plasmas are also called thermal/high-temperature/hot plasma. In contrast, plasma used for material processing are usually obtained when gases are excited into energetic states by electric fields, which results in electrons having much higher energy than other species. Therefore these plasmas are called nonequilibrium plasma, or nonthermal/low-temperature/cold plasma (Lieberman et al. (2005), Desmet et al. (2009)).

Since polymer materials usually have very low melting temperature, generally only nonthermal or cold plasma are used for polymer surface modifications. Dependent on the gases used in the plasma process for polymer surface modifications, the interaction between plasma and polymer surface can be roughly divided into three categories. (1) If the processing gas is nonreactive inert gas (e.g. Ar and He), ion bombardment and vacuum UV contribute to the modification of polymer surface, which can result in removal of surface atoms and forming of free bonds, which will later on form crosslinking or react with species from environment. (2) With a reactive but non film-forming gas (e.g. CO_2, NH_3), besides the ion bombardment effect, new chemical groups from the processing gas can be inserted into the structure of the surface layer of the processed polymer material, therefore new groups can be incorporated onto the surface. (3) If the processing gas can form a film through plasma polymerization (e.g. C_4F_8), polymerized film can be grafted onto the polymer substrate at the same time. For plasma polymerization, usually film grafting and ablation happen at the same time, as shown in Figure 1.2. According to surface modification procedure, plasma polymer surface modifications can be divided into direct modification or indirect modification methods. For direct modification, polymer surface chemistry is modified by plasma treatment with inert or reactive gases or plasma polymerization film grafting directly. While for indirect method, functional groups grafting on the direct modified surface, plasma post-irradiation grafting or plasma syn-irradiation grafting will be used to immobilize other molecules of interest (Desmet et al. (2009)). In this thesis, plasma polymer surface modifications will be discussed according to its application in three areas of bioengineering field, which will be elaborated in details in section 1.2.

1.1.3 Electrospinning for biopolymer surface/structure modification

While bulk polymers are usually used for biomedical devices, polymers with microstructures are getting more and more attention in tissue engineering and drug delivery field. Mimic the architecture of extracellular matrix has been a major challenge when developing scaffolds for tissue engineering, and the development of techniques in preparing polymer micro/nanofibers has greatly improved the capability to prepare polymer scaffold with proper microstructures. Common techniques used for preparing polymer micro/nanofibers can be divided into three categories: electrospinning, self-assembly and phase separation, among which electrospinning is the most widely used method due to its simplicity and low cost of setting up. (Vasita et al. (2006))

Fibrous structures exhibiting sufficient porosity are desirable in scaffold engineering because porosity plays an important role in cell infiltration. In addition, fiber alignment is conducive to cell migration and, under certain conditions, may also enhance cell infiltration. A common approach to increase porosity in electrospun construct is to incorporate sacrificial structures (e.g., salt grains, ice particles, and fibers), which can be later easily removed to produce a porous construct. However, leaching of the sacrificial structure(s) often leads to the collapse of the construct (Nam et al. (2007)). Polymer fiber electrospinning on special templates to achieve deposition control have been shown to be a more efficient method of fabricating porous fibrous constructs (Blakeney et al. (2011)). Especially, fiber electrospinning onto surface-patterned templates enables control of both fiber density and alignment (Zhang and Chang (2007, 2008)). Three-dimensional (3D) patterns on templates have been produced through machining of metal and ice or knitting of metal wire. However, there're intrinsic limitations for these methods: surface patterns created by linear cutting or knitting are limited, and it's hard to achieve high resolution control of the pattern geometry. In this thesis, a 3D-patterned PDMS was fabricated to obtain scaffolds with different structure and the biological effects were studied.

1.2 Plasma surface modifications

In this section the application of plasma polymer surface modifications for three typical surface modification purposes will be discussed: plasma polymerization for functional surface coating, plasma surface modification for biocompatibility and biointegration improvement, and the plasma assisted surface modification for controlled adsorption of proteins and/or cells.

1.2.1 Surface modification by plasma-assisted polymer coating deposition

As shown in Figure 1.2, plasma polymerization is a really versatile method to coat surface with a thin film. Monomer in gas or vapor phase is introduced to form the plasma, fragmented reactive radicals then combine to each other and form polymers in the gas phase (plasma-state polymerization) and get grafted onto the activated polymer surface. The polymers formed in the plasma usually don't have the same structure and composition as polymers achieved by conventional polymerization techniques. Besides, since plasma polymerization occurs with monomers in the fragmented status, unsaturated bonds or cyclic structures are not necessary to ensure polymerization anymore, so various monomers can be introduced into the plasma for deposition of a plasma polymer coating on the surface.

Plasma polymerization has found application in various fields, including electronics and optics fields, as well as biomaterial and bioengineering fields. For bioengineering applications, plasma polymerization has been applied to deposit different kinds of films, and generally they can be divided into two groups which have opposite functionality: plasma polymer film that can resist protein/cell attachment and therefore provide hemocompatibility; and plasma polymer film that can promote protein attachment/conjugation and therefore enhance biocompatibility. A summary of plasma polymerization for different surface coatings can be found in Table 1.2.

For the first group, fluorocarbon (FC) film and polyethylene glycol (PEG) films are most commonly used. For example, it's found that fluorocarbon film deposited by radio frequency glow discharge on small diameter synthetic vascular graft and glass slide can decrease the

adsorption of platelets ex vivo and in vitro (Kiaei et al. (1992)), mainly due to the interaction between fribrinogen from blood plasma and the fluorocarbon film with super low surface energy (Kiaei et al. (1995)). Besides, plasma deposited PEG-like film was found being able to retain the nonfouling property of polyethylene glycol and resist both protein adhesion and cell attachment (Brétagnol et al. (2006)).

For the second group, films in rich of functional groups (e.g., carboxyl, hydroxyl, amine and aldehyde groups) are usually the objective. Usually they can promote protein/cell attachment directly due to the increased surface energy, or they can incorporate chemical groups which serve as conjugation sites for other bioactive molecules. For example, amine-based monomers including allylamine, diaminocyclohexane, and heptylamine are widely used for plasma polymerization and deposition of film providing primary amine group, while acrylic acid and propanoic acid are used for the grafting of film providing carboxyl group (Siow et al. (2006)). Via these films in rich of functional groups, bioactive molecules including collagen, gelatin and small peptide [Arg-Gly-Asp-Cys (RGDS)] can be conjugated onto surface through carbodiimide reaction.

Since plasma polymerization is really complicated process, it's always necessary to optimize the plasma condition for each monomer that's used as the precursor. It has been reported that the character of the deposited plasma film is closely related to the plasma chemistry, since monomers can react in different ways in plasma (Guerin et al. (2002)), due to the different combinations or plasma conditions such as power, pressure, flow rate and duty factors, and certain plasma condition will favor one of those different chemical pathways. Generally speaking, low wattage, low discharge power and low duty cycle are beneficial for retention of the functional groups of the monomer and suppress crosslinking reactions, which is usually the requirement for plasma polymerization process.

Due to the plasma reaction process, there's usually an inherent concern about the stability and aging of the plasma polymerized thin films (Siow et al. (2006)). Generally speaking, films become more stable when plasma power increases and resulted in deposition of film with higher degree of crosslinking.

In this thesis, a fluorocarbon film aimed at enhance surface strength while maintaining low surface friction (Chapter 3) and a PEG-like film (Chapter 4) aimed at providing a nonfouling surface and decreasing protein/cell adhesion are deposited through plasma polymerization and deposition processes.

1.2.2 Surface modification with non-coating plasma

As shown in Figure 1.3, plasma treatment doesn't form film grafting or deposition. Instead, chemical functionalities are introduced onto the surfaces or free radicals are created depending on the processing gas is reactive or inert. At the same time, surface wettability and roughness are usually increased, and chain scission and/or cross-linking are possible.

A comprehensive summary of plasma treatment of different kinds of biopolymer are shown in Table 1.3. It can be seen that plasma surface treatments with different gases have been

studied extensively for traditional biopolymer surface modifications according to the effects on protein adsorption and cell attachment/growth. Generally, inert gas (Ar and He) plasma doesn't lead to incorporation of new surface functionalities on the polymer surface, but free radicals will be created and can react with atmospheric oxygen. O_2, CO and CO_2 plasma treatment can incorporate various oxygen containing chemical groups (e.g. carboxyl, peroxide, hydroxyl groups, etc). N_2, NH_3 and N_2/H_2 plasma introduce primary, secondary and tertiary amines as well as amides. It's usually the case that plasma treatment doesn't incorporate unique functionality and is not a selective technique.

As to the effect on polymer surface biocompatibility, plasma treatments generally enhance external cell matrix protein adsorption on biopolymer surfaces, therefore can improve surface biocompatibility after treatment. It's found that simple air plasma, Ar plasma, O_2 plasma or NH_3 plasma are able to enhance cell growth. Some comparison study shown that incorporation of $–NH_2$ via NH_3 plasma treatment is superior compared to O_2, SO_2 for improving cell growth on polymer surfaces. Besides, due to the functional groups incorporated through plasma treatment, conjugation of bioactive molecules is also possible. Even though plasma treatment of traditional biopolymer in bulk state has been studied extensively, its effect on modern biomaterials (e.g. fibrous biopolymer scaffolds) is of great interest. In this thesis, the effect of plasma treatments on Poly(L-lactide) (PLLA) microfibrous scaffolds biocompatibility and the feasibility of conjugating heparin onto plasma treated PLLA scaffolds are also studied.

1.2.3 Plasma-assisted surface patterning

Surface patterning for cell culture is a method aimed at creating surface areas with different chemistry which can control protein adsorption and cell attachment, and therefore produce patterns of single or multiple cells. The ability to precisely control the shape and spreading area of attached cells or cell-cell contacts through surface patterning is very useful for many fundamental studies of cell behaviors, including cell proliferation, differentiation and molecular signaling pathways. For example, it's found that by controlling the geometry of single cell, it's possible to control cell fate and cell differentiation ability. (Chen et al. (1997), McBeath et al. (2004)). Besides, it's also a critical tool for manipulating cells in ordered organizations on transducers for cell based sensing and cell based drug discovery concepts. Various methods have been investigated to achieve this objective (Falconnet et al. (2006)), and plasma treatment has also been tried to assist in the processes (Ohl et al. (1999)).

Possible procedure of applying plasma treatment for surface chemical patterning is shown schematically in Figure 1.4. Since plasma treatment can change material surface topography and chemistry (e.g. hydrophilicity) easily, masking the surface partially during plasma treatment will be able to induce surface chemistry contrast and therefore difference in cell response. Metal mask fabricated from laser cut or conventional microstructure metallic grid masks has been used due to their simplicity (Vargo et al. (1992)), but defects of surface patterns were found where contact between the metal mask and the substrate is not intimate. To solve this problem, traditional micro-lithography was incorporated to replace mechanical mask and combined with plasma treatment for surface patterning (Lhoest et al. (1996)). An example of plasma assisted surface chemical patterning for cell culture is shown in Figure 1.5 (Ohl et al. (1999)). Compared to other surface patterning methods, plasma treatment combined with stencil

mask for surface patterning has various advantages: fast, sterile, clean process without toxic solvent and cost effective since it's not relying on clean room facility.

To take advantage of the stencil mask and avoid the disadvantages of current masks, mechanical masks made of Si or PDMS were made by using microfabriation techniques in this thesis. Combined with plasma treatment (both plasma polymer film deposition and plasma treatment) and new patterning mechanism, the fabricated masks are applied to make chemical patterned surface for single cell culture successfully, and also enable further study of patterning effect on cell behavior, which will be discussed in chapter 5, and chapter 6.

1.3 Research objectives

Plasma polymer film deposition of fluorocarbon film have been used as a hemocompatible coating material for catheters used in angioplasty surgery, and the film deposition chemistry has been studied in details previously (Tajima et al. (2007)). While hemocompatibility is a primary requirement for such coating materials, low friction is also required to avoid damaging surrounding tissue. Therefore, in this thesis the nanomechanial properties of the plasma deposited fluorocarbon film were investigated. The objective is to check the surface mechanical property evolution during plasma processing and make sure that the coating can provide advantageous surface mechanical property besides the hemocompatibility.

To create non-fouling surface, plasma coating of PEG-like film is also very useful and effective. While quite a few attempts have been made in previous studies, almost all of them require special plasma system configuration. In this thesis a more universal process was set up to deposit PEG-like film with a plasma system which doesn't require any special set up, and the plasma condition was also optimized through detailed study on the film deposition process to deposit PEG-like film with desired nonfouling property.

Besides surface modification to avoid interaction with biomolecules, the ability of plasma treatment to improve protein/cell affinity and biomolecule immobilization on polymer surface is also of great importance for bioengineering applications, especially for biopolymers with microstructures, e.g. polymer micro/nanofibrous membranes. At the same time, methods which can effectively modify surface chemistry of polymer nano/micro structures without affect the bulk property become critical for the successful application of these polymer structures in tissue engineering and drug delivery fields. (Yoo et al. (2009)) Therefore, in this study plasma treatment was investigated to modify PLLA microfibrous scaffold surface chemistry for two objectives: (1) improve cell affinity and cell infiltration into the PLLA microfibrous scaffolds for tissue engineering applications; (2) incorporate functional groups onto the PLLA microfiber surface for immobilization of bioactive molecules for both tissue engineering and drug delivery applications.

With the ability to create both cell adhesive and cell nonadhesive surfaces, it's straightforward to crate patterned surface which can control protein adsorption and cell adhesion by incorporating microfabrication techniques. Even though various methods have been developed for this objective, simple, cost effective method are always desired to expand the

application of surface chemical patterning methods. In this thesis, new methods were proposed with the objective of make the existing methods more versatile, stable and more effective.

Finally, besides surface chemistry modification, structural modification of the polymer microfibrous scaffolds via patterned electrospinning was also studied to improve cell incorporation and therefore enhance biointegration. The aim is to increase porosity of the scaffold and insure cell infiltration. To achieve this goal, new templates were designed to fabricate polymer microfibrous scaffolds with different morphology and structure, which may have applications in different bioengineering fields.

1.4 Outline of the dissertation

In Chapter 2, the plasma apparatus used for the polymer surface modifications and the electrospinning system are first introduced. Then all the analytical techniques used for study in this thesis as well as involved instruments are explained in details. Two different capacitively coupled plasma apparatus were used for: (a) functional films deposition through plasma polymerization, including fluorocarbon film deposition and PEG-like film deposition, and (b) polymer surface modification to improve biocompatibility and incorporate functional groups for biomolecule immobilization. The operation mechanisms of all analytical tools were then explained; i.e., SFM, AFM, SEM, goniometer, FTIR, and XPS, were used to characterize various surface modifications (e.g. surface mechanical property, surface roughness and morphology, ad surface chemistry) and optimize the film deposition or surface modification condition. Finally, experimental methods used to evaluate biological effects of surface modification are explained, i.e., cell culture and staining, cell proliferation rate study and cell infiltration study.

In Chapter 3, FC films were grafted onto Ar plasma-treated LDPE surfaces by plasma polymerization and deposition. The evolution of the surface morphology of the grafted FC films was investigated at different scales with an AFM. Nanoscale sliding experiments performed with a SFM provided insight into the nanotribological properties of Ar plasma-treated LDPE surfaces, with and without grafted FC films, in terms of the applied normal load and number of sliding cycles. The observed trends are explained in the context of microstructure models accounting for the morphological and structural changes at the LDPE surface resulting from the effects of plasma treatment (e.g., selective etching of the amorphous phase, chain crosslinking, and FC film grafting) and surface sliding (e.g., crystalline lamellae alignment along the sliding direction). Nanoindentation experiments elucidated the effect of plasma treatment on surface viscoelasticity and contact stiffness. The results demonstrate that plasma polymerization and grafting of FC films is an effective surface modification method for tuning the nanomechanical/tribological properties of polymer surfaces.

In Chapter 4, capacitively coupled plasma of diglyme monomer was used to deposit films chemically similar to PEG on LDPE and Si substrates pretreated with Ar plasma. The topography, thickness, chemical characteristics, and compositions of films synthesized under different plasma conditions were examined by AFM, ellipsometry, goniometry, FTIR, and XPS. The effect of the substrate pretreatment conditions on the wettability and thickness of the films deposited on LDPE was found to be significant, while that of the diglyme plasma treatment time on the film composition was shown to be secondary. Film chemical functionalities demonstrated

a dependence on both diglyme plasma power and substrate material. Activation of the LDPE surface by bombarding Ar^+ ions and subsequent low-power treatment with diglyme plasma was more conducive to the formation of films with chemical characteristics similar to those of PEG. The results demonstrate the potential of the present technique to deposit thin polymer films with specific chemical characteristics on different surfaces.

In Chapter 5, the low-power diglyme plasma polymer film deposited in Chapter 4 was found to exhibit nonfouling behavior and recognized as PEG-like film, as evidenced by the significant decrease in protein adsorption and cell attachment on substrates coated by these films. Different chemical patterns were produced on substrates with grafted PEG-like films using Si or PDMS membrane shadow masks fabricated by photolithography and simple one-step plasma etch process. Culture of single human mesenchymal stem cells on chemically patterned polystyrene dishes demonstrated a strong dependence of the actin structure and nuclear morphology on the cell shape and spreading area. The presented surface chemical patterning method for single cell culture was also utilized to study cell shape regulation of smooth muscle cell proliferation. It was found that both cell shape and size affect the shape and volume of cell nuclei, which could be related to the cell shape and size effects on cell proliferation rate, and revealed the important modulation of nuclei geometry on DNA synthesis and smooth muscle cell proliferation.

In Chapter 6, a new method of surface chemical patterning for single cell culture was presented for long-term single cell culture on various substrates. Surface chemical patterning of polystyrene dishes for long-term single-cell culture was accomplished by oxygen plasma treatment through the windows of the PDMS membrane mask that produced hydrophilic surface areas of different shapes and sizes, followed by overnight incubation with either Pluronic F108 solution or a mixture of Pluronic F108 solution and fibronectin. Selective cell attachment on the pattern areas of polystyrene dishes was characterized by cell seeding experiments and XPS measurements. Activation of the hydrophilic areas of patterned polystyrene surfaces by serum proteins from cell culture medium was conducive to cell attachment on the pattern areas of dishes incubated with only Pluronic solution, and preferential adsorption of fibronectin on hydrophilic pattern areas promoted selective cell attachment on patterned dishes incubated with a mixture of Pluronic solution and fibronectin. Long-term (two weeks) cell culture experiments showed the effect of surface patterning on the shape of cells and nuclei and demonstrated the stability of the produced single-cell patterns in serum medium. To patterning substrates beyond polystyrene, Parylene C film was selected as a coating material, and surface patterning of Parylene C film for single-cell culture was accomplished by combining plasma-assisted surface chemical modification, soft lithography, and protein-induced surface activation. Hydrophilic patterns were produced on Parylene C films deposited on glass substrates by oxygen plasma treatment through the windows of PDMS shadow masks. After incubation first with Pluronic F108 solution and then serum medium activation overnight, surfaces seeding with mesenchymal stem cells in serum medium resulted in single-cell patterning. Both methods provide means of surface patterning with direct implications in single-cell culture.

In Chapter 7, PLLA microfibrous membrane was treated with mild Ar and Ar-NH_3/H_2 plasma to examine the effect of different plasma treatments on cells attachment and growth on the membrane surface as well as cell infiltration into the membrane. Goniometry, atomic force

microscope and X-ray photoelectron spectroscopy measurements shown that the PLLA fiber surface chemistry was successfully modified with decreased contact angle for both plasma treatments and incorporation of $–NH_2$ on Ar-NH_3/H_2 plasma treated surface, while without affecting the integrity of the microfibrous structure and the fiber surface roughness. Culturing of bovine aorta endothelial cells and bovine smooth muscle cells on treated PLLA microfibrous membrane surface showed that for these two type of cell lines, both Ar and Ar-NH_3/H_2 plasma treatments improved cell spreading for initial stage of attachment, and more importantly can enhance cell growth rate effectively, especially for Ar plasma treatment. In vitro cell infiltration experiment with bovine aorta endothelial cells and in vivo implanting of PLLA membranes under rat skin showed that both plasma treatments can enhance cell ingrowth on the PLLA membranes effectively, which is of important interest in tissue engineering.

In Chapter 8, Ar-NH_3/H_2 plasma treatment was used to incorporate $–NH_2$ groups onto Poly(L-lactide) (PLLA) microfibrous membrane surface for heparin conjugation. The density of incorporated $–NH_2$ group was determined by chemical derivative method combined with XPS measurement. It's found that plasma power, gas composition and H_2 plasma post treatment time don't affect N/C ratio significantly, instead they affect the ratio of $–NH_2$/N and therefore affect the ratio of $–NH_2$/C, while plasma treatment time has effect on both N/C and $–NH_2$/N ratios. The surface functionalization of PLLA microfibrous membrane with Ar-NH_3/H_2 plasma was found being able to increase the amount of covalently immobilized heparin significantly compared to hydrolysis method, and the immobilization of heparin was confirmed by the decrease of platelets attachment after blood test. The effect of heparin conjugation on in vitro bovine endothelial cell infiltration on the PLLA microfibrous membrane was also studied, and it was found that cell attachment and growth was enhanced on heparin conjugated PLLA microfibrous membrane surfaces, independent on the amount of heparin immobilized (in the range examined by the study).

In Chapter 9, PDMS templates with different micropatterns were fabricated by combining photolithography, Si wet etching, and PDMS molding techniques. Electrospinning of PLLA nanofibers on PDMS templates possessing various micropattern geometries produced scaffolds with different nanofiber conformities and alignments, increased porosity, and microwells of various shapes and dimensions. The effects of the nanofiber arrangement and porosity of micropatterned scaffolds on the morphology, migration, and infiltration of cells were examined by in vitro and in vivo experiments. Cell study results revealed a strong effect of the scaffold micropattern geometry on cell morphology, migration, and infiltration. The wide range of nanofiber organization and porous structures of the PLLA scaffolds fabricated indicate that the present method provides a powerful means of engineering the two- and three-dimensional structure of electrospun nanofibrous scaffolds and materials.

Finally, the main findings from Chapters 3-9 are summarized and future research directions are discussed in Chapter 10.

Table 1.1. Polymers used for biomedical devices (Visser et al. (1996)).

Polymers	Properties	Application
PE	Tough, resistance to fats and oils, low cost	Tubing (catheters, drainage) Total hip and knee joint replacement
PTFE	Thermally and chemically stable Difficult to process Hydrophobic, excellent lubricity	Vascular graft
PP	Rigid, good chemical resistance, good tensile strength, good stress crack resistance	Tubing (catheters, drainage) Total hip and knee joint replacement
PVC	Hard, brittle, not suitable for long-term applications, require addition of plasticizer for flexibility	Tubing (blood transfusion, feeding, and dialysis)
PDMS	Silicon-oxygen backbone, low temperature sensitivity, high oxygen permeability, excellent flexibility and stability	Catheters, drainage tubing, insulation for peacemaker leads, vascular graft, membrane of oxygenators, finger joints, blood vessels, heart valves, breast implants, outer ears, chin and nose implants
PMMA	Hydrophobic, linear chain polymer, glassy at room temperature, good light transmittance, toughness, stable	Intraocular lenses, hard contact lenses

Table 1.2. Representative overview of plasma-polymerized, deposited polymers on surfaces (Desmet et al. (2009)).

Substrates	Monomer	Year
PE and mica	acrylic acid	1990
LDPE	allyl phenyl Sulphone, allyl amine,	1993
KBr windows and Si wafers	propylamine, unsaturated allylamine, propargylamine,	1995-1996
covered with gold glass slides and PVC-films	1-propanol, allyl alcohol, and propargyl alcohol	
	propargyl alcohol, propargyl acid, methylbutynol, allyl alcohol, acrylic acid, acrylic aldehyde, furfuryl alcohol, ethylene glycol, ethylene glycol dimethylether	1996
Si, KCl and PET	allylalcohol	1996
glass coverslip, wrapped with an Al foil	acrylic (propenoic) acid and propanoic acid	1996
Al substrate	allyl amine/1,7-octadiene and acrylic acid hexane	1996
KBr pellets and Si wafers	benzene, 1,2,4-trifluorobenzene, and hexafluorobenzene	1998
Al foil	allylalcohol/1,7-octadiene	1998
(oxidized) Al	acrylic acid	1998
polyimide	1,3-diaminopropane, ethylene diamine	1999
6-well TCP, Al foil	acrylic acid /1,7-octadiene	1999
PTFE	allylalcohol, acrylic acid, allylamine and acrylonitrile	2001
stainless steel chips	isopropyl alcohol	2002
Ti alloy	allylamine	2002
polysulfone membranes, Al foil and glass	ethylenediamine, diaminocyclohexane	2003
metal sheet, coated with epoxy resin and Al.	allylalcohol, allylamine, acrylic acid/ethylene or butadiene as initiator	2003
polysulfone	n-butylamine, allylamine, and allyl alcohol	2003
uncoated silicone, silicone wafers coated with Au or Al, indium tin oxide glass and glass	aniline	2004
PS	isopropyl alcohol	2004
Si	styrene	2004
PLA (3D substrate)	allylamine	2005
Si	ethylene	2005
Si	allylalcohol	2005
Si	tetrafluoroethylene	2005
PU	allylalcohol	2006
Si	allylamine	2006
glass	styrene	2007
PET	PEO	2007
PLLA (3D)	acrylic acid	2007
PS	acrylic acid, hydroxyethylmethacrylate, N-vinyl-2-pyrrolidinone, N-vinylform-amide, allylamine, and hexylamine	2008
PLGA (scaffolds)	heptylamine	2008
Silicone and PP	NH_3/ethylene	2008
Silicone	ethylene and styrene with allylamine or allylalcohol	2008
perfluorinated poly(ethylene-co-propylene) and PET	n-heptylamine or allylamine	2008
glass	acetylene and protein (FITC-BSA)	2008
Si	allylamine	2008
glass	hexane and allylamine	2008
PE	maleic anhydride	2008

Table 1.3. Representative overview of plasma treatment of polymer surfaces (Desmet et al. (2009)).

Substrates	**Plasma**	**Year**
PP, PVC, PTFE, PC, PU, PMMA	NH_3 and N_2/H_2	1969
PE, PP, PVF, PS, nylon 6, PET, PC, cellulose acetate butyrate, poly(oxymethylene)	He and O_2	1969
PET, PP	O_2	1989
PP	CO_2	1990
polyimide (Kapton film)	Ar, N_2,O_2, CO, CO_2, NO, and NO_2	1992
LDPE	SO_2	1993
LDPE	CO_2,NH_3 with subsequent grafting	1993
perfluorinated ethylene-propylene copolymer and PTFE	NH_3 and H_2O vapor	1995
PE	CO_2	1995
PP	He, Ne, Ar, H_2,N_2,O_2	1995
PET	CO_2	1997
PS, LDPE, PP, PET	Ar	1997
PS, PDMS, phenol-formaldehyde resin	O_2	1998
PVDF	NH_3 and N_2/H_2	1999
polysulfone	CO_2	1999
polysulfone	CO_2 and N_2	1999
PP, PS, and PTFE	NH_3 and Ar	2000
PS	NH_3 and N_2/H_2	2003
poly(ethylene naphthalate)	N_2	2003
PLLA	O_2,N_2, Ar and NH_3	2003
PLLA, PLGA	NH_3	2003
polysulfone	NH_3	2003
PP	O_2,NH_3 and N_2	2004
PLGA	O_2	2004
PLA	air or water/ NH_3 plasma	2005
PU	air plasma	2005
PS	N_2 and CO_2	2005
polyethersulfone	N_2,NH_3, Ar/NH_3 and O_2/NH_3	2005
PCL	air plasma	2005
PEOT/PBT	Ar	2006
PP, LDPE	air plasma	2006
PLA	NH_3	2006
PLLA (scaffolds)	Ar	2006
PLLA (3D scaffolds)	NH_3	2007
starch	O_2	2007
poly(L/DL-lactide) 80/20%	O_2,NH_3 or SO_2/H_2	2007
PU	O_2	2007
PCL nanofibers	Ar (remote plasma)	2007
PLLA (scaffold)	O_2	2007
PC	He	2007
PE	Ar	2007
PLGA	CO_2	2008
PTFE	Ar (remote and direct)	2008
PP microporous membrane	Air plasma	2008
PP microbeads	He/NH_3/H_2O and He/O_2/H_2O	2008
PCL	O_2	2008

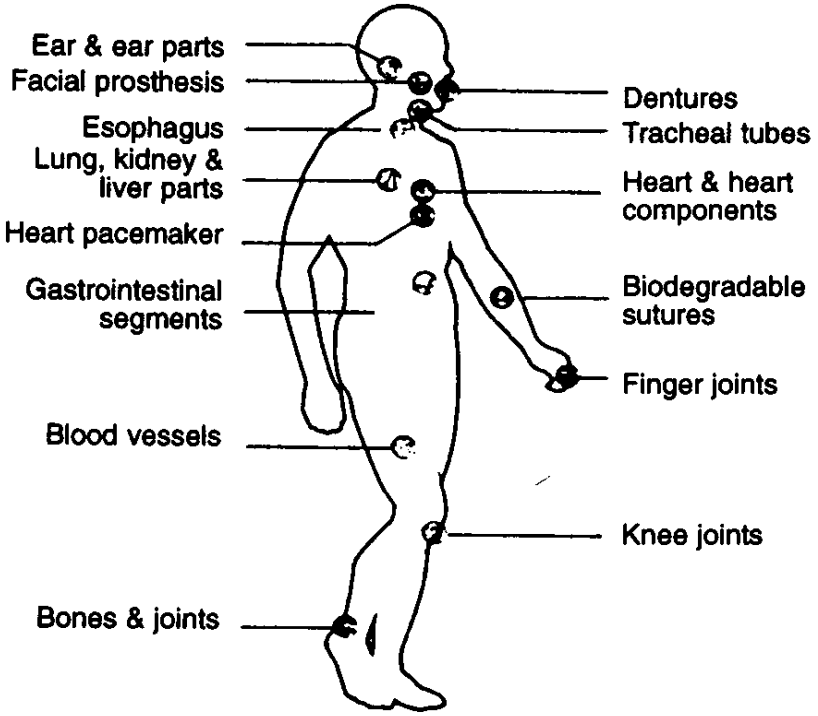

Ear & ear parts: acrylic, polyethylene, silicone, poly(vinyl chloride) (PVC)
Dentures: acrylic, ultrahigh molecular weight polyethylene (UHMWPE), epoxy
Facial prosthesis: acrylic, PVC, polyurethane (PUR)
Tracheal tubes: acrylic, silicone, nylon
Heart & heart components: polyester, silicone, PVC
Heart pacemaker: polyethylene, acetal
Lung, kidney & liver parts: polyester, polyaldehyde, PVC
Esophagus segments: polyethylene, polypropylene (PP), PVC
Blood vessels: PVC, polyester
Biodegradable sutures: PUR
Gastrointestinal segments: silicones, PVC, nylon
Finger joints: silicone, UHMWPE
Bones & joints: acrylic, nylon, silicone, PUR, PP, UHMWPE
Knee joints: polyethylene

Figure 1.1. Common clinical applications and types of polymers used in medicine (Rosato et al. (1983)).

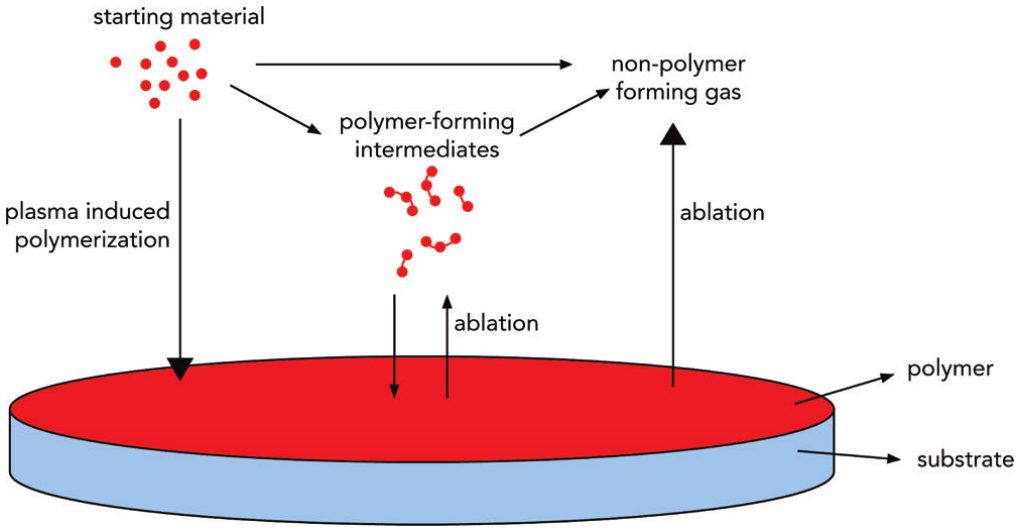

Figure 1.2. A schematic representation of competitive ablation polymerization (Desmet et al. (2009)).

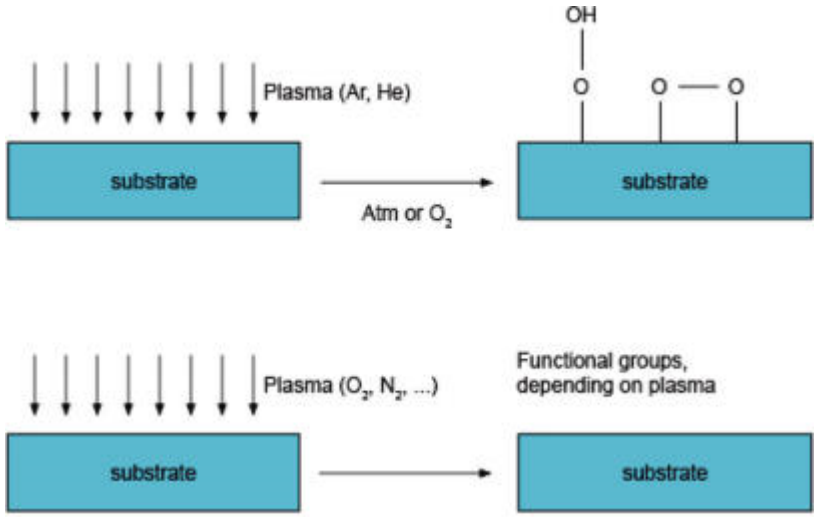

Figure 1.3. A schematic representation of plasma treatment with different plasma gases (Desmet et al. (2009)).

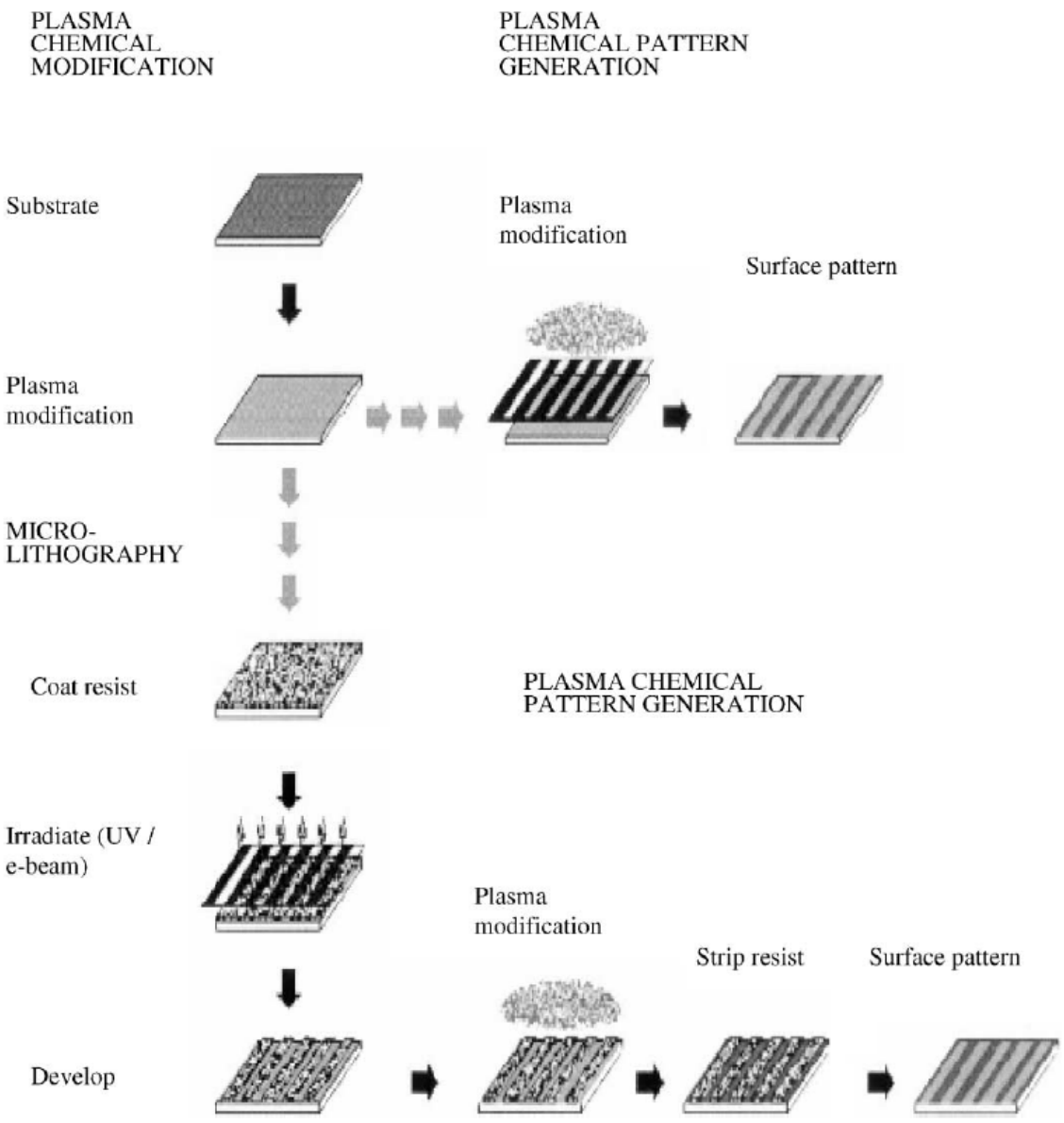

Figure 1.4. Schematic of processing procedures of plasma-induced chemical micro-patterning (Ohl et al. (1999)).

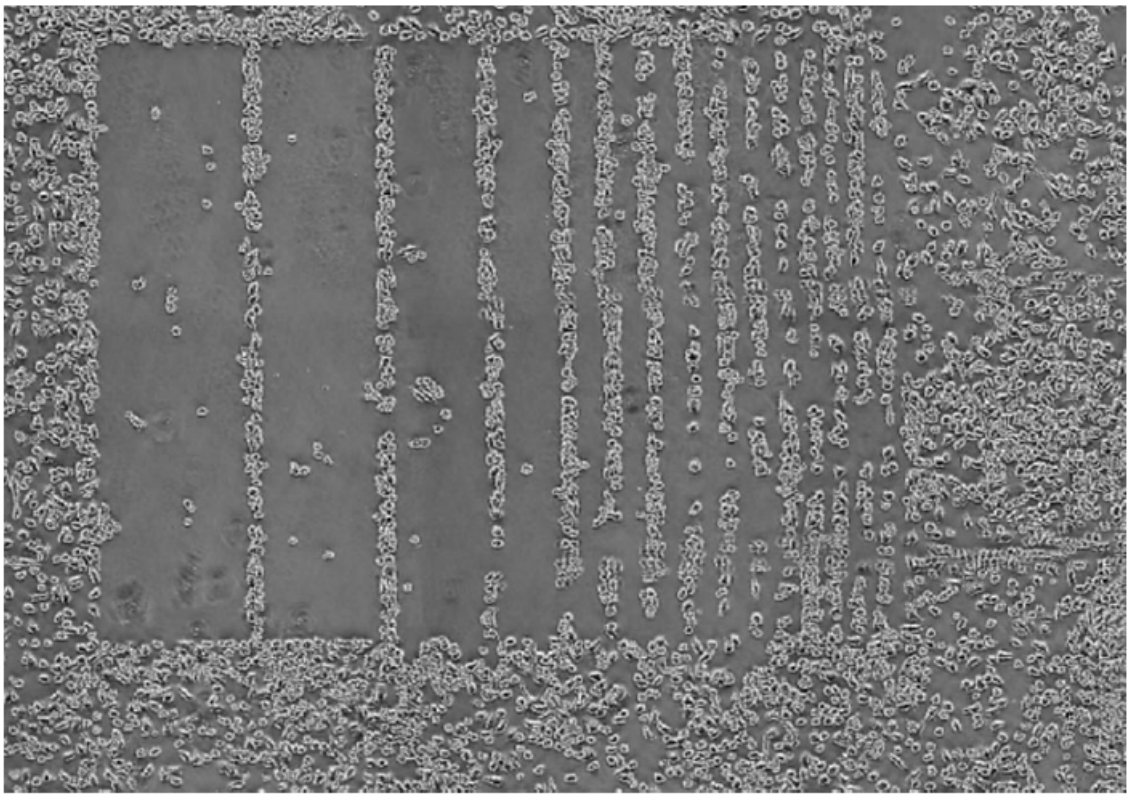

Figure 1.5. Micropatterned growth of epithelial cells (KB nasopharyngeal carcinoma cell line) on a logarithmic stripes pattern (Ohl et al. (1999)).

Chapter 2

Experimental Procedures

2.1 Introduction

In this chapter, the experimental apparatus, procedures, and analysis techniques used in this thesis are explained. Two capacitively coupled plasma systems were employed in this thesis for polymer surface chemistry modification: the plasma apparatus for plasma polymer film deposition (Chapters 3-5), and the plasma apparatus for plasma polymer surface treatment (Chapters 7-8). An electrospinning system was used to prepare PLLA micro/nanofibrous scaffolds and fabricate polymer scaffolds with various fibrous structures (Chapter 9). Different analysis techniques were used to characterize the mechanical, structural and chemical properties of the plasma-treated polymer surfaces and the electrospun scaffolds, including Surface force microscopy (SFM), Atomic force microscope (AFM), Scanning electron microscope (SEM), goniometer for contact angle measurement, Attenuated total reflection-Fourier transform infrared spectroscopy (ATR-FTIR), and X-ray photoelectron spectroscopy (XPS). The effects of polymer surface modification by plasma treatment and structural modification by electrospinning on cells was studied with a set of cell culture and study experiments, which will also be introduced in this chapter.

2.2 Experimental apparatus

2.2.1 Plasma apparatus for plasma film deposition and plasma treatment

A radio-frequency (RF) generated capacitively coupled plasma reactor (Plasma-Thermal Parallel Plate Plasma Etcher RTE73 AMNS-500-E, Plasma therm Inc., Kresson NJ) with a plate diameter 29.4 cm and the plate-to-plate distance 5 cm was used for the fluorocarbon film deposition in Chapter 3 and the PEG-like film deposition in Chapter 4 and 5. The system was pumped by a mechanical pump and a root blower. Samples were placed on the bottom grounded electrode, which was cooled with circulating water to maintain the substrate temperature at 16 ~ 17 °C, and gases were introduced into the chamber via a showerhead upper electrode that was powered by the rf generator. For fluorocarbon film deposition, flow rate of the precursor gas was controlled by the mass flow controller; for PEG-like film deposition, a cylinder containing the diethylene glycol dimethyl ether chemical was connected to the chamber though the shower head and the monomer vapor was introduced into the chamber driven by vapor pressure. The system schematic is shown in Figure 2.1.

A RF capacitively coupled plasma reactor (Plasmalab 80plus, Oxford Instruments, Tubney Woods, Abingdon, Oxfordshire, OX13 5QX, UK) with a plate diameter of 20 cm and plate-to-plate distance equal to 2 cm was used for plasma treatment of polymer surface in Chapter 7 and Chapter 8. The system was pumped by roots pump with dual stage rotary as backing pump, and the chamber pressure is adjustable. Samples were placed on the bottom grounded electrode, for which the temperature can be adjusted with a heater and cooling system.

Gases were introduced into the chamber via a showerhead upper electrode which was powered by the RF generator, and gas flow rate was controlled by the mass flow controller. The system schematic is shown in Figure 2.2.

2.2.2 Electrospinning system for fabricating micro/nanofibrous scaffolds

The common experimental setup for polymer nanofiber electrospinning is shown in Figure 2.3. Polymer solutions are feed to a needle tip connected to a high voltage supply, which charges the polymer solution. Mutual charge repulsion induces repulsive force in the polymer solution that can overcome surface tension of the solution, and polymer jet can be formed and ejected from the tip of the needle. The charged polymer jet undergoes instabilities and gradually thins in air primarily due to elongation and solvent evaporation, and eventually forms randomly oriented nanofibers that can be collected on a stationary or rotating grounded metallic collector. This technique offers opportunity to control the composition, thickness, porosity and structure of the nanofiber meshes using a relatively simple experimental setup, therefore is getting widely used in tissue engineering area. (Vasita et al. (2006))

To prepare microfibrous scaffolds used in Chapter 7 and 8, biodegradable PLLA (1.09 dL/g inherent viscosity) (Lactel Absorbable Polymers, Pelham, AL) was used to fabricate microfibrous membranes by electrospinning, as described previously (Kyle et al. (2010)). The PLLA pellets were first dissolved in hexafluoroisopropanol with ultrasonic water bath (19% w/v), then the solution was delivered by a programmable pump to an electrically charged needle connected to high voltage (12 kV), which ejected polymer fibers with diameter of hundreds of nanometer to micrometer at the tip. The electrostatically charged fiber were driven to fly towards a grounded collecting drum which was kept at 8 cm away, resulting in a nonwoven microfibrous membrane collected on the drum. During electerospinning, the alignment of the microfibers was controlled by adjusting the rotational speed of the collecting drum and the thickness of the membrane was controlled by collecting time. A low speed of rotation (150 rpm) was used to prepare randomly oriented fibers and a high speed of rotation (800 rpm) can be used to prepare aligned fibers. When collecting PLLA mircro/nanofibers on the patterned PDMS templates in Chapter 9, the same system was used except that the grounded template was held stationary at a position 8cm away from the needle tip.

2.3 Surface and thin-film analysis techniques

The effect of the plasma treatment on the mechanical and tribological properties of polymer surface was characterized with SFM. Topography, surface energy, and chemical composition of plasma-treated and plasma polymer film deposited surfaces were studied by AFM, SEM, goniometry, ATR-FTIR and XPS. In this section, operation mechanisms and measurement methods are explained (Tajima (2006)).

2.3.1 Surface force microscopy (SFM)

The modification of the nanomechanical properties of the plasma-treated polymer surfaces is studied with a scanning force microscope (SFM) consisting of an Multimode^{TM} scanning probe microscope (Nanoscope II, Digital Instruments, Santa Barbara, CA) with three

capacitive force transducers (Triboscope, Hysitron, Inc., Minneapolis, MN) shown in Figure 2.4. The center transducer is used for nanoindentation and the two transducers located at both sides are used for nanoscratching. Applied forces are generated electrostatically whereas displacements are measured capacitively.

To determine the change on the mechanical and tribological properties, conospherical diamond tips (Figure 2.5) of nominal radius of curvature R = 1 and 20 μm and the inclined angle θ = 45° are used to indent and scratch the polymer surfaces. The relationships between the contact radius a and the tip penetration depth h are determined from the geometrical relationships

$$a_s = R\sin\left[\cos^{-1}\left(1-\frac{h}{R}\right)\right] \tag{2.1}$$

$$a_c = \left(\sqrt{2}-1\right)R + h \tag{2.2}$$

where a_s and a_c are the contact radii of the spherical apex and conospherical tip. Depending on the penetration depth, the cross-sectional area A, which is a function of h, is calculated from the value of a obtained either from equations (2.1) or (2.2). Before each test, the tip is cleaned with isopropanol to remove any contaminants and/or polymer debris from previous experiments. Nanoindentation and nanoscratching are performed by using those two tips with different radii.

Nanoindentation. The elastic stiffness of plasma treated polymer is determined from nanoindentation experiments. Important parameters and data analysis methods for nanoindentation are outlined here. The normal force (L) versus indentation depth (h) curve obtained from a polymer sample is shown in Figure 2.6. h_{max} is the maximum penetration depth, h_c is the contact depth that is the vertical distance from the tip to the actual contact is made, and h_f is the residual indentation depth upon full unloading. For a given maximum normal load $L_{\max}$, the tip penetrates into the polymer to a maximum indentation depth $h_{\max}$. The actual penetration depth, referred to as the contact depth h_c, is less than $h_{\max}$ (Figure 2.7) because of the deformation of the surface during the indentation (Oliver and Pharr 1992).

The variation of the normal load with indentation depth during unloading is represented by the power-law relationship,

$$L = \alpha(h - h_f)^m \tag{2.3}$$

where α and m are constants determined by curve fitting. The measured load and displacement are L_{max} and h_{max} at the maximum applied load. Upon unloading, the elastic displacements are recovered quickly. The stiffness S is obtained as the average slope of the upper one-third of the unloading curve as shown in Figure 2.6.

$$S = \frac{dL}{dh} \tag{2.4}$$

The reduced elastic modulus E_r is determined from the calculated stiffness S and the measured maximum contact depth $h_{\max}$ by using the following relationship (Bulychev and Alekhin (1987)).

$$E_r = \frac{S}{2}\left[\frac{\pi}{A(h_{\max})}\right]^{1/2} \tag{2.5}$$

where $A(h_{max})$ is the area of contact at maximum indentation depth. Because of the uncertainty in the measurement of h_c in the case of viscoelastic materials and the pile-up of polymer around the tip at maximum load, which is difficult to estimate in situ, the polymer stiffness and the reduced modulus are obtained in terms of $h_{\max}$. The relationships between the elastic modulus of the material and the reduced modulus is

$$\frac{1}{E_r} = \frac{(1-\nu^2)}{E} + \frac{(1-\nu_i^{\,2})}{E_i} \approx \frac{(1-\nu^2)}{E} \tag{2.6}$$

where E and v are Young's modulus and Poisson's ratio for the sample and E_i (~1140 GPa) and v_i (~0.07) are the corresponding parameters for the indenter made of diamond. Since $E_i >> E$, the second term in equation (2.6) can be ignored. The detail theory and mechanism of nanoindentation have been explained elsewhere (Oliver and Pharr (1992, 2004), Hysitron Inc.).

Nanoscratching. Nanoscratching experiments are carried out in order to evaluate the frictional characteristics of the original and plasma-treated polymer. The loaded tip is traversed over the specimen surface and is then unloaded at the same rate as for the loading. The tangential (friction) force F is measured by a two-parallel plate transducer located at both sides in Figure 2.4 and is used to calculate the coefficient of friction μ for the maximum normal load applied, i.e., $\mu = F/L$, as a function of sliding distance. To examine the extent of plasma-induced modification (i.e., crosslinking) on the frictional characteristics, the steady-state frictional force and the coefficient of friction are plotted as a function of average scratch depth $\bar{h}$ (Figure 2.8).

2.3.2 Atomic force microscopy (AFM)

Morphology (topography) of the plasma treated polymer surfaces was studied at various scales with an AFM (Dimension 3100, Veeco Instruments Inc. Plainview, NY) operated in tapping mode to avoid surface damage of the soft surfaces. The schematic of the AFM is shown in Figure 2.9. The tip was mounted on a piezoelectric scanner (piezo) allowing extremely precise movement in the x, y, and z directions, and the sample is placed on a vibration isolating table.

The head of the AFM consists of the laser beam source, piezo tube scanner, mirrors, and the removable cantilever holder, as shown in Figure 2.10. When operated under tapping mode, a piezo stack excites the cantilever's substrate vertically, causing the tip to bounce up and down. As the cantilever bounces vertically, the reflected laser beam is deflected in a regular pattern over a photodiode array, generating a sinusoidal electronic signal. The signal is converted to a root mean square amplitude value. Figure 2.11 showed a cantilever oscillating in free air at its resonant frequency, and Figure 2.12 showed the same cantilever at the sample surface. Although

the piezo stack continues to excite the cantilever's substrate with the same energy, the tip is deflected in its encounter with the surface. The reflected laser beam ("return signal") reveals information about the vertical height of the sample surface and some characteristics of the sample material itself.

During tapping mode scanning, the cantilever is oscillated at or near its resonance frequency with amplitude ranging typically from 20nm to 100nm. The frequency of oscillation can be at or on either side of the resonant frequency. The tip lightly "taps" on the sample surface during scanning, contacting the surface at the bottom of its swing. The feedback loop maintains constant oscillation amplitude by maintaining a constant RMS of the oscillation signal acquired by the split photodiode detector. The vertical position of the scanner at each (x,y) data point in order to maintain a constant "setpoint" amplitude is stored by the computer to form the topographic image of the sample surface. By maintaining constant oscillation amplitude, a constant tip-sample interaction is maintained during imaging.

Surface images are obtained from 1 μm × 1 μm, 5 μm × 5 μm, and 10 μm × 10 μm area scans using a resolution of 512 × 512 pixels. The sampling length represents the scale at which the roughness parameters are determined from the AFM images. Thus, the 1 μm × 1 μm and 10 μm × 10 μm area scans may be considered to be indicative of the nanoscale and microscale surface topographies. For a quantitative evaluation of the topography changes, the centerline average roughness (CLA) R_a, root-mean-square roughness R_q, skewness S, and kurtosis K, are calculated from surface height data z_i obtained from AFM area scans by using numerical integration and the following relationships:

$$R_a = \frac{1}{N}\sum_{i=1}^{N}\left|z_i - \bar{z}\right| \quad (2.7)$$

$$R_q = \left[\frac{1}{N}\sum_{i=1}^{N}\left|z_i - \bar{z}\right|^2\right]^{1/2} \quad (2.8)$$

$$S = \frac{1}{R_q^3}\frac{1}{N}\sum_{i=1}^{N}\left(z_i - \bar{z}\right)^3 \quad (2.9)$$

$$K = \frac{1}{R_q^4}\frac{1}{N}\sum_{i=1}^{N}\left(z_i - \bar{z}\right)^4 \quad (2.10)$$

where N is the number of surface height data (i.e., N = 512 × 512 = 262144) and $\bar{z}$ is the mean-height distance. To consider the experimental scatter, roughness data are calculated as averages of four measurements obtained from two samples for each treatment. More details on AFM operation mechanisms are found elsewhere (Digital Instruments (1997)).

2.3.3 Scanning electron spectroscopy (SEM)

A SEM (TM-1000, Hitachi, Pleasanton, CA) is used to examine topography of different surfaces: plasma treated polymer microfibrous membrane, attached platelets on membrane, patterned collector for electrospinning, patterned electrospun polymer microfibrous membrane, etc.

SEM is a type of electron microscope that images a sample by scanning it with a high-energy beam of electrons in a raster scan pattern. The electrons interact with the atoms that make up the sample producing signals that contain information about the sample's surface topography, composition, and other properties such as electrical conductivity. The types of signals produced by an SEM include secondary electrons, back-scattered electrons, characteristic X-rays, light (cathodoluminescence), specimen current and transmitted electrons. Secondary electron detectors are common in all SEMs, but it is rare that a single machine would have detectors for all possible signals. The signals result from interactions of the electron beam with atoms at or near the surface of the sample. In the most common or standard detection mode, secondary electron imaging, the SEM can produce very high-resolution images of a sample surface, revealing details about less than 1 to 5 nm in size. Due to the very narrow electron beam, SEM micrographs have a large depth of field yielding a characteristic three-dimensional appearance useful for understanding the surface structure of a sample. A wide range of magnifications is possible, from about 10 times (about equivalent to that of a powerful hand-lens) to more than 500,000 times, about 250 times the magnification limit of the best light microscopes. Back-scattered electrons are beam electrons that are reflected from the sample by elastic scattering. Back-scattered electrons are often used in analytical SEM along with the spectra made from the characteristic X-rays. Because the intensity of the back-scattered electrons signal is strongly related to the atomic number (Z) of the specimen, BSE images can provide information about the distribution of different elements in the sample. Characteristic X-rays are emitted when the electron beam removes an inner shell electron from the sample, causing a higher energy electron to fill the shell and release energy. These characteristic X-rays are used to identify the composition and measure the abundance of elements in the sample.

In a typical SEM, an electron beam is thermionically emitted from an electron gun fitted with a tungsten filament cathode. Tungsten is normally used in thermionic electron guns because it has the highest melting point and lowest vapour pressure of all metals, thereby allowing it to be heated for electron emission, and because of its low cost. Other types of electron emitters include lanthanum hexaboride (LaB6) cathodes, which can be used in a standard tungsten filament SEM if the vacuum system is upgraded and field emission guns, which may be of the cold-cathode type using tungsten single crystal emitters or the thermally-assisted Schottky type, using emitters of zirconium oxide.

The electron beam, which typically has an energy ranging from 0.5 keV to 40 keV, is focused by one or two condenser lenses to a spot about 0.4 nm to 5 nm in diameter. The beam passes through pairs of scanning coils or pairs of deflector plates in the electron column, typically in the final lens, which deflect the beam in the x and y axes so that it scans in a raster fashion over a rectangular area of the sample surface.

When the primary electron beam interacts with the sample, the electrons lose energy by repeated random scattering and absorption within a teardrop-shaped volume of the specimen

known as the interaction volume, which extends from less than 100 nm to around 5 µm into the surface. The size of the interaction volume depends on the electron's landing energy, the atomic number of the specimen and the specimen's density. The energy exchange between the electron beam and the sample results in the reflection of high-energy electrons by elastic scattering, emission of secondary electrons by inelastic scattering and the emission of electromagnetic radiation, each of which can be detected by specialized detectors. The beam current absorbed by the specimen can also be detected and used to create images of the distribution of specimen current. Electronic amplifiers of various types are used to amplify the signals which are displayed as variations in brightness on a cathode ray tube. The raster scanning of the Cathode-ray tube display is synchronised with that of the beam on the specimen in the microscope, and the resulting image is therefore a distribution map of the intensity of the signal being emitted from the scanned area of the specimen. The image may be captured by photography from a high resolution cathode ray tube, but in modern machines is digitally captured and displayed on a computer monitor and saved to a computer's hard disk.

The schematic of SEM is shown in Figure 2.13. Electron beam is ejected by the electron gun and focused by the condenser to decrease spot size down to 100nm ~ 1µm to insure spatial resolution. Scan coil can bend the electron beam laterally and realize scanning of the beam in x, y direction. When the electrons reach specimen surface, different signals can be produced due to electro-specimen interaction, as shown in Figure 2.14. Secondary electrons are from atoms on the specimen surface activated due to inelastic collision between the beam electron and the atom, which usually have energy less than 50 eV. Due to the low energy of the secondary electrons, only signal from the super surface layer can be detected, therefore secondary electron signal is the most widely used signal for surface topography detection. More details on SEM operation mechanisms are found elsewhere (Zhou et al. (2006), Scanning_electron_microscope at Wiki.org).

2.3.4 Contact angle goniometry

The wettability of different surfaces is quantified in terms of static contact angle measurements obtained at room temperature with a drop shape analysis system (DSA10, Krüss GmbH, Hamburg, Germany) shown in Figure 2.15. Droplets of deionized water (0.2-0.4 µL) are applied to the sample surface with a syringe, and the droplet image is taken within a few seconds from application. The angle between the baseline of the droplet and the tangent at the water/air boundary are measured from both sides of the two-dimensional projection of the droplet using the DSA1 software (Krüss GmbH, Hamburg, Germany). The hydrophilic surface has contact angle less than 90° with high surface energy. On the contrary, the hydrophobic surface has contact angle more than 90° with low surface energy. Droplet shapes from hydrophilic and hydrophobic surfaces are shown in Figures 2.16.

2.3.5 Attenuated total reflected-Fourier transform infrared spectroscopy (ATR-FTIR)

Dominant chemical groups of the polymer films deposited by plasma processing were identified with a FTIR spectrometer (Nicolet Avatar 360, Thermo Fisher Scientific, Waltham, MA), using a Ge crystal of refractive index equal to 4.0 and incidence angle fixed at 45°. Spectra

were collected by operating the FTIR in attenuated total reflectance (ATR) mode in the range of mid-infrared, approximately 4000–400 cm^{-1} (30–2.5 μm). For each measurement, 32 scans were obtained at a resolution of 4 cm^{-1}.

FTIR is a technique which can measure the infrared spectrum absorption of a solid, liquid or gas. The principle of absorption spectroscopy is to measure how well a sample absorbs light at each wavelength, and the most straightforward way to do this is to shine a monochromatic light beam at a sample, measure how much of the light is absorbed, and repeat measurement for each different wavelength. Fourier transform spectroscopy is a less intuitive way to obtain the same information. Rather than shining a monochromatic beam of light at the sample, this technique shines a beam containing many different frequencies of light at once, and measures how much of that beam is absorbed by the sample. Next, the beam is modified to contain a different combination of frequencies, giving a second data point. This process is repeated many times. Afterwards, a computer takes all these data and works backwards to infer what the absorption is at each wavelength.

The beam described above is generated by starting with a broadband light source-one containing the full spectrum of wavelengths to be measured. The light shines into a certain configuration of mirrors, called a Michelson interferometer, which allows only certain wavelengths to pass through but blocks others due to wave interference. The beam is modified for each new data point by moving one of the mirrors, and this changes the set of wavelengths that pass through. As shown schematically in Figure 2.17. After data collecting, computer processing is required to turn the raw data (light absorption for each mirror position) into the desired result (light absorption for each wavelength). The processing required turns out to be a common algorithm called the Fourier transform, and that’s the origin of the name "Fourier transform spectroscopy".

ATR accessory operates by measuring the changes that occur in a totally internally reflected infrared beam when the beam comes into contact with a sample, as indicated in Figure 2.18. The infrared beam is directed onto an optically dense crystal with a high refractive index at a certain angle. This internal reflectance creates an evanescent wave that extends beyond the surface of the crystal into the sample held in contact with the crystal. This evanescent wave propagates only a few microns (0.5 μm - 5 μm) beyond the crystal surface and into the sample. Consequently, there must be good contact between the sample and the crystal surface. In regions of the infrared spectrum where the sample absorbs energy, the evanescent wave will be attenuated or altered. The attenuated energy from each evanescent wave is passed back to the IR beam, which then exits the opposite end of the crystal and is passed to the detector in the IR spectrometer, and the system then generates an infrared spectrum. More details on ATR-FTIR operation mechanisms are found elsewhere (Fourier_transform_infrared_spectroscopy at Wiki.org, PerkinElmer, ATR-FTIR Technical Note).

2.3.6 X-ray photoelectron spectroscopy (XPS)

XPS, or also called as electron spectroscopy for chemical analysis (ESCA) was used to determine the polymer surface chemical composition after plasma treatment, chemical derivatization and molecules/protein adsorption. This technique is capable of measuring the

binding energy variations of the core-level electrons of atoms at the surface of the sample. XPS permits analysis of the outermost 20-100 Å of a sample in a diameter between 150 μm and 1000 μm. XPS spectra are obtained with a Perkin-Elmer PHI 5400 ESCA system (without charge neutralization or monochromator) using Al Kα X-ray source at 54.7º relative to the analyzer axis (Figure 2.19). In order to avoid the contamination on the sample surface during the measurement, the pressure in the main chamber during spectral acquisition is maintained at 10^{-8} torr. A diagram of a sample installation chamber, a main chamber, an X-ray source, a concentric hemispherical analyzer, and a detector are shown in Figure 2.20 and the operation mechanisms of XPS are described herein.

X-rays are generated by bombarding a metal target (anode) with high energy electrons from a heated filament. In this dissertation, Al $K\alpha_{1,2}$ X-ray source with photon energy 1486.6 eV is used. $K\alpha_{1,2}$ are the most intense peaks in emitted X-rays. Relatively high level of incident energy causes a release of electrons from an atom's internal shell. The atom can either emit photon or undergo an Auger transition to recover from this ionized state. The released electron retains all the energy from the striking photon, and then escape from the atom as shown in Figure 2.21. The relationship between the applied photon energy, kinetic and binding energies of the ejected electrons are related by the equation below.

$$h\nu = E_K + E_B + \phi_{sp} \tag{2.11}$$

where h is a Plank's constant (6.62×10^{-34} J s), ν is frequency (Hz) of the radiation, $h\nu$ is X-ray beam incident energy for Al Kα radiation = 1486.6 eV, E_K is electron kinetic energy, and E_B is electron binding energy of the core-level electrons**.** Accurate measurement of E_B can provide the information of the electronic structure of the sample. The sum of E_K and E_B does not exactly equal to the applied photon energy as shown in the equation (2.11). The difference is the work function of the spectrometer ϕ_{sp}, which is the maximum energy required to eject an electron from the highest occupied level into a vacuum. Work function of the spectrometer is calculated by subtracting vacuum level E_{vac} from Fermi level E_f.

$$\phi_{sp} = E_f - E_{vac} \tag{2.12}$$

The work function of the spectrometer is calibrated by measuring a clean gold (Au) sample and adjusting the instrument settings (Fermi level at 0 eV) so that the known E_B value for Au is obtained ($4f_{7/2}$ core level at E_B = 83.98 eV). The linearity of the E_B scale is then calibrated by using the energy difference between two widely spaced lines of a sample (e.g., Cu $2p_{3/2}$ = 932.67 eV, Cu $3p_{3/2}$ = 75.14 eV) to their known values. Once the spectrometer energy scale has been calibrated, the work function is assumed to remain constant as long as the spectrometer is maintained in an ultrahigh vacuum (UHV) environment. If the pressure of the spectrometer is not maintained in UHV range, particularly when exposed to a reactive gas, different species may adsorb to components in the analyzer. This will change the work function, requiring recalibration.

When the calibration of the work function is finished, E_B can be calculated from equation (2.11) by measuring E_K. E_K of ejected electrons from the sample is measured at the detector after isolating the electrons of interest in the analyzer. An electron lens system shown in Figure 2.20 focuses ejected electrons from the sample in the main chamber into a centric hemispherical

analyzer consisting of two plates carrying an electron potential. Two hemispheric surfaces of different radii are mounted with a uniform gap between their surfaces (see Figure 2.20). A potential difference between the hemispheres determines the field, and hence the force acting on the electron entering the analyzer as shown in equation below.

$$F = qE = m(V^2/R) \tag{2.13}$$

where F is a force, V is a speed of electrons, R is a trajectory radius, E is an electrical field established by potential difference between the two plates, m is a electron mass, and q is an electron charge. The trajectory radius is controlled by the electric field and the kinetic energy of the electron ($E_K = 0.5\ mV^2$). Only electrons with the appropriate kinetic energy and an acceptable entry angle will reach the diametrically opposed exit. All others hit one of the surfaces of the hemisphere. This means that the hemispherical analyzer behaves like a filter of electrons.

Electrons are either accelerated or decelerated by biasing the whole analyzer with respect to the ground by applying a pass energy U. Lower pass energies provide higher spectral resolution, while higher pass energies permit more rapid data acquisition with low signal-to-noise ratio. The number and E_K of electrons exit from the analyzer was detected by the position sensitive detector system and then processed with the computer to plot E_B, calculated from measured E_K by using equation (2.11), versus the number of electrons ejected from the analyzer.

For insulators such as polymers, Fermi levels of the sample and the spectrometer are different. Consequently, the work function determined by the conducting calibration sample cannot be used to determine the binding energy for the insulator. The entire binding energy (E_B) scale is shifted to the internal references (C-C/C=C/C-H peak at 285eV) after the peak acquisition was completed.

Chemical composition of the material surface was first obtained from the survey scan from 1-mm-diameter surface areas using the pass energy of 187 eV and the resolution of 1.0 eV in this dissertation. The plot with binding energy (0 ~ 1100 eV) as an independent axis and the peak ‘intensity’ as a dependent axis is obtained from the computer attached to the analyzer. Each peak indicates the chemical composition of these particular surfaces.

After chemical composition is identified by survey scans, details of each chemical component can be observed in the high resolution scan. The spectrum composed of a number of subpeaks, attributed to chemical shifts from different atoms and groups bound to carbons can be identified from the high resolution scan. Quantitative information is obtained from the ratio of the areas under the fitted peaks.

In this dissertation, high resolution scans are obtained from 1-mm-diameter surface areas using pass energy of 35.75 eV and the resolution of 0.05 eV. Relative atomic concentrations are determined from Gaussian-Lorenzian (GL) curve fits using the RBD AugerScan 2 software (RBD Enterprises, Inc., Bend, OR) after Shirley subtraction of the background noise (Shirley (1972)). Same full width at half maximum (FWHM) is used for curve-fitting all components in the C1s spectrum.

2.4 Cell culture and study

Cell seeding and culture are used to check the biological effects of different plasma assisted polymer surface modifications on cells, as well as the effect of electrospun scaffold structure on cells. The cell seeding, culturing, staining and imaging procedures are explained in this section.

2.4.1 Cell culture and staining

Different cell lines including bovine aorta endothelial cells (BAECs), bovine smooth muscle cells (BSMCs), human mesenchymal stem cells (hMSCs) are used for studies in this thesis. The cells are usually seeded on plasma treated or patterned surface/structure with proper medium. After certain incubation time, the cells were then fixed in 4% paraformaldehyde (PFA) (Fisher Scientific Co., Pittsburgh, PA) for 15 min and permeabilized with 0.5% Trition X-100 (EM Chemicals, Inc., Gibbstown, NJ) for 5 min. To check cell morphology, cell actin and nuclei are usually stained. Alexa-phalloidin (Invitrogen Co., Carlsbad, CA) was used to stain the cells for 1 h in dark space for actin filament evaluation, and the cell nuclei were stained with 300 nM of 4',6-diamidino-2-phenyindole (DAPI) (Invitrogen Co., Carlsbad, CA) for 5 min. After PBS wash, Vector-Shield antifade solution (Vector Laboratories, Burlingame, CA) was applied onto sample surface for fluorescence microscopy measurements, and cell imaging was then performed with fluorescence microscopes or confocal microscopes.

2.4.2 Cell proliferation rate study

For cell proliferation study, cells are usually seeded on different surfaces, cultured for 24 h, and then incubated for 1h with 10 μM EdU (Invitrogen, Carlsbad, CA). Then the samples were fixed with 4% PFA, permeabilized with 0.5% Triton X-100, blocked with 3 mg/ml bovine serum albumin and stained with click-it EdU kit (Invitrogen, Carlsbad, CA). The percentage of cells that incorporated EdU (i.e., the cells with DNA synthesis) was correlated to the proliferation rate of the studied cells.

2.4.3 Cell infiltration study

In vitro cell infiltration model. BAECs are usually used to study in vitro cell infiltration on polymer microfibrous scaffolds due to their migration ability. Microfibrous membranes with ~ 250 mm thickness were produced by electrospinning and were subsequently cut into 0.7 cm x 0.7 cm membranes. Untreated control membranes were sterilized in 70% ethanol while under ultraviolet light for 30 min and subsequently washed five times with sterile phosphate buffered saline (PBS). Three microfibrous membranes representing both control group and study groups were then attached to non-tissue-culture-treated polystyrene dishes via sterile double-sided tape. BAECs are seeded at 100% confluency onto the membranes and kept for 5 days or longer in serum medium in an incubator, then the whole membrane was fixed with 4% PFA and then stained with DAPI before put in in optimal cutting temperature (OCT) compound (TissueTek, Elkhart, IN) on dry ice. Cross-sections of 20-um thickness were taken in the transverse plane in a -20 ºC cryosectioner. The DAPI fluorescent signals from the cells within these cryosections are then checked under a fluorescence microscope to determine the cell ingrowth results.

In vivo cell infiltration model under rat skin. Under rat skin implantation is usually used to study the in vivo cell infiltration on polymer microfiberous scaffolds. Untreated control membranes were sterilized in 70% ethanol while under ultraviolet light for 30 min and subsequently washed five times with sterile phosphate buffered saline (PBS). Three membranes representing both control group and study groups are implanted in the subcutaneous cavity of SD rats as following. For implantation, rats were anesthetized with isofluorane and the incision site marked and disinfected with 70% ethanol. Incisions can be made on both sides and middle of abdominal wall of the rat. Scaffolds with different treatments were implanted to one side of the incision and tucked subcutaneous away from the incision. Interrupted 5-0 Monocryl (Ethicon, Inc., Somerville, NJ) mattress sutures were used to sew the cut. All animals were monitored daily by a veterinarian and insure that no adverse events are noted in any of the animals. At the end of the experiments, the rats were returned to the operating room, where they were given general anesthesia and an overdose of euthanasia solution, then implants and surrounding tissue was taken out and embedded in OCT on dry ice. Cross-sections of 10-um thickness were taken in the transverse plane in a -20 ºC cryosectioner. Then the sections were fixed with 4% PFA, stained with DAPI, and examined under a fluorescence microscope to determine the cell infiltration results.

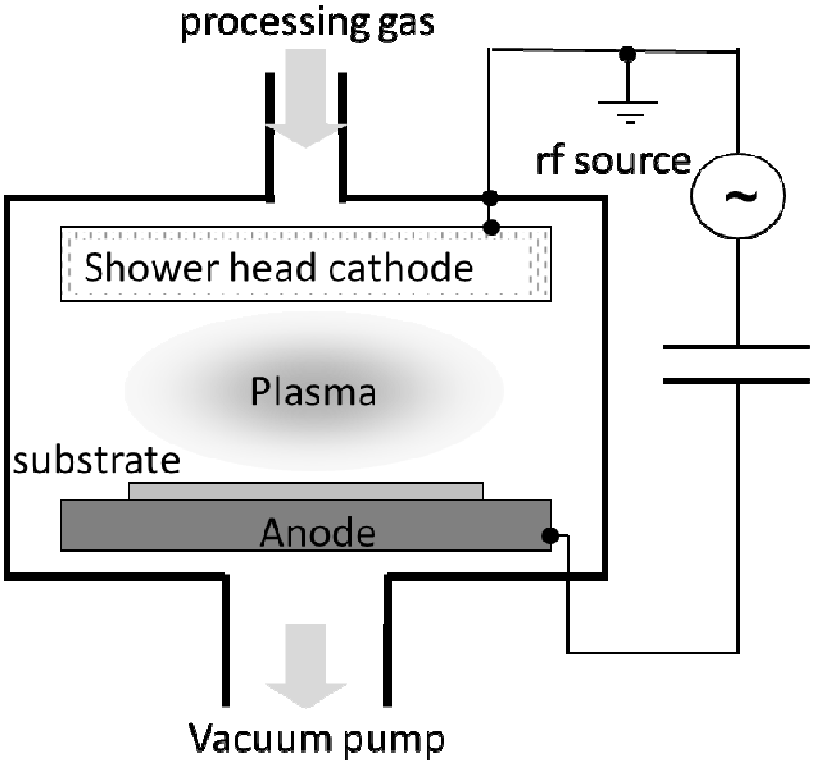

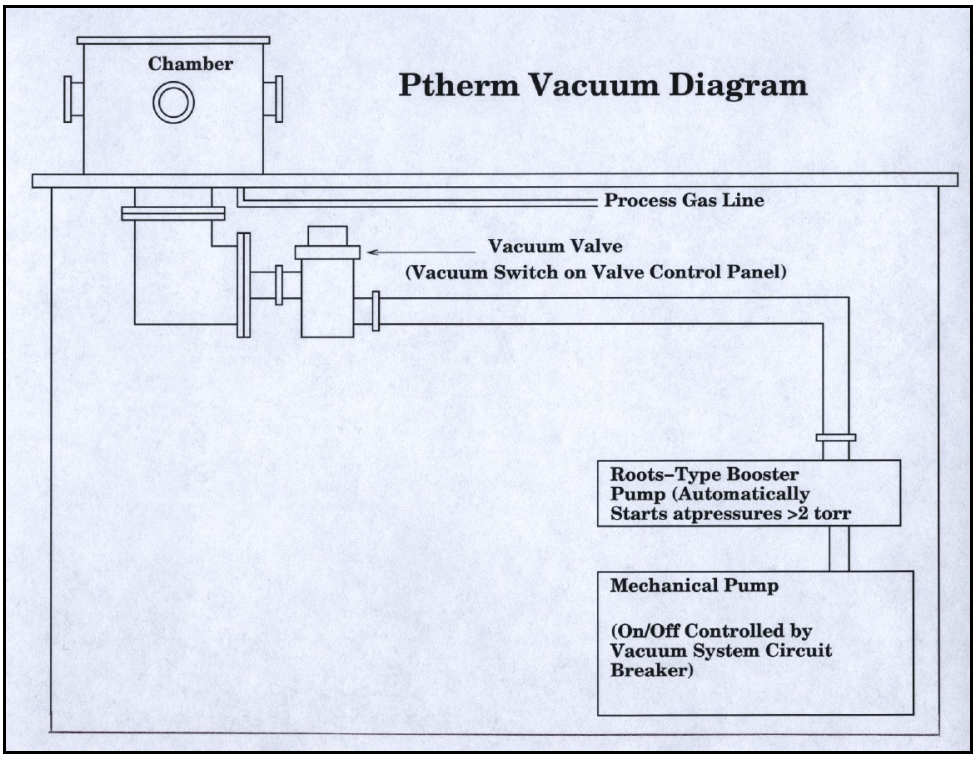

Figure 2.1. Schematic of plasma apparatus for plasma polymer film deposition (Tajima (2006)).

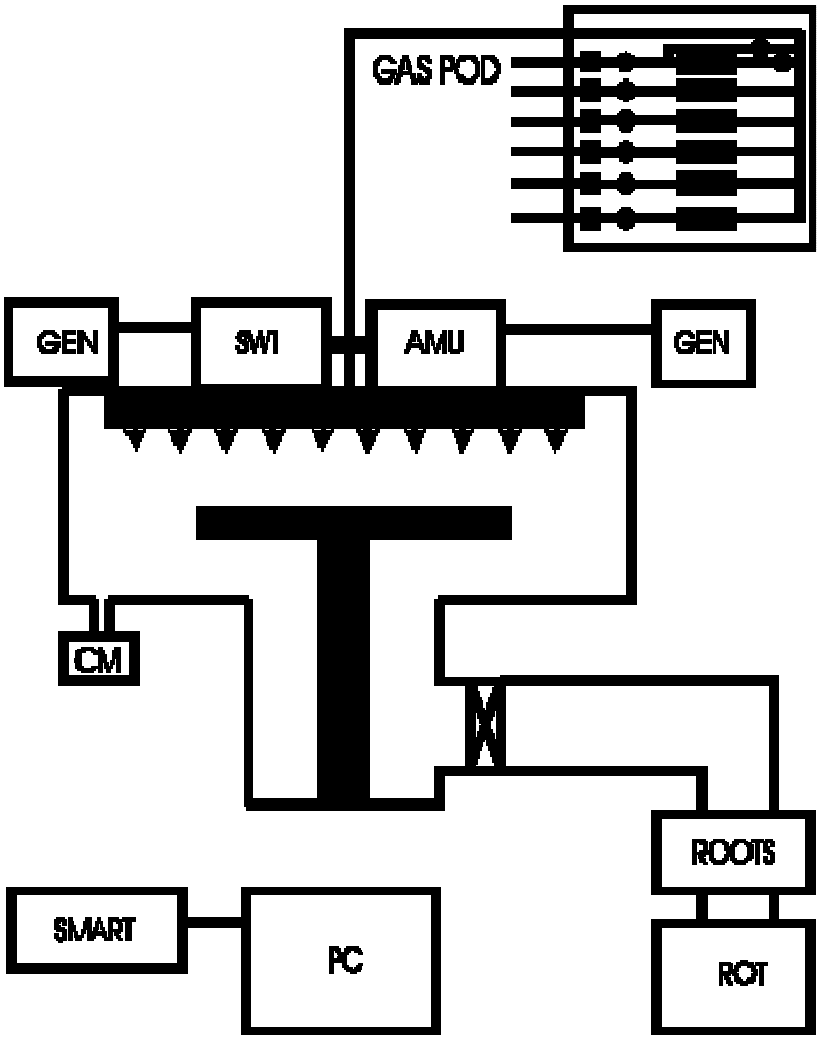

Figure 2.2. Schematic of plasma apparatus for plasma treatment of polymer surface (oxfordplasma.de).

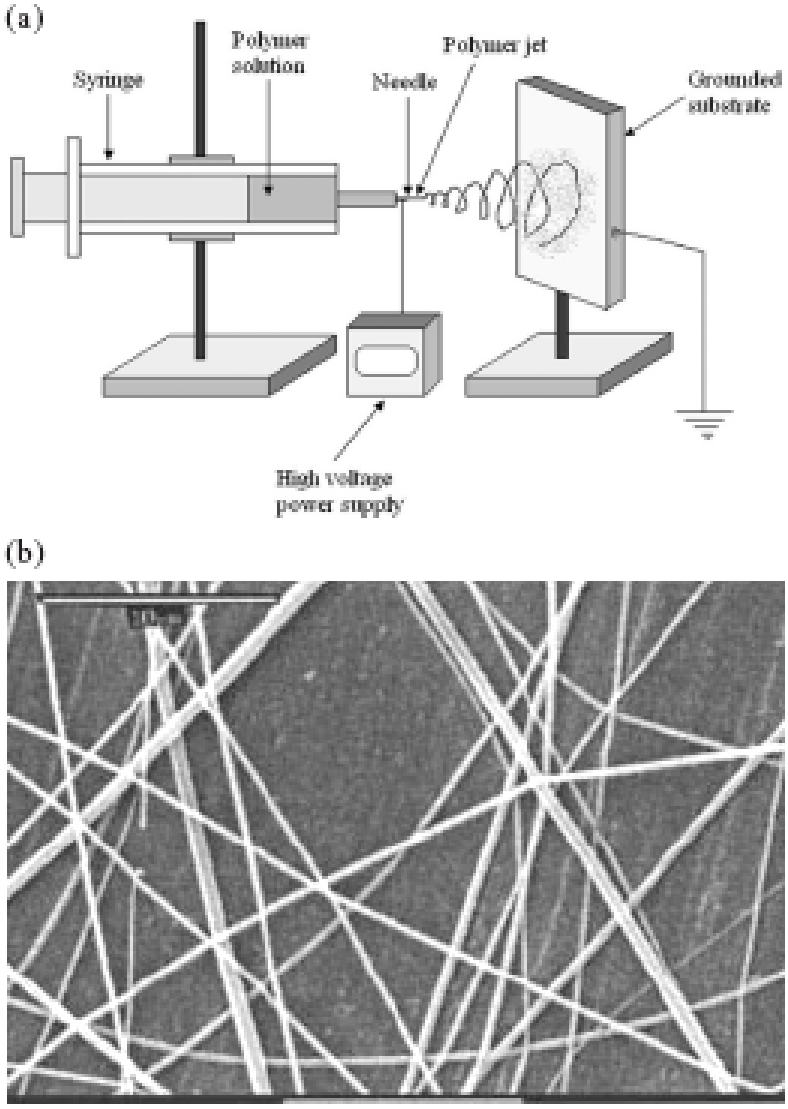

Figure 2.3. (a) Schematic of the electrospinning process. (b) Scanning electron micrograph of poly(lactic-co-glycolic acid) (PLGA) nanofibers synthesized using the electrospinning technique (scale bar = 10 μm) (Katti et al. (2004)).

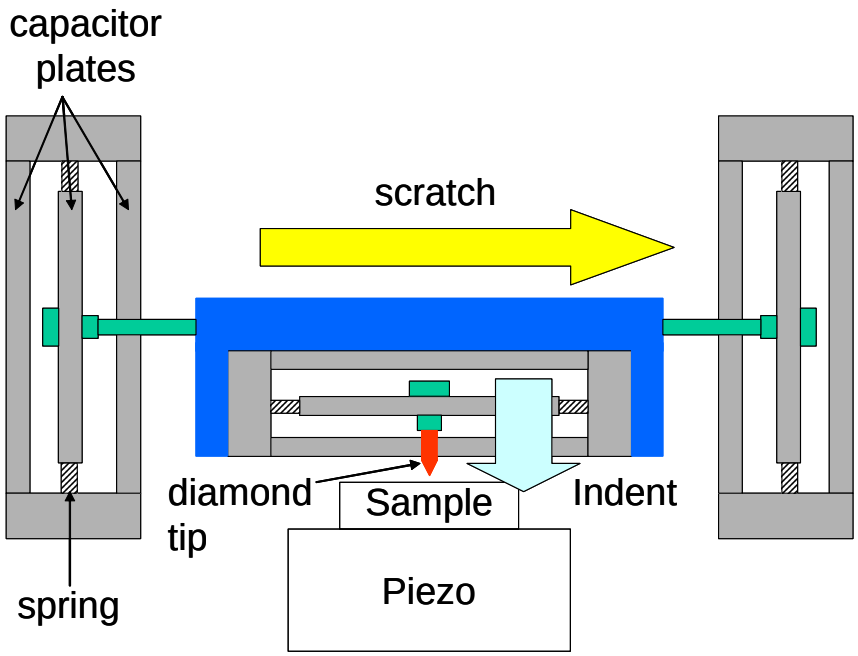

Figure 2.4. Schematic of 2-D capacitive plates of SFM (Tajima (2006)).

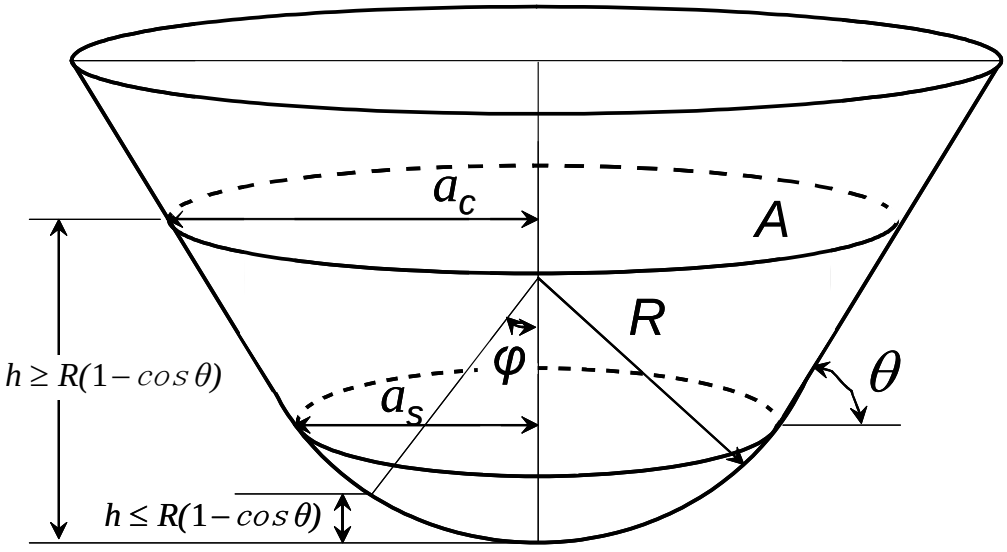

Figure 2.5. Schematic of conoshperical tip dimension (Tajima (2006)).

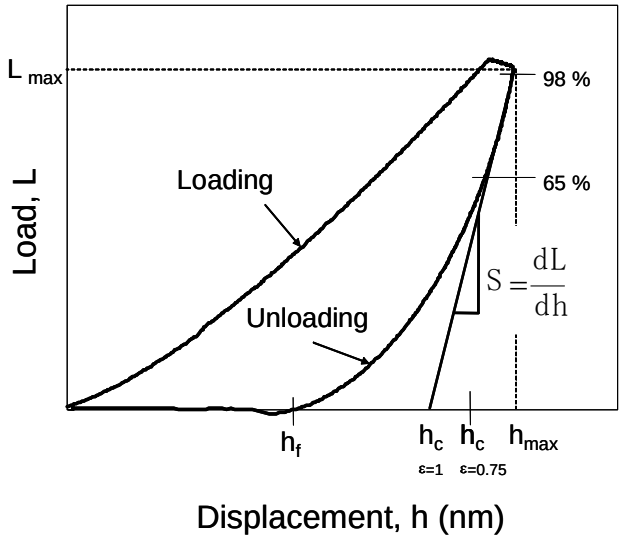

Figure 2.6. Nanoindentation of polymer substrate (Tajima (2006)).

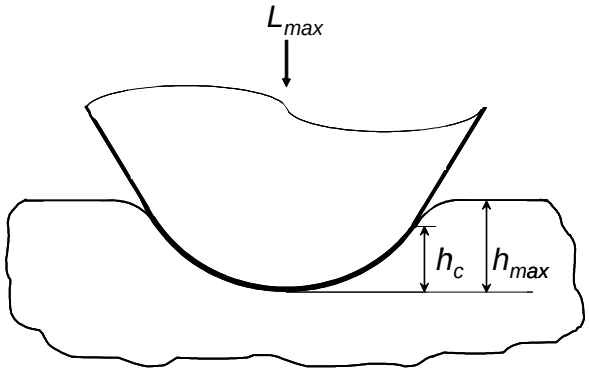

Figure 2.7. Tip depth during the indentation (Tajima (2006)).

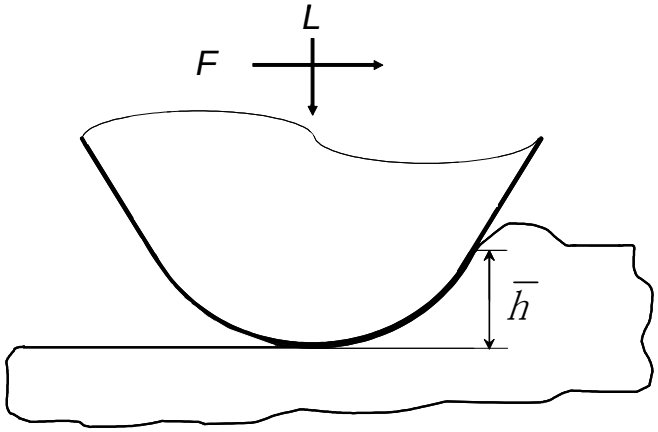

Figure 2.8. Tip depth during the scratching (Tajima (2006)).

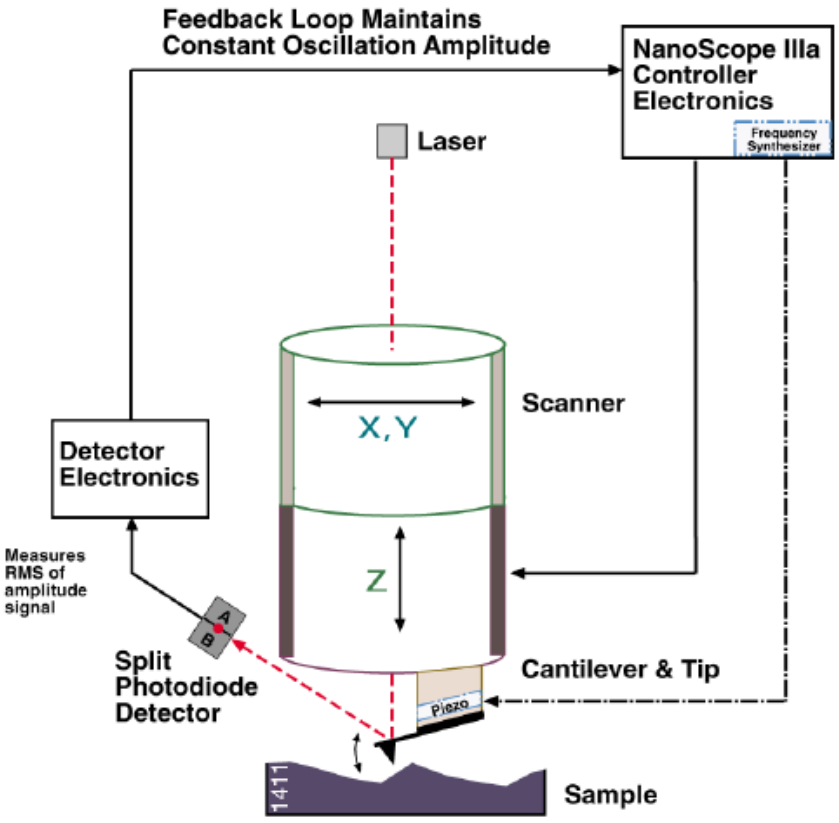

Figure 2.9. Schematic of the Veeco DI 3100 AFM working in tapping mode (Digital Instruments (1997)).

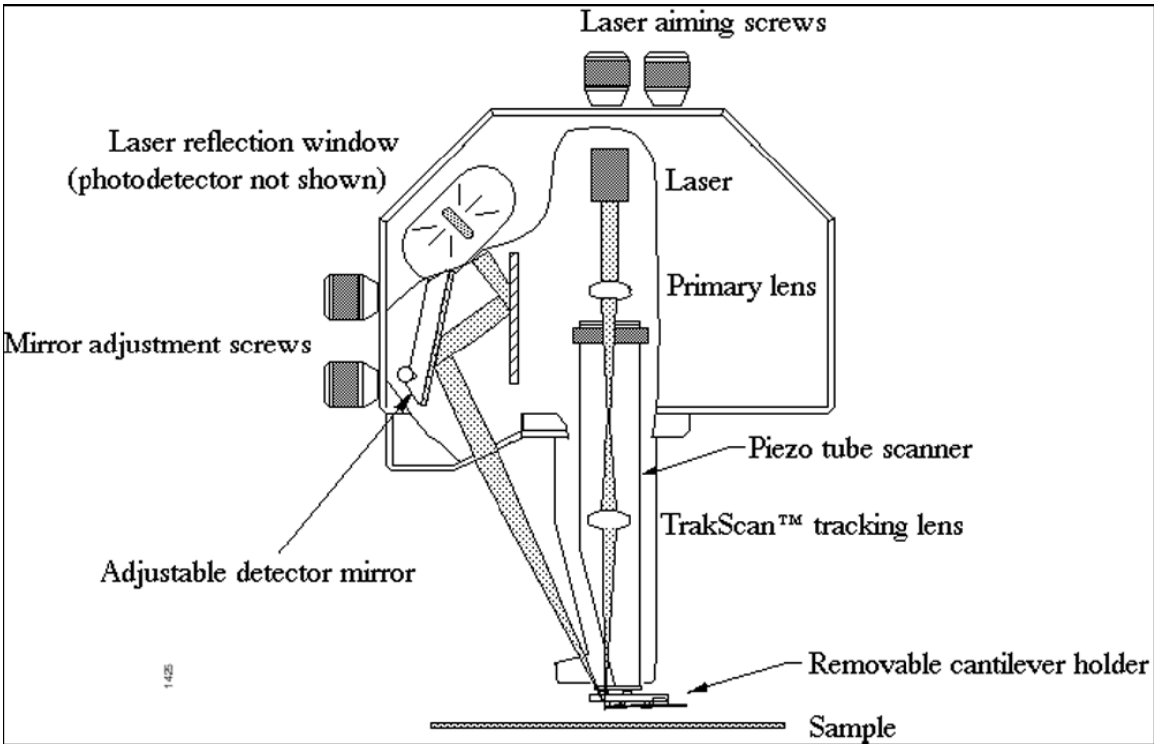

Figure 2.10. Schematic of Veeco DI 3100 AFM head (Digital Instruments (1997)).

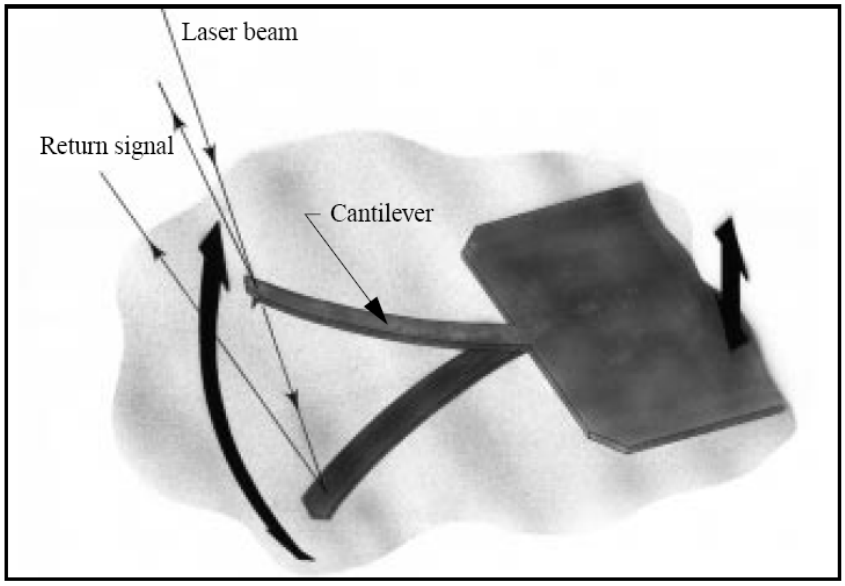

Figure 2.11. Tapping cantilever in free air (Digital Instruments (1997)).

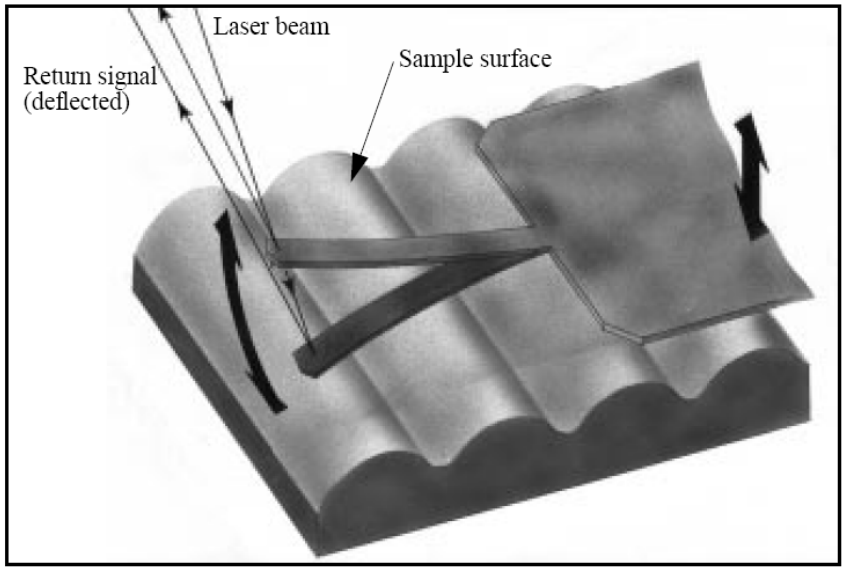

Figure 2.12. Tapping cantilever on sample surface (Digital Instruments (1997)).

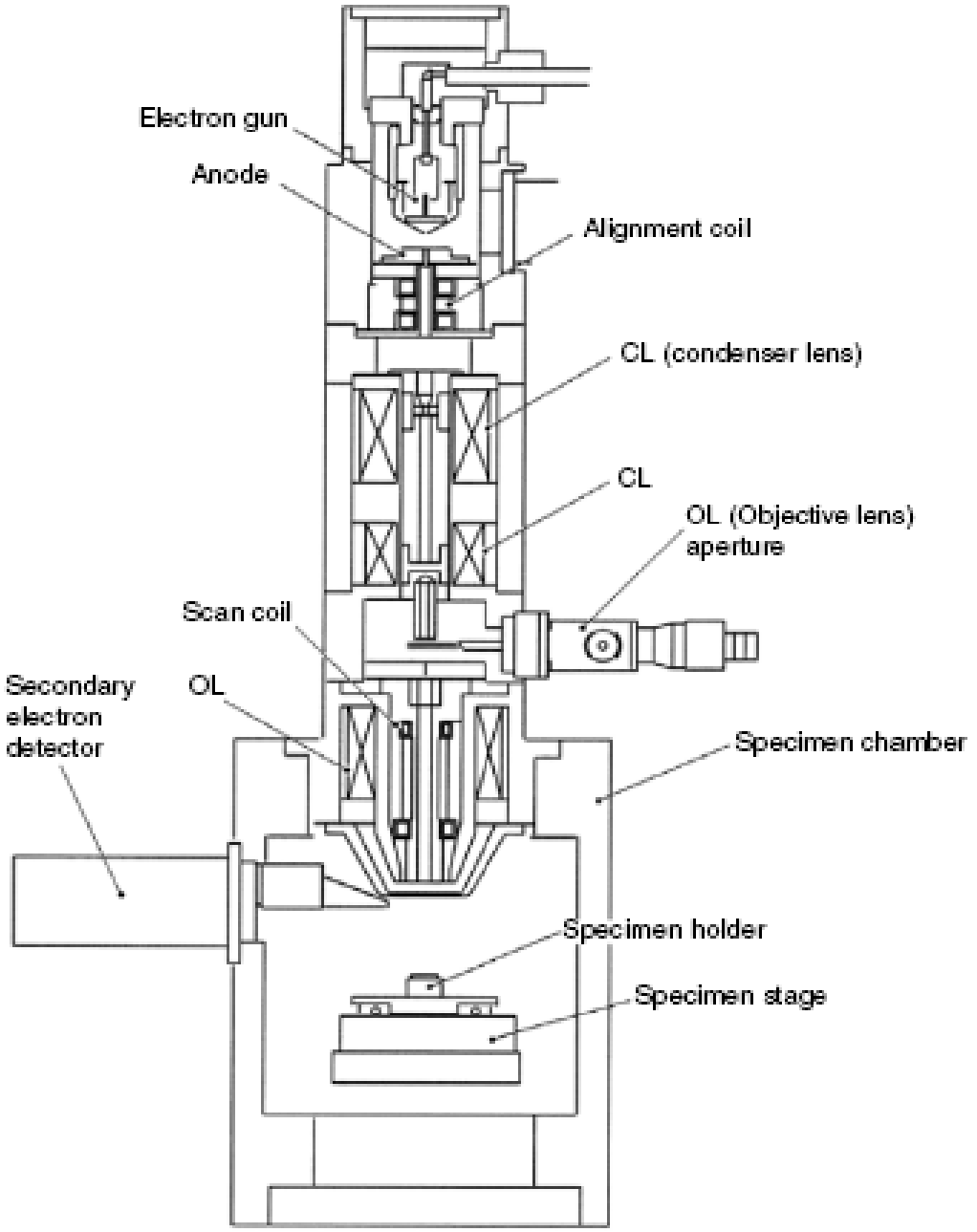

Figure 2.13. Schematic of scanning electron microscope (Zhou et al. (2006)).

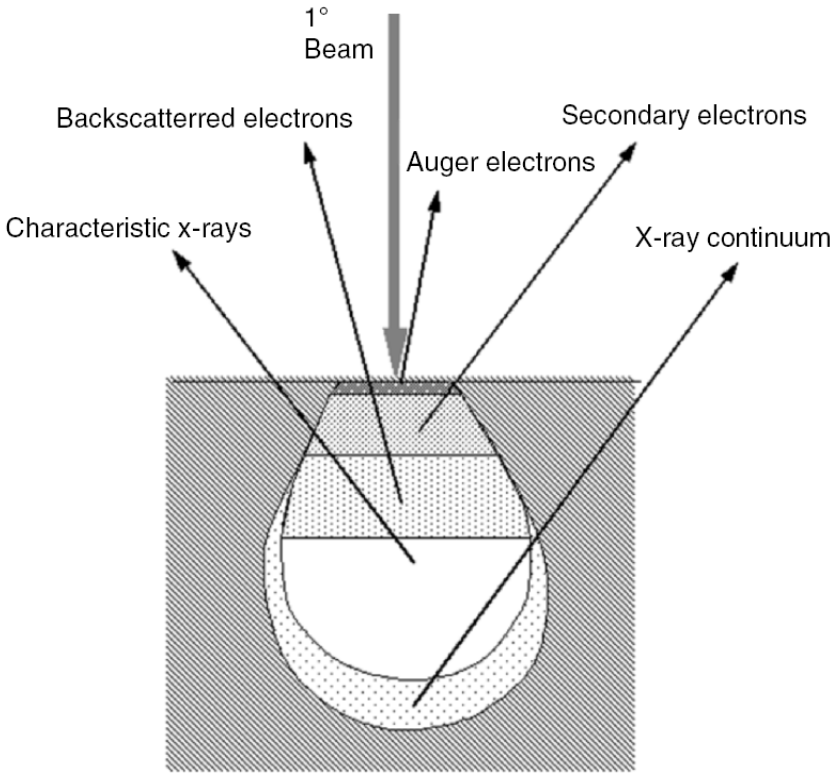

Figure 2.14. Schematic of signals generated by interaction between electron beam and specimen in scanning electron microscope (Zhou et al. (2006)).

Figure 2.15. Kruss contact angle system (Tajima (2006)).

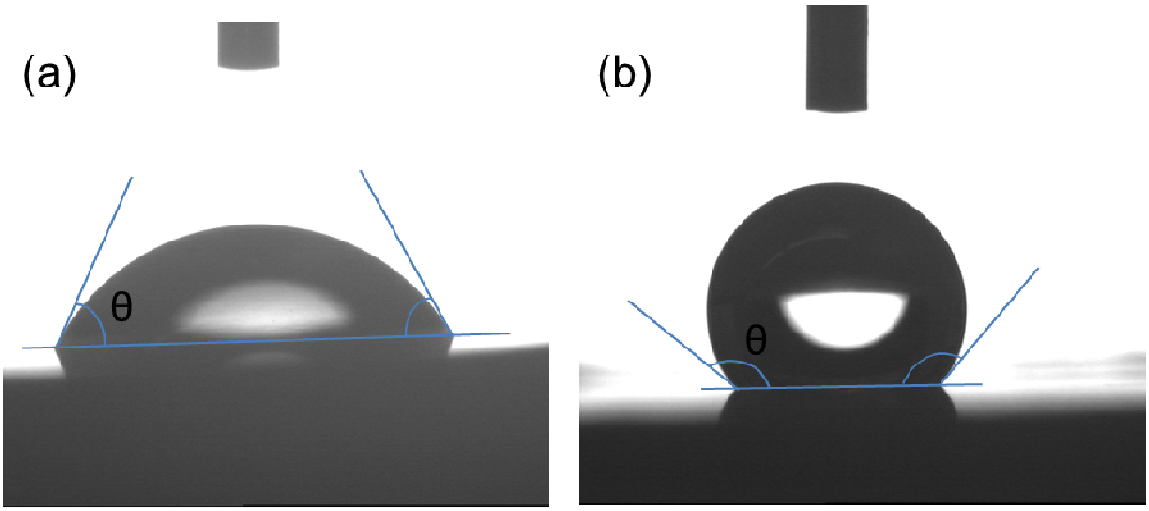

Figure 2.16. Droplet shape from (a) hydrophilic surface (b) hydrophobic surface.

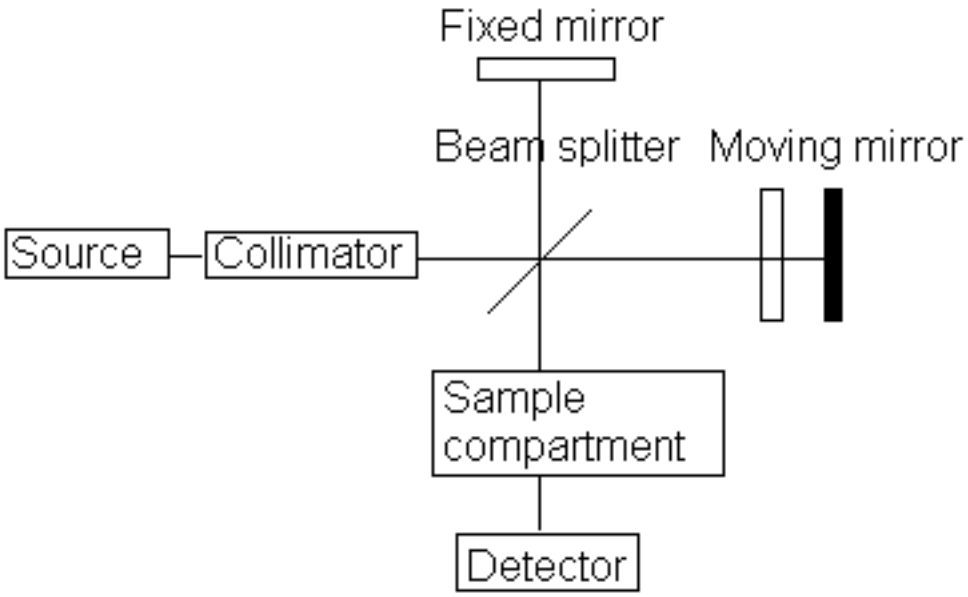

Figure 2.17. Schematic diagram of a Michelson interferometer configured for FTIR (Fourier transform infrared spectroscopy at Wikipedia.org)

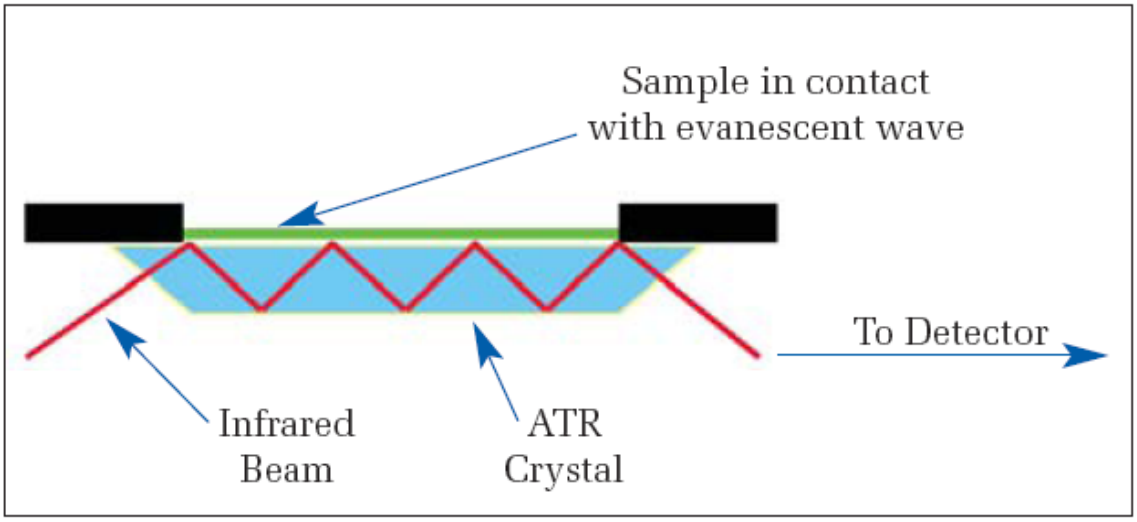

Figure 2.18. Schematic of a multiple reflection ATR system (PerkinElmer, ATR-FTIR Technical Note).

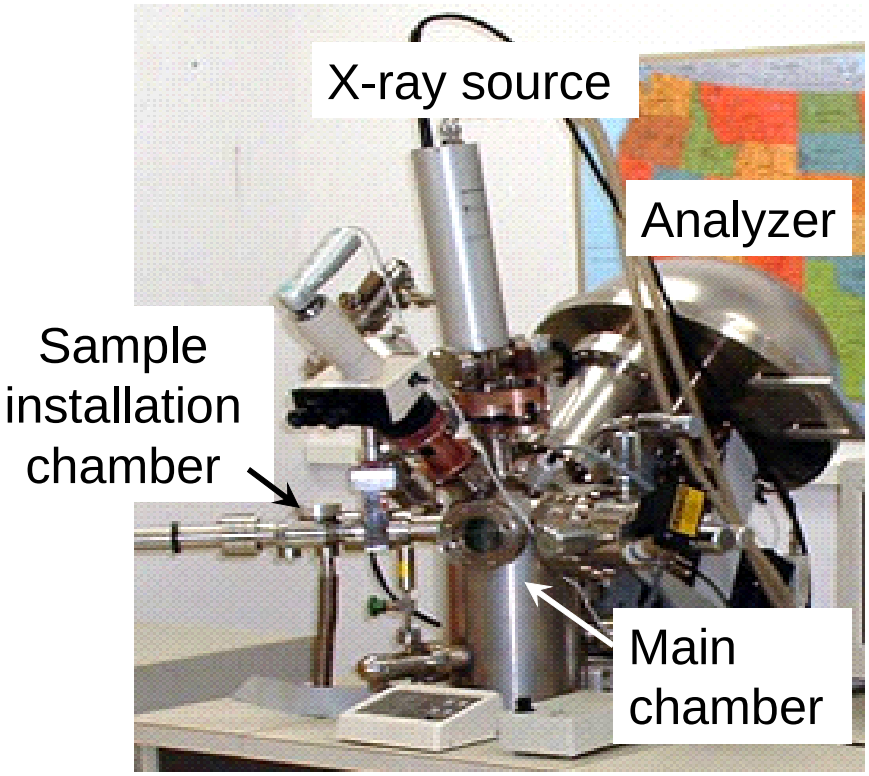

Figure 2.19. Perkin-Elmer PHI 5400 ESCA system (Tajima (2006)).

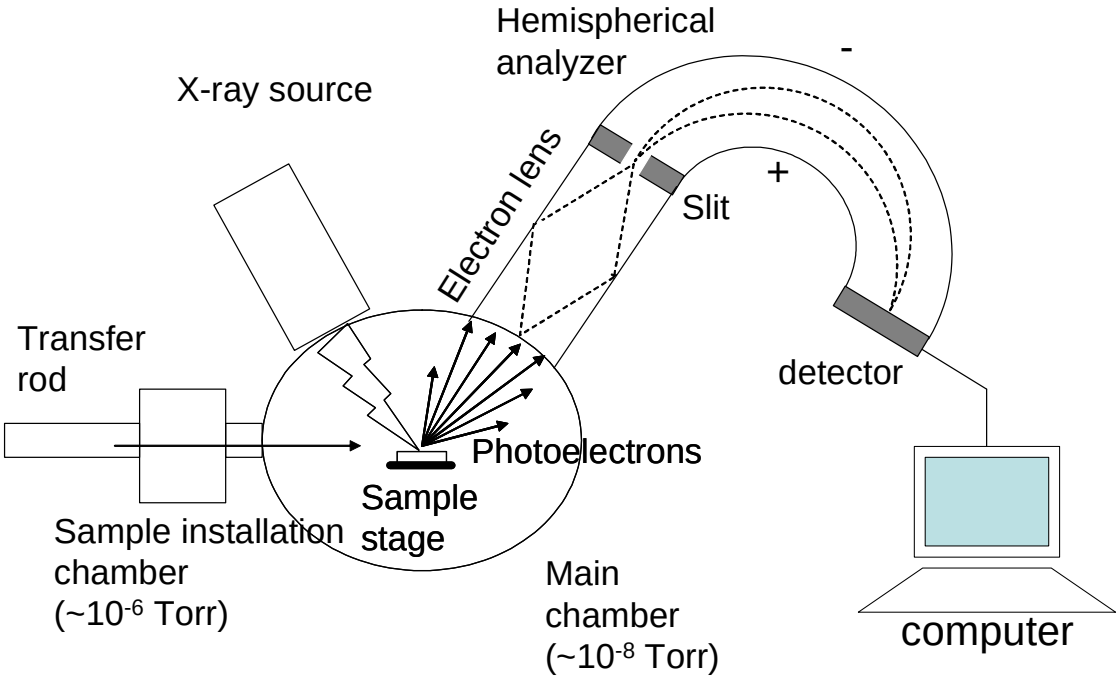

Figure 2.20. Schematic of XPS (Tajima (2006)).

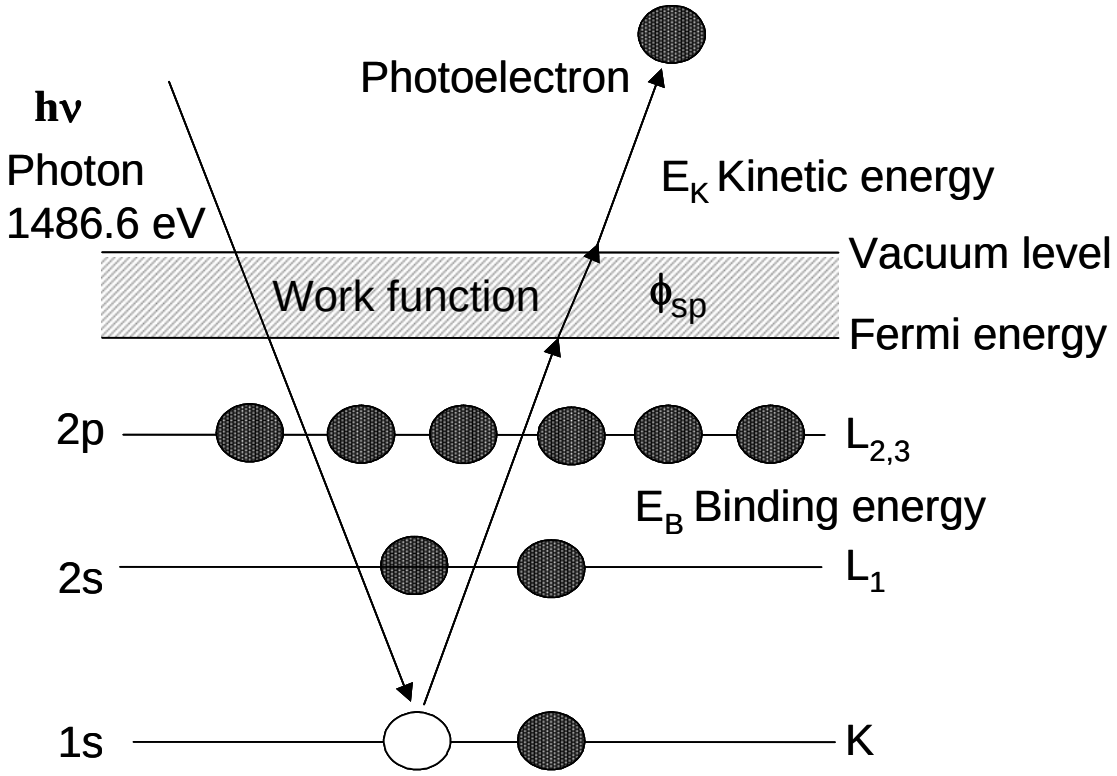

Figure 2.21. Photoemission principle (Tajima (2006)).

Chapter 3

Nanoscale Mechanical and Tribological Properties of Fluorocarbon Films Grafted onto Plasma-Treated Low-Density Polyethylene Surfaces

3.1 Introduction

Polymers are used as structural materials in various medical applications, including bioimplants and instruments for minimally invasive surgical procedures. For example, ultra-high-molecular-weight polyethylene is used to replace damaged cartilage in total joint arthroplasty or to reconstruct diseased joints, whereas LDPE is the main structural material of catheters used in intravenous operations, such as the treatment of diseased arteries where blood flow is restricted by plague deposited onto the inner walls of the lumen. In almost all of the medical applications, the *in vivo* performance of a biomaterial is strongly dependent on its surface behavior in the biological environment. Thus, effective catheterization requires that the biochemical and tribological properties of biopolymer surfaces are customized and maintained throughout the operation. Surface treatments of biopolymers resulting in low friction and good hemocompatibility, which is essential for preventing vessel clotting and thrombosis, are therefore of high importance in intravenous operations.

FC films exhibiting low surface energy, chemical stability, low friction, and good biocompatibility can be deposited by different techniques (Lau et al. (2001), Tang et al. (2005), Favia et al. (1998), Yang et al. (1997)). Because of these combined properties, FC films find use in many industrial and biomedical applications, including dielectric layers of integrated circuits, lubricant films of magnetic storage devices and microelectromechanical systems, and passivation coatings of biomedical instruments. Plasma polymerization and deposition is one of the most commonly used coating methods because of its simplicity and compatibility with most microfabrication processes. In addition, this technique can be used to sterilize bioimplants and surgical instruments.

The broad applicability of FC films has motivated numerous studies aimed to provide insight into the plasma physics of the deposition process and to characterize synthesized FC films. Plasma chemistry, plasma-solid surface interaction, and film growth mechanism in plasma polymerization and deposition of FC films have been studied extensively for different plasma systems, precursor compositions, and plasma conditions (Cunge et al. (1999), Agraharam et al. (1999), Takahashi et al. (2000), Sasaki et al. (2000), Zheng et al. (2005), Tajima et al. (2007), Joshi et al. (2006), Liu et al. (2010)). Thermal stability of FC films used in integrated circuits has also been a topic of significant interest (Agraharam et al. (2000)). Interaction of FC films with different biomolecules and biosystems (Kiaei et al. (1992, 1995), Favia et al. (1996)) and their

stability under the effects of a biological environment or mechanical deformation (Lewis et al. (2008), Holvoet et al. (2010)) have also drawn significant research attention because they control the efficacy of these films as passivation coatings of bioimplants and medical devices. In addition to demonstrating good hemocompatibility characteristics (e.g., FC films can interact with fibrinogen to prevent platelet attachment) (Favia et al. (1998), Yang et al. (1997), Kiaei et al. (1992, 1995), Favia et al. (1996)), FC films synthesized by glow discharge can also enhance the biocompatibility of metal devices such as stents by inhibiting leaching of toxic metal ions into the biological system (Nelea et al. (2009), Lewis et al. (2010)). Therefore, FC film grafting onto biopolymer surfaces appears to be a promising method for improving catheterization performance. This prospect has stimulated several studies of FC film grafting on different biopolymer surfaces by plasma polymerization and deposition (Tajima et al. (2007), Kiaei et al. (1992, 1995), Favia et al. (1996)).

Despite insight into plasma chemistry of FC film deposition Cunge et al. (1999), Agraharam et al. (1999), Takahashi et al. (2000), Sasaki et al. (2000), Zheng et al. (2005), Tajima et al. (2007), Joshi et al. (2006), Liu et al. (2010)), physics of plasma-polymer surface interaction, and plasma-assisted polymer surface modification (Tajima et al. (2005, 2006, 2006, 2007)), knowledge of nanoscale mechanical and tribological properties of FC films grafted onto LDPE surfaces remains relatively sparse and empirical. In this chapter, this gap of knowledge will be bridged by elucidating the nanomechanical/tribological behavior of thin FC films covalently bonded onto LDPE surfaces. The effects of plasma parameters (e.g., plasma power and treatment time) on FC film thickness and surface morphology were first investigated by ellipsometry and AFM, respectively. The nanomechanical/tribological properties of the grafted FC films were then studied by SFM, and the effects of normal loading and repetitive sliding were examined in the context of surface structure models of the plasma-treated LDPE substrate.

3.2 Experimental procedures

3.2.1 Sample preparation

Pellets of LDPE (Sigma-Aldrich, St. Louis, MO) placed on AFM metal disks were first heated at 160°C for 2 min by a hot plate. The partially melted and softened pellets were then compressed against the AFM disks by preheated clean glass slides, heated at 160°C for an additional 3 min to further smoothen the film surfaces, cooled down to room temperature in ambient air, and, finally, peeled off from the glass plate.

3.2.2 Film synthesis

FC films were synthesized in a RF capacitively coupled plasma reactor (RTE73 AMNS-500-E, Plasma Therm, Kresson, NJ) equipped with two electrode plates of diameter equal to 29.4 cm, which were placed apart by a distance of 5 cm. The upper electrode was grounded, whereas the lower electrode (sample holder) was connected to an rf generator. To remove any surface contaminants and enhance surface activation, the LDPE samples were exposed to Ar plasma (power = 150–200 W, treatment time = 5 min, Ar flow rate = 50 sccm, working pressure ≈ 70–80 mTorr). Subsequently, octafluorocyclobutane (C_4F_8) gas was introduced into the chamber, and FC films were grafted onto the Ar plasma-treated LDPE surfaces by plasma polymerization and

deposition (power = 50–250 W, treatment time = 2−10 min, C_4F_8 gas flow rate = 50 sccm, working pressure ≈ 50–100 mTorr) (Tajima et al. (2007)).

3.2.3 Microanalysis techniques

Ellipsometry, AFM, and SFM studies were carried out to examine the effect of plasma conditions on the thickness, surface morphology (roughness), and nanomechanical/tribological properties of the FC films, respectively. For statistical analysis and to check reproducibility, several measurements were obtained from different surface regions of each film and several substrates coated with FC films synthesized under identical plasma conditions. In the statistical analysis, the measured data were assumed to follow normal distributions.

Deposition Rate. FC film deposition rate was determined from the measured thickness of films deposited on 10-cm-diameter p-type Si(100) wafers. The refractive index and thickness of these films were measured with an ellipsometer (AutoEL II, model A9822, Rudolph Technologies, Flanders, NJ) at a wavelength of 633 nm and a spectroscopic reflectrometer (210 XP Scanning UV Nanospec/DUV Microspectrophotometer, Nanometrics, Milpitas, CA), respectively. The film thickness was determined by spectroscopic reflectrometry, using the film refractive index obtained by ellipsometry. Film thickness and refractive index measurements from eight different surface regions of each FC film deposited on Si(100) substrates were used in the statistical analysis.

Surface Morphology and Roughness. The surface topography and roughness of untreated and Ar plasma-treated LDPE, with and without a grafted FC film, were examined with an AFM (Dimension 3100, Veeco Instruments Inc. Plainview, NY) operated in the tapping mode. AFM imaging was performed with 10-nm-radius Si tips attached to Si microcantilevers with a spring constant of 46 N/m (NSC15/AlBS, MicroMasch, Wilsonville, OR). Surface topography analysis was carried out at various imaging scales (i.e., 1×1, 5×5, and 10×10 μm^2 scan areas) in a clean laboratory environment. For each scan size, the root-mean-square roughness R_q was determined from a statistical analysis of surface height data acquired from two different surface regions of two identical samples (i.e., four AFM images for each type of sample surface).

Nanomechanical/Tribological Testing. The nanomechanical/tribological properties of the synthesized FC films were examined in light of sliding and indentation experiments performed with an SFM consisting of an AFM (Nanoscope II, Digital Instruments, Santa Barbara, CA) and a capacitive force transducer (Triboscope, Hysitron, Minneapolis, MN). Three types of SFM experiments were conducted: single and repetitive unidirectional sliding tests and standard nanoindentation tests. For statistical analysis and to ensure reproducibility, for each sliding and indentation experiment at a given normal load, three measurements were obtained from different regions of two identical samples (i.e., six measurements for each type of sample surface).

Single sliding tests were carried out with a 20-μm-radius conospherical diamond tip under loads in the range of 50–400 μN, with all other testing conditions fixed (loading rate = 50 μN/s, sliding speed = 0.27 μm/s, sliding distance = 16 μm). In each sliding test, the steady-state coefficient of friction was calculated as the average of all friction coefficient data acquired in the sliding distance range of 6–16 μm.

Repetitive sliding tests were performed with a conical diamond tip of radius equal to 1 μm radius. Each test comprised a total of 10 traversals (hereafter referred to as sliding cycles) of the loaded SFM tip over a given track of distance equal to 8 μm. In these experiments, the normal load was varied in the range of 150–900 μN, while the loading rate and the sliding speed were set equal to 50 μN/s and 0.27 μm/s, respectively. The coefficient of friction corresponding to each sliding cycle was calculated as the average of the friction coefficient data collected in the distance range of 3–7 μm.

The elastic stiffness of the treated surfaces was obtained from nanoindentation tests performed with the conospherical diamond tip used in the single sliding tests, using a trapezoidal force function with loading and unloading rates both equal to 25 μN/s, hold period (under maximum load) fixed at 10 s, and maximum indentation load in the range of 50–400 μN. Time-dependent (viscoelastic) deformation during the hold period was taken into account in the calculation of the elastic contact stiffness, as explained below.

3.3 Results and discussion

Statistical results are presented next for three different surfaces: untreated and Ar plasma-treated LDPE surfaces with and without covalently bonded FC films. For brevity, these surfaces will hereafter be referred to as LDPE, Ar/LDPE, and FC/Ar/LDPE, respectively. Error bars in the plots indicate one standard deviation above and below the corresponding mean values.

3.3.1 Film deposition rate versus plasma power

Figure 3.1 shows the FC film deposition rate as a function of plasma power for different deposition times. In all cases, the deposition rate increased up to a critical plasma power (~150 W), then decreased with further increasing plasma power, in agreement with a previous study (Tajima et al. (2007)). This trend can be explained by considering that plasma-assisted polymer grafting comprises two competitive processes – film deposition by plasma polymerization and film sputtering by bombarding energetic ions. Below a critical power, film deposition due to monomer activation, fragmentation, and polymerization is the dominant process, while sputter etching is secondary because of the low kinetic energy of impinging ions, hence, deposition rate increases with plasma power. Alternatively, above a critical power, sputter etching is dominant because high-energy ion bombardment plays a primary role in the film grafting process, thus deposition rate decreases with increasing plasma power. Figure 1 also shows a higher deposition rate for 2 min deposition time than 5 or 10 min, for which the difference is insignificant. The initially high deposition rate can be attributed to the dependence of sticking coefficient on surface energy. Because the surface energy of the native SiO_2 layer at the surface of the Si(100) substrate is higher than that of the FC film, a higher sticking coefficient is expected during the initial stage of film deposition onto the SiO_2 surface than at a later stage when the SiO_2 surface has been fully covered by the FC film.

3.3.2 Surface morphology and roughness

Figure 3.2 shows AFM images of surface morphologies of FC films grafted onto Ar plasma-treated LDPE surfaces for 100 W C_4F_8 plasma power and deposition time equal to 2, 5, and 10 min. The images reveal characteristic features of the nanoscale (left column) and microscale (right column) surface morphologies of LDPE, Ar/LDPE, and FC/Ar/LDPE. Untreated LDPE demonstrates a relatively smooth surface, which appears to be fairly featureless at both scales (Figure 3.2(a)). Ar plasma treatment resulted in the formation of numerous nanostructures (Figure 3.2(b)), attributed to selective etching of the amorphous phase at the LDPE surface by bombarding Ar^+ ions.[22] Subsequent short-time (2 min) exposure to C_4F_8 plasma did not alter significantly the nano/microscale surface morphologies produced from Ar plasma treatment (Figure 3.2(c)), suggesting conformal grafting of a thin FC film. However, longer exposure to the C_4F_8 plasma (5 min) resulted in a coarser nanomorphology consisting of worm-like structures (Figure 3.2(d)), whereas even longer C_4F_8 plasma treatment (10 min) partially restored surface smoothness (Figure 3.2(e)).

The evolution of the FC film surface morphology shown in Figure 3.2 can be described by the Stranski-Krastanov film growth model (Ohring et al. (2002)). For short-time C_4F_8 plasma treatment, the FC film does not fully cover the LDPE surface, and film growth occurs in layered mode, resulting in a thin film conformal to the topography of the plasma-treated LDPE surface. Alternatively, for long-time C_4F_8 plasma treatment, film growth at the fully covered LDPE surface occurs in island mode, involving the nucleation, growth, and merger of islands of the film material. This growth mode leads to the formation of a thick film with a relatively coarse surface texture.

The effect of the duration of C_4F_8 plasma treatment on surface morphology can be quantified in terms of roughness measurements obtained at different scales. Figure 3.3 shows the root-mean-square roughness R_q of LDPE, Ar/LDPE, and FC/Ar/LDPE surfaces as a function of scan area. The general trend is for R_q to increase with scan area (scale) and plasma treatment time. Ar plasma treatment induced surface roughening only at the nanoscale (scan area = 1 μm^2), whereas subsequent exposure to C_4F_8 plasma for 2 min did not change the roughness at any scale. These observations are attributed to the presence of nanoscopic asperity features on the Ar/LDPE surface (Figure 3.2(b)) and conformal film deposition (Figure 3.2(c)), respectively. Increasing the C_4F_8 plasma treatment to 5 min resulted in a twofold increase in roughness, attributed to film growth change from layer-by-layer to the formation and coalescence of islands of the film, resulting in a coarser surface morphology (Figure 3.2(d)). Although increasing the duration of C_4F_8 plasma treatment to 10 min increased more the microscale roughness (scan area >25 μm^2), an opposite effect was encountered at the nanoscale (scan area = 1 μm^2) due to the formation of nanoscopic surface features (Figure 3.2(e)).

3.3.3 Coefficient of friction

Figure 3.4 shows the coefficient of friction of LDPE, Ar/LDPE, and FC/Ar/LDPE as a function of average sliding depth, obtained as the average normal displacement of the SFM tip in the sliding distance range 6–16 μm. While Ar plasma treatment increased friction significantly, grafting of an FC film onto the Ar plasma-treated LDPE surface restored low friction to a level close to that of LDPE. The slightly lower friction coefficient of FC/Ar/LDPE than that of LDPE

at relatively small sliding depths (light loads) suggests that the grafted FC film exhibits lower friction than the untreated LDPE.

The above friction characteristics can be attributed to structural differences of the LDPE, Ar/LDPE, and FC/Ar/LDPE surfaces, shown schematically in Figure 3.5. LDPE is a semicrystalline thermoplastic material consisting of crystalline (lamellae) and amorphous phases. Surface shearing during sliding causes stiff lamellae to orient nearly parallel to the sliding direction (Klapperich et al. (1999)), and large strain gradients to develop in the soft amorphous phase. Energetic Ar^+ ion bombardment induces chain crosslinking and etching of the weak amorphous phase at the LDPE surface, which increases the surface concentration of crystalline lamellae (Tajima et al. (2006, 2007)). The significantly higher friction coefficient of the Ar/LDPE surface is therefore attributed to the enhancement of the surface shear resistance due to chain crosslinking and increased concentration of the strong crystalline lamellae. The lower friction of FC/Ar/LDPE is a consequence of the low shear strength of the FC film, covalently bonded to the crosslinked LDPE surface.

Figure 3.6 shows the variation of the friction coefficient of LDPE, Ar/LDPE and FC/Ar/LDPE with sliding cycles for a load of 800 μN. The evolution of the coefficient of friction of LDPE provides a reference for evaluating the effects of Ar plasma treatment and FC film grafting on friction behavior. The gradual decrease of the coefficient of friction of LDPE with sliding cycles is due to the progressive lamellae alignment along the sliding direction, a process known to decrease the surface shear strength of polyethylene (Klapperich et al. (1999)). The significantly higher friction coefficient of Ar/LDPE than that of LDPE, especially during the first 4 sliding cycles, is attributed to the higher shear resistance of the surface due to chain crosslinking and the increased concentration of crystalline lamellae. The sharp decrease of the coefficient of friction of Ar/LDPE with the increase of the sliding cycles is due to accumulation of plastic shearing in the near-surface region, resulting in lamellae alignment along the sliding direction and possible fragmentation of some of the crosslink bonds, which are detrimental to the surface shear resistance. The higher steady-state friction coefficient of Ar/LDPE than that of untreated LDPE may be attributed to the crosslinked material below the sliding track. Exposure of the Ar/LDPE surface to C_4F_8 plasma for 10 min resulted in grafting of an easily sheared FC film (~400 μm thick) onto the crosslinked LDPE surface that provided low and stable friction through the duration of testing. FC film grafting onto the Ar/LDPE surface reduced friction significantly without altering the structure of the plasma-crosslinked LDPE. Thus, after about 6 sliding cycles, FC/Ar/LDPE and Ar/LDPE demonstrated similar friction characteristics.

Figure 3.7 shows the variation of the friction coefficient of FC/Ar/LDPE with sliding cycles for an FC film thickness equal to ~400 μm and normal load in the range of 150–800 μN. The gradual decrease of the coefficient of friction with sliding cycles at all loads is similar to that observed in Figure 3.6. In addition, the coefficient of friction increased with the load. This trend can be attributed to the effect of the crosslinked LDPE substrate. Because the penetration depth of the SFM tip increased with the applied load, shearing within the crosslinked LDPE became more dominant at higher loads. This intensified the friction force applied to the SFM tip, leading to an increase in the coefficient of friction.

3.3.4 Contact stiffness and time-dependent deformation

Contact deformation of LDPE, Ar/LDPE, and FC/Ar/LDPE was examined by nanoindentation. Figure 3.8(a) shows the loading function used in all of the nanoindentation experiments, and Figure 3.8(b) shows the indentation response of LDPE due to this loading function. Contact stiffness was obtained as the slope of the unloading curve at the maximum indentation load (depth). Because of the effect of time-dependent (viscoelastic) deformation on contact stiffness, the elastic stiffness S_e was calculated from the following relationship (Tang et al. (2003), Zhou et al. (2006)):

$$\frac{1}{S_e} = \frac{1}{S} - \frac{\dot{h}}{\dot{P}_u} \tag{3.1}$$

where S is the measured contact stiffness, $\dot{h}$ is the rate of depth change at the end of the hold period (i.e., just before the onset of unloading), and $\dot{P}_u$ is the unloading rate. Since $\dot{P}_u$ was fixed in the present experiments (25 μN/s), only $\dot{h}$ had to be determined to enable the calculation of S from Equation (3.1). This was accomplished by studying the variation of the indentation depth with time during the hold period, as shown in Figure 3.8(c) for LDPE, for example. Using a best-fit approach, the function that best fitted ($R^2 > 0.99$) the depth data of treated and untreated LDPE surfaces during the hold period was found to be of the form

$$h = h_o + Ct^{1/2} \tag{3.2}$$

where t is the hold time, h_o is the indentation depth at the start of the hold period ($t = 0$), and C is a constant intrinsic of the viscoelastic behavior of the material surface.

Substituting Equation (3.2) into Equation (3.1) gives

$$\frac{1}{S_e} = \frac{1}{S} - \frac{C}{2t_0^{1/2}\dot{P}_u} \tag{3.3}$$

where t_0 is the hold period (= 10 s).

Since $t_0^{1/2}\dot{P}_u$ was the same in all cases, constant C may be used to characterize the effect of viscoelasticity on surface stiffness. Figure 3.9 shows the variation of C with maximum indentation load for LDPE, Ar/LDPE, and FC/Ar/LDPE. As expected, the effect of viscoelasticity on the contact stiffness increases nonlinearly with the applied load for all material surfaces. The very similar C values of LDPE and Ar/LDPE suggest that structural modification as a result of Ar plasma treatment was confined to the outermost surface layer of LDPE and, therefore, did not affect the viscoelastic behavior controlled by the bulk material. Grafting of a relatively thick (~800 nm) FC film onto the Ar plasma-treated LDPE surface resulted in lower C values, indicating a weaker viscoelastic effect on contact stiffness in the presence of a covalently bonded thick FC film.

Figure 3.10 shows the contact stiffness (Equation (3.3)) of LDPE, Ar/LDPE, and FC/Ar/LDPE as a function of depth at maximum indentation load. Although Ar plasma treatment increased the concentration of crystalline lamellae and induced chain crosslinking in the near-surface region, it also increased the surface roughness. Thus, the lower contact stiffness of Ar/LDPE may be associated with the decrease in the real contact area due to surface roughening. Deposition of an approximately 800-nm-thick FC film enhanced surface conformity, resulting in contact stiffness similar to that of untreated LDPE. Thus, FC film grafting restored the original stiffness characteristics of the material without altering the crosslinked near-surface region of the Ar plasma-treated LDPE.

3.4 Conclusions

In this chapter, plasma-assisted surface polymerization and grafting of FC films on LDPE surfaces was investigated as a means of modifying the surface properties. AFM and nanoscale sliding and indentation experiments revealed a dependence of the surface morphology and nanomechanical/tribological properties on plasma treatment parameters, applied normal load, and sliding cycles. Sliding friction behavior was interpreted in the context of surface structure models, which account for the effect of plasma treatment on the modification of the surface texture (e.g., lamellae exposure and chain crosslinking) and the effect of the sliding process on the evolution of the surface microstructure (e.g., lamellae alignment along the sliding direction). The contribution of viscoelastic deformation on contact stiffness was examined in the context of nanoindentation experiments. The results of this study demonstrate that plasma-enhanced surface modification is an effective process of tailoring the morphology, structure, mechanical, tribological, and chemical behavior of polymer surfaces.

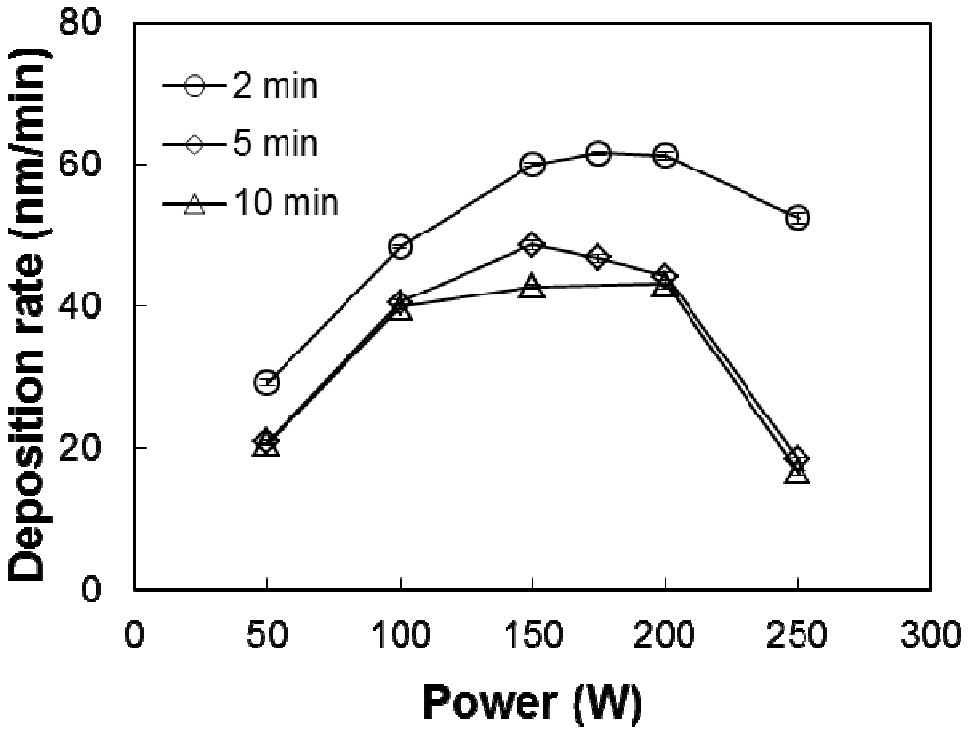

Figure 3.1. Fluorocarbon film deposition rate versus plasma power for different deposition times.

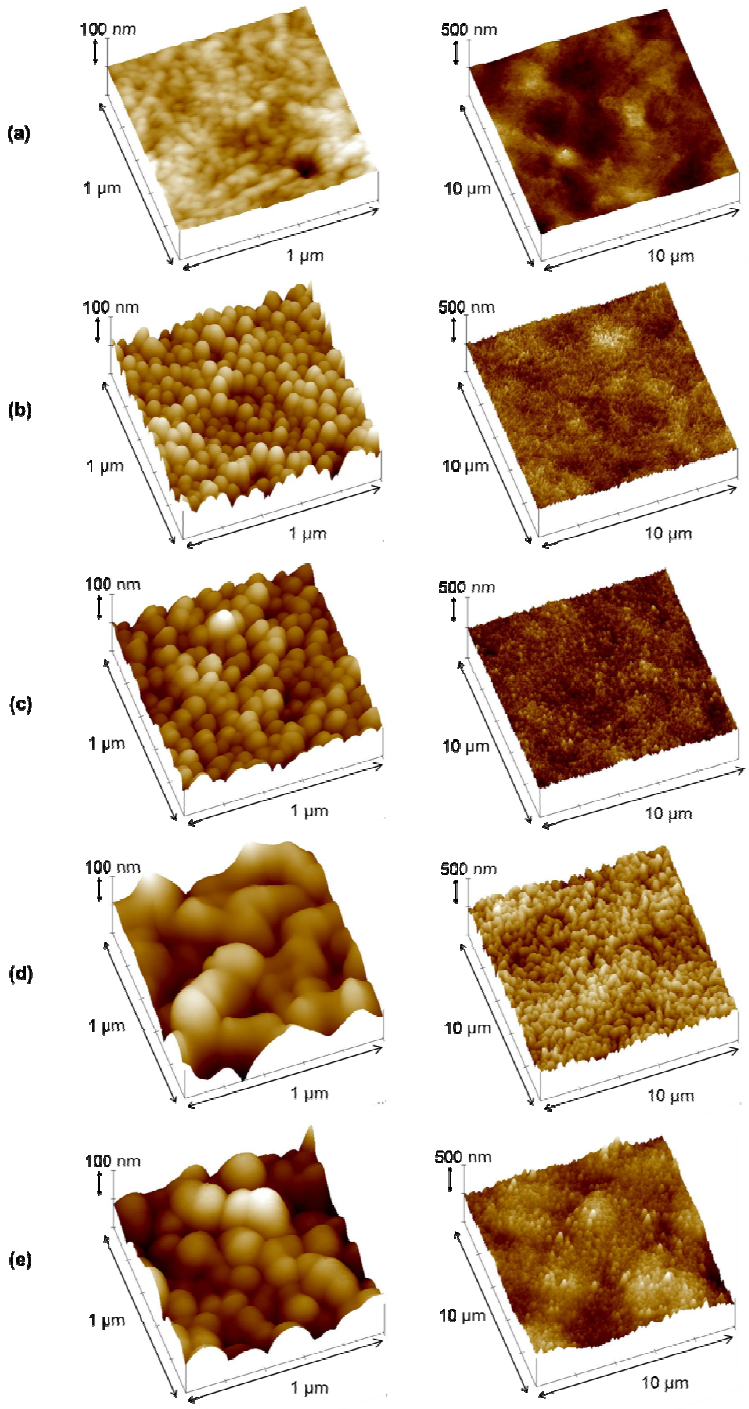

Figure 3.2. AFM images of nanoscale (left column) and microscale (right column) surface topographies of (a) untreated and (b)–(e) plasma-treated LDPE surfaces (plasma treatment conditions: (b) Ar (150 W, 5 min), (c) Ar (150 W, 5 min), C_4F_8 (100 W, 2 min), (d) Ar (150 W, 5 min), C_4F_8 (100 W, 5 min), and (e) Ar (150 W, 5 min), C_4F_8 (100 W, 10 min).

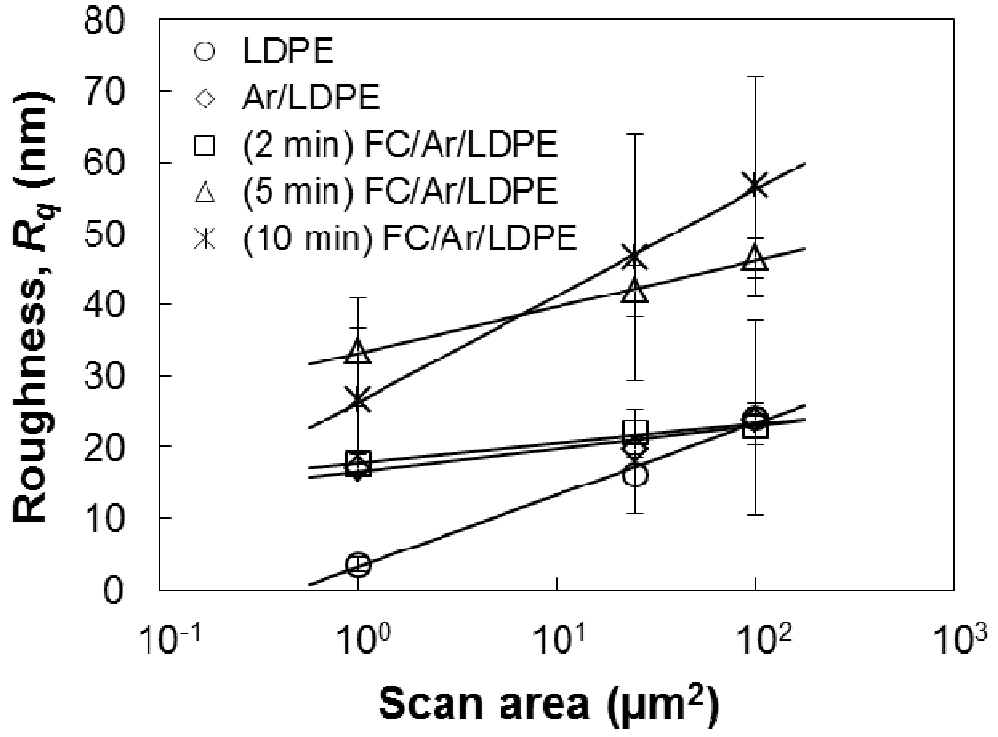

Figure 3.3. Root-mean-square roughness R_q of LDPE, Ar/LDPE, and FC/Ar/LDPE surfaces versus scan area obtained from AFM images at various scales (plasma treatment conditions: Ar (150 W, 5 min), C_4F_8 (100 W, 2–10 min)).

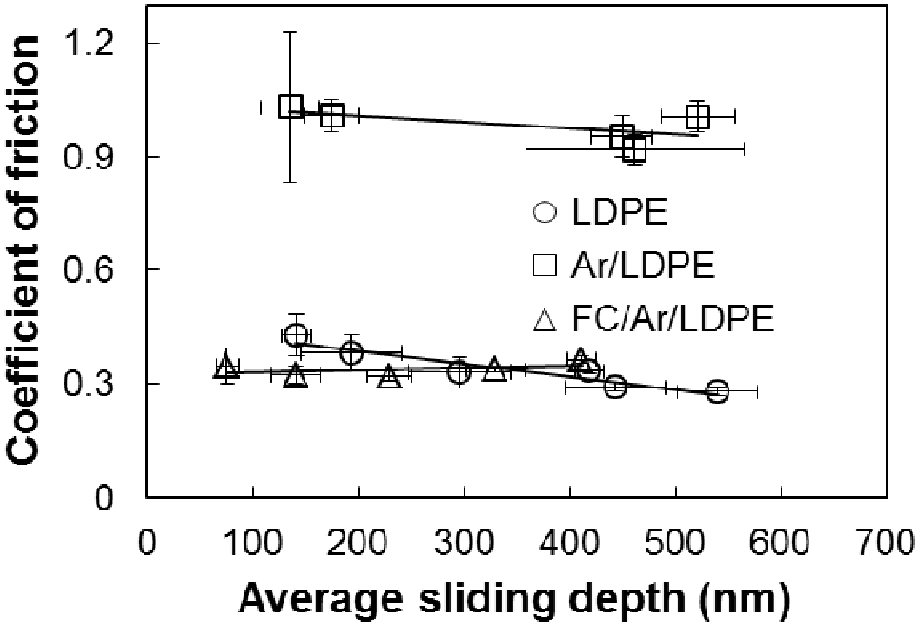

Figure 3.4. Coefficient of friction of LDPE, Ar/LDPE, and FC/Ar/LDPE versus average sliding depth measured with a 20-μm-radius conospherical diamond tip under loads in the range of 50–400 μN (plasma treatment conditions: Ar (150 W, 5 min), C_4F_8 (100 W, 10 min)).

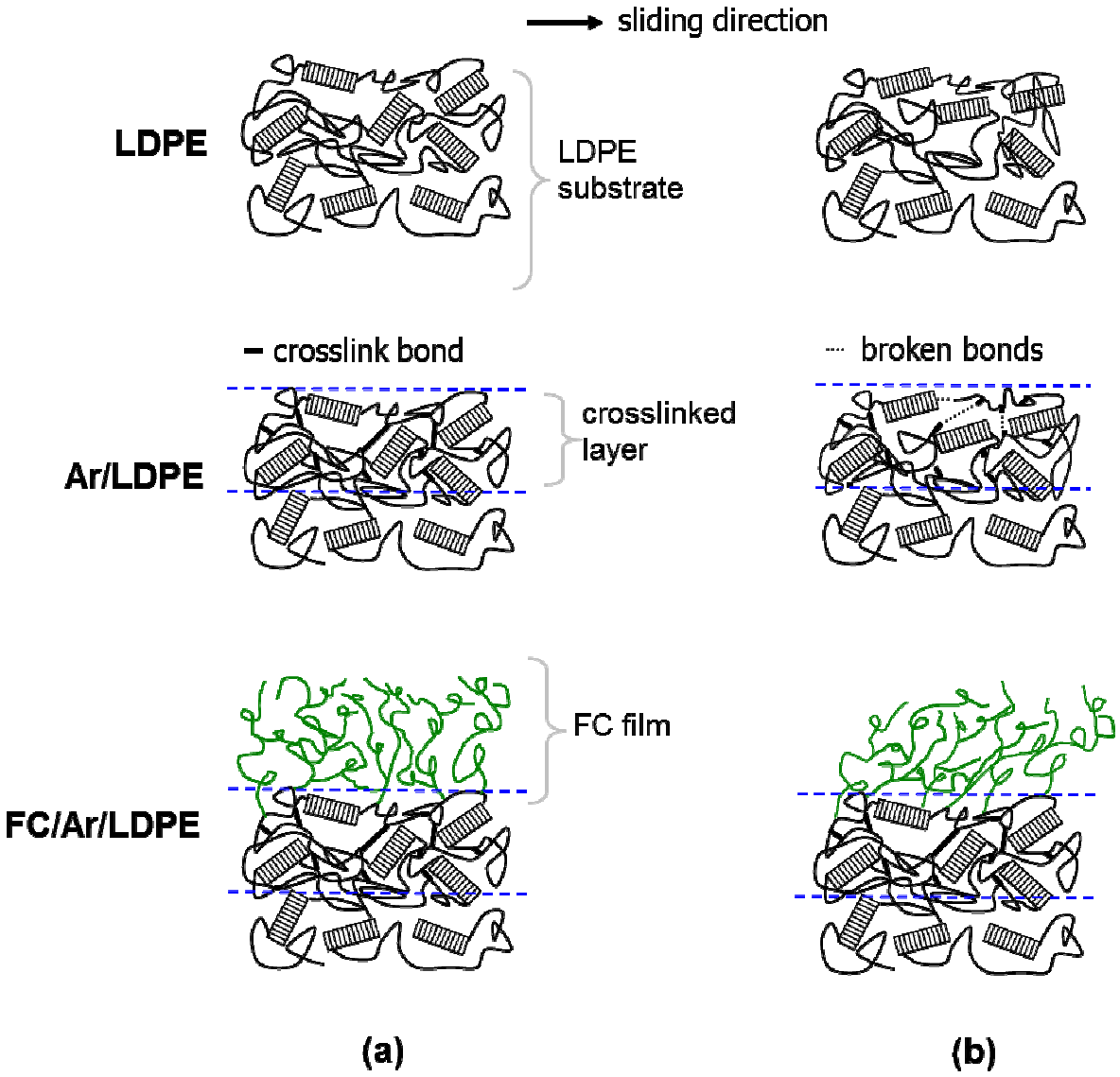

Figure 3.5. Schematics of surface microstructures of LDPE, Ar/LDPE, and FC/Ar/LDPE (a) before and (b) after sliding. Interfaces between the FC film, crosslinked near-surface region of the Ar plasma-treated LDPE, and unmodified bulk of LDPE are designated by dashed lines.

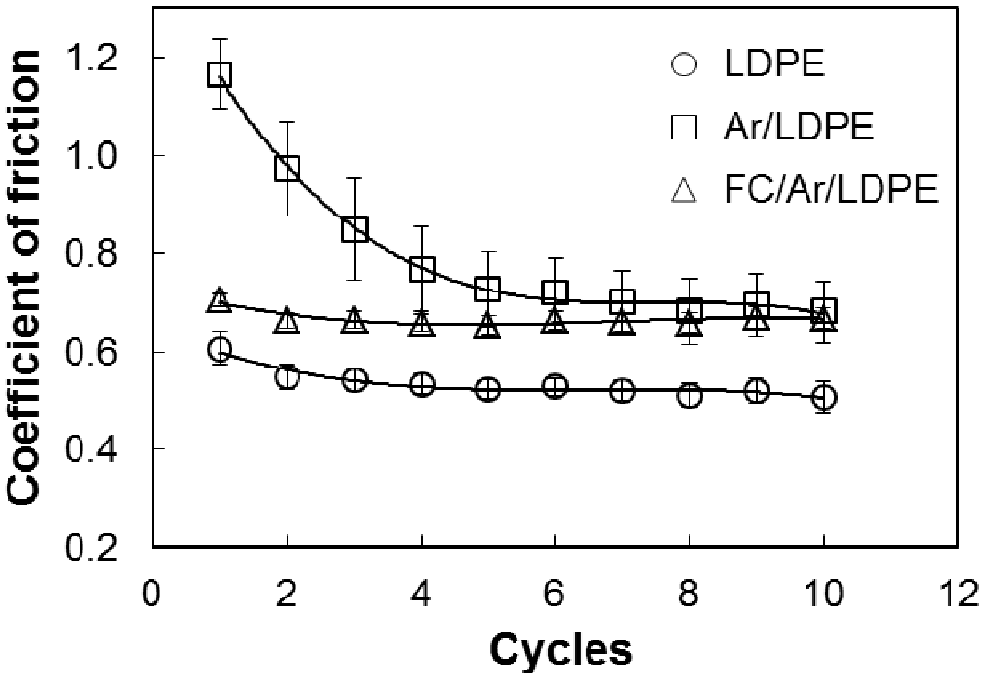

Figure 3.6. Coefficient of friction of LDPE, Ar/LDPE, and FC/Ar/LDPE versus sliding cycles measured with a 1-μm-radius conospherical diamond tip under a load of 800 μN (plasma treatment conditions: Ar (150 W, 5 min), C_4F_8 (100 W, 10 min)).

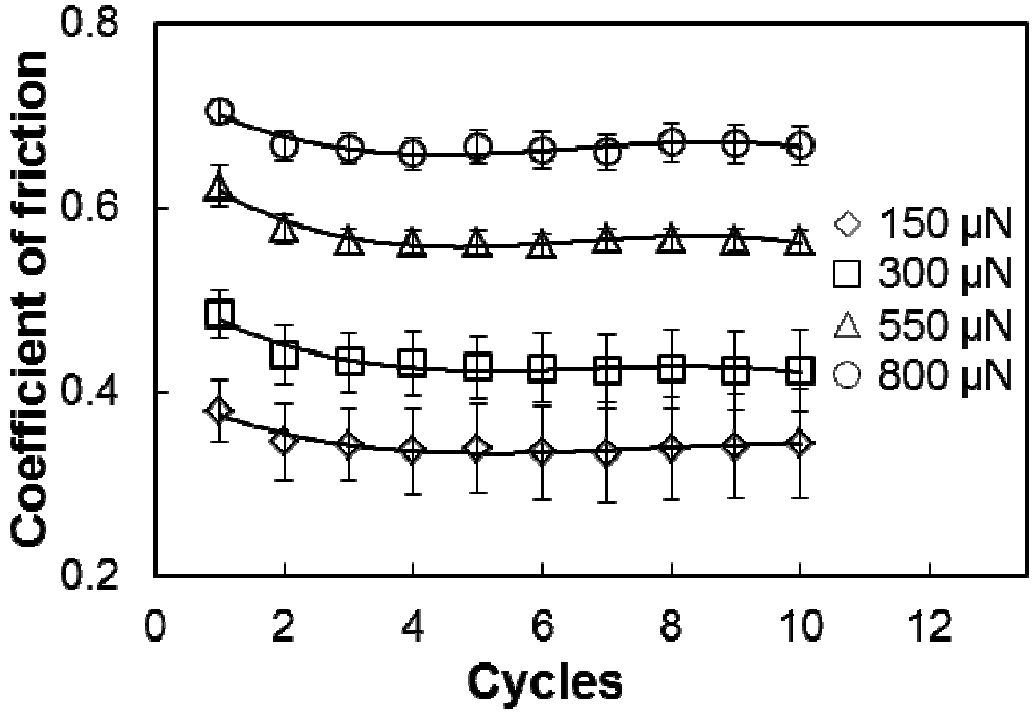

Figure 3.7. Coefficient of friction of FC/Ar/LDPE versus sliding cycles measured with a 1-μm-radius conospherical diamond tip under loads in the range of 150–800 μN (plasma treatment conditions: Ar (150 W, 5 min), C_4F_8 (100 W, 10 min)).

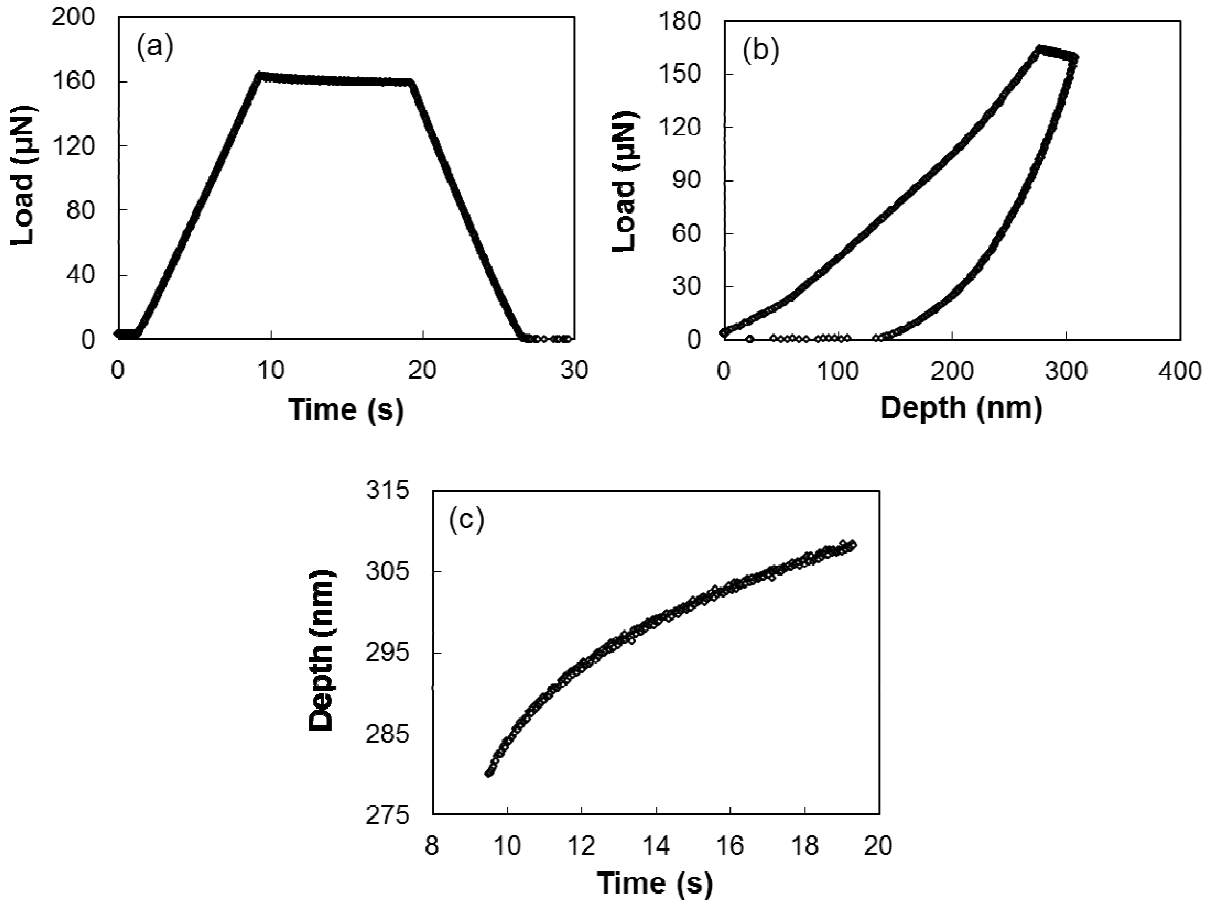

Figure 3.8. Nanoindentation results of LDPE: (a) load versus time, (b) load versus depth, and (c) depth versus time under constant load (hold period).

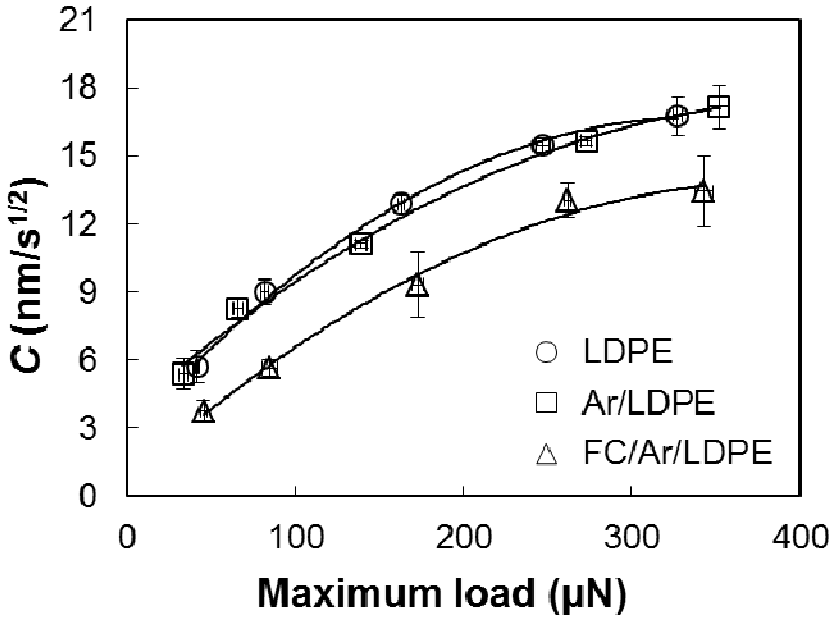

Figure 3.9. Stiffness parameter *C* (Equation (3.3)) of LDPE, Ar/LDPE, and FC/Ar/LDPE versus maximum load measured with a 20-μm-radius conospherical diamond tip (plasma treatment conditions: Ar (200 W, 5 min), C_4F_8 (100 W, 20 min)).

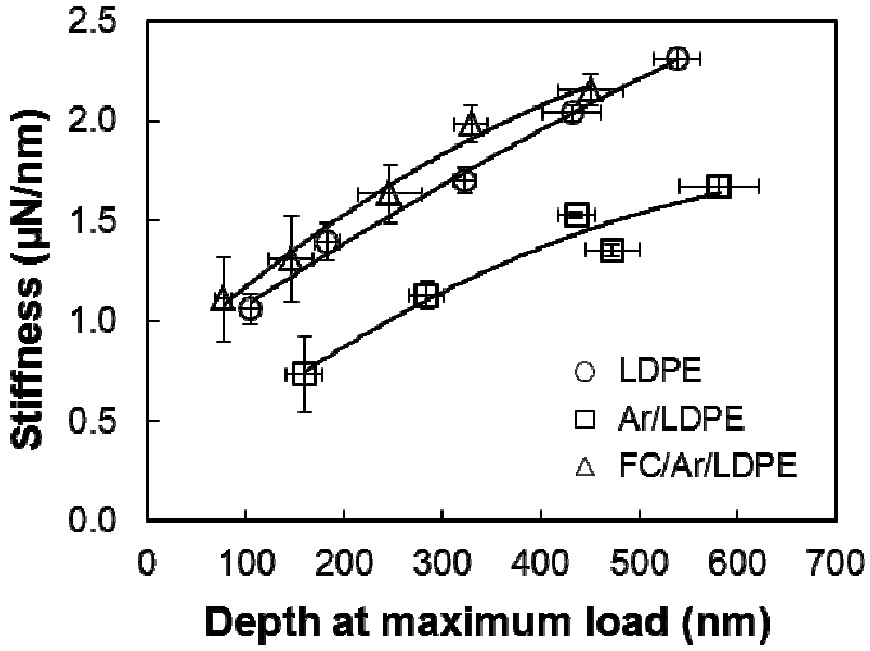

Figure 3.10. Elastic stiffness (Equation (3.3)) of LDPE, Ar/LDPE, and FC/Ar/LDPE versus depth at maximum load measured with a 20-μm-radius conospherical diamond tip (plasma treatment conditions: Ar (200 W, 5 min), C_4F_8 (100 W, 20 min)).

Chapter 4

Synthesis of Polyethylene Glycol-Like Films from Capacitively Coupled Plasma of Diethylene Glycol Dimethyl Ether Monomer

4.1 Introduction

Polymers are prime structural materials for bioimplants and biodevices used to perform tests in vitro. For example, biodevices for restoring heart function and blood circulation in partially closed arteries, such as artificial heart valves, vascular grafts, and catheters for intravenous percutaneous transluminal coronary angioplasty, are fabricated from polymer materials. Because these devices are exposed to blood either upon implantation or during the operation procedure, they must be properly pretreated to prevent thrombosis and clotting in vivo due to protein adsorption and platelet adhesion. PEG is a polymer of particular interest because of its unique properties such as water solubility, hydrophilicity, nontoxic behavior, and nonimmunogenic characteristics. More importantly, the antifouling characteristics of PEG toward cells (Brétagnol et al. (2006)), protein or platelet molecules (Harris et al. (1992)), and bacteria (Dong et al. (2007)) make PEG an ideal coating material for bioimplants and medical devices.

PEG molecular attachment to different surfaces has been accomplished by various methods, such as covalent immobilization (coupling) (Dong et al. (2007), Lee et al. (1997), Popat et al. (2004)), chemical bonding (Alcantar et al. (2000)), monolayer self-assembly (Prime et al. (1991)), and copolymerization induced by ultraviolet radiation (Wang et al. (2001)). In particular, plasma-assisted polymerization of monomers with repeated CH_2CH_2O units has been used to synthesize films demonstrating PEG-like chemical characteristics (Brétagnol et al. (2006, 2007), Goessl et al. (2001), Ademovic et al. (2005), Palumbo et al. (2001)). Plasma polymerization is advantageous because it is easily reproduced, can be applied to a wide range of material surfaces, yields good film bonding to different substrates, and may also be used to sterilize a bioimplant prior to the film deposition during the same process run. Therefore, deposition (grafting) of PEG-like films by plasma-assisted polymerization is a promising surface modification method for bioimplantable components and medical devices, such as total joint replacements, vascular grafts, and catheters for coronary angioplasty.

Different methods for tuning the plasma environment have been used to enhance PEG-like film grafting, such as adjusting the input power by a pulsed alternating-current plasma source to reduce monomer fracture, while maintaining monomer fragment recombination and film growth (Brétagnol et al. (2007), Ademovic et al. (2005)), or using monomers with more CH_2CH_2O repeated units, although heating the entire system was necessary to maintain the monomer in its vapor phase (Goessl et al. (2001), Palumbo et al. (2001)). In this chapter, a capacitively coupled plasma source and diglyme monomer was used to simplify the system

configuration by eliminating heating. The main objectives were to use plasma polymerization and deposition to synthesize films from diglyme monomer on LDPE and Si(100) surfaces pretreated with Ar plasma, and identify the plasma treatment conditions resulting in the deposition of film chemically similar to PEG. Experimental results from various microanalysis studies are presented to elucidate the effects of diglyme and Ar plasma conditions on the film thickness, composition, and chemical characteristics.

4.2 Experimental procedures

4.2.1 Sample preparation

Pellets of LDPE (Sigma-Aldrich, St. Louis, MO) placed on AFM metal disks were heated at 160°C for 2 min by a hot plate. The partially melted and softened pellets were then compressed against AFM disks by preheated and cleaned glass slides, heated at 160°C for an additional 3 min to further smoothen the film surfaces, cooled down to room temperature in ambient air, and, finally, peeled off from the glass plate. Silicon substrates (0.8×0.8 cm^2) were cut off from a 10-cm-diamter p-type Si(100) wafer. Before film deposition, the Si(100) substrates were rinsed with 49% HF for 10 min.

4.2.2 Film synthesis

Films were synthesized in a RF capacitively coupled plasma reactor (RTE73 AMNS-500-E, Plasma Therm, Kresson, NJ) equipped with two electrode plates of diameter equal to 29.4 cm, using a plate-to-plate distance fixed at 5 cm. The upper electrode was grounded, while the lower electrode (sample holder) was connected to the RF generator. To remove any surface contaminants, the substrates were subjected to a 5 min pretreatment with Ar plasma under conditions of 50 or 150 W rf plasma power, 50 sccm Ar gas flow rate, and working pressure in the range of 57–70 mTorr, depending on the plasma power. Subsequently, 99.5% pure diglyme vapor [CH_3–O–(CH_2–CH_2–O)$_2$–CH_3] (Sigma-Aldrich, St. Louis, MO) was introduced into the chamber at a constant pressure of ~10 mTorr. Film synthesis by plasma polymerization and deposition was investigated under diglyme plasma conditions of 1–20 W rf power and ~10–20 mTorr working pressure, using a plasma treatment time in the range of 5–30 min. Before each experiment, the chamber was cleaned with O_2 plasma for 5 min under conditions of 300 W rf power and 100 sccm O_2 flow rate.

4.2.3 Microanalysis techniques

The thickness, surface morphology (roughness), wettability, and composition of the films were examined with an ellipsometer, AFM, goniometer, FTIR spectrometer, and XPS, respectively. Several measurements were obtained from different surface regions of each film and different substrates coated with the same film to ensure reproducibility and to perform a statistical analysis. To calculate mean and standard deviation values, the measured data were assumed to follow normal distributions.

Surface Morphology and Roughness. The surface topographies and roughness of untreated and plasma-treated LDPE and Si(100) were examined with an AFM (Dimension 3100, Veeco Instruments Inc. Plainview, NY) operated in the tapping mode to avoid surface damage of the soft film surfaces. AFM imaging was performed with 10-nm-radius silicon tips attached to silicon microcantilevers possessing a spring constant of 46 N/m (NSC15/AlBS, MicroMasch, Wilsonville, OR). Surface topography analysis was carried out at different imaging scales (i.e., 1 × 1, 5 × 5, and 10 × 10 μm^2 scan areas) in clean laboratory environment. For each scan size, the root-mean-square roughness R_q, center-line average roughness R_a, skewness S, and kurtosis K were determined from a statistical analysis of surface height data obtained from two different surface regions of two identical samples (i.e., four AFM images per surface).

Film Thickness and Refractive Index Measurements. Samples with Si(100) substrates were used to obtain film thickness and refractive index measurements due to the much lower surface roughness of these samples compared to those with LDPE substrates. The refractive index and thickness of films deposited on p-type Si(100) wafers of 10 cm diameter were measured with an ellipsometer (AutoEL II, model A9822, Rudolph Technologies, Flanders, NJ) at a wavelength of 633 nm and a spectroscopic reflectrometer (210 XP Scanning UV Nanospec/DUV Microspectrophotometer, Nanometrics, Milpitas, CA), respectively. The film thickness was determined from spectroscopic reflectrometry, using the film refractive index determined from the ellipsometry measurements. For statistical analysis, film thickness and refractive index measurements were obtained from six different surface regions of each film deposited on Si(100).

Contact Angle Measurements. Static contact angle measurements were obtained from films deposited under different plasma conditions. The film wetting characteristics were examined with a drop-shape analysis system (DSA10, Krüss GmbH, Hamburg, Germany) at room temperature. Droplets of deionized water (~6 μL) were applied to the film surface by a syringe, and the droplet configuration was captured by a camera. Then, the angle between the droplet baseline and the tangent at the water/air boundary was measured, and the contact angle was calculated as the average of the left and the right contact angle measurements. For statistical analysis, six contact angle measurements were obtained from three different surface regions of two identical samples.

Chemical Analysis. Dominant chemical groups in the films were identified with a FTIR spectrometer (Nicolet Avatar 360, Thermo Fisher Scientific, Waltham, MA) equipped with a Ge crystal of refractive index equal to 4.0 using a 45° incidence angle. Spectra were collected by operating the FTIR in the ATR mode. For each measurement, 32 scans were obtained with a resolution of 4 cm^{-1}. A background correction was performed before each measurement to eliminate any ambient contributions. ATR-FTIR spectra were obtained as averages of six measurements taken from two different locations of three identical samples.

Film chemical composition analysis was carried out with an XPS system (Perkin-Elmer PHI 5400 ESCA) without charge neutralization or monochromator, equipped with an Al-Kα X-ray source of photon energy equal to 1486.6 eV. A take-off angle of 54.7º relative to the analyzer axis was used throughout the XPS analysis. During spectral acquisition, the pressure in the main chamber was maintained at ~10^{-7} Torr. Survey spectra were acquired in the binding energy range of 0–1100 eV with pass energy of 178.95 eV. High-resolution XPS spectra of the C1s and O1s

core level peaks were collected with pass energy of 35.75 eV. After performing a Shirley background subtraction, chemical functionalities were determined by curve fitting the C1s spectra with Gaussian distributions of full width at half maximum (FWHM) fixed at 1.7 eV. To compensate for surface charging effects, the C–H peak at 285.0 eV was used as a reference. To ensure the accuracy of the curve fitting method, atomic concentrations determined by curve fitting were compared with measured values. XPS results were deduced from four measurements obtained from two different surface regions of two identical samples.

4.3 Results and discussion

4.3.1 Film surface morphology

Figure 4.1 shows representative 5×5 μm^2 AFM images of untreated and plasma-treated LDPE surfaces. The original surface (Figure 4.1(a)) comprises relatively large-wavelength asperities free of submicrometer features. Ar plasma treatment at a power of 50 W led to the formation of numerous nanoscopic asperities and the disappearance of microscale surface waviness (Figure 4.1(b)). Significantly more distinct surface features resulted from Ar plasma treatment at a relatively high power of 150 W (Figure 4.1(c)). The trend for the nanoscale roughness to increase with the Ar plasma power is in qualitative agreement with earlier studies (Tajima et al. (2006)), where high plasma power was found to induce preferential etching of the amorphous phase of LDPE, resulting in the exposure of nanocrystalline domains (lamellae) and nanoscale surface roughening. Film deposition under diglyme plasma conditions of 2.5 W power and 30 min treatment time on LDPE pretreated with 150 W Ar plasma induced further surface roughening (Figure 4.1(d)). Contrary to LDPE, the exposure of Si(100) to the same Ar and diglyme plasma conditions did not yield discernible changes in the surface topography. AFM imaging revealed that the roughness of the Ar plasma-treated Si(100) surfaces (with or without a film) was similar to that of the original wafer surface (i.e., $R_q < 0.5$ nm). This is expected because of the significantly higher plasma etch resistance of Si(100) compared to that of LDPE. The main finding from AFM imaging is that diglyme film deposition was conformal to the substrate surface and increased slightly the roughness of the Ar plasma-treated LDPE surfaces.

Figure 4.2 shows the effect of Ar and diglyme plasma treatment on the surface roughness of LDPE. The figure shows the root-mean-square roughness at different length scales (upper plot) and a comparison of other topography parameters for length scale fixed at 5×5 μm^2 (lower plots). Both plasma treatments resulted in nanoscopic modification of the surface topography. The trend for the R_q roughness of each surface to increase with the scan area is attributed to the presence of larger wavelengths in the surface topographies of the larger scan areas. The R_a and R_q data show a consistent trend for nanoscale roughening with increasing Ar plasma power. The statistically indifferent R_a and R_q values obtained before and after diglyme plasma treatment (i.e., roughness data for treatment conditions denoted by (c) and (d), respectively) confirm that film deposition was conformal and that nanoscale surface roughening was mainly a result of Ar plasma etching. The S and K values indicate that diglyme plasma treatment restored the Gaussian surface height distribution ($S \approx 0$) that was altered during the high power (150 W) Ar plasma treatment and also resulted in slight broadening of the asperity height distribution, as indicated by the slightly lower K value of the film surface.

4.3.2 Film thickness and surface contact angle measurements

Table 4.1 shows the effect of diglyme plasma treatment conditions on the thickness, refractive index, and contact angle of films deposited on Si(100) and LDPE substrates. To deposit films of similar thickness (in the range of 55–68 nm) for FTIR analysis, the plasma power was increased from 2.5 to 20 W, while the treatment time was decreased from 30 to 5 min. The contact angle of the clean Si(100) substrate (~37^o) is typical of the native silicon dioxide (SiO_2) layer at the Si(100) surface, whereas the ~39^o contact angle for 1 W diglyme plasma power is comparable to the ~45^o contact angle reported for a PEG film grafted onto a LDPE substrate (Wang et al. (2001)). The decrease of the contact angle of the films deposited on LDPE from ~92^o to ~39^o with the decrease of the plasma power from 20 to 1 W indicates that low power diglyme plasma treatment was beneficial to the formation of films that exhibit characteristics very similar to those of PEG. This is also supported by the decrease of the refractive index of the films deposited on Si(100) with the plasma power, considering that lower refractive index implies less crosslinking (Holmberg et al. (2002)) and that PEG molecular chains generally exhibit low levels of crosslinking. In contrast to the films deposited on LDPE, the films synthesized on Si(100) demonstrated similar contact angles throughout the examined power range, indicating a possible substrate effect on the film composition.

4.3.3 Film surface chemistry and composition

Figure 4.3(a) shows a typical ATR-FTIR spectrum of a film deposited on LDPE for 2.5 W diglyme plasma power. Peak assignments were made according to data from the literature (Ademovic et al. (2005), Palumbo et al. (2001)). The strong C–H peak (assigned to LDPE) is attributed to the large sampling depth (~600 nm), whereas the C–O peak is characteristic of PEG. In addition, the film spectrum contains two small peaks assigned to C=O and COOH. Figure 4.3(b) shows the dependence of the C–O peak intensity on the diglyme plasma treatment conditions. The intensification of the C–O peak with the decrease of the plasma power suggests that the film chemical composition is closer to that of PEG. High plasma power promoted fragmentation of the diglyme molecules. The produced small fragments recombined at the polymer surface to form chemical groups different from those in the original diglyme molecule. Thus, the PEG chemical character of the film was influenced by the increase of the diglyme plasma power.

The O/C atomic ratio of the films was determined from the XPS spectra of the C1s and O1s core level peaks of the films deposited on LDPE and Si(100). Figure 4.4 shows the effect of the diglyme plasma power on the O/C atomic ratio. (For pure PEG, the O/C ratio is equal to ~0.5.) The variation of the O/C ratio with the plasma power suggests that low-power diglyme plasma treatment yielded film characteristics very similar to those of PEG. The statistically different O/C curves of the films deposited on LDPE and Si(100) illustrate a substrate effect on the film chemical composition.

Figure 4.5 shows XPS spectra of the C1s core level peak of films deposited on LDPE for different diglyme plasma power. The absence of a Si peak from the XPS spectra of the films deposited on Si(100) (not shown here) and similar thickness of the films deposited on LDPE and Si(100) suggest that the substrates were fully covered by the films. The spectra were fitted with

four Gaussian distributions corresponding to different types of carbon bonding (denoted by C1–C4 for convenience). The two dominant peaks centered at approximately 285.0 and 286.5 eV are assigned to C–C(C–H) (C1) and C–O (C2), respectively, while the two small peaks at about 288.0 and 289.2 eV are assigned to O–C–O(C=O) (C3) and COOR(COOH) (C4), respectively (Brétagnol et al. (2006, 2007), Ademovic et al. (2005)). Figure 4.5 shows that the decrease of the plasma power led to the intensification of C2 and the decrease of C1, whereas the effect on C3 and C4 was secondary. Similar trends were observed in the XPS spectra of the C1s core level peak of the films deposited on Si(100).

Figure 4.6 shows the dependence of the C1 and C2 film fractions on the diglyme plasma power. The two types of carbon bonding demonstrate opposite trends with the increase of the plasma power. The enhancement of C2 and the simultaneous decay of C1 with the decrease of the plasma power provide additional evidence for the formation of films that possessed characteristics similar to those of PEG. The highest C–O fraction (~72%) obtained for 1 W diglyme plasma power is very close to the ~70% C–O fraction reported for PEG-like films, synthesized under the same diglyme plasma power, that demonstrated good anti-fouling properties (Brétagnol et al. (2006)). The variation of the C1 and C2 fractions with the plasma power shown in Figure 4. 6 is also in agreement with the findings of previous studies (Brétagnol et al. (2006), Palumbo et al. (2001)). The C3 and C4 fractions are not shown in Figure 4. 6 because they did not show a dependence on the variation of the plasma power. (For LDPE substrate, C3 = 9.6 ± 0.02 % and C4 = 2.7 ± 1.1 %, while for Si(100) substrate, C3 = 8.8 ± 1.10 % and C4 = 2.8 ± 0.53 %.) The results shown in Figures 7.4 and 6 reveal chemical differences between the films deposited on the LDPE and Si(100) substrates. The higher C2 and lower C1 fractions of the films deposited on LDPE compared to those deposited on Si(100) indicate a substrate effect on the film composition. Molecular attachment and ordering at the film/substrate interface depend on the roughness, hydrophilicity, and chemical reactivity of the substrate, and control the film structure and chemical behavior. For example, the chemical characteristics of a film covalently bonded to the hydrophobic (~121^{o}) LDPE substrate would differ from those of a film deposited on the hydrophilic (~37^{o}) SiO_2 layer of the Si(100) substrate. In addition, film grafting may also be affected by the high density of free bonds at the LDPE surface produced by Ar plasma pretreatment. Therefore, differences in the film wetting and chemical characteristics, such as those revealed by the data given in Table 4.1 and Figures 7.4 and 6 may be inferred to the previous substrate effects.

To examine the effect of the diglyme plasma treatment time on the film deposition, a series of treatments were performed at a fixed power of 2.5 W and treatment time of 10, 20, and 30 min (Tables 2 and 3). Table 4.2 shows that both the thickness and the refractive index of the films deposited on Si(100) increased with the diglyme plasma treatment time. This trend of the film refractive index may be attributed to intermolecular reactions in the bulk of the thicker films, resulting in a higher degree of crosslinking (van Os et al. (1999)). However, XPS results (not shown here) did not reveal an effect of the diglyme plasma treatment time on the surface chemical composition of the films deposited on Si(100), in agreement with the indifferent contact angle measurements. Table 4.3 shows that increasing the diglyme plasma treatment time from 10 to 20 min yielded a significantly lower contact angle and notable changes in the chemical functionalities of the films deposited on LDPE. However, less pronounced differences in contact angle and chemical groups were found for the films deposited on LDPE after 20 and

30 min of plasma treatment. To investigate the reason for these differences, contact angle and chemical composition measurements were obtained from samples of Ar plasma-treated LDPE. The high contact angle (~121^{o}) of Ar plasma-treated LDPE is attributed to nanoscale surface roughening due to preferential etching of the amorphous phase.[13] In addition to surface roughening, bombarding Ar^{+} ions may cause chain scission and bond fragmentation, increasing the polymer surface reactivity. Upon the sample exposure to the ambient conditions, activated molecules at the pretreated LDPE surface reacted with oxygen and water molecules to form C–O, C=O, and COOH moieties. The fact that the contact angle and the C–O, O–C–O(C=O), and COOR(COOH) fractions corresponding to 10 min diglyme plasma treatment are relatively closer to those of the Ar plasma-treated LDPE surface suggests that treatment with a 2.5 W diglyme plasma for 10 min did not result in complete coverage of the LDPE substrate by the film. Hence, the significant differences in the wetting and chemical characteristics for 10 min diglyme plasma treatment versus 20 and 30 min treatment may be attributed to exposed surface regions of the Ar plasma-treated LDPE that affected the contact angle and XPS measurements. Longer plasma treatments (i.e., 20 and 30 min) resulted in full substrate coverage by the film, indicated by consistent contact angle measurements and chemical composition results.

The effect of the Ar plasma pretreatment on the film thickness and chemical character can be evaluated by comparing the results given in Table 4.4 for relatively low (50 W) and high (150 W) Ar plasma power. Film deposition was performed under diglyme plasma conditions favoring the deposition of continuous PEG-like films, i.e., 1 W power, ~10 mTorr working pressure, and 30 min treatment time. The similar thickness, refractive index, and contact angle of the films deposited on Si(100) after Ar plasma pretreatment at 50 and 150 W power indicate that the film deposition conditions were very similar. XPS results showed insignificant differences in the chemical compositions of the films deposited on LDPE that was previously exposed to low and high power Ar plasma, suggesting that the chemical composition of these films was not affected by the Ar plasma pretreatment conditions. However, lower contact angle and higher C–O/C–H fraction (determined from the FTIR spectra) were found for the films deposited on the LDPE substrate exposed to 150 W Ar plasma power. The lower contact angle is attributed to the effect of nanoscale surface roughening, which intensified with the increase of the Ar plasma power (Tajima et al. (2006)), and the lower contact angles that characterize rougher hydrophilic surfaces (Holmberg et al. (2002)). The decrease of the C–O/C–H peak ratio with the Ar plasma power may be attributed to the decrease of the film thickness. This can be explained by considering the reduced density of free bonds at the LDPE surface due to the less energetic Ar^{+} ion bombardment under low power Ar plasma conditions, which produced a detrimental effect on film grafting during the diglyme plasma treatment.

4.4 Conclusions

In this chapter, thin films exhibiting PEG-like chemical characteristics were deposited on LDPE and Si(100) substrates under different conditions of capacitively coupled diglyme plasma. A significant enhancement of the PEG chemical composition of the films deposited on LDPE was observed under low-power diglyme plasma treatment conditions. Film chemical functionalities did not show a dependence on the duration of the diglyme plasma treatment. However, the effect on the bulk structure and composition of the films could have been significant. Substrate pretreatment with Ar plasma did not affect significantly the overall film

characteristics. The results of this study demonstrate the efficacy of capacitively coupled plasma treatment to produce conformal PEG-like films with tailored chemical characteristics. Such capability is important to the design of chemically patterned surfaces for biological and medical analyses.

Table 4.1. Thickness, refractive index, and contact angle of films deposited on Si(100) and LDPE versus diglyme plasma treatment conditions.

diglyme plasma treatment conditions			film properties			
			Si(100) substrate[a]			LDPE substrate[a]
power (W)	pressure (mTorr)	time (min)	thickness (nm)	refractive index	contact angle[b](deg.)	contact angle[c] (deg.)
1	~10	30	32.9 ± 1.4	1.39 ± 0.02	59.2 ± 2.5	38.8 ± 2.4
2.5	~11	30	55.9 ± 0.8	1.46 ± 0.01	57.2 ± 1.9	51.7 ± 2.9
5	~13	20	61.7 ± 0.5	1.49 ± 0.01	55.2 ± 1.3	59.4 ± 1.5
10	~15	10	67.5 ± 0.8	1.52 ± 0.01	62.1 ± 0.2	83.6 ± 2.9
20	~20	5	55.1 ± 0.4	1.54 ± 0.01	61.5 ± 1.1	92.3 ± 1.9

[a]Ar plasma pretreatment (power = 150 W; pressure ≈ 60 mTorr; gas flow rate = 50 sccm; time = 5 min).

[b]contact angle of Ar plasma-treated Si(100) = 37.2 ± 0.8 deg.

[c]contact angle of Ar plasma-treated LDPE = 121.2 ± 0.8 deg.

Table 4.2. Thickness, refractive index, and contact angle of films deposited on Si(100) versus diglyme plasma treatment time.[a]

diglyme plasma treatment time (min)	thickness (nm)	refractive index	contact angle (deg.)
10	26.7 ± 0.9	1.34 ± 0.02	58.8 ± 3.5
20	37.3 ± 0.5	1.43 ± 0.01	58.5 ± 2.0
30	55.9 ± 0.8	1.46 ± 0.01	57.2 ± 1.9

[a]power = 2.5 W; pressure ≈ 11 mTorr.

Table 4.3. Contact angle and chemical composition of films deposited on LDPE versus diglyme plasma treatment time.[a]

diglyme plasma treatment time[b] (min)	contact angle (deg.)	chemical component fraction (%)		
		C–O	O–C–O(C=O)	COOR(COOH)
0	121.2 ± 0.8	37.13 ± 1.52	19.70 ± 1.39	5.17 ± 0.51
10	82.8 ± 3.7	57.83 ± 1.78	14.00 ± 1.85	3.50 ± 0.17
20	56.5 ± 3.6	64.20 ± 2.29	11.17 ± 1.01	2.47 ± 0.21
30	51.7 ± 2.9	64.08 ± 1.31	9.35 ± 0.66	2.50 ± 0.96

[a]power = 2.5 W; pressure ≈ 11 mTorr.

[b]zero diglyme treatment time implies only Ar plasma pretreatment.

Table 4.4. Thickness, refractive index, contact angle, and C–O/C–H peak ratio (determined from FTIR spectra) of films deposited on Si(100) and LDPE versus Ar plasma pretreatment conditions.

Ar plasma pretreatment conditions[a]			film[b] properties				
			Si(100) substrate			LDPE substrate	
power (W)	Pressure (mTorr)	time (min)	thickness (nm)	refractive index	contact angle（deg.）	contact angle （deg.）	C–O/C–H
150	~60	5	32.9 ± 0.8	1.39 ± 0.02	59.2 ± 2.5	38.8 ± 2.4	0.186
50	~58	5	30.8 ± 1.5	1.35 ± 0.03	58.5 ± 1.6	47.1 ± 3.5	0.115

[a]gas flow rate = 50 sccm.

[b]diglyme plasma treatment (power = 1 W; pressure ≈ 10 mTorr; time = 30 min).

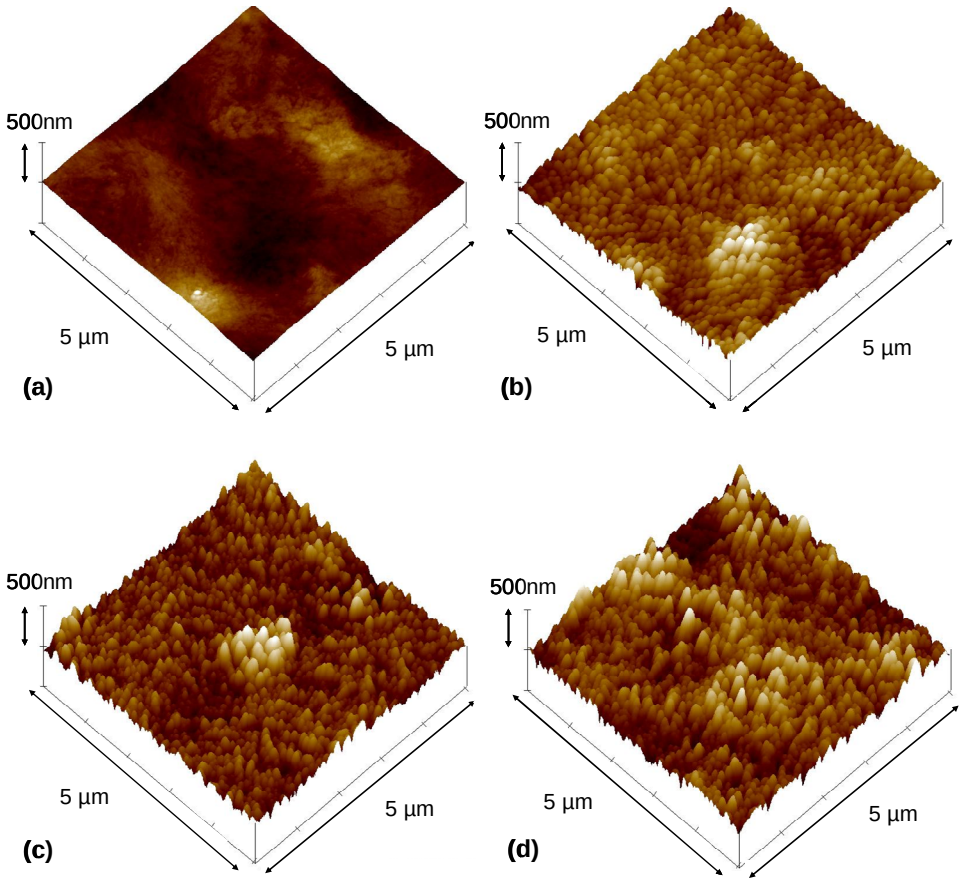

Figure 4.1. AFM surface topography images of LDPE surfaces: (a) no treatment, (b) 50 W Ar plasma treatment, (c) 150 W Ar plasma treatment, and (d) 150 W Ar plasma pretreatment followed by a 30 min treatment with 2.5 W diglyme plasma.

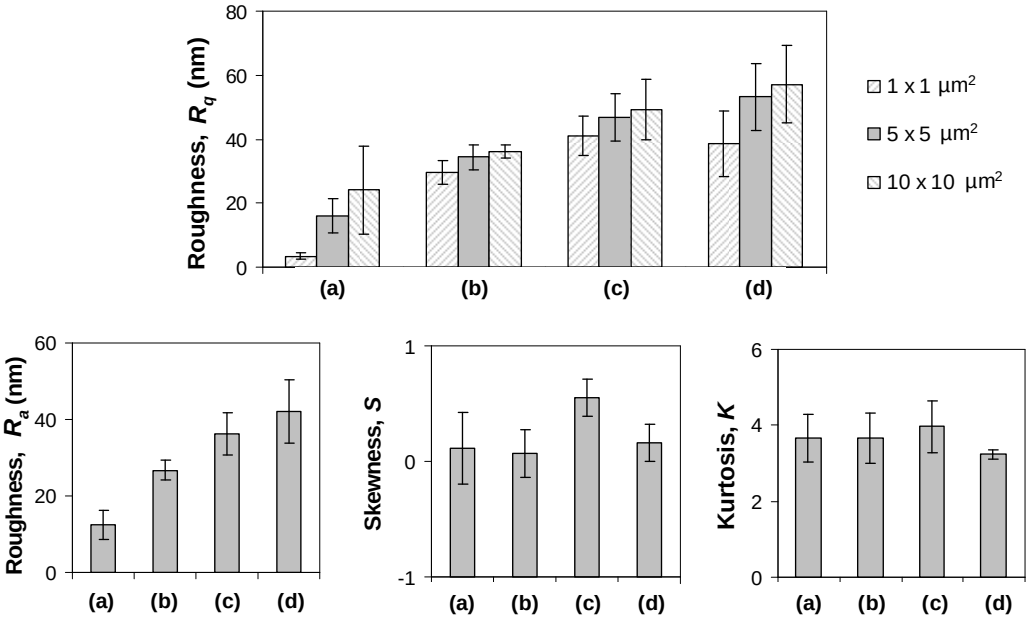

Figure 4.2. Statistical surface topography parameters obtained from 1 × 1, 5 × 5, and 10 × 10 μm^2 AFM surface images of LDPE surfaces: (a) no treatment, (b) 50 W Ar plasma treatment, (c) 150 W Ar plasma treatment, and (d) 150 W Ar plasma pretreatment followed by a 30 min treatment with 2.5 W diglyme plasma.

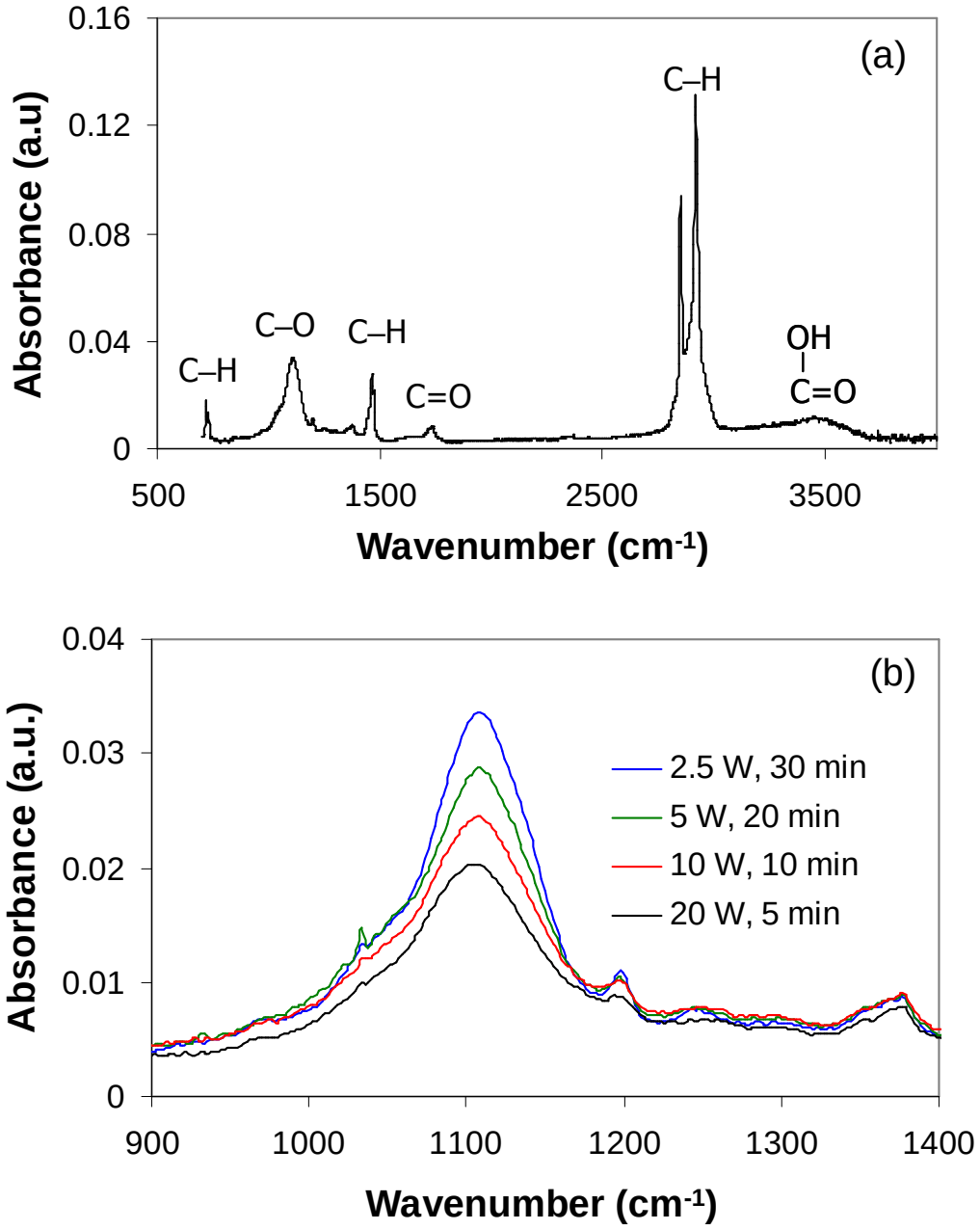

Figure 4.3. (a) FTIR spectrum of a film synthesized after a 30 min treatment with 2.5 W diglyme plasma on a LDPE substrate pretreated with 150 W Ar plasma, and (b) effect of diglyme plasma treatment conditions on the C–O peak intensity of films deposited on LDPE substrates pretreated with 150 W Ar plasma.

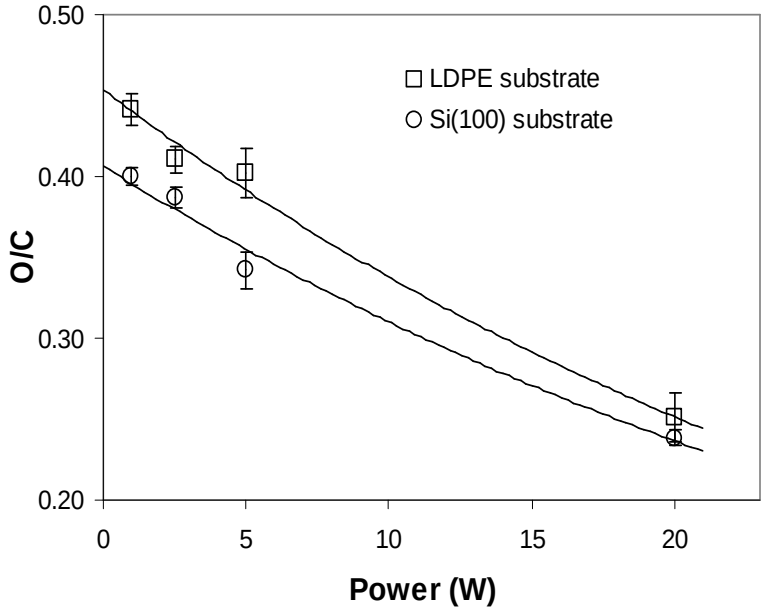

Figure 4.4. O/C atomic ratio determined from the XPS spectra of the O1s and C1s core level peaks of films deposited on (□) LDPE and (○) Si(100) substrates versus diglyme plasma power. (Corresponding diglyme plasma treatment conditions are given in Table 4.1.)

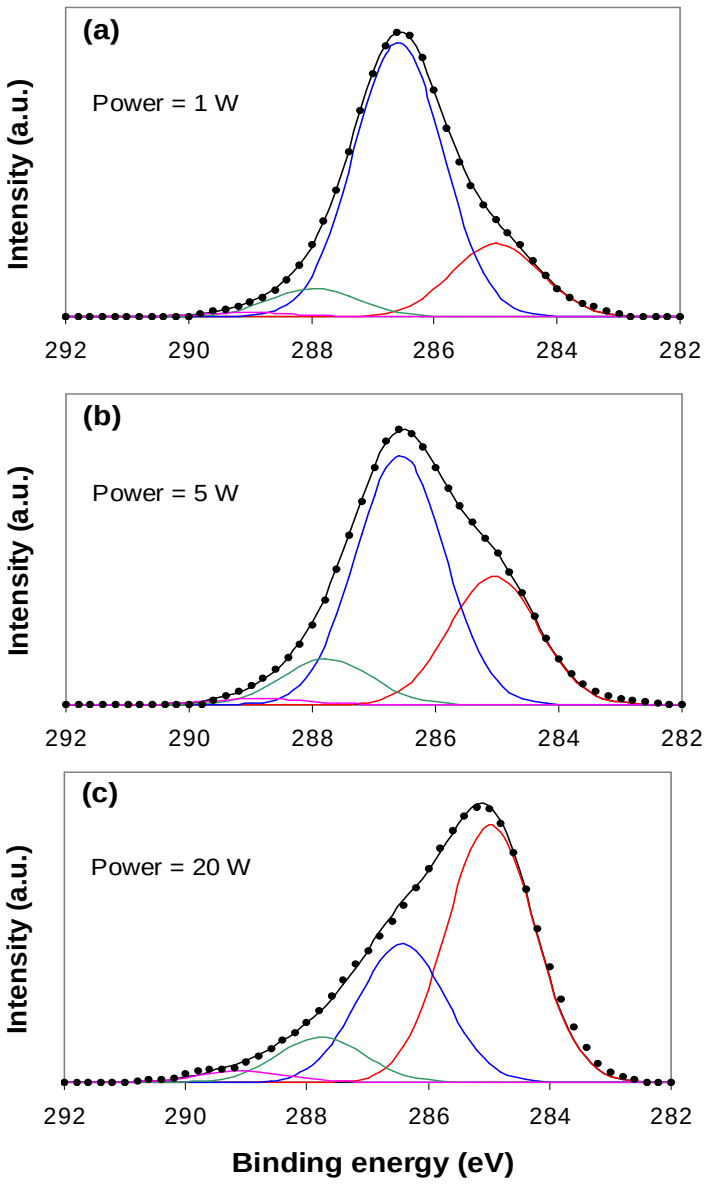

Figure 4.5. XPS spectra of the C1s core level peak of films deposited on LDPE substrates pretreated with 150 W Ar plasma for diglyme plasma power equal to (a) 1 W, (b) 5 W, and (c) 20 W. Each spectrum was curve fitted with four Gaussian distributions centered at about 285.0, 286.5, 288.0, and 289.2 eV, assigned to C–C(C–H), C–O, O–C–O(C=O), and COOR(COOH), respectively. (Corresponding diglyme plasma treatment conditions are given in Table 4.1.)

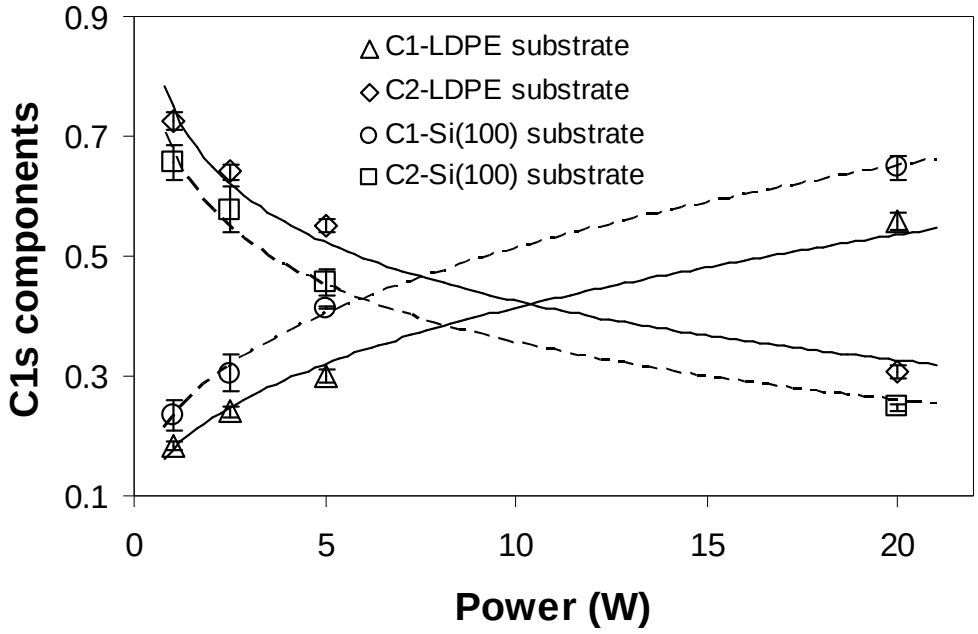

Figure 4.6. Fractions of C–C(C–H) (C1 curves) and C–O (C2 curves) determined from the XPS spectra of the C1s core level peak of films deposited on LDPE and Si(100) substrates versus diglyme plasma power. (Corresponding diglyme plasma treatment conditions are given in Table 4.1.)

Chapter 5

Plasma-assisted Surface Chemical Patterning for Single-cell Culture and Cell Shape-regulation of Smooth Muscle Cell Proliferation

5.1 Introduction

Single-cell patterning is of great importance in cell biology, biosensor technology, and tissue engineering. This technique can be used to control the cell shape and spreading area, which are known to affect various cell functions, such as migration, division, and differentiation. PDMS soft lithography, including microcontact printing and membrane-based patterning, is a common method of patterning biological arrays (Whitesides et al. (2001)). By using a PDMS stamp or membrane, the surface chemical characteristics can be modified to produce localized surface regions possessing either nonfouling or fouling behaviors. For example, to obtain surface patterns for cell culture, a PDMS stamp was used to deposit a self-assembled monolayer that promoted cell adhesion (e.g., hexadecanethiol) on gold or silver surfaces, which were subsequently coated with another monolayer that resisted cell adhesion (e.g., alkanethiol terminated by ethylene glycol groups) (Ostuni et al. (1999), Luo et al. (2008), Tan et al. (2004)). Fabrication of protein arrays for cell patterning was accomplished by using a PDMS stamp to transfer ECM (e.g., fibronectin and collagen) onto surfaces coated with different nonfouling materials (Tan et al. (2004), Bernard et al. (1998), Roca-Cusachs et al. (2008)). Another surface patterning method for cell culture is to create isolated areas for cell attachment by transferring ECM proteins to a substrate surface through the window arrays of a PDMS membrane (Jackman et al. (1999)) and then coating the rest of the surface with a cell adhesion inhibitor, such as bovine serum albumin (BSA) protein (Roca-Cusachs et al. (2008), Ostuni et al. (2000), Wang et al. (2002)). Surface cell patterning has also been accomplished by coating microwell arrays of PDMS with fibronectin and the surrounding areas with BSA protein (Ostuni et al. (2001)).

Despite the extensive use of methods based on soft lithography, other promising methods for cell patterning exist, such as surface chemical patterning that combines photolithography and plasma polymerization/deposition of thin films which either inhibit or promote cell adhesion (Andreas Goessl et al. (2001), Brétagnol et al. (2007)), surface patterning of ECM proteins using photoresist (PR) as the lift-off mask (Lee et al. (2008)), laser-assisted modification of the surface chemistry and topography in conjunction with surface patterning (Hopp et al. (2008)), and fabrication of microwell arrays on Si surfaces with an atomic force microscope to trap single cells (Choi et al. (2008)). In plasma-assisted surface patterning, deposition of a background layer that prevents cell adhesion (e.g., PEG-like film) is followed by grafting of a film that promotes cell attachment (e.g., fluorocarbon) using a PR mask. However, there are two main difficulties with the former process: (a) the solvent used in the lift-off step may deplete the nonfouling

property of the thin background layer and (b) the wet-etch process may degrade the longevity of the cell pattern because the chemical residue is harmful to sensitive cells (e.g., neuron and human stem cells).

In this chapter, a simple cell-sensitive process of surface chemical patterning that combines plasma-assisted polymerization and deposition with plasma etching through the window arrays of a shadow mask is developed. Using this method to synthesize the background nonfouling layer is advantageous because of the easiness of the one-step dry coating process, applicability over a wide range of substrate materials, good bonding of the nonfouling layer to the substrate, and sterility of the process. Surface areas for cell attachment were obtained by partial plasma etching of the nonfouling layer through the windows of a special shadow mask fabricated by photolithography. In particular, the PEG-like film was removed from those areas exposed by the mask windows to create areas for cell attachment, while the PEG-like film in the surrounding surface areas was protected by the mask. The surface patterning method is presented in four steps: (1) deposit a nonfouling PEG-like film (background layer), (2) fabricate Si and PDMS membrane shadow masks for patterning the substrate surface by Ar plasma etching, (3) form single-cell patterns on substrates patterned with a nonfouling PEG-like film using a shadow mask, and (4) study the effect of the pattern shape and size on the morphology of the attached cells. The nonfouling behavior of the PEG-like film and the efficacy of the present method to produce chemically patterned surfaces for single-cell culture are examined in the context of protein adsorption, cell attachment, and cell patterning results presented in the following sections.

With the introduced surface patterning method, cell shape regulation on smooth muscle cell (SMC) proliferation is also studied in this chapter. It is well known that vascular SMCs play an important role in vascular remodeling and disease development. In atherosclerotic lesions, SMCs migrate from the vascular wall into the lumen, demonstrating a phenotypic change from contractile to proliferative phenotype. It has been reported that in-vitro isolation of SMCs from three-dimensional (3D) ECM, where the cells exhibit elongated, spindle-shape morphology, and sub-culture in culture dishes promotes spread-out morphology and proliferative phenotype (Owens et al (1995), Thyberg et al (1998), Dilley et al (1987)). Distinct SMC populations with different cell shapes (spindle or epithelioid/rhomboid) and phenotypes (differentiated or proliferative) have also been isolated from arteries (Hao et al. (2002)). However, it is not well understood if the cell shape directly affects SMC proliferation. In this study, in-vitro culture system is used to examine the effects of SMC morphology on SMC proliferation.

Micropatterning technology offers powerful tools to manipulate the microenvironment for cell growth, migration, and differentiation (Whitesides et al (2001), Tsang et al (2004)). Recent studies have shown that micropatterned matrix strips and microgrooves restrict SMC spreading in one direction, resulting in more elongated SMC morphology and lower proliferation rate (Thakar et al. (2003), Sarkar et al. (2005), Yim et al. (2005)). However, the underlying mechanisms require further investigation. Although the micropatterning methods used in these studies provide effective means of manipulating the SMC morphology for biochemical and biological analysis, changes in the SMC morphology are usually accompanied by changes in the spreading area. The cell spreading area has been observed to regulate cell proliferation in many cell types (Folkman et al. (1978), Singhvi et al. (1994), Chen et al. (1997), Bhadriraju et al. (2002)). To distinguish the effects of the cell shape and the cell spreading area, micropatterned

islands of well-defined shape and area are created with the presented method and used in the study to evaluate cell shape effects on SMC proliferation.

5.2 Experimental procedures

5.2.1 Sample preparation

Three different substrates, namely low-density polyethylene (LDPE), Si(100), and polystyrene dishes were used in the cell-culture studies. Approximately 1-mm-thick LDPE disk substrates were fabricated by compressing LDPE pellets (Sigma-Aldrich, St. Louis, MO) between clean glass slides heated at 160°C. Other substrates used for cell culture were silicon pieces (0.8×0.8 cm^2) cut from a 10-cm-diamter p-type Si(100) wafer and TCP Petri dishes (Thermo Fisher Scientific, Waltham, MA), both used in their as-received condition.

5.2.2 Synthesis of PEG-like films

Film grafting on different substrates was performed in a radio-frequency capacitively coupled plasma reactor (RTE73 AMNS-500-E, Plasma Therm, Kresson, NJ) with a plate diameter of 29.4 cm and plate-to-plate distance equal to 5 cm. Before film grafting, the chamber was cleaned with O_2 plasma (300 W power; 100 sccm O_2 gas flow rate) for 10 min, and the substrate surfaces were exposed to Ar plasma (150 W power; 50 sccm Ar gas flow rate) for 5 min to remove any surface contaminants. Subsequently, diethylene glycol dimethyl ether (diglyme) vapor ($CH_3–O–(CH_2–CH_2–O)_2–CH_3$, Sigma-Aldrich, St. Louis, MO) of 99.5% purity was introduced into the chamber at a pressure of ~10 mTorr. Film grafting by plasma polymerization and deposition was performed under conditions of 1–20 W power, ~10–15 mTorr working pressure, and 5–30 min treatment time. More details of the synthesis and physicochemical characterization of the grafted films can be found elsewhere (Cheng et al. (2009)).

5.2.3 Protein adsorption assay

Fluorescein isothiocyanate (FITC)-labeled bovine serum albumin (BSA) was used to evaluate protein adhesion on films grafted onto LDPE disks from diglyme plasma. Disks with the grafted films were covered with a FITC-BSA solution of 100 $\mu g/cm^2$ area density and incubated for 1 h at room temperature in a dark space. Then, the samples were washed twice with deionized water and allowed to dry in a clean laboratory environment before observation with an upright fluorescence microscope (Zeiss HAL 100, Carl Zeiss MicroImaging, Thornwood, NY). The amount of absorbed FITC-BSA was determined from the green color intensity in the fluorescence photographs. An untreated LDPE surface coated with only tris(hydroxymethyl)methylamine (FITC-BSA solvent) was used as black reference, whereas an untreated LDPE surface coated with FITC-BSA that not washed before observation was used as bright reference.

5.2.4 Cell adhesion

Bovine aorta endothelial cells (BAECs) were used to study cell adhesion on films grafted on various substrates (i.e., LDPE, Si, and TCP dishes) under different diglyme plasma conditions. After film grafting, cells were seeded on different substrates with serum medium consisting of Dulbecco's Modified Eagle's Medium (DMEM), 10% fetal bovine serum (FBS), and 1% penicillin streptomycin (PS) and stored in an incubator with 5% CO_2 at 37°C for 24 h. Cells seeded on TCP dishes were observed with an inverted microscope (TE 300, Nikon, Melville, NY) operated in phase-contrast mode. Because phase-contrast photographs of the cells seeded on LDPE and Si(100) substrates could not be obtained, the cells were fixed with 4% paraformaldehyde (PFA), permeabilized with 0.5% Triton X-100, and the cell actin and nucleus were stained with Alexa-Phalloidin 488 and 4',6-diamidino-2-phenylindole (DAPI), respectively. Fluorescence photographs of the stained BAECs were obtained with the inverted Nikon microscope.

5. 3 Mask fabrication and surface patterning

5.3.1 Si shadow mask

A Si shadow mask was fabricated from a p-type Si(100) wafer of thickness equal to ~525 μm with both sides coated with a ~0.6-μm-thick SiN film. Two chromium masks with a feature lateral spacing of 1000 μm were used to fabricate the Si mask. Features of design dimensions were produced on mask (2), whereas the features on mask (1) were enlarged by 372 μm compared to those on mask (2) to allow etching of a 425-μm-thick Si layer. The fabrication process is shown schematically in Figure 5.1. Briefly, the wafer back side was spin coated with a 4-μm-thick layer of OCG 825 PR, and after exposure to UV light through mask (1) and development, the pattern was transferred first to the PR and then to the SiN layer at the wafer back side by reactive ion etching (RIE). Subsequently, the back side of the wafer was etched with a 30% KOH solution to remove ~425 μm of the exposed Si and the SiN layer was etched away by immersing the wafer into a 49% HF solution for 2 h. Then, the front side of the wafer was spin coated with a 4-μm-thick layer of OCG 825 PR, exposed to UV light through the windows of mask (2) which was roughly aligned to the backside features, and after development and hard baking, was etched trough by RIE. Finally, the wafer was saw-cut into 1.7 × 1.7 cm^2 pieces, each having window arrays of specific shape and size.

The sloped (θ=54.7°) sidewalls produced from the 30% KOH etch (Figure 5.1(f)) are due to the anisotropic etch of Si(100). Because of this effect, the fabrication process shown in Figure 5.1 can be simplified to produce windows of square and rectangular shapes by extending the 30% KOH etch step (Figure 5.1(f)) to etch through the wafer thickness until the desired window size is obtained. Despite the well-defined slope that characterizes the anisotropic etch process, the window size cannot be accurately controlled with this one-step etch process due to variations in the wafer thickness. Therefore, to control the window size and/or obtain other pattern shapes (e.g., circular or oval) a dry etch step (Figure 5.1(j)) was incorporated in the fabrication process of the shadow mask after the wet etch step (Figure 5.1(f)). In addition to a precise control of the window size and shape, the shadow masks produced by the fabrication process shown in Figure 5.1 are relatively thick and, therefore, not likely to fracture during handling. Figure 5.2(a) shows windows of different shapes and sizes fabricated at the front side of a Si shadow mask with the process that includes both wet and dry etch steps (Figure 5.1). The

window areas are between 500 and 4000 μm^2, while the window shape index SI (defined as SI $= 4 \cdot \pi \cdot A / P^2$, where A and P are the projected area and the perimeter of the feature, respectively) is in the range of 0.1–1.0. Figure 5.2(b) shows square and rectangular windows at the front side of a Si mask produced with a similar fabrication process with a single wet etch step. The slightly distorted shapes of the circular and square windows are due to tilting of the wafer during observation.

5.3.2 PDMS membrane mask

The fabrication of the PDMS mask is similar to that used in earlier studies (Jackman et al. (1999)). Micropost arrays of ~50 μm in height and 200 μm in lateral spacing were fabricated on a p-type Si(100) wafer using SU-8 2050 PR (MicroChem, Newton, MA) to obtain the master wafer. Before coating with PDMS, the master wafer was exposed to perfluoro-1,1,2,2-tetrahydrooctyltrichlorosilane (United Chemical Technology, Bristol, PA) vapor overnight in a desiccator to prevent PDMS adhesion to the master features. Then, the master wafer was spin coated with a mixture (10:1) of Sylgard 184 silicone elastomer kit (Dow Corning, Midland, MI) to produce a ~30-μm-thick PDMS film and cured at 65°C for 4 h. Finally, the PDMS membrane was cut into 1.7 × 1.7 cm^2 pieces, each having window arrays of specific shape and size, which were then carefully peeled off from the master wafer.

Although the fabrication of the PDMS membrane mask is much more straightforward than that of the Si mask, the shape and size of the windows on the PDMS mask cannot be controlled as precisely as with the Si mask. Transferring the design pattern to the master wafer was influenced by damping of the light intensity during the exposure to UV light due to the large thickness of the SU-8 PR. Thus, the micropost cross-section areas were larger at the top and smaller at the bottom, with only the top micropost areas having the design dimensions. Therefore, the portion of the microposts responsible for generating the holes in the PDMS mask did not possess the desired geometry and size, causing the feature size and SI to deviate slightly from the design specifications. Photographs of pattern features on the PDMS membrane mask are not shown here for brevity.

5.3.3 Surface chemical patterning for single cell culture

After film grafting, the shadow mask and the plasma-treated TCP dish surface were brought into contact with the smooth side of the mask faced flat against the dish surface. The grafted film was then removed from those areas exposed through the mask windows by Ar plasma etching, the mask was lifted, and the dish patterned with surface areas of exposed polystyrene surrounded by areas of the grafted film was released. Surface patterns of different shape and size were produced on dish surfaces coated with the PEG-like film (1 W diglyme plasma power; 40 min treatment time) with the PDMS membrane mask.

Both Si and PDMS membrane masks can be used in the present surface patterning process. The pattern transfer from the shadow mask to the substrate surface depends on the plasma etching conditions and surface contact intimacy. For the Si mask, the optimum plasma etching conditions were 10 W power, 10 sccm Ar gas flow rate, and 1 min treatment time, while for the PDMS membrane mask, the best pattern transfer results were obtained under plasma

etching conditions of 30 W power, 30 sccm Ar gas flow rate, and 2 min treatment time. For the Si shadow mask, an enlargement of the pattern transferred to the substrate surface was observed with the increase of plasma power and/or treatment time due to the intense and/or prolonged interactions between energetic Ar^+ ions and the film material under the shadow mask. In addition, since PDMS adheres well to most surfaces, the PDMS membrane mask can stick firmly to the substrate surface, which is critical to the accuracy of the transferred pattern. However, distortion of the transferred pattern was observed in a few occasions due to deformation of the flexible PDMS membrane mask during handling.

TCP dishes were used as substrates in all of the single-cell patterning studies. This was advantageous because post-treatment of the TCP dishes before cell seeding was not necessary since plasma etching of the grafted film through the mask windows had exposed the original dish surface on which the cells could attach easily. Alternatively, because the cells did not attach well on bare PDMS, when a PDMS film was used as the substrate, the plasma-etched surface with the PDMS membrane mask was treated with a fibronectin solution to coat the exposed areas before lifting the mask to release the patterned surface for cell seeding.

The patterned dishes were UV sterilized for 30 min and then washed with phosphate buffered saline (PBS) to remove any film debris. Human mesenchymal stem cells (hMSCs) were used for cell seeding. After 24-h incubation, the cells were fixed with 4% PFA and stained for actin and nuclei. Phase-contrast photographs of living hMSCs and fluorescence photographs of stained hMSCs were obtained with Nikon or Zeiss microscopes.

5.4. Cell shape-regulation of smooth muscle cell proliferation

5.4.1 Surface micropatterning and cell culture

Single-cell surface micropatterning was achieved on TCP dishes with the previously discribed method with PDMS membrane mask. Human aortic SMCs (Cascade, Portland, OR) were then cultured in serum medium and maintained the incubator at 37°C. SMCs between passage 6 and 20 were used in the experiments.

5.4.2 Immunostaining, microscopy, and morphological analysis

For immunostaining and microscopy, cells were fixed with 4% PFA, permeabilized with 0.5% Triton X-100, and blocked with 1% BSA. Cell actin and nuclei are stained with Alexa phalloidin and DAPI. Fluorescence images were collected by a Zeiss LSM (Carl-Zeiss Microimaging, Thornwood, NY) confocal microscope (100X objective). Multiple Z-section images (~0.3–0.4 μm thick sections) were obtained for each specimen. For 3D analysis, serial pictures of the nucleus were reconstructed into a 3D structure using the software Imaris (Bitplane, St. Paul, MN), which was then used to calculate the nucleus volume. For two-dimensional (2D) analysis, the optical sections were projected onto a single plane to construct an overall image of the specimen. The cell shape index (CSI) and the nucleus shape index (NSI) were calculated from the 2D images of the cells. The cell boundaries were outlined with the Scion IMAGE (Scion, Fredrick, MD) software. The spreading area (i.e., cell projected area) and the perimeter of the cell were measured, and the CSI was calculated from the relationship CSI =

$4Pi \cdot Area/(Perimeter)^2$. The CSI assumes values between 1 (circular shape) and 0 (elongated, linear morphology). A similar relationship was used to calculate the NSI in terms of the measured nucleus projection area and nucleus perimeter.

5.4.3 Cell proliferation analysis

SMCs seeded on surfaces with different patterns and cultured for 24 h were incubated for 2 h with 10 μM 5-bromo-2'-deoxyuridine (BrdU) (Sigma-Aldrich, St. Louis, MO). Then, the samples were fixed with 4% PFA, permeabilized with 0.5% Triton X-100, and incubated for 30 min in 2N HCl at 37 ºC. Subsequently, the samples were washed and incubated for 30 min in a buffer containing PBS, 0.05% Tween 20, and 1 mg/ml BSA to minimize background adsorption of antibodies. The samples were incubated with the primary antibodies against BrdU (PharMingen, San Diego, CA) and a FITC-anti-mouse antibody. After washing with PBS, the stained samples were counterstained with DAPI for 5 min, mounted in VectaShield (Vector Laboratories, Burlingame, CA), and observed with a fluorescence microscope. The percentage of SMCs that incorporated BrdU (i.e., the cells with DNA synthesis) was correlated to the proliferation rate of SMCs. Mean and standard deviation values were calculated for each group of data. The Student's t-test was used to analyze experimental groups with two samples.

5.5 Results and discussion

5.5.1 Unpatterned surfaces

Protein adsorption. Adsorption of FITC-BSA protein on untreated and plasma-treated LDPE surfaces can be interpreted in light of the fluorescence intensity results shown in Figure 5.3. The color intensities for the black and bright reference surfaces were set equal to 0 and 100%, respectively. The significant increase in BSA adsorption as a result of Ar plasma treatment is attributed to surface charging and the formation of hydrophilic chemical groups. The subsequent exposure to diglyme plasma suppressed BSA adsorption dramatically, especially for low-power (1.0 and 2.5 W) plasma treatment. The increase in BSA adsorption for higher plasma power (5 and 20 W) indicates a depletion of the nonfouling film character under those plasma conditions. In fact, the fluorescence intensity for 20-W plasma power is close to that of the untreated surface, but still significantly lower than that of the Ar plasma-treated surface.

Cell culture. Figure 5.4 shows phase-contrast photographs illustrating the effect of plasma treatment conditions on the morphology of BAECs incubated for 24 h in serum medium. The cells attached and spread on the TCP dish surface treated with Ar plasma (Figure 5.4(a)). However, subsequent treatment with diglyme plasma affected the morphology of BAECs significantly. Film grafting under low-power (1 W) diglyme plasma conditions was particularly effective in preventing cell attachment, resulting in cell aggregation and formation of cell clusters (Figure 5.4(b)). The surface chemical characteristics of this film have been found to be similar to that of pure PEG (Cheng et al. (2009)). However, film grafting at higher diglyme plasma power (i.e., 5 and 10 W) was not effective in preventing cell attachment and spreading (Figures 5.4(c) and 5.4(d)). A comparison of Figures 5.4(a), 5.4(c), and 5.4(d) shows that high diglyme plasma power resulted in cell morphologies similar to those of cells seeded on Ar plasma-treated dish surfaces.

Figure 5.5 shows fluorescence photographs of BAECs seeded on LDPE substrates exposed to different plasma conditions. The cell actin organization indicates that only the film grafted under the conditions of 1-W diglyme plasma power inhibited cell attachment and spreading. Only one cell cluster (Figure 5.5(b)) was found on the entire sample surface because the unattached cells formed clusters floating in the medium which were washed away during the staining process. This finding illustrates a correlation between cell affinity for surface attachment and surface chemistry. Since the chemical character of the films grafted at higher diglyme plasma power (i.e., 5 and 10 W) is less similar to PEG than those of the film grafted at 1 W diglyme plasma power (Cheng et al. (2009)), it may be inferred that cell attachment was controlled by surface functionalities that characterize the chemical behavior of PEG. Thus, the film grafted under the conditions of 1-W diglyme plasma power is referred to as PEG-like film. Similar results were obtained with other substrates (i.e., Si, SiO_2, and PDMS) treated under identical diglyme plasma conditions. This illustrates the effectiveness of the PEG-like film to prevent cell adhesion on various substrates in full serum medium.

5.5.2 Patterned surfaces for single-cell culture.

The previous results of BSA protein adsorption and BAEC adhesion indicate that low-power diglyme plasma polymerization and deposition can be used to graft films that mimic the nonfouling property of PEG on different substrates, such as polystyrene, LDPE, PDMS, Si, and SiO_2. The intriguing concept of a surface patterning method that uses this biologically nonfouling film is examined next.

Cell culture. TCP dishes coated with PEG-like film (1 W power; 40 min treatment time) were patterned for single-cell culture. For surface patterning with the Si mask, the hMSCs were seeded in reduced serum medium (DMEM + 1% FBS) to prevent nonspecific cell attachment. However, for surface patterning with the PDMS membrane mask, the hMSCs were seeded in full serum medium without the occurrence of nonspecific cell attachment. This indicates that the integrity of the PEG-like film was better preserved with the compliant PDMS membrane mask than the stiff Si shadow mask. Figures 5.6(a)-5.6(e) show phase-contrast photographs of single hMSCs after 24-h incubation in reduced serum medium on TCP dishes patterned with the Si mask that was fabricated with the two-step etch process. While the cells on the unpatterned dish surface spread freely on the dish surface (Figure 5.6(a)), cell spreading on the patterned surfaces was controlled by the pattern size and shape (Figures 5.6(b)-5.6(e)). The cells extended lamellipodia in different directions, even outside the pattern boundaries (e.g., Figure 5.6(b)), seeking for additional area to attach. However, the nonfouling property of the PEG-like film prevented cell spreading outside the pattern boundary. Fluorescence photographs of single hMSCs seeded on dishes patterned with the Si mask fabricated with one-step etch process show cells of only square or rectangular shape (Figure 5.6(f)). Time-lapse videos showing the movement of hMSCs on patterned TCP dishes can be found in the Supporting Information.

Effect of pattern geometry on cell morphology. Staining for cell actin and nuclei was used to examine the effect of the pattern shape and area on the cell morphology. hMSCs seeded on TCP dishes patterned with the PDMS membrane mask were fixed after 24-h incubation in serum medium and the cell actin and nuclei were stained for observation. Fluorescence photographs of hMSCs seeded on patterns of different shape and size, shown in Figure 5.7, reveal an effect of

the cell shape and size on the actin organization and nucleus morphology. Circular hMSCs showed fairly round nuclei and actin alignment along the radial direction and around the fairly round nucleus, while elongated hMSCs showed nucleus elongation and actin alignment along the major axis of their elliptical shapes. A comparison of circular hMSCs with different spreading areas shows decay in the organization of the actin structure with decreasing spreading area. These findings indicate that cell patterning could have further implications on cell behavior, which is worthy of more in-depth investigation.

The results of single-cell culture on patterned dish surfaces demonstrate the efficacy of the present fabrication process that is based on grafting a nonfouling PEG-like film by plasma polymerization and deposition and then selectively removing the film by Ar plasma etching through the windows of a shadow mask to produce a chemically patterned surface. The easiness of the patterning process and the high yield of surface patterning (~100%) for single-cell culture obtained with the PDMS membrane mask enable statistical studies of the cell shape and size effect on cell behavior, such as proliferation. Although the PDMS membrane mask is more effective than the Si shadow mask in producing single-cell patterns on relatively stiff substrates, both masks can produce surface patterns of cell clusters. Because of the stickiness and low stiffness of the ~30-μm-thick PDMS mask, careful handling must be exercised to prevent tear, fracture, or excessive deformation leading to window distortion during surface patterning. Repeated use of the PDMS mask depends on the deterioration rate due to plasma etching. Under the plasma etching conditions of the present process, the PDMS mask was used for 5-6 times without evidence of plasma-induced deterioration. Although the Si mask does not have the limitations of the PDMS mask, contact with the substrate surface is relatively less intimate due to the high stiffness of silicon, resulting in enlargement of the transferred pattern. Another difference is the lower feature density of the Si mask compared to that of the PDMS mask. However, the Si mask is effective in surface patterning of soft substrates (e.g., PDMS) because the compliance of the substrate enhances intimate contact across the mask/substrate interface, and since the Si mask can be easily cleaned, it can be used in several surface patterning runs.

5.5.3 Cell shape-regulation of smooth muscle cell proliferation.

Regulation of SMC Proliferation by the Cell Shape and Spreading Area. Arrays of adhesion islands with different CSI and spreading areas were created by the micropatterning method described in previous texts. To study the effect of the cell spreading area, the CSI was set at 0.45 and the spreading area was decreased to from 1500 μm^2 to 300 μm^2. From previous study (Thakar et al. (2009)), the effect of decreasing the CSI from 1.0 to 0.45 on the SMC proliferation was insignificant while decreasing the CSI from 0.45 to 0.30 yielded a decrease in SMC proliferation by ~60%. Similarly, decreasing the cell spreading area from 1500 to 1000 μm^2while keeping the CSI fixed at ~0.45 did not produce an effect on the SMC proliferation rate, while as shown in Figure 5.8, decreasing the cell spreading area further to 500 and 300 μm^2 significantly decreased SMCs proliferation rate. These results reveal the existence of a threshold for cell shape and spreading area effects on SMC proliferation.

Regulation of the Nucleus Shape and Volume by the Cell Shape and Spreading Area. It was postulated that the cell shape and spreading area modulate the nucleus morphology, affecting DNA synthesis and SMC proliferation. Three cases of cell spreading area equal to 1500 μm^2 and

different micropattern shapes and three cases of CSI ≈ 0.45 and different spreading areas were examined to elucidate the dependence of the nucleus morphology on the cell shape and spreading area and SMC proliferation (Figure 5.9A). As evidenced from Figures 5.9A-B, the cells conformed to the designed shape of the spreading area with small deviations. Elongated cells (CSI ≈ 0.30) exhibited more elongated nucleus of insignificant volume change; however, the decrease in the spreading area did not affect significantly the nucleus shape (Figure 5.9C), implying a greater sensitivity of the change in nucleus shape on the cell shape change. In contrast, the decrease in the cell spreading area produced a significant decrease in the nucleus volume, suggesting that the change of the nucleus volume is mostly regulated by the cell spreading area. Since both the cell shape and the cell spreading area regulate SMC proliferation, it is likely that both the shape and the volume of the nucleus affect DNA synthesis and, in turn, cell proliferation.

5.6 Conclusions

In this chapter, a surface chemical patterning process was developed by combining grafting of a film exhibiting nonfouling behavior (i.e., PEG-like film) onto different substrates (i.e., LDPE, polystyrene, PDMS, Si, and SiO_2) and Ar plasma etching through the window arrays of a Si or PDMS membrane mask fabricated by photolithography. The efficacy of this process to produce surface patterns for single-cell culture was demonstrated by results revealing the attachment and spreading behavior of hMSCs on TCP dish surfaces with patterns of different shapes and sizes. Actin and nuclei staining showed a strong dependence of the hMSC morphology on the size and shape of the cell spreading area. The present patterning process includes only dry process steps and is fairly straightforward, clean, and fast, making it particularly suitable for studying the behavior of single cells.

Micropatterning SMCs on islands of different geometry with the presented method established an effective means of obtaining a direct evidence of cell shape effects on cell proliferation. Previous study shows that SMC proliferation is independent of the variation in the cell spreading area in the range of 1000–1500 μm^2, but significant decrease was observed when cell spreading is confined within much smaller areas (e.g., 300 and 500 μm^2). A plausible explanation for this behavior is that SMC proliferation is not be affected when there is sufficient cell spreading (e.g., >1000 μm^2) and decreases only when spreading is restricted to significantly smaller areas (e.g., 300–500 μm^2). An important insight into the threshold of shape and spreading effects on SMC proliferation was obtained by analyzing the nucleus morphology (shape and volume). The nucleus shape was found to decrease when the CSI decrease to a low value (e.g., 0.30) but not for changes in the cell spreading area. The change in the nucleus shape showed a good correlation with the decrease in DNA synthesis for CSI ≈ 0.30. This finding suggests that the change in the nucleus shape mediates the cell shape effect on DNA synthesis and provides evidence for the existence of a CSI threshold for the nucleus shape effect. On the other hand, the nucleus volume was found to decrease with cell spreading area but not affected much by the cell shape. A significant decrease in the nucleus volume was encountered by confining cell spreading over small areas (e.g., 300 and 500 μm2), indicating a good correlation with the decrease in DNA synthesis in SMCs. These results provide strong evidence that changes in the nucleus morphology (either shape or volume) could modulate DNA synthesis and, in turn, SMC proliferation.

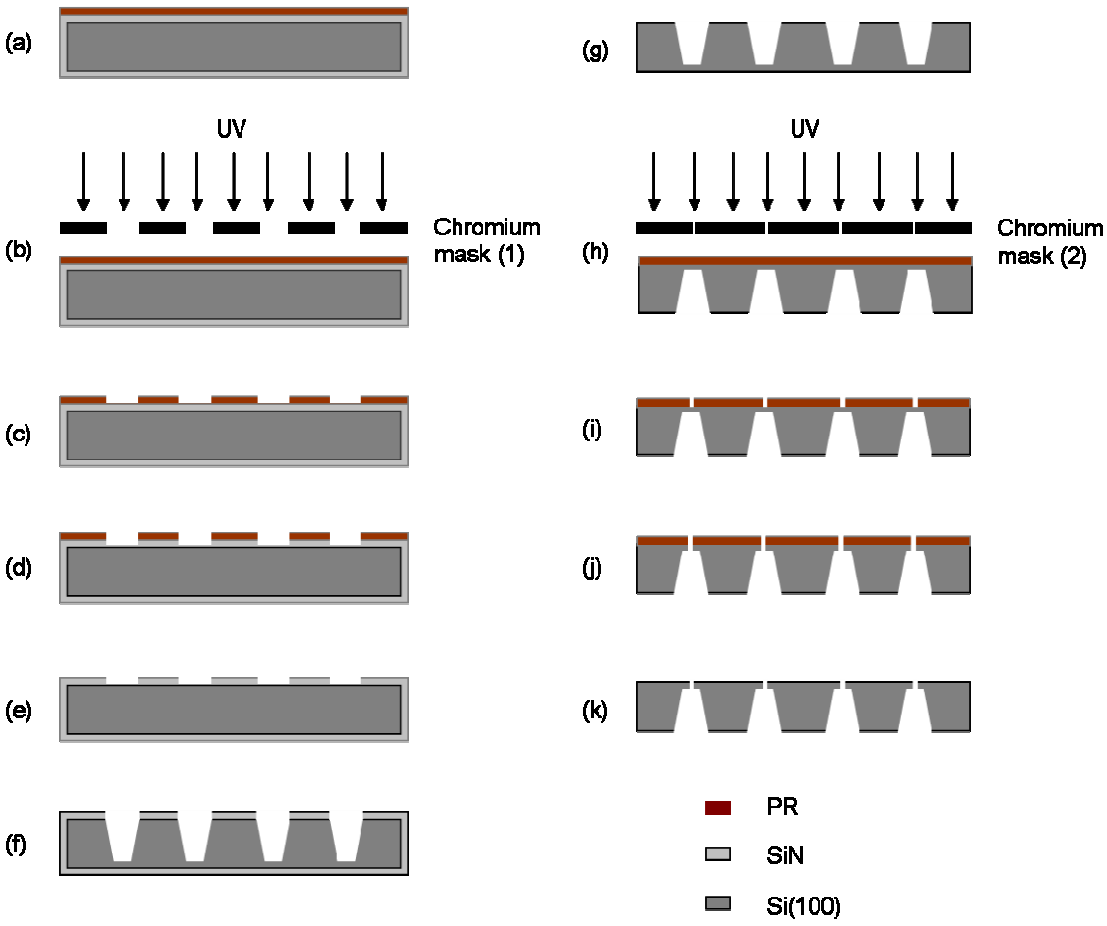

Figure 5.1. Fabrication process of a Si shadow mask: (a) spin coating of the back side of a SiN-coated wafer with PR; (b) PR exposure to UV light; (c) PR development; (d) RIE of the SiN layer; (e) PR stripping; (f) wet etching of the wafer with 30% KOH; (g) removal of the SiN layer by a 49% HF wet etch; (h) spin coating of the wafer front side with PR followed by exposure to UV light; (i) PR development; (j) etching through the Si wafer by RIE; and (k) PR stripping.

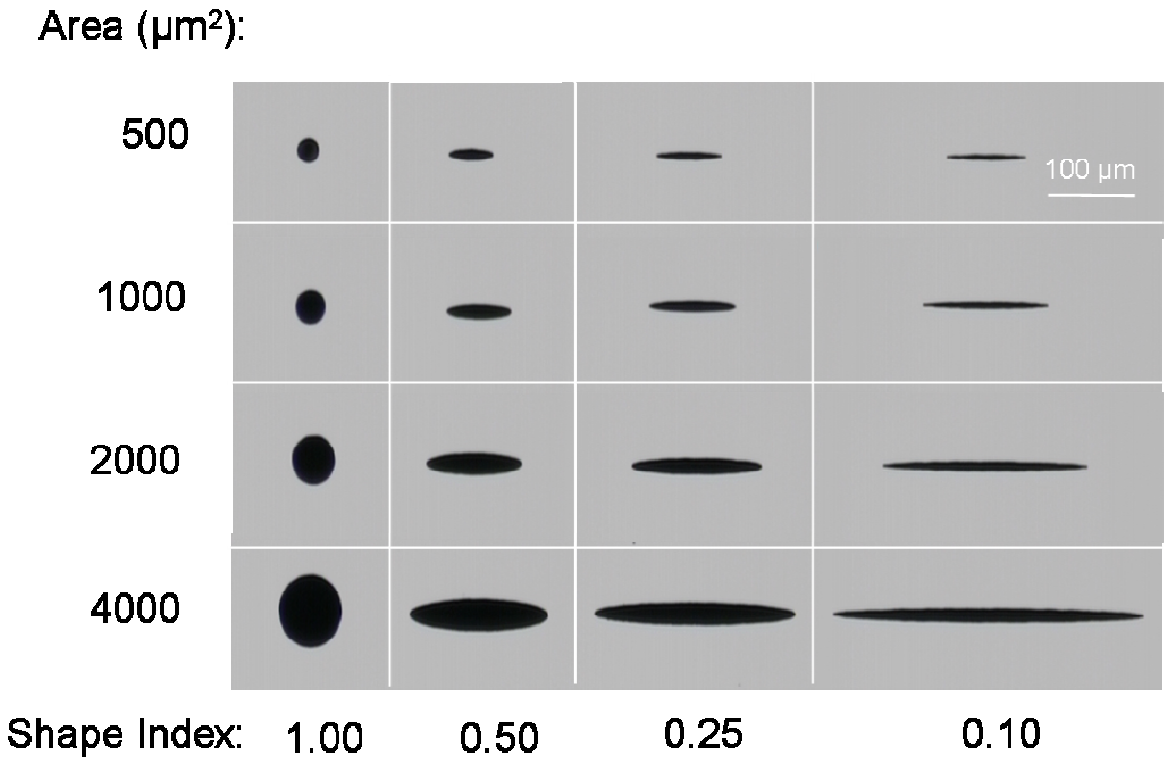

(a)

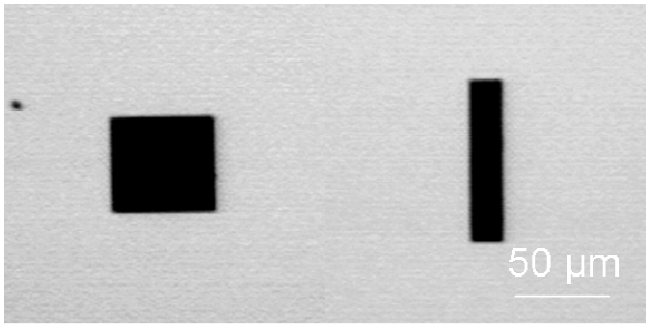

(b)

Figure 5.2. Windows of different shape and size fabricated at the front side of a Si shadow mask by a process including (a) dry and wet etch steps and (b) a single wet etch step.

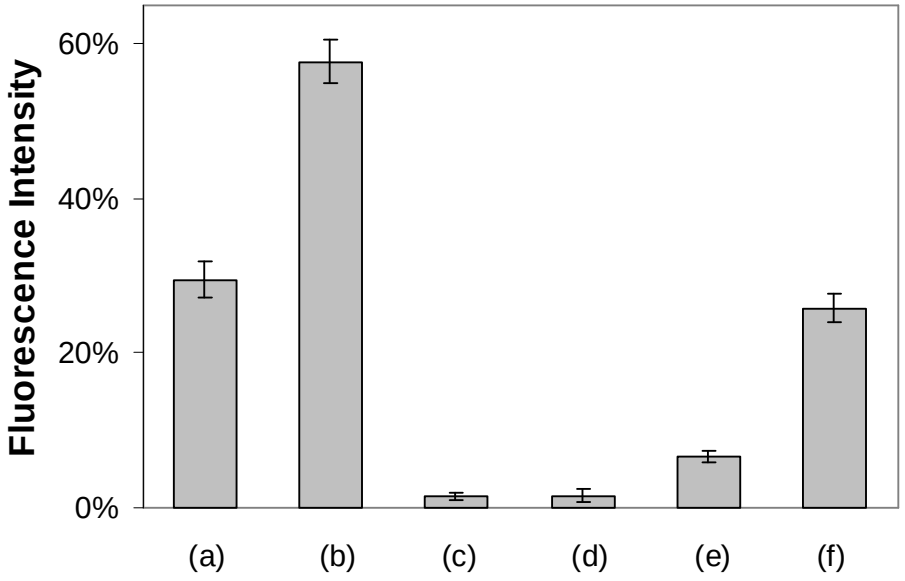

Figure 5.3. Fluorescence intensity of FITC-labeled BSA protein adsorbed on LDPE surfaces: (a) no treatment, (b) Ar plasma treatment, and (c-f) Ar plasma treatment followed by diglyme plasma treatment at a power of (c) 1 W (30 min), (d) 2.5 W (30 min), (e) 5 W (20 min), and (f) 20 W (5 min).

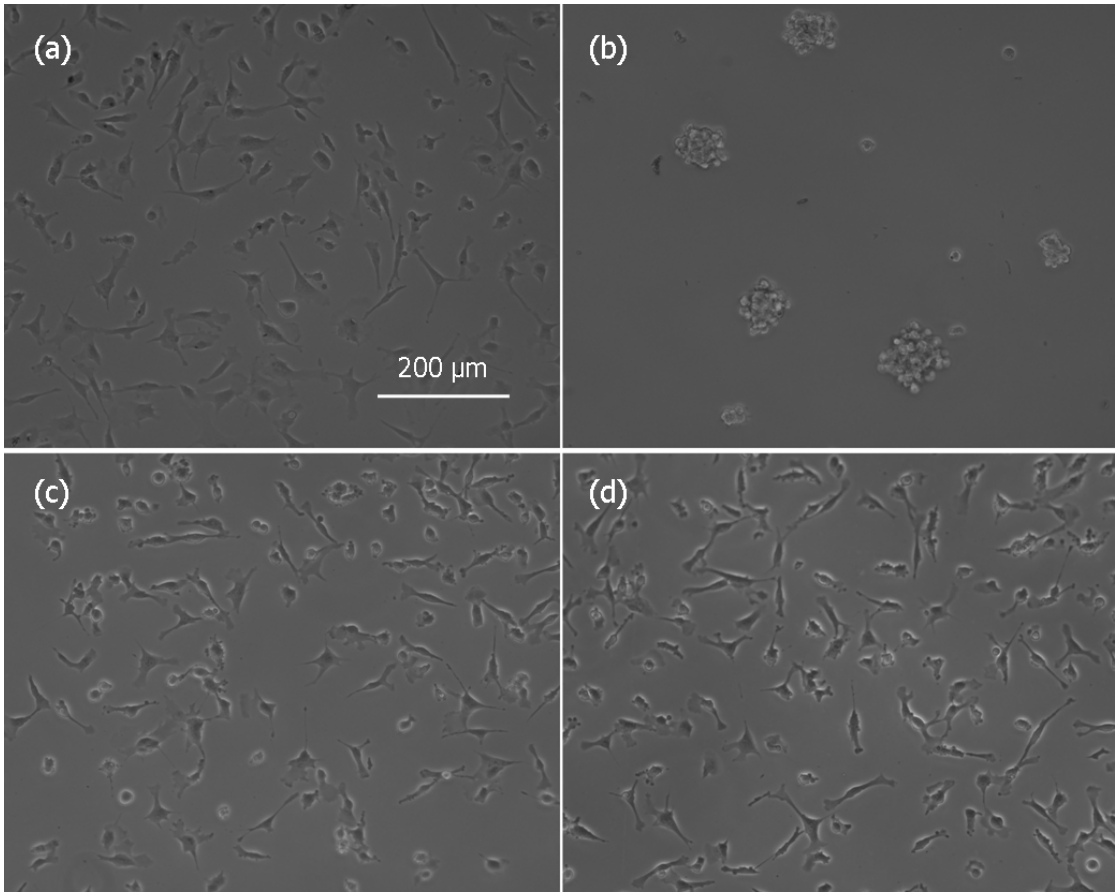

Figure 5.4. Morphology of BAECs after 24-h incubation in serum medium on dish surfaces subjected to (a) Ar plasma treatment and (b-d) Ar plasma treatment followed by 30-min diglyme plasma treatment at a power of (b) 1 W, (c) 5 W, and (d) 10 W.

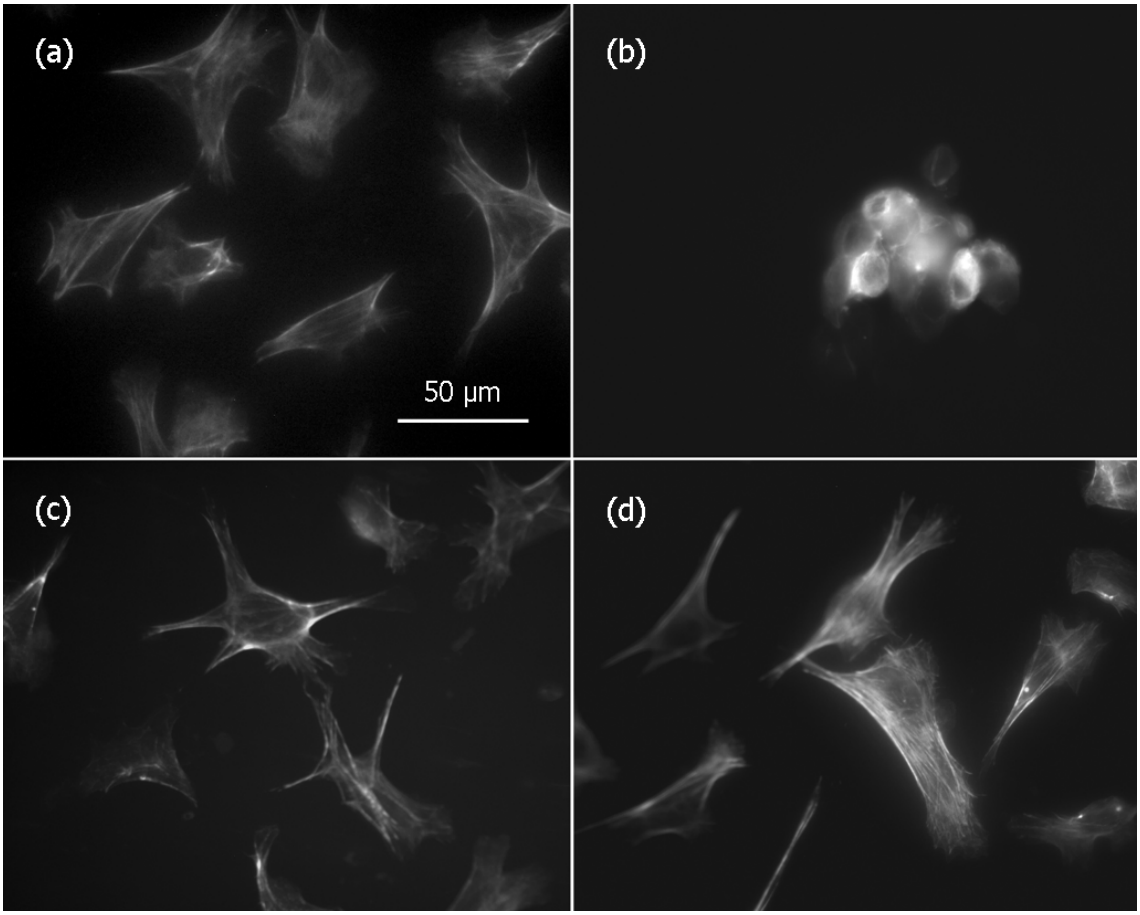

Figure 5.5. Actin structure of BAECs after 24-h incubation in serum medium on LDPE surfaces subjected to (a) Ar plasma treatment and (b-d) Ar plasma treatment followed by 30-min diglyme plasma treatment at a power of (b) 1 W, (c) 5 W, and (d) 10 W.

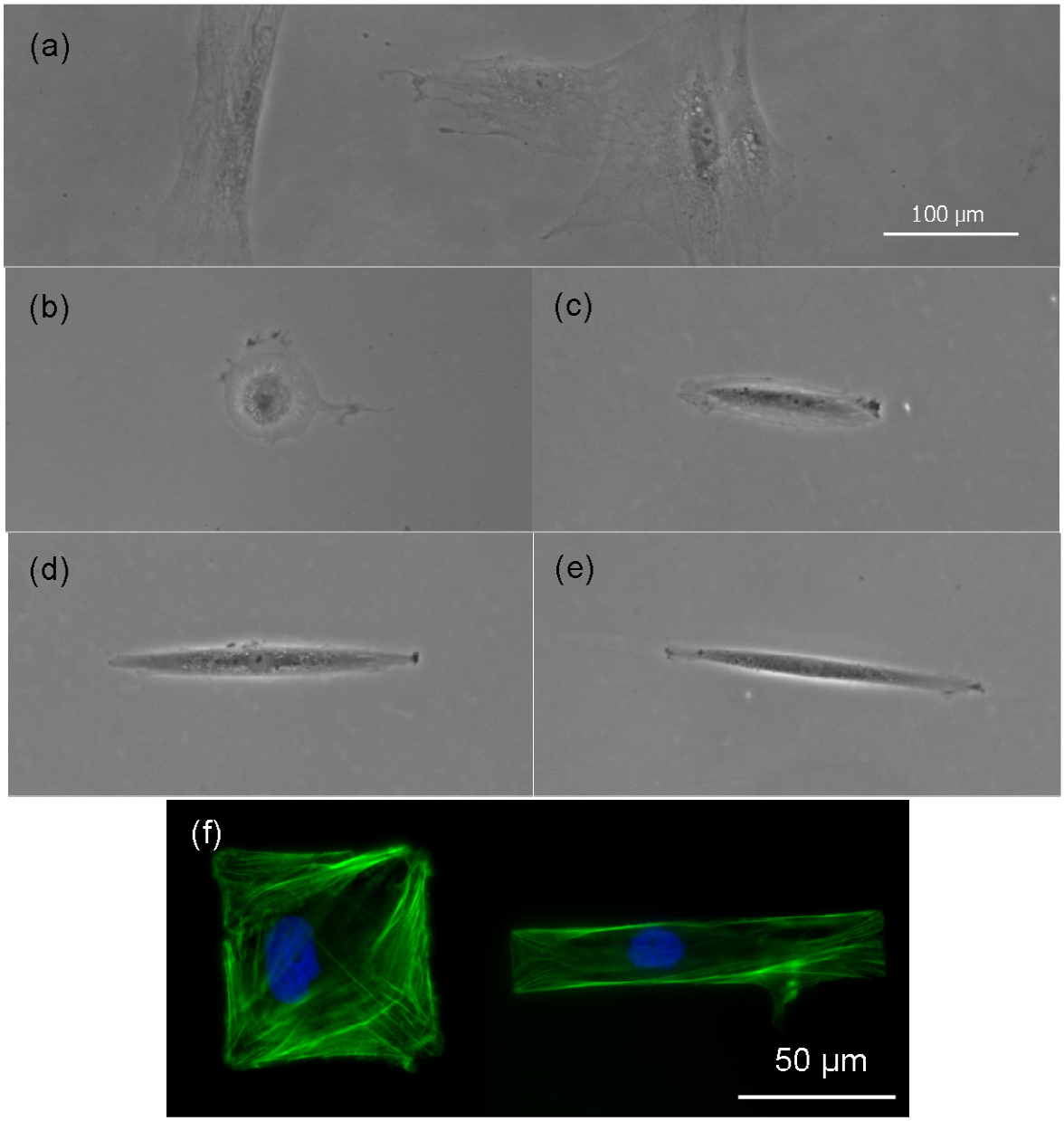

Figure 5.6. Phase-contrast photographs of single hMSCs after 24-h incubation in reduced serum medium on (a) unpatterned and (b-e) patterned dish surfaces. The circular and elliptical patterns have areas equal to 4000 µm2 and SI equal to (b) 1.0, (c) 0.5, (d) 0.25, and (e) 0.1. (f) Fluorescence photographs of single hMSCs with spreading areas equal to ~4000 μm^2 obtained after 24-h incubation in reduced serum medium.

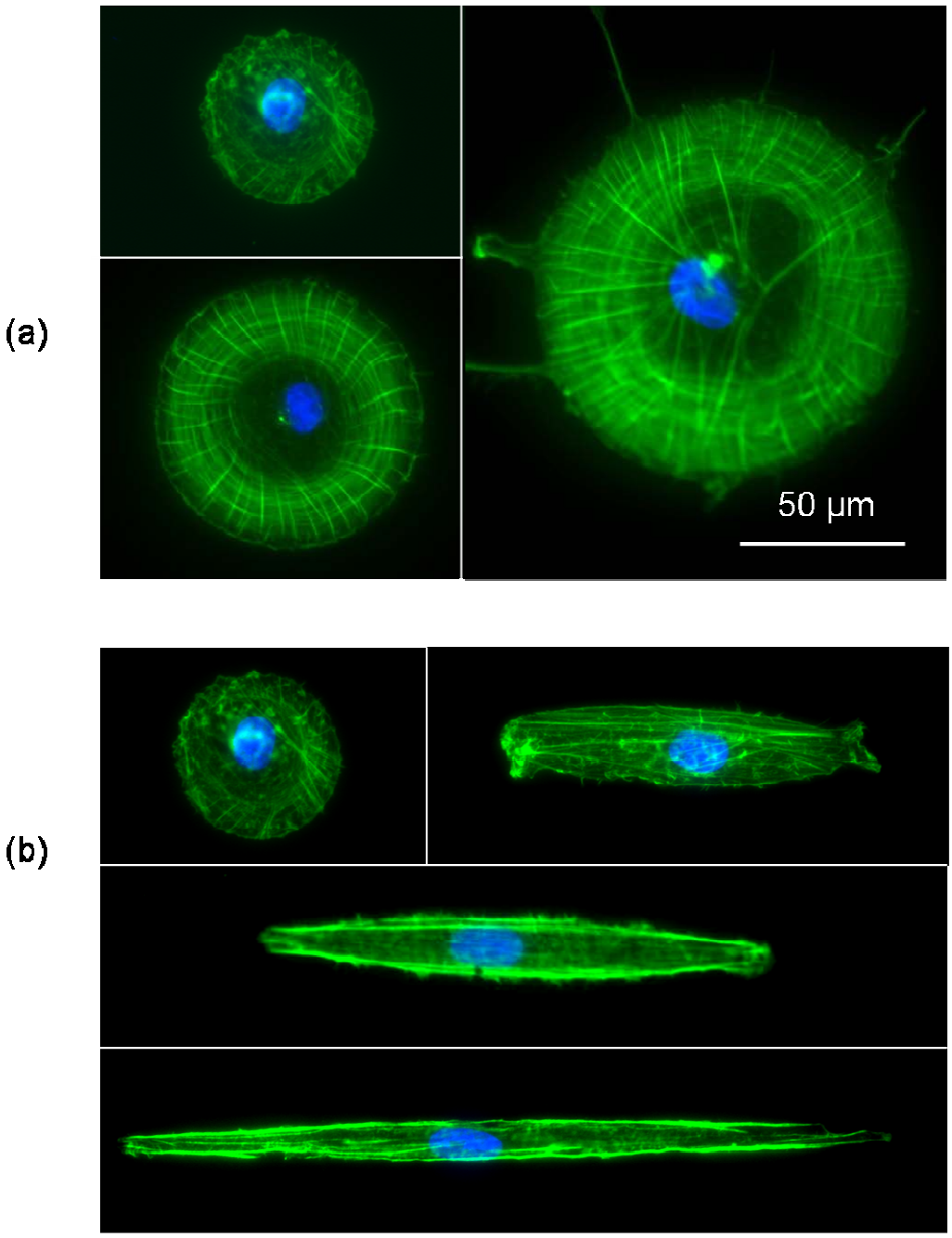

Figure 5.7. Fluorescence photographs of single hMSCs obtained after 24-h incubation in serum medium on dish surfaces patterned with a PDMS membrane mask followed by actin and nucleus staining: (a) cells of same shape and spreading area equal to 2000, 5000, and 10000 μm^2 and (b) cells of spreading area equal to 2000 μm^2 and different shapes of SI = 1.0, 0.5, 0.25, and 0.1.

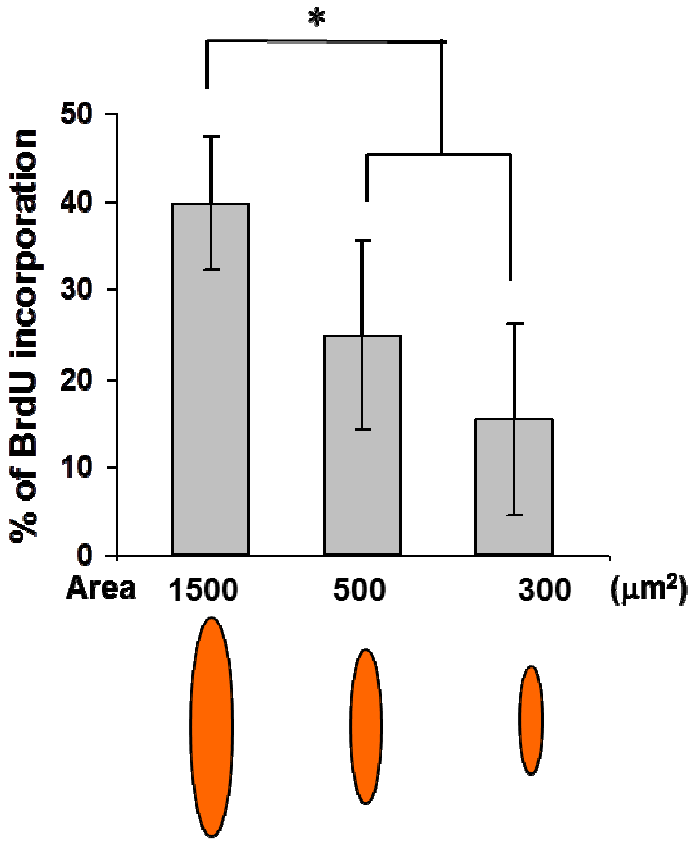

Figure 5.8. Cell spreading area effects on SMC proliferation (24 h-culture). SMCs were cultured on micropatterned matrix islands of the same shape (CSI ≈ 0.45) and different spreading area (i.e., 1500, 500, and 300 μm^2) and BrdU incorporation was analyzed subsequently (~50 cells per group; 3 independent experiments). The asterisk indicates the statistical significance ($P < 0.05$) between specified data.

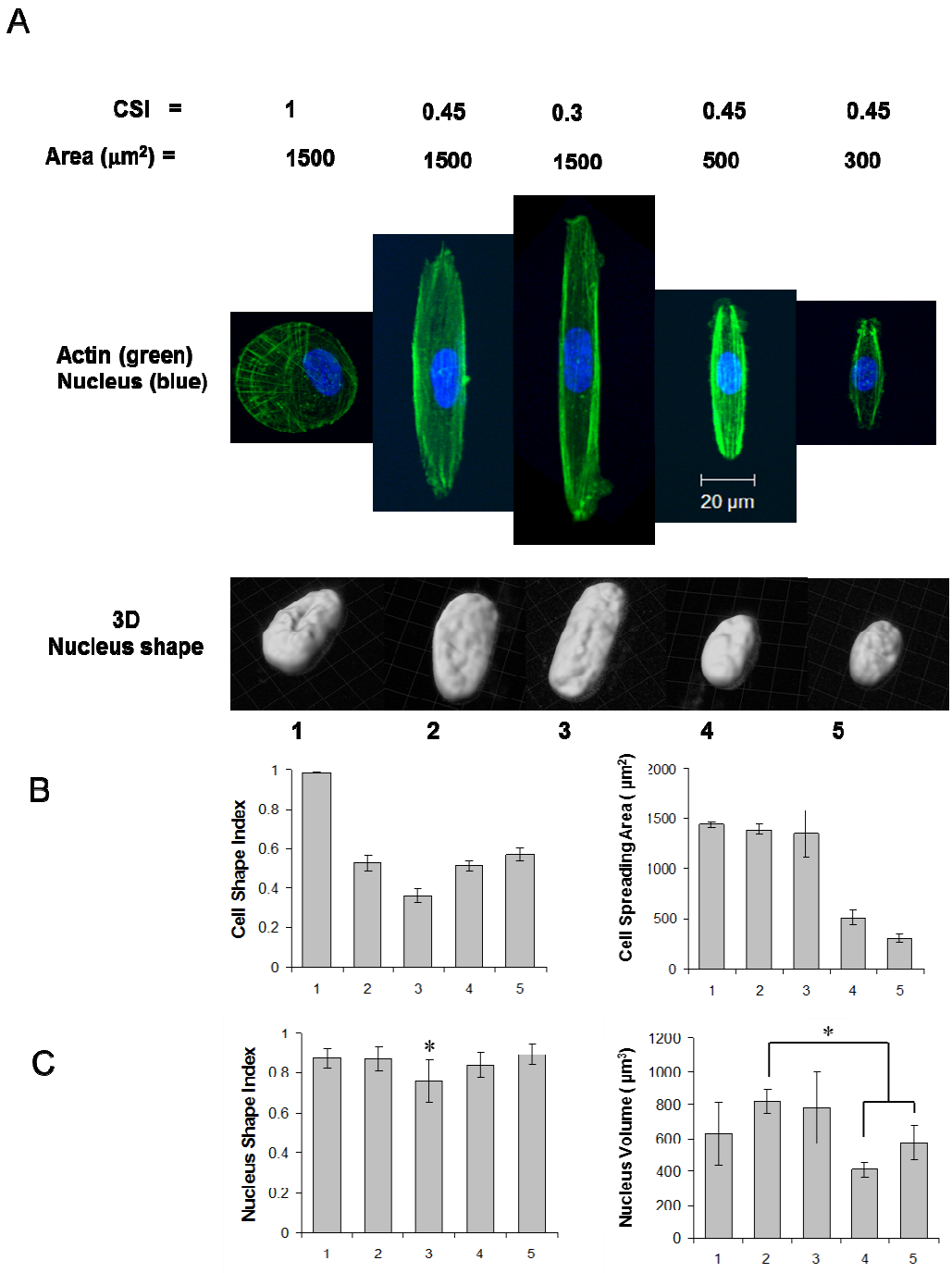

Figure 5.9. Cell shape and spreading area effects on nucleus morphology (24-h culture). SMCs of specific shape and spreading area were subjected to fluorescence staining for actin filaments (green) and nucleus (blue). **A.** Confocal microscopy images of actin filaments and 3D reconstruction of the nucleus shape. **B.** Calculated CSI and cell spreading area (3-10 cells per group). **C**. Calculated NSI and nucleus volume (3-10 cells per group). The asterisk indicates the statistical significance ($P < 0.05$) between all data or specified data.

Chapter 6

Surface Chemical Patterning of Polystyrene and Parylene C for Long-term Single-cell Culture

6.1 Introduction

Micropatterning for single-cell culture has received increased attention in recent years because it enables precise control of the cell shape and size, which is important in studying cell behavior (Chen et al. (1997), Thomas et al. (2002), Thakar et al. (2009)). Chemical patterning methods that produce surface patterns exhibiting prolonged stability are of particular importance to long-term cell culture, such as cell differentiation (McBeath et al. (2004)). Numerous surface patterning methods have been developed for cell culture (Falconneta et al. (2006)). Microcontact printing and membrane-based patterning have been widely used for single-cell culture by transferring a pattern of an external cell matrix protein (e.g., fibronectin) to a surface and then blocking the surrounding areas by nonfouling molecules (e.g., Pluronic) (Chen et al. (1997), Thakar et al. (2009), McBeath et al. (2004), Whitesides et al. (2001), Tan et al. (2004), Ostuni et al. (2000), Roca-Cusachs et al. (2008)). Selective molecular adsorption or coating deposition on substrates using traditional photolithography methods have been extensively explored for cell patterning, such as surface patterning of coatings using a photoresist as the lift-off mask (Falconnet et al. (2004), Thomas et al. (1999), Goessl et al. (2001), Brétagnol et al. (2007)) or creating surface patterns of different materials to induce selective molecular adsorption (Lussi et al. (2004), Detrait et al. (1998)). In other patterning methods, surface coatings were used first to provide a nonfouling property to the substrate, such as plasma polymerization of polyethylene glycol (PEG)-like thin films and poly-L-lysine (PLL)-g-PEG coatings, and then cell adhesive areas were produced by localized chemical modification of the film by plasma treatment through a membrane mask (Cheng et al. (2009)), or exposure to ultraviolet light through a chromium mask (Azioune et al. (2009)). Among these methods, surface blocking by Pluronic molecules is particularly effective in producing stable surface patterns. For example, surface patterns for culture of smooth muscle cells and endothelial cells blocked by Pluronic F127 molecules were found to be stable in serum medium for more than four weeks (Tan et al. (2004)).

Pluronic is a copolymer comprising polyethylene oxide (PEO) and polypropylene oxide (PPO) segments that can adsorb on some hydrophobic surfaces to prevent protein adsorption and cell attachment (Tan et al. (2004), Nejadnik et al. (2009)). The adsorption of Pluronic molecules involves the attachment of PPO segments to the hydrophobic surface, while the PEO segments extend outward from the surface, forming a brush-like nonfouling film. However, this configuration is not favored on highly hydrophilic surfaces, and the PEO segments lay flat on the surface (Nejadnik et al. (2009)). Therefore, the chemical behavior of Pluronic molecules adsorbed on hydrophobic and hydrophilic surfaces should differ significantly. For example, the competitive adsorption of Pluronic F68 and fibronectin molecules on the hydrophobic and

hydrophilic areas of plasma-modified polystyrene surfaces was used to achieve cell attachment only to the hydrophilic polystyrene areas (Detrait et al. (1998 and 1999)).

The traditional photolithography method used in previous studies to produce hydrophilic surface patterns on polystyrene cannot be directly applied on cell culture dishes because it requires a clean-room facility and, more importantly, uses chemicals that could be harmful to sensitive cells. To overcome this limitation, a dry lithography method that can be directly applied to polystyrene Petri dishes is introduced in this chapter. The main objectives of this investigation were to identify the plasma treatment conditions and incubation solution of a surface patterning method resulting in selective cell attachment, examine changes in surface chemistry caused by this method, and explore the implications of such patterning method in long-term cell culture. This method uses oxygen plasma treatment through the windows of a polydimethylsiloxane (PDMS) membrane mask to form hydrophilic patterns on regular culture dishes, and relies on surface hydrophilicity resulting in selective molecular (Pluronic, fibronectin, or serum proteins) adsorption to produce chemical patterns for single-cell culture. Patterned dishes were incubated either with Pluronic F108 solution or a mixture of Pluronic F108 solution and fibronectin. Cell culture experiments and X-ray photoelectron spectroscopy (XPS) measurements were performed to elucidate the underlying mechanisms of selective cell attachment. In addition, long-term cell culture experiments were carried out to study the effect of the surface patterning on the shape of cells and nuclei and demonstrate the stability of the produced patterns.

To further extend the application of this method on various substrates, surface patterning for single cell culture was also realized on Parylene C film surface in this chapter. Parylene C is widely used as a coating material in bioMEMS and implantable biomedical devices because of its excellent biocompatibility, chemical stability, and straightforward deposition on various substrates, including glass. By combining Parylene C film deposition, oxygen plasma treatment through the windows of PDMS shadow masks, incubation with a Pluronic F108 solution, and surface activation by incubation with serum medium, preferential attachment of single cells on the hydrophilic surface areas of chemically patterned Parylene C films was achieved and therefore the method can be applied on all substrates which can be coated with a layer of Parylene C film.

6.2 Experimental procedures

6.2.1 Fabrication of PDMS mask

Fabrication of the PDMS membrane mask was based on a method reported in a previous study (Jackman et al. (1999)). Briefly, micropost arrays of height equal to ~50 μm and lateral spacing of 200 μm were fabricated on a p-type Si(100) wafer using SU-8 2050 photoresist (MicroChem, Newton, MA) to obtain a master wafer. Before coating with PDMS, the master wafer was exposed to perfluoro-1,1,2,2-tetrahydrooctyltrichlorosilane (United Chemical Technology, Bristol, PA) vapor overnight in a desiccator to prevent strong adhesion of the PDMS to the master wafer. Then, the master wafer was spin coated with a mixture (10:1) of Sylgard 184 silicone elastomer kit (Dow Corning, Midland, MI) to obtain a ~30-μm-thick PDMS film and cured at 65^{o}C for 4 h. Finally, the PDMS membrane mask was cut into 1.7 × 1.7 cm^2 pieces, each having window arrays of specific shape and size, which were carefully peeled off

from the master wafer using a pair of tweezers and a piece of glass slide. PDMS masks with window areas of 2000 μm^2 and shape index (SI) equal to 1.0, 0.5, 0.25, and 0.1 ($SI = 4\pi A / P^2$, where A and P are the projected area and perimeter of a pattern area, respectively) were used in long-term cell culture experiments.

6.2.2 Surface chemical patterning of polystyrene and parylene C

Pluronic F108 (BASF, Mount Olive, NJ) powder was dissolved in phosphate buffer saline (PBS) to obtain a solution of 1% (wt/vol) Pluronic concentration. After overnight storage at 4°C, the solution was passed through a filter of average pore size equal to 0.2 μm to obtain a sterilized stock. Sterilized polystyrene (PS) Petri dishes (BD Falcon, Franklin Lakes, NJ) were used in their as-received condition. To produce hydrophilic surface patterns, the PDMS mask was conformably placed on the dishes, and the entire dish surfaces were exposed to oxygen plasma for 1 min in a small plasma-etch system (Plasma Prep II, SPI supplies/Structure Probe, West Chester, PA). Dish areas exposed to the plasma became hydrophilic (contact angle ≈ 0°), whereas areas covered by the PDMS mask maintained their hydrophobic character (contact angle ≈ 80°). After the PDMS mask was removed, the patterned dishes were first sterilized with ultraviolet light for at least 30 min and then incubated with either Pluronic F108 solution or Pluronic F108 solution mixed with fibronectin (Sigma-Aldrich, St. Louis, MO) for surface blocking. After overnight incubation at 4°C, the dishes were washed with PBS three times and seeded with cells.

For surface patterning of Parylene C, Parylene C films of ~0.5 μm in thickness were deposited on glass substrates using a commercial coating system (PDS 2010 LABCOTER 2, Indianapolis, IN). Hydrophilic surface patterns were created in the same way as PS described previously. Film areas exposed to the plasma became hydrophilic (contact angle ≈ 0°), while areas covered by the mask maintained their hydrophobic character (contact angle ≈ 90°). Similarly, the Parylene C surface was incubated either with a solution of Pluronic F108 copolymer in PBS or a mixture of Pluronic F108 solution and fibronectin in PBS overnight at 4°C, washed with PBS three times and seeded with cells.

6.2.3 Surface chemistry analysis

Adsorption of Pluronic and fibronectin molecules on hydrophilic and hydrophobic pattern areas of PS dishes was investigated by X-ray photoelectron spectroscopy (XPS). PS samples cut from the bottom of cell culture dishes were partially covered with a PDMS membrane mask and treated with oxygen plasma. Then, the partially treated PS samples were incubated with PBS, Pluronic F108 solution, or Pluronic F108 mixed with fibronectin overnight, washed with PBS three times, and dried in air before the XPS analysis. A spectrometer without charge neutralization or monochromator (Perkin-Elmer PHI 5400 ESCA) equipped with an Al-Kα X-ray source of photon energy equal to 1486.6 eV was used to perform the XPS experiments. A take-off angle of 54.7º relative to the analyzer axis was used in all XPS experiments. During spectral acquisition, the pressure in the main chamber was maintained at ~10^{-7} Torr. Survey spectra were acquired in the binding energy range of 0–1100 eV with pass energy of 178.95 eV. High-resolution XPS spectra of the C1s, N1s, and O1s core level peaks were collected with pass energy of 35.75 eV. To compensate for surface charging effects, the C–H peak at 285.0 eV was

used as a reference. The atomic concentration of nitrogen (determined from the N1s core level peak after Shirley background subtraction) was used to analyze the adsorption of fibronectin on different sample surfaces. For statistical analysis, XPS results were obtained as averages of four measurements acquired from two different surface regions of two identical samples.

6.2.4 Protein adsorption and cell culture on patterned surface

Bone marrow mesenchymal stem cells (MSCs) were used to perform cell culture experiments. Cells were seeded with either serum-free medium or serum-containing medium consisting of Dulbecco's Modified Eagle's Medium (DMEM), 10% fetal bovine serum (FBS), and 1% penicillin streptomycin. Subsequent to incubation with 5% CO_2 at 37°C for 1 h, floating cells were washed away and fresh serum medium was added. After 2-week incubation, the cells were fixed with 4% paraformaldehyde (PFA), permeabilized with 0.5% Triton X-100, and the cell actin and nucleus were stained with Alexa-Phalloidin 488 and 4',6-diamidino-2-phenylindole (DAPI), respectively. Phase contrast pictures of fixed MSCs were obtained with an inverted microscope (TE 300, Nikon, Melville, NY), and fluorescence photographs of stained MSCs were obtained with an upright microscope (Zeiss HAL 100, Carl Zeiss MicroImaging, Thornwood, NY). The area and shape index of cells and nuclei were calculated from fluorescence images of cell actin and nucleus. Cell and nucleus boundaries were outlined with software (Scion IMAGE, Fredrick, MD). The measured cell spreading area and perimeter and the nucleus projection area and perimeter were used to calculate the cell shape index (CSI) and nucleus shape index (NSI). A shape index of 1 and 0 corresponds to circular and linear shapes, respectively.

To check protein adsorption on patterned Parylene C surface, Fluorescein isothiocyanate (FITC)-collagen type I (Sigma-Aldrich, St. Louis, MO) was used to examine protein adsorption on the chemically patterned Parylene C film surfaces. After incubation with 0.01% Pluronic solution for 1 h, the patterned Parylene C surface was first washed with PBS three times and then incubated with FITC-collagen solution (200 µg/mL) overnight at room temperature. Fluorescence pictures were obtained after washing the incubated surface with PBS three times to check the amount of absorbed collagen.

6.3 Results and discussions

6.3.1 Surface patterning of polystyrene for single cell culture

The dependence of cell attachment on the adsorption configuration of Pluronic molecules at hydrophobic and hydrophilic PS surfaces was studied by seeding MSCs in serum medium on three different dishes: (a) untreated (control), (b) incubated with 1% Pluronic solution for 1 h, and (c) oxygen plasma-modified and then incubated with 1% Pluronic solution for 1 h (washed three times with PBS before cell seeding). While MSCs attached on the untreated dish and to a less extent on the oxygen plasma-treated dish incubated with 1% Pluronic solution, they did not attach on the untreated dish incubated with 1% Pluronic solution. After overnight incubation, floating MSCs were collected and reseeded on an untreated tissue culture dish. It was observed that these cells attached and spread well on the untreated dish surface, indicating that the previous differences in cell attachment were not due to the cytotoxicity of Pluronic molecules.

Instead, this difference in MSC attachment is attributed to the adsorption of Pluronic molecules on the untreated PS surface in a brush-like nonfouling configuration, as opposed to the plasma-treated dish on which the Pluronic molecules laid flat on the surface (Nejadnik et al. (2009)). This finding also suggests that, in the presence of serum, MSCs attached to the hydrophilic PS surface covered by Pluronic molecules.

To examine how the adsorption of Pluronic molecules on the hydrophilic PS surfaces affected cell attachment, oxygen plasma-modified dishes were incubated with six different solutions overnight, namely PBS, 0.01% Pluronic F108 solution, 1% Pluronic F108 solution, and each of the former solutions mixed with 25 μg/mL fibronectin. After washing the PS surfaces with PBS three times, MSCs were seeded and incubated with either plain DMEM or serum medium for 4 h before they were examined under a microscope. Figure 6.1 shows representative images from these experiments. MSC incubation with plain DMEM did not result in cell attachment on the surfaces incubated with only Pluronic solution even after 4 h. However, MSCs attached and spread on all other surfaces, including the surface incubated with only PBS. Although adsorption of Pluronic on a hydrophilic PS surface does not result in a nonfouling conformation (Nejadnik et al. (2009)), Figure 6.1 shows that, in the absence of serum, adsorbed Pluronic molecules can still block cell attachment. However, the adsorption of Pluronic on the hydrophilic PS surface did not prevent the adsorption of fibronectin. Thus, the addition of fibronectin in the Pluronic solution was conducive to cell attachment, depending on the Pluronic concentration. Indeed, for 25 μg/mL fibronectin, increasing the Pluronic concentration from 0.01% to 1% increased the number of floating cells, indicating less fibronectin adsorption for hydrophilic PS covered with more Pluronic molecules.

In the case of MSCs incubated with serum medium, differences in cell attachment were only observed in the early stage of incubation. MSCs attached rapidly on all surfaces in less than 1 h except for the surfaces incubated with only Pluronic solution. However, no difference in cell attachment could be discerned following incubation in serum medium for 4 h. This finding suggests that serum proteins from the medium modified or activated the hydrophilic PS surfaces covered by Pluronic molecules, and this activation process was beneficial to cell attachment (Castner et al. (2002)). Because this modification/activation process is relatively slow, MSC attachment on the dish surfaces treated with only Pluronic did not occur during the initial stage of incubation. This is also supported by the fact that the increase in Pluronic concentration increased the time for cell attachment since the activation process was prolonged when the hydrophilic PS was covered with more Pluronic molecules.

For single-cell patterning, PS dishes with hydrophilic patterns produced by plasma treatment through the windows of PDMS masks were incubated with different solutions before seeding with MSCs in serum medium. An untreated dish was used as control [Figure 6.2(a)]. The fact that MSCs attached everywhere on the patterned dish incubated with PBS [Figure 6.2(b)] compared to the control dish suggests that selectivity in cell attachment cannot be solely accomplished by modifying the surface hydrophilicity. Dishes treated with Pluronic solutions of concentration in the range of 0.001%–1% (with or without the addition of 25 μg/mL fibronectin) were seeded with MSCs in serum medium. Incubation with low concentration (≤0.01%) Pluronic alone resulted in fast single-cell patterning [Figure 6.2(c)]. Increasing the Pluronic concentration to 1% increased the time for cell attachment and decreased the number of attached cells

significantly [Figure 6.2(d)]. The addition of 25 μg/mL of fibronectin in Pluronic solutions of concentration ≤0.01% resulted in random cell attachment [Figure 6.2(e)], indicating that fibronectin adsorbed on both hydrophilic and hydrophobic pattern areas. Increasing the Pluronic concentration above 0.1% restored single-cell patterning [Figure 6.2(f)]. Thus, for a given concentration of fibronectin, the Pluronic concentration must be above a threshold to prevent fibronectin adsorption on untreated PS, which is necessary for single-cell patterning. Therefore, while fibronectin enhanced the attachment of MSCs on the hydrophilic pattern areas, it was necessary to increase the Pluronic concentration to achieve single-cell patterning. For cell seeding in serum medium, the time for cell attachment on the hydrophilic areas of the patterned dish incubated with 0.01% Pluronic solution was comparable to that of the patterned dish incubated with 0.1% Pluronic solution and 25 μg/mL fibronectin.

Adsorption of Pluronic and fibronectin on untreated and oxygen plasma-treated dishes was further examined in light of the XPS measurements. Representative C1s spectra of PS surfaces with different treatments are shown in Figure 6.3. The C1s peak of oxygen plasma-treated PS [Figure 6.3(b)] differs slightly from that of the untreated surface [Figure 6.3(a)]. This small change in the C1s peak is attributed to incorporation of oxygen functionalities on the surface of plasma-treated PS. Incubation with 1% Pluronic solution did not yield a discernible effect on the C1s peak of untreated PS [Figure 6.3(c)], evidently due to desorption of the Pluronic molecules during drying. However, incubation with Pluronic significantly changed the C1s peak of oxygen plasma-treated PS [Figure 6.3(d)], implying relatively stable adsorption of the Pluronic molecules. The previous observations are supported by XPS results of the O/C ratio. For the PS surfaces with C1s spectra shown in Figures 6.3(a)–6.3(d), the corresponding O/C ratio was found equal to 0.26, 0.33, 0.35, and 0.50. Therefore, it is confirmed that Pluronic molecules adsorbed on the hydrophilic PS areas and, hence, affected cell attachment, despite the fact that molecular assembly did not result in a nonfouling configuration. The nitrogen concentration of hydrophobic and hydrophilic PS surfaces incubated first with 0.01% Pluronic overnight and then with 10% FBS medium for 1 h was also measured with the XPS after washing the samples with PBS. The nitrogen concentration on the hydrophobic and hydrophilic PS surfaces was found equal to 6.05 at% and 8.85 at%, respectively, implying that hydrophilic PS surfaces exhibited higher protein concentrations than hydrophobic PS surfaces. This explains cell attachment on the hydrophilic PS surface activated with serum medium.

Figure 6.4 shows the nitrogen content of hydrophobic and hydrophilic PS surfaces incubated with Pluronic solution mixed with fibronectin for Pluronic concentration in the range of 0–1%. The significant decrease in the nitrogen concentration of the PS surfaces incubated with high-concentration Pluronic solutions, especially unmodified PS, indicates that the adsorption of Pluronic molecules prevented fibronectin adsorption, in agreement with the results of a previous study (Dewez et al. (1997)). Although fibronectin adsorption on the hydrophilic PS surfaces also decreased in the presence of Pluronic, the significantly higher nitrogen concentration of the hydrophilic PS surfaces explains the selective attachment of cells on the hydrophilic areas. The decrease in Pluronic concentration led to increased fibronectin adsorption on both hydrophilic and hydrophobic PS surfaces. This trend provides insight into the experiments with MSCs incubated with different Pluronic solutions containing fibronectin. Although Pluronic suppressed fibronectin adsorption on the untreated PS surfaces significantly, fibronectin also adsorbed on the hydrophobic areas of the patterned dish surface. Therefore, to

enable single-cell patterning, the Pluronic concentration must be above a threshold so that to prevent excessive fibronectin adsorption on the hydrophobic areas.

An interesting phenomenon was observed with MSCs seeded on patterned dishes after incubation with a mixture of 0.01% Pluronic solution and 25 μg/mL fibronectin for more than two days. While initially MSCs spread outside the pattern areas, at a later time they retracted within the pattern areas. This finding suggests that prolonged incubation was conducive to the cell sensing the chemical differences between hydrophilic and hydrophobic pattern areas, resulting in cell migration back to the hydrophilic areas of higher fibronectin concentration.

To examine the long-term stability of the patterned surfaces, MSCs were seeded on patterned dishes incubated with either relatively low-concentration Pluronic solution or high-concentration Pluronic solution containing fibronectin. All of the produced patterns remained stable even after incubation in serum medium for more than 2 weeks. Figure 6.5 shows MSCs seeded on patterned PS surfaces treated with 1% Pluronic solution that contained 25 μg/mL fibronectin after incubation with serum medium for 2 weeks. These MSCs were confirmed to be alive by cell live/dead assay results (not shown here). The circular [Figure 6.4(a)] and elliptical [Figures 6.4(b)–6.4(d)] patterns on the dish surfaces are occupied by single MSCs that have spread out to fully cover only these hydrophilic areas of higher fibronectin concentration. The long-term stability of the patterned single cells on the PS dish surfaces produced by the present method was also observed in cell culture experiments with neuron stem cells and bovine aorta endothelial cells. Because of the similarity of these results with those for MSCs, results from these experiments are not shown here for brevity.

Figure 6.6 shows representative fluorescence pictures of MSCs obtained after 2 weeks of incubation in serum medium revealing the cell nuclei and actin structure. Circular MSCs show fairly round nuclei and actin alignment along the radial direction and around the fairly round nucleus [Figure 6.6(a)], whereas elongated MSCs show nucleus elongation and actin alignment along the major axis of their elliptical shapes [Figures 6.6(b)-6.6(d)]. In general, actin remodeling occurs within one day and then stabilizes. Indeed similar actin remodeling has been observed in single MSCs of circular and elongated shapes after 1 day of incubation [16]. According to a previous study Pluronic was as a non-adhesive coating [7], the patterned surface is expected to be stable for more than 4 weeks. Because actin remodeling stabilized within 24 h of incubation and the normal time period of differentiation studies is ~2 weeks, in particular for this cell type, a 2 week incubation of MSCs may be referred to as long-term culture. Cell and nucleus geometry measurements obtained from such fluorescence pictures are shown in Figure 6.7. The spreading area [Figure 6.7(a)] and shape index [Figure 6.7(b)] of the cells followed the design parameters, although the spreading area exhibited ~10%–15% variation. For similar cell spreading area, the nucleus projection area did not change with the cell shape [Figure 6.7(c)]. However, the nucleus shape changed with the cell shape [Figure 6.7(d)], though the change in nucleus shape index was relatively less pronounced compared to the cell shape index.

Because the present patterning method is based on dry lithography and hydrophilicity-dependent surface patterning, it can be easily used to synthesize different patterns on the same dish surface. After creating a specific hydrophilic pattern on a PS dish, the PDMS mask can be lifted and another mask with windows of different sizes and shapes can be placed conformably

on the same dish surface to produce different hydrophilic patterns. Thus combinations of different single-cell patterns can be easily obtained on the same dish surface without the need to design a new chromium mask.

6.3.2 Surface patterning of parylene C for single cell culture

Besides PS substrate, the discussed method was also applied onto Parylene C film surface with proper modifications. To examine if the adsorption of Pluronic molecules on the hydrophobic and hydrophilic Parylene C surfaces affected MSC attachment, untreated and oxygen plasma-treated (1 min) glass coverslips coated with Parylene C films were incubated with 0.1% Pluronic F108 in PBS for 1 h. After washing three times with PBS, the surfaces were seeded with MSCs in serum medium. Overnight incubation resulted in MSC attachment and spreading on the plasma-treated (hydrophilic) surface [Figure 6.8(d)] but not the untreated (hydrophobic) surface where the cells were still floating [Figure 6.8(c)]. However, MSCs attached on both control samples, i.e., untreated [Figure 6.8(a)] and plasma-treated [Figure 6.8(b)] Parylene C surfaces that had not been incubated with Pluronic solution. This profound difference in MSC attachment indicates that the oxygen plasma changed the surface chemical behavior of Parylene C from hydrophobic to hydrophilic, affecting significantly the adsorption of Pluronic molecules. MSCs did not attach on the hydrophobic areas because the brush-like configuration of the adsorbed Pluronic molecules repelled protein adsorption and cell attachment. However, because this brush-like molecular arrangement was not thermodynamically favored on the hydrophilic areas, protein adsorption and, in turn, MSC attachment on these areas was not prevented. This observation is consistent with previous results showing that the adsorption configuration of Pluronic molecules on a Parylene C surface of increased hydrophilicity (induced by the electrowetting-on-dielectric local effect) allowed protein adsorption and cell attachment (Fan et al. (2008)).

These marked differences in cell attachment between hydrophilic and hydrophobic Parylene C surfaces covered with Pluronic molecules provide an effective means of surface patterning for single-cell culture. MSC attachment to the hydrophilic areas of a patterned Parylene C surface incubated with 0.1% Pluronic solution overnight was found to be limited [Figure 6.9(b)], presumably because of the large distance between cells that had a negative effect on cell signaling. Although decreasing the Pluronic concentration to 0.01% was conducive to single cell attachment on the hydrophilic areas, the improvement was marginal [Figure 6.9(a)]. Thus to enhance cell attachment on the hydrophilic areas, the Pluronic solution was enriched with fibronectin. This necessitated an increase in Pluronic concentration to at least 0.1% (for the concentration range of this study) to prevent fibronectin adsorption and cell attachment on the hydrophobic areas. For a low Pluronic concentration (0.01%), single-cell patterning was not accomplished because MSCs attached on both hydrophilic and hydrophobic areas [Figure 6.9(c)]. Increasing the Pluronic concentration to 0.1% restored single-cell patterning [Figure 6.9(d)]; however, a high Pluronic concentration may not be beneficial to the long-term cell viability.

To further enhance cell attachment, a surface activation step with serum medium was added before cell seeding. Briefly, after incubating a chemically patterned Parylene C surface with 0.01% Pluronic solution for 1 h and washing three times with PBS, the whole surface was incubated with serum medium overnight at 37°C to activate the hydrophilic areas before cell

seeding. MSCs attached and spread on the serum-activated areas after incubation for 1 h [Figure 6.9(e)], producing a much higher yield of single-cell patterning than patterned Parylene C surfaces that had not been previously activated with serum, as shown by the cell patterning yield data of Figure 6.9(f). The data represent the percentages of single-cell pattern areas after washing away all floating cells. A 100% yield was not obtained because of the low cell density used to promote the attachment of a single cell on each pattern area.

Adsorption of the amphiphilic Pluronic molecules on the patterned Parylene C surfaces occurred by the preferential attachment of the hydrophobic poly-propylene oxide (PPO) and hydrophilic poly-ethylene oxide (PEO) segments to the hydrophobic and hydrophilic Parylene C areas, respectively [Figure 6.10(d)]. Significant differences in MSC attachment are attributed to protein adsorption on the hydrophilic areas covered with Pluronic molecules laying flat on the surface [Figure 6.10(e)] but not on the hydrophobic areas because of steric repulsion of the freely sawing PEO segments. It is believed that gradual modification of the hydrophilic areas by serum proteins played a key role in the preferential attachment of MSCs on the hydrophilic areas of the activated Parylene C surface [Figure 6.10(f)], resulting in a high yield of single-cell patterning [Figure 6.9(e)]. Preferential protein adsorption on the hydrophilic areas covered with Pluronic molecules was confirmed by FITC-collagen adsorption tests, and fluorescence photographs revealed significantly more FITC-collagen adsorption on the pattern areas [Figure 6.10(g)], confirming that incubation with serum medium resulted in the activation of the hydrophilic pattern areas. Cultures in serum medium showed that the surface patterns were stable for more than two weeks.

6.4 Conclusions

In this chapter, a simple method of surface patterning PS dishes for single-cell culture was developed by combining plasma-assisted surface modification through the windows of PDMS masks to produce hydrophilic and hydrophobic surface areas and overnight incubation with Pluronic solutions, with and without the addition of fibronectin. Compared to other methods, the present method does not require precise control of the patterning process and is effective in producing a wide range of pattern shapes and sizes for single-cell culture. In addition, long-term (two weeks) cell culture experiments revealed the effect of surface patterning on the shape of the cells and nuclei and demonstrated the stability of the produced single-cell patterns in serum medium.

Besides, the discussed surface patterning method for single-cell culture was extended using Parylene C film deposition and surface chemical modification by oxygen plasma treatment through the windows of a PDMS shadow mask, and relies on the effect of surface hydrophilicity on the adsorption configuration of Pluronic molecules and surface activation by serum proteins. Since Parylene C is a widely used coating material, the present method can be applied to other substrate materials that cannot be easily patterned with traditional microcontact printing methods.

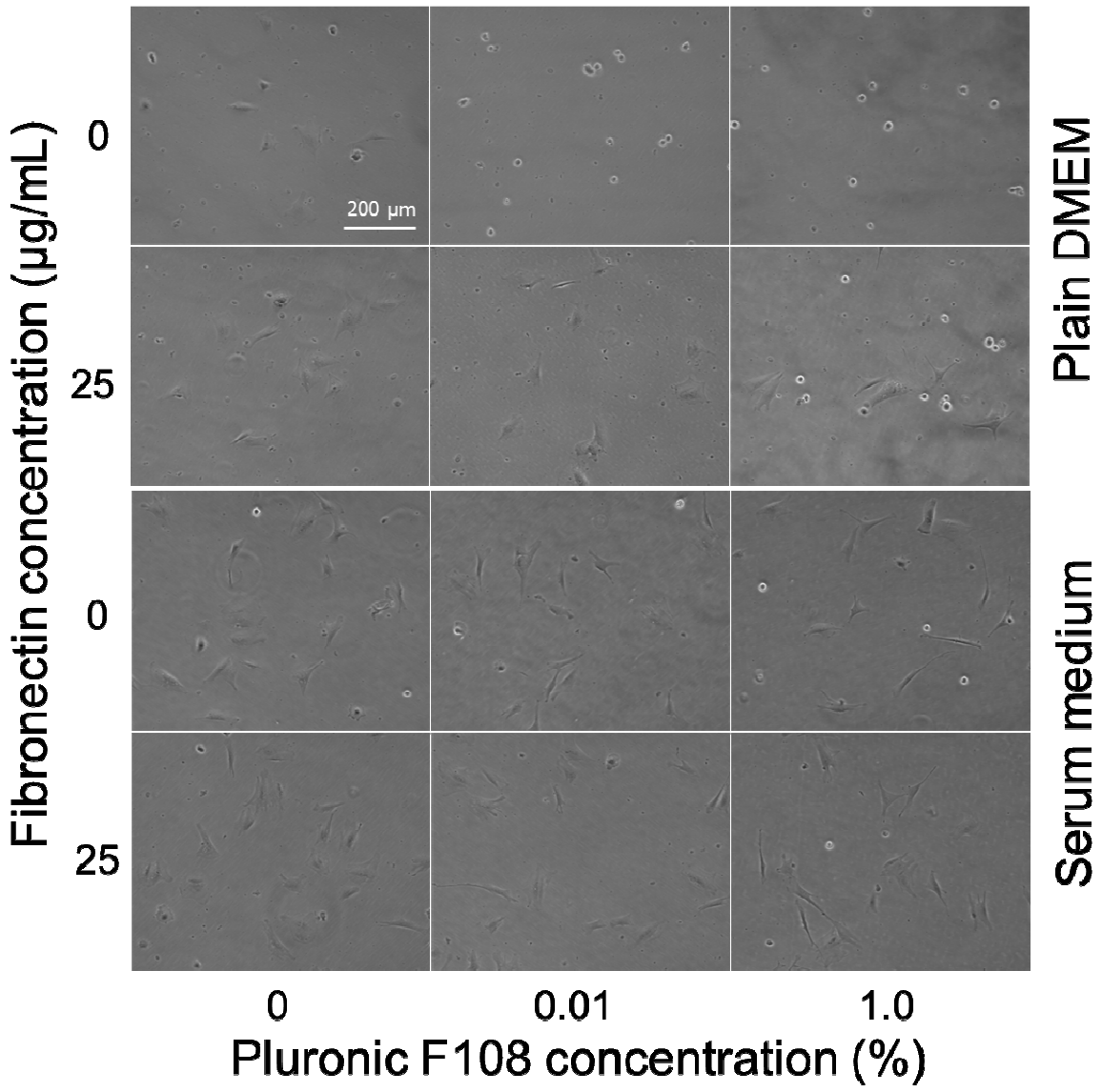

Figure 6.1. MSCs seeded on plasma-treated PS surfaces treated with different solutions after incubation with either plain DMEM or serum medium for 4 h.

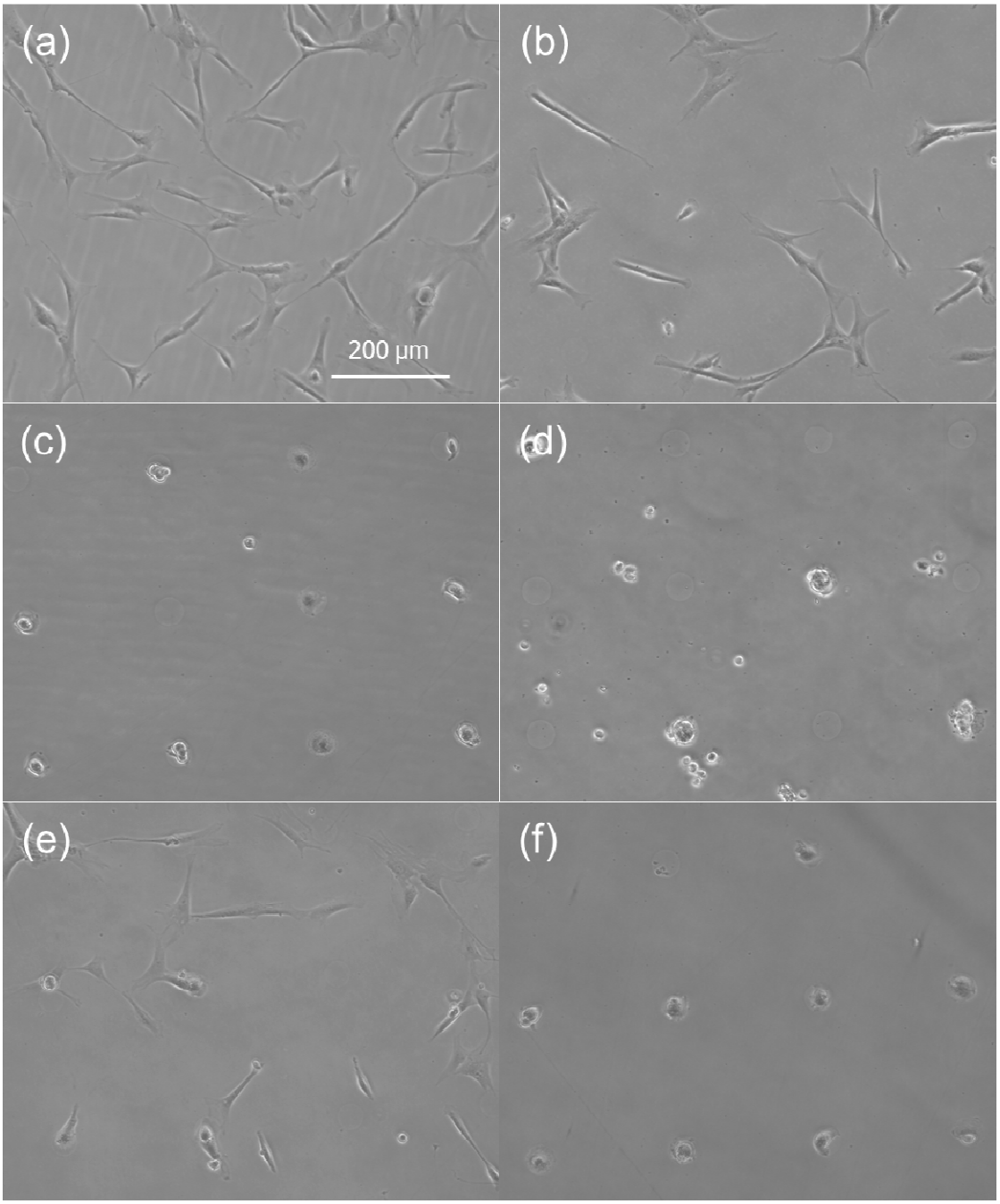

Figure 6.2. MSCs seeded on patterned PS surfaces treated with different solutions after incubation with serum medium overnight: (a) untreated (control), (b) PBS, (c) 0.01% Pluronic F108, (d) 1% Pluronic F108, (e) 0.01% Pluronic F108 and 25 µg/mL fibronectin, and (f) 1% Pluronic F108 and 25 µg/mL fibronectin.

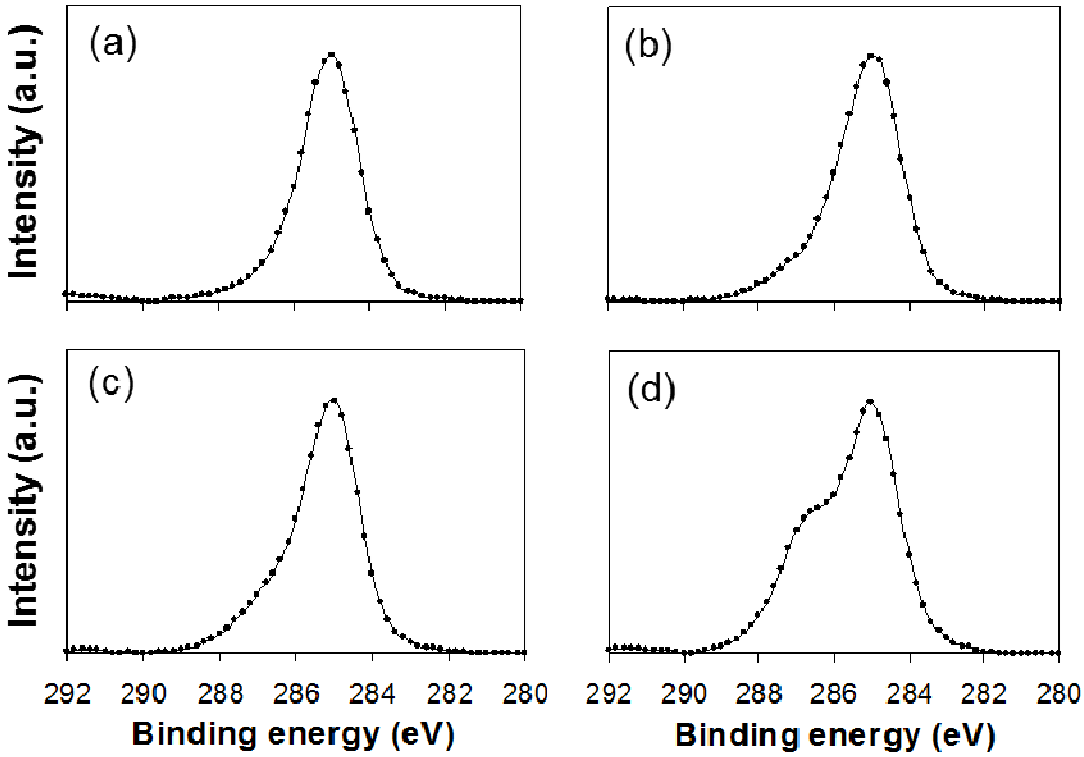

Figure 6.3. C1s peak of different PS surfaces: (a) untreated (control), incubated with PBS, (b) oxygen plasma treated, incubated with PBS, (c) untreated, incubated with 1% Pluronic F108 solution, and (d) oxygen plasma treated, incubated with 1% Pluronic F108 solution.

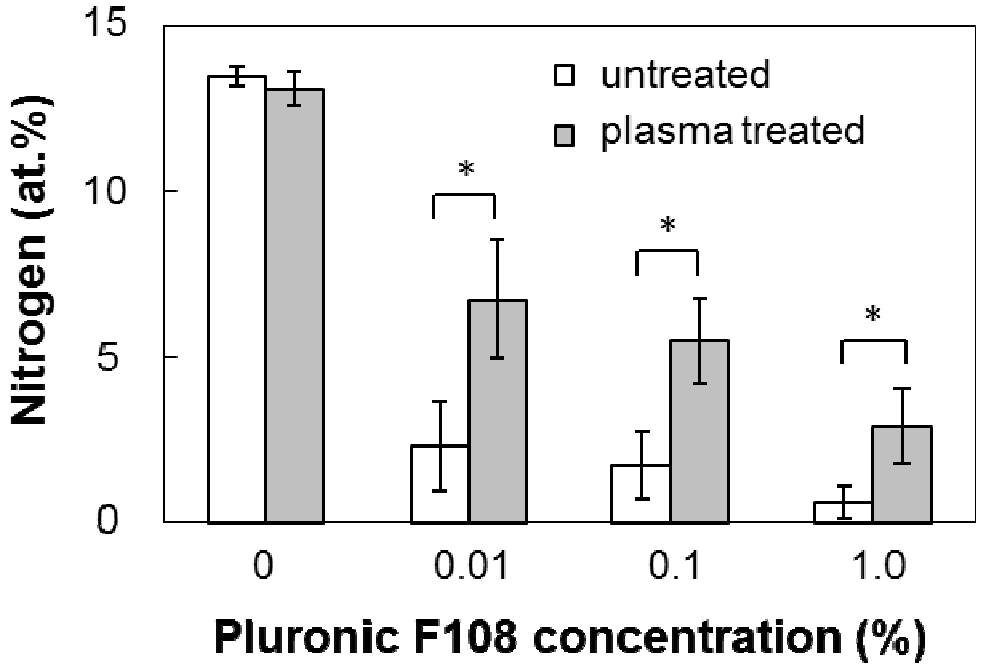

Figure 6.4. Nitrogen concentration of untreated and oxygen plasma-treated PS surfaces incubated with Pluronic F108 solutions of different concentrations that contained 25 μg/mL fibronectin. A statistically significant difference ($P<0.05$) between specified groups is indicated by an asterisk.

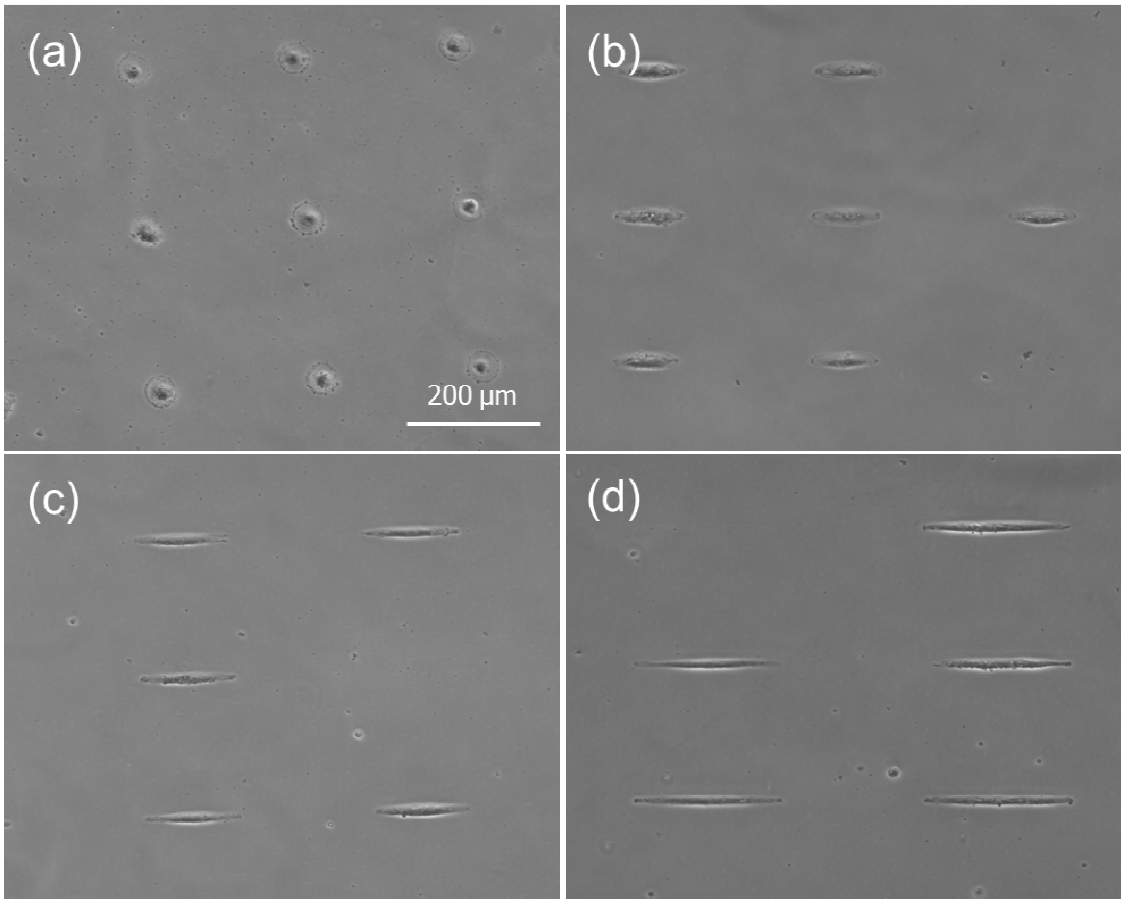

Figure 6.5. Single MSCs cultured on patterned PS surfaces treated with 1% Pluronic F108 solution containing 25 μg/mL fibronectin after incubation with serum medium for 2 weeks. The designed pattern area is 2000 μm^2, whereas the pattern shape index is equal to (a) 1.0, (b) 0.5, (c) 0.25 and (d) 0.1.

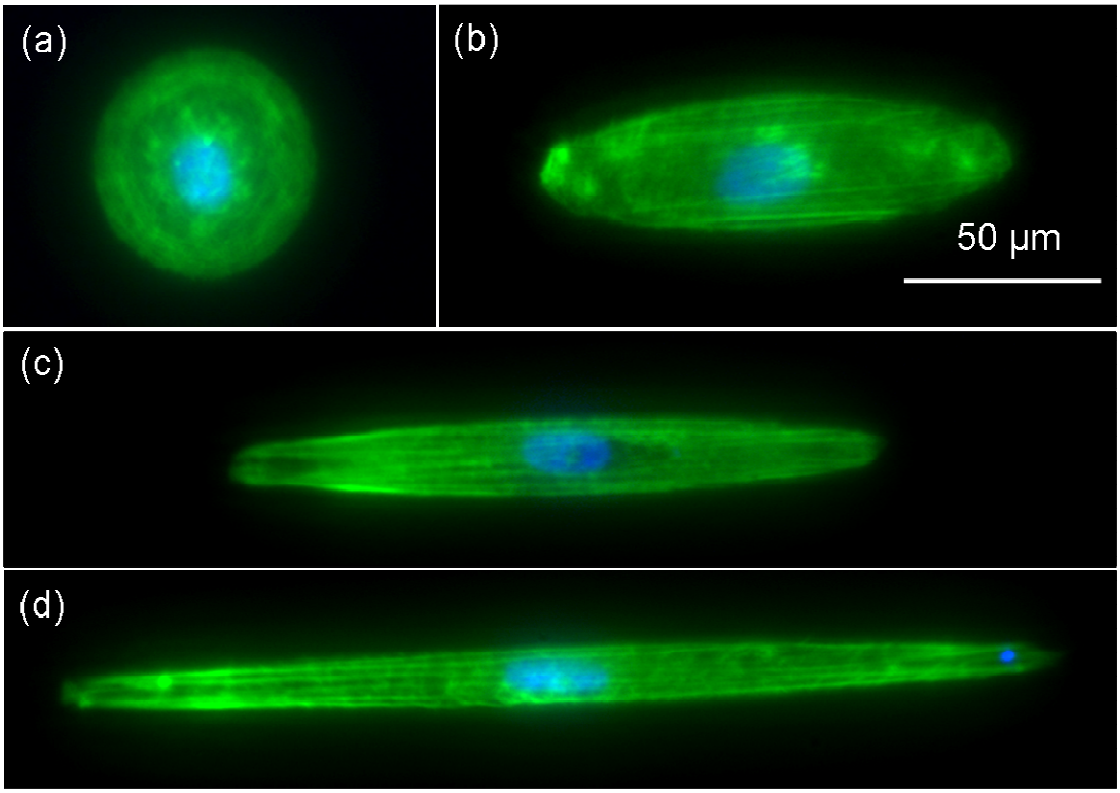

Figure 6.6. Nuclei and actin staining of MSCs cultured on patterned PS surfaces for 2 weeks in serum medium. The designed pattern area is 2000 μm^2, whereas the pattern shape index is equal to (a) 1.0, (b) 0.5, (c) 0.25, and (d) 0.1.

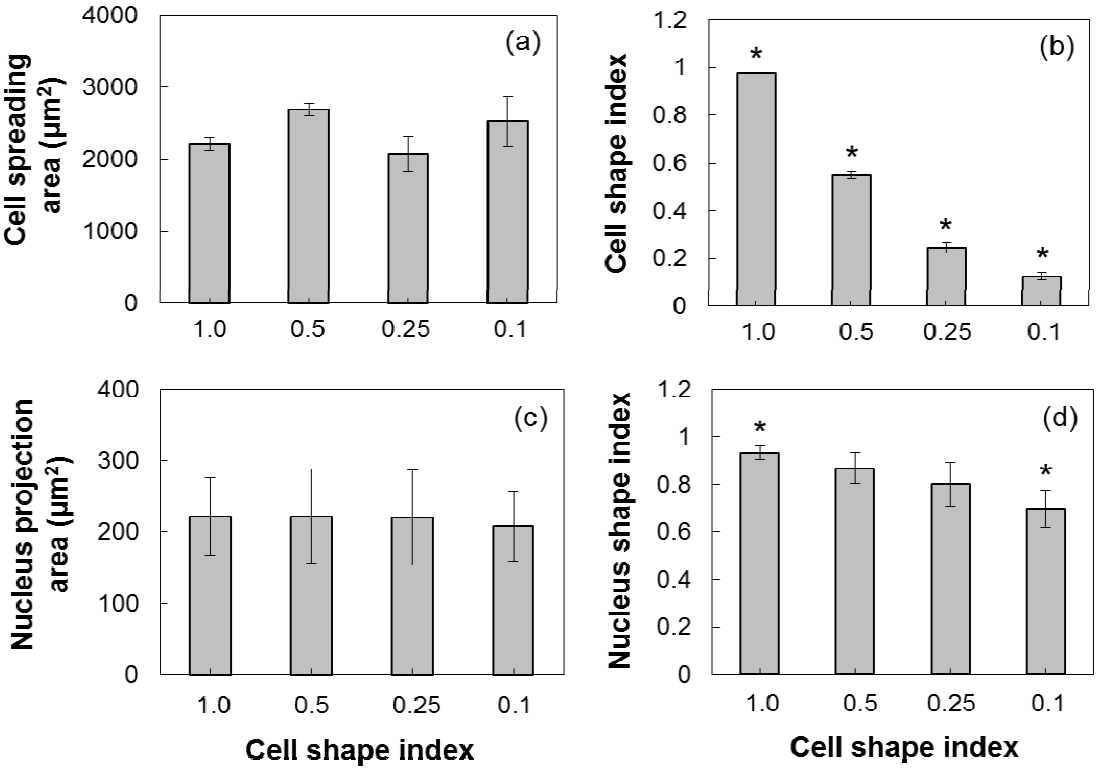

Figure 6.7. Cell spreading area and shape effects on nucleus morphology. MSCs cultured on patterned PS surfaces for 2 weeks in serum medium were subjected to fluorescence staining for actin filaments and nucleus, and the cell spreading area (a), CSI (b), nucleus projection area (c), and NSI (d) were measured from two-dimensional images. Statistically significant differences ($P<0.05$) compared to all other groups (10–20 cells per group) are indicated by an asterisk.

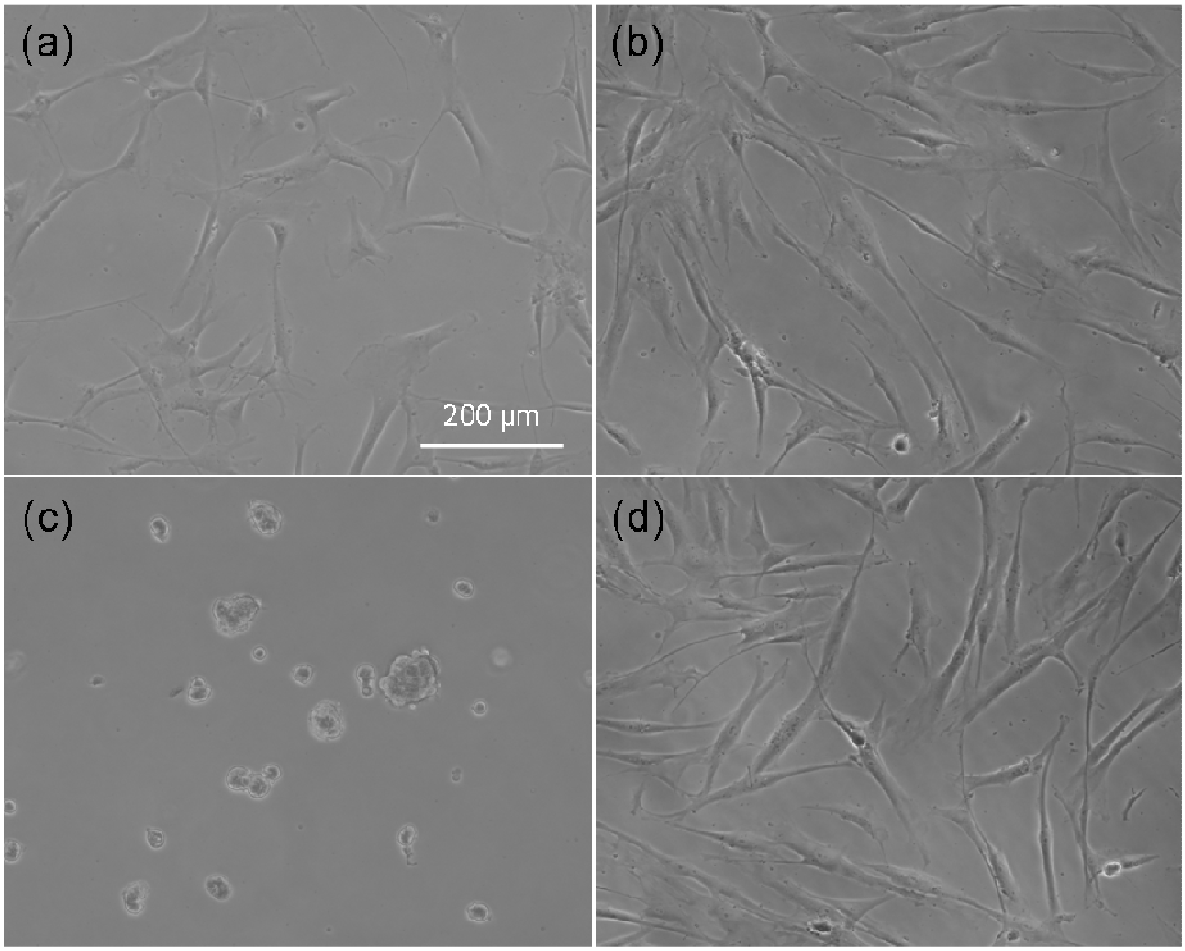

Figure 6.8. MSCs seeded on chemically different Parylene C surfaces: (a) untreated (hydrophobic), (b) oxygen plasma-treated (hydrophilic), (c) untreated and incubated with 0.1% Pluronic F108 solution, and (d) oxygen plasma-treated and incubated with 0.1% Pluronic F108 solution.

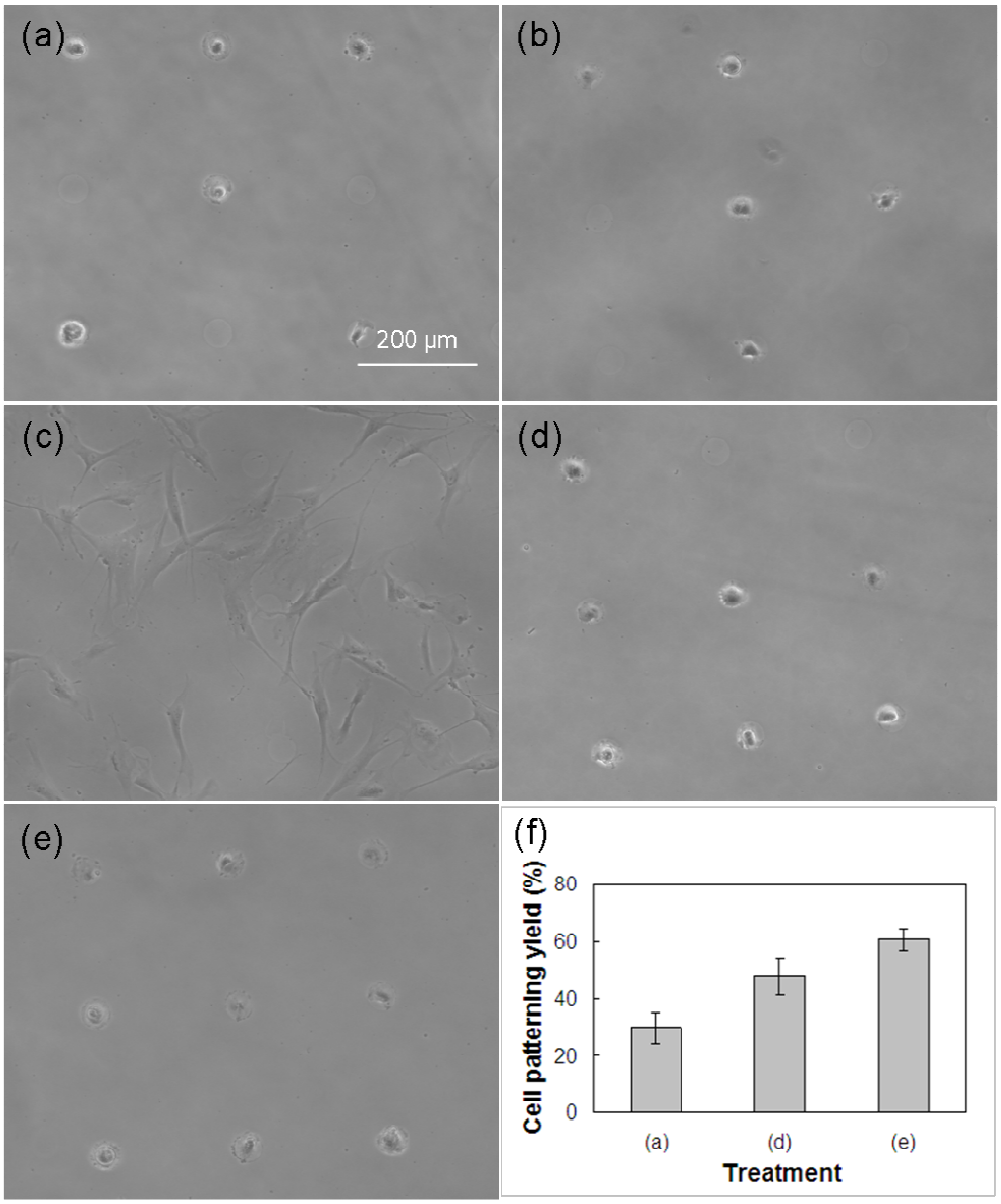

Figure 6.9. MSCs on chemically patterned Parylene C surfaces incubated with different solutions: (a) 0.01% Pluronic F108, (b) 0.1% Pluronic F108, (c) 0.01% Pluronic F108 mixed with 25 µg/mL fibronectin, (d) 0.1% Pluronic F108 mixed with 25 µg/mL fibronectin, and (e) 0.01% Pluronic F108 followed by incubation with 10% serum medium. Statistical results of cell patterning yield corresponding to incubation with solutions (a), (d), and (e) are compared in (f).

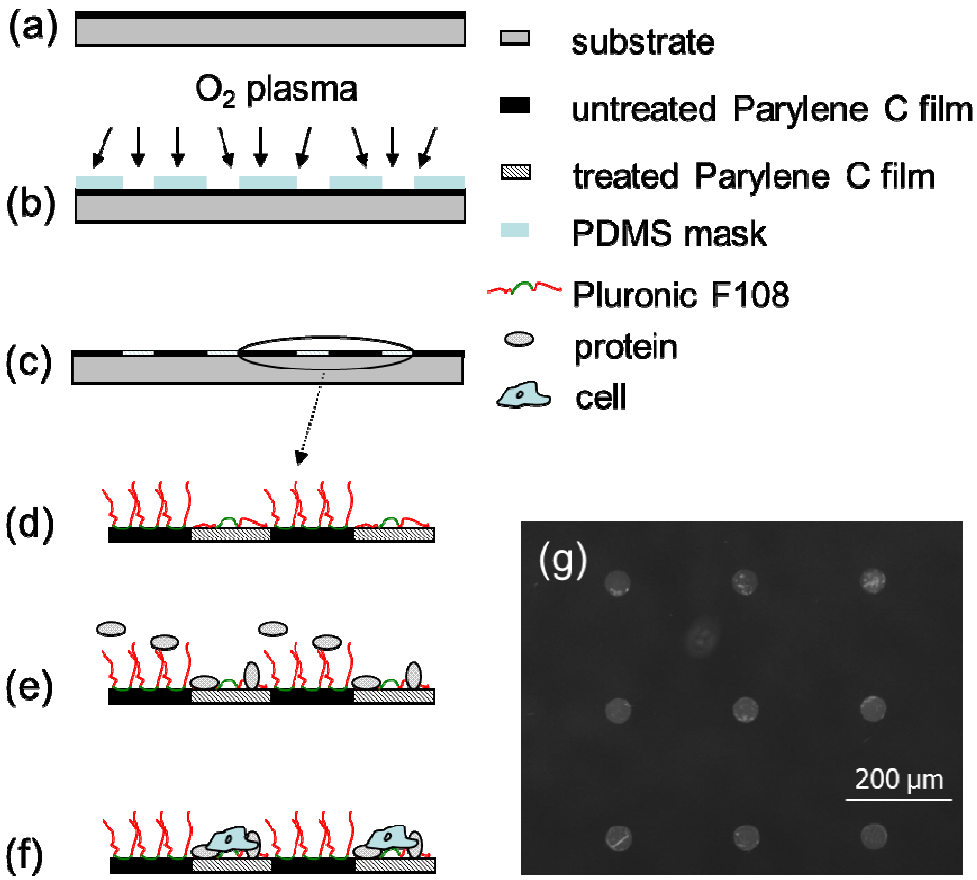

Figure 6.10. Schematics of (a-c) surface chemical patterning process, (d) surface incubation with Pluronic F108 solution, (e) surface activation by serum proteins, and (f) selective attachment of single cells on hydrophilic surface areas; (g) fluorescence photograph showing FITC-collagen adsorption on a chemically patterned Parylene C surface incubated with 0.01% Pluronic F108 solution.

Chapter 7

Plasma Surface Chemical Treatment Enhances Cell Adhesion, Growth and Infiltration in Electrospun Poly(L-lactide) Microfibrous Scaffolds

7.1 Introduction

Poly(L-lactide) (PLLA) microfibrous structures produced by electrospinning are of particular interest in bioengineering because their porosity and biodegradability make them ideal candidates for scaffolds. However, because PLLA surfaces (solid or fibrous) are hydrophobic, cell attachment and growth on PLLA scaffolds is limited. Therefore, various surface treatment methods have been used to modify the surface chemical behavior of PLLA surfaces to improve biocompatibility (Yoo et al. (2009)). Plasma-assisted surface modification is a commonly used method of tuning the biochemical properties of surfaces to specific application needs because it enables a wide range of surface functionalities that improve biocompatibility either directly or indirectly through biomolecule surface immobilization. For instance, surface functionalization by hydrophilic chemical groups (e.g., –COOH and $–NH_2$) using reactive gas plasma treatment and surface chemical modification by film deposition (Gugala et al. (2006), Latkany et al. (1997), Harvey et al. (2003), Baek et al. (2008), Prabhakaran et al. (2008), Martins et al. (2009), Park et al. (2007), Barry et al. (2005), Park et al. (2007), Guptaa et al. (2002)), or polymer surface coating by various external cell matrix proteins (e.g., collagen, gelatin, and laminin) (Koh et al. (2008), He et al. (2005), Ma et al. (2005), Chen et al. (2011), Feng et al. (2010), Shen et al. (2007), Yang et al. (2002)) and other bioactive molecules using plasma treatment (Paaletta et al. (2010), Jia et al. (2008)) have been shown to improve the biocompatibility of polymer materials.

In addition to the significant effort devoted to increase the surface hydrophilicity of biopolymers to promote bioactive molecular and protein attachment, the direct effect of plasma surface treatment on biocompatibility has also received significant attention. Surface treatment with simple plasmas (e.g., air, Ar, O_2, and NH_3) has been reported to enhance cell growth (Latkany et al. (1997), Harvey et al. (2003), Baek et al. (2008), Prabhakaran et al. (2008), Martins et al. (2009), Park et al. (2007)). NH_3 plasma treatment, resulting in $–NH_2$ surface functionalization, has been shown to be more effective in improving cell growth on polymer surfaces than O_2 and SO_2 plasmas (Gugala et al. (2006), Latkany et al. (1997), Park et al. (2007)). Also, plasma-synthesized polymer coatings rich in $–NH_2$ and –COOH groups (Park et al. (2007), Guptaa et al. (2002)) have been reported to increase cell growth on scaffolds. However, relatively less is known about the effect of inert gas plasma treatment of polymers on cell growth (Baek et al. (2008), Martins et al. (2009)), while information about the effect of different plasma treatments on cell infiltration in three-dimensional structures is sparse. To induce detectable chemistry modification, the inert gas plasma treatment conditions used in previous studies were

so intense that they damaged the structure of the polymer fibers due to thermal heating or induced fiber roughening due to excessive plasma etching. Because intense plasma treatment of polymers results in both morphological and chemical surface modification, it is difficult to determine the effect of each type of modification on the resulting biocompatibility characteristics. Thus, mild plasma conditions conducive to chemical surface modification are preferred to avoid surface damage leading to reduced mechanical strength of the scaffold material and to elucidate the effect of plasma-induced surface chemical changes on biocompatibility.

In this chapter, surface chemical modification of PLLA microfibrous scaffolds was realized by Ar and NH_3 plasmas under relatively mild conditions. Inert (Ar) plasma treatment was selected to remove surface contaminants and produce *ex situ* oxygen surface functionalities (e.g., –OH and –COOH) upon the exposure of the activated PLLA surfaces to the ambient (Tajima et al. (2005)), while reactive (NH_3) plasma treatment was used to produce *in situ* nitrogen-containing surface functionalities (e.g., $–NH_2$). The NH_3 plasma treatment was optimized by mixing NH_3 with Ar gas, followed by a post-treatment with H_2 plasma to maximize the fraction of $–NH_2$ surface functionalities. The plasma-treated scaffold surfaces were characterized by contact angle, scanning electron microscope (SEM), atomic force microscope (AFM), and X-ray photoelectron microscope (XPS) measurements. Surface chemical modification by NH_3 plasma treatment was studied by tracking the nitrogen content at the surface, while the incorporation of amine functional groups was examined using the chemical derivative method described in a previous study (Favia et al. (1996)). Bovine aorta endothelial cells (BAECs) and bovine smooth muscle cells (BSMCs) were used to examine the effect of plasma treatment on cell attachment and growth. Both *in vitro* and *in vivo* experiments were performed to obtain further insight into the effect of plasma treatment on cell infiltration into the PLLA microfibrous scaffolds.

7.2 Experimental procedures

7.2.1 Sample preparation

Poly(L-lactide) (PLLA) with an inherent viscosity of 1.09 dL/g (Lactel Absorbable Polymers, Pelham, AL) was used to fabricate microfibrous scaffolds by electrospinning, as described previously (Kyle et al. (2010)). PLLA pellets were dissolved in an ultrasonic water bath of 19% w/v hexafluoroisopropanol and the solution was delivered by a programmable pump to an electrically charged needle under a high voltage (12 kV), which ejected polymer fibers of diameter between hundreds of nanometers to 1 µm. The electrostatically charged fibers were collected on the surface of a grounded drum kept at a fixed distance of 8cm from the needle tip, resulting in the formation of a nonwoven microfibrous scaffold on the drum surface. Fiber alignment during electrospinning was controlled by adjusting the rotational speed of the drum, while the scaffold thickness was controlled by the electrospinning time. A low rotational speed of 150 rpm was used in this study, resulting in randomly oriented fibers. The scaffolds used for surface topography and chemistry characterization and cell culture were ~100 µm thick, while those used in the *in vitro* and *in vivo* cell infiltration studies were ~250 µm thick. Film thickness measurements were obtained with a thickness gage (Mitutoyo America, Aurora, IL).

7.2.2 Plasma treatment of PLLA microfibrous scaffolds

Surface modification of the PLLA microfibrous scaffolds was performed in a radio-frequency capacitively coupled plasma reactor (Plasmalab 80plus, Oxford Instruments, Oxfordshire, UK) with plate diameter of 20 cm and plate-to-plate distance equal to 2 cm. Before processing, the chamber was cleaned with Ar plasma (300 W power; 100 sccm Ar gas flow rate; 0.9 Torr pressure) for 5 min. Ar plasma treatment was performed under the conditions of 30 W power, 100 sccm Ar gas flow, and 0.5 Torr pressure for 2 min. For NH_3 plasma treatment, a plasma treatment with a mixture of Ar and NH_3 (30/70 sccm) gases was performed first for 5 min (50 W power; 0.5 Torr pressure), followed by a H_2 plasma treatment for 0.5 min (10 W power; 50 sccm H_2 gas flow rate; 0.5 Torr pressure) to maximize the incorporation of primary amine groups. Hereafter, this treatment condition will be referred to as the Ar-NH_3/H_2 plasma treatment.

7.2.3 Characterization of plasma-treated surfaces

Surface morphology. The surface morphologies of the plasma-treated microfibrous scaffolds were examined with a field emission SEM (TM-1000, Hitachi, Pleasanton, CA) and an AFM (Dimension 3100, Veeco Instruments, Plainview, NY) operated in tapping mode to avoid surface damage of the soft surfaces. AFM imaging was performed with 10-nm-radius silicon tips attached to silicon cantilevers of spring constant equal to 46 N/m (NSC15/AlBS, MicroMasch, Wilsonville, OR).

Contact Angle Measurements. Static contact angle measurements were obtained for PLLA microfibrous membranes or solid membranes with different treatments. The surface wetting characteristics were examined with a drop-shape analysis system (DSA10, Krüss GmbH, Hamburg, Germany). Deionized water droplets（~6 μL) were delivered to the film surface by a syringe at room temperature, and the droplet configuration was captured by a camera. Then, the angle between the droplet baseline and the tangent of the water/air boundary was measured, and the contact angle was calculated as the average of the left and right contact angles. For statistical analysis, six contact angle measurements were obtained from three different surface regions of two identical samples.

Chemical Analysis. Scaffold surface chemical composition analysis was carried out with an XPS system (Perkin-Elmer PHI 5400 ESCA) without charge neutralization or monochromator, equipped with an Al-Kα X-ray source of photon energy equal to 1486.6 eV. A take-off angle of 54.7º relative to the analyzer axis was used throughout the XPS analysis. During spectral acquisition, the pressure in the main chamber was maintained at ~10^{-7} Torr. Survey spectra were acquired in the binding energy range of 0–1100 eV with pass energy of 178.95 eV. High-resolution XPS spectra of C1s, O1s and N1s core level peaks were collected with pass energy of 35.75 eV to determine atomic fraction of PLLA membranes with different treatments. XPS results were deduced from at least three measurements obtained from different surface regions. To detect the presence of –NH_2 groups, untreated and plasma-treated scaffolds were exposed to trifluoromethyl benzaldehyde (TFBA) vapor (Fisher Scientific, Pittsburgh, PA) for 45 min and then degased for 1 h in a vacuum of ~2 Torr before XPS detection.

7.2.4 Cell spreading and proliferation rate study

Bovine aorta endothelial cells (BAECs) and bovine smooth muscle cells (BSMCs) were used to study cell adhesion and proliferation on ~100-mm-thick plasma-treated scaffolds. Before cell seeding, untreated (control) scaffolds were sterilized in 70% ethanol under the effect of ultraviolet (UV) light for 30 min, washed five times with sterile phosphate buffered saline (PBS), and sterilized by a 30-min UV treatment. Cells were seeded on different substrates with serum medium consisting of Dulbecco's modified Eagle's medium (DMEM), 10% fetal bovine serum (FBS), and 1% penicillin streptomycin, and kept in a humidified incubator (37 ºC, 5% CO_2) for 5 or 24 h. To study cell adhesion and spreading, cells were fixed with 4% paraformaldehyde (PFA) after incubation for 5 or 24 h, permeabilized with 0.5% Triton X-100, and the cell actin and nucleus were stained with Alexa-Phalloidin 488 and 4',6-diamidino-2-phenylindole (DAPI), respectively. Fluorescence photographs of stained BAECs were obtained with an upright fluorescence microscope (Zeiss HAL 100, Carl Zeiss MicroImaging, Thornwood, NY).

For cell proliferation study, BAECs and BSMCs seeded on different surfaces and cultured for 24 h were incubated for 1 h with 10 µM EdU (Invitrogen, Carlsbad, CA). Then the samples were fixed with 4% paraformaldehyde, permeabilized with 0.5% Triton X-100, blocked with 3 mg/mL bovine serum albumin, and stained with click-it EdU kit (Invitrogen, Carlsbad, CA). The percentage of BAECs and BSMCs that incorporated EdU (i.e., the cells with DNA synthesis) was correlated to the proliferation rate of two cell lines. To ensure repeatability, each cell proliferation experiment was repeated three times.

7.2.5 In vitro cell infiltration model

Plasma-treated scaffolds of ~250 mm thickness fabricated by electrospinning were cut into 0.7 × 0.7 cm^2 samples. Untreated (control) scaffolds were sterilized in 70% ethanol while exposed to UV light for 30 min and then washed five times in PBS. Three scaffolds representing each group were then attached to non-tissue-culture-treated polystyrene dishes by sterile double-sided tape. BAECs were seeded at 100% confluency onto the scaffolds and kept for 5 days in serum medium in the incubator. Sufficient media was used in each dish to avoid changing the medium during the 5-day incubation.

At the fifth incubation day, the whole scaffold was fixed and stained with DAPI and then placed on an optimal cutting temperature (OCT) compound (TissueTek, Elkhart, IN) on dry ice. Cross-sections of 20 µm thickness were obtained with in a cryosectioner in the transverse plane at –20ºC. DAPI fluorescent signals of the cells in these cryosections were viewed under the previously mentioned Zeiss microscope. To ensure consistency, a minimum of 30 cryosections of each scaffold were examined.

7.2.6 In vivo cell infiltration model

To investigate the effect of plasma treatment on cell infiltration *in vivo*, three scaffolds of each group were implanted in the subcutaneous cavity of Sprague-Dawley rats (Charles River Laboratories, Wilmington, MA) by the following method. First, the rats were anesthetized with isofluorane and the incision site was marked and disinfected with 70% ethanol. Then, three

incisions were made on both sides and middle of abdominal wall, and scaffolds of different plasma tretament were implanted to one side of the incision and tucked subcutaneous away from the incision. The cut was sewed with interrupted 5-0 Monocryl (Ethicon, Inc., Somerville, NJ) mattress sutures. All animals were monitored daily by a veterinarian and there were no adverse events noted with any of the animals. After 5 days, the rats were returned to the operating room where they were given general anesthesia and an overdose of euthanasia solution, and the implants and surrounding tissue was removed and embedded in OCT on dry ice. Cross-sections of 10 µm thickness were obtained with cryosectioner in the transverse plane a –20ºC. Then, the sections were fixed with 4% PFA, stained with DAPI, and examined under the Zeiss microscope. A minimum of 30 cryosections of each scaffold were examined to ensure consistency between sections.

7.3 Results and discussion

7.3.1 Surface chemistry and morphology

Contact angle and Surface morphology. Contact angle measurements of untreated and plasma-treated electrospun PLLA microfibrous scaffolds and PLLA membranes fabricated by thermal molding are given in Table 1. The significant decrease in contact angle observed with plasma-treated scaffolds indicates a more hydrophilic behavior. The nearly zero apparent contact angle of the Ar-NH_3/H_2 plasma-treated scaffolds may be due to capillary effects and the highly porous fibrous structure. Contact angle measurements obtained with nonfibrous PLLA membranes confirmed that surface treatment with Ar and Ar-NH_3/H_2 plasmas enhanced the surface hydrophilicity, although the decrease in contact angle was not as pronounced as for the scaffolds. AFM measurements revealed insignificant differences in surface roughness between untreated and Ar- or Ar-NH_3/H_2 plasma-treated membranes (the corresponding root-mean-square roughness was found equal to about 9.5, 26.8, and 6.7 nm). Therefore, these contact angle differences may be attributed mainly to the modification of the surface chemistry by the plasma treatment, with the dramatic decrease in contact angle of the scaffold surfaces attributed to surface roughness and porosity effects on the contact angle measurements. The results given in Table 1 indicate a general trend for Ar-NH_3/H_2 plasma treatment to produce more hydrophilic PLLA surfaces than Ar plasma treatment.

Figure 7.1 shows SEM and AFM images of surface morphologies of the untreated and plasma-treated scaffolds. A comparison of the SEM images shown in Figure 7.1 (top row) does not show any discernible structural changes due to plasma treatment of the scaffolds, indicating that the plasma conditions used to alter the surface chemical behavior did not damage the fibers. The AFM images shown in Figure 7.1 (second and third rows) reveal very smooth fiber surfaces for both untreated and plasma-treated scaffolds. Although plasma treatment normally roughens polymer surfaces as a result of ion etching (Tajima et al. (2005), Cheng et al. (2009)), this effect was not observed with PLLA fibers in this study. This may be attributed to the structure of the electrospun PLLA fibers consisting of stretched polymer chains oriented parallel to the longitudinal direction of the fiber. This fiber structure resulted in a uniform and smooth surface exhibiting higher etch resistance than that of polymer surfaces consisting of randomly oriented, recoiled molecular chains. Thus, the relatively mild plasma treatment conditions used in this study resulted only in surface chemical modification of the scaffold surfaces.

Surface chemical modification by plasma treatment. Figure 7.2 shows XPS results revealing the presence of different surface functionalities due to plasma treatment. The XPS survey spectra shown in Figure 7.2A indicate that Ar plasma treatment did not produce any new peaks. This is expected because Ar plasma only creates free bonds, which form –OH and –COOH bonds upon the exposure of the sample to the atmospheric conditions. The N1s peak in the XPS survey spectrum corresponding to the Ar-NH_3/H_2 plasma treatment reveals the incorporation of nitrogen into the scaffold surface structure. Figure 7.2B shows C, O, and N contents (calculated from the C12, O1s, and N1s core level peaks of XPS survey spectra, respectively) of untreated and plasma-treated scaffolds. The data confirm that Ar plasma did not change the surface chemical composition significantly, as opposed to Ar-NH_3/H_2 plasma that resulted in the incorporation of N surface functionalities. The similar C and O contents of the untreated and Ar plasma-treated scaffolds provide additional evidence that the mild Ar plasma conditions didn't induce significant chemical modification of the scaffold surface.

XPS survey spectra of scaffolds chemically treated with TFBA were used to determine if the N1s peak in the XPS survey spectra of the Ar-NH_3/H_2 plasma-treated scaffolds was due to–NH_2 surface groups, incorporated to the surface as shown schematically in Figure 7.3A. The presence of the F1s peak only in the spectrum of the Ar-NH_3/H_2 plasma-treated scaffolds, shown in Figure 7.3B, confirms the incorporation of primary amine groups at these scaffold surfaces. The fraction of NH_2 with respect to C atoms was determined to be ~1.5% with this method.

The above results indicate that the applied plasma treatments were conducive to only chemical surface modification, as the scaffold surface morphology was not altered. For a conclusion, the physic-chemical measurements on the untreated and plasma treated PLLA microfibrous membrane showed that the applied plasma treatments are actually really mild and don't induce any surface roughness change. While both plasma treatments enhanced the surface hydrophilicity, Ar plasma did not produce detectable chemical changes in the surface composition of the treated scaffolds, whereas Ar-NH_3/H_2 plasma resulted in surface functionalization by –NH_2 groups.

7.3.2 Effect of plasma treatment on cell morphology, cell proliferation and cell infiltration

Cell culture and effect of plasma treatments on cell morphology. Staining for cell actin was used to examine the cell morphology after a short incubation time of 5 h. Figures 4A-F show that during the initial stage of cell attachment, both BAECs and BSMCs attached and spread more on the plasma-treated scaffold surfaces than the untreated surfaces. To examine if this higher surface affinity of the cells was due to increased adsorption of serum protein on the plasma-treated surfaces, the N fraction obtained from XPS measurements was used to determine the amount of protein adsorbed onto untreated and plasma-treated surfaces after incubation in serum medium. As shown in Figure 7.4G, the difference in protein adsorption between untreated and plasma-treated scaffold surfaces is statistically insignificant. Since surface morphology measurements did not show any effect of plasma treatment on surface roughness, the only factor responsible for the enhancement of cell spreading on the plasma-treated surfaces was the increased hydrophilicity and incorporation of –OH, –COOH, and –NH_2 functionalities, which seems to promote protein adsorption in configurations which are more conducive to cell

attachment and spreading. Therefore, although the amount the protein absorbed onto the fibrous scaffold surfaces was similar, configuration differences in the absorbed protein could affected cell spreading.

A similar trend in cell spreading was found for both BAECs and BSMCs after a relatively long incubation time of 24 h. Figure 7.5 shows that cell spreading on the Ar-NH_3/H_2 plasma-treated surfaces is even better than that on the Ar plasma-treated surfaces. This may be indicative of the beneficial effect of the presence of $–NH_2$ groups at the scaffold surface, and is consistent with the findings of a previous study showing that NH_3 plasma treatment improves cell adhesion in the presence of shear stresses (Huang et al. (2006)).

Effect of plasma treatments on cell proliferation. EdU assay was used to examine the effect of plasma treatment on the rate of cell proliferation. Figure 7.6 shows that both plasma treatments increased the cell proliferation rate significantly compared to control (untreated) scaffolds. This is attributed to plasma-induced surface chemical modification (functionalization) and is consistent with the results shown in Figures 7.4 and 7.5. However, it appears that Ar plasma treatment was more effective in increasing the proliferation rate of both BAECS and BSMCs than Ar-NH_3/H_2 plasma treatment, although the latter was more in promoting cell spreading (Figure 7.5). This is consistent with a previous study showing Ar plasma to enhance cell outgrowth more than other plasma treatments (Latkany et al. (1997)), but the Ar plasma conditions in that study were significantly more intense than those of this study. In the absence of any changes in the surface morphology (roughness) by plasma treatment, the only plausible reason for the different proliferation rates obtained with the two plasma treatments is that the surface chemical modification produced by Ar plasma treatment resulted in serum protein adsorption in a configuration that enhanced cell growth, despite the fact that Ar-NH_3/H_2 plasma treatment was more effective in promoting cell spreading. Since changes in the surface chemical composition of the scaffold exposed to Ar plasma treatment were not detected with XPS, it may be inferred that the Ar plasma only caused minor surface activation. It appears that this surface activation was more conducive to cell growth than surface functionalization by $–NH_2$ groups, which is widely known to enhance surface biocompatibility. Clearly, further studies must be conducted to elucidate the effect of plasma conditions on the biochemical characteristics of microfibrous scaffolds.

Effect of plasma treatments on cell infiltration. Both *in vitro* and *in vivo* experiments were conducted to investigate the effect of plasma treatment on cell infiltration in the three-dimensional microfibrous structure of the PLLA scaffolds. Figure 7.7 shows representative cross-section images of scaffolds with DAPI stained BAECs obtained after incubation for 5 days. The cells were seeded at the top surface of the scaffolds. The cell density on the untreated scaffold surface is low and cell infiltration in the depth direction is very limited (Figure 7.7A). After Ar or Ar-NH_3/H_2 plasma treatment, significantly more cells were observed at the top scaffold surface and cell infiltration in the depth direction was more apparent (Figures 7.7B-C). This trend is consistent with the cell spreading and proliferation results presented above. Thus, in addition to improving cell spreading and proliferation, both plasma treatments improved *in vitro* cell infiltration in the scaffold structure. Because plasma treatment was performed in the gas phase and in view of the highly porous structure of the thin PLLA scaffolds, it is likely that plasma-induced surface activation occurred through the scaffold thickness, which explains the

enhancement of cell infiltration observed with the plasma-treated scaffolds. However, because it is difficult to quantify cell ingrowth into the scaffolds, it is not possible to distinguish differences in cell infiltration between the two plasma treatments.

Figure 7.8 shows representative cross-section images of scaffolds subcutaneously implanted under the skin of Sprague-Dawley rats. For untreated PLLA scaffold, it can be seen that very low cell density and minimal cell infiltration were observed with untreated scaffolds (Figure 7.8A). However, plasma treatment enhanced cell infiltration, increasing the cell density and ingrowth depth significantly (Figures 7.8B-C). However, similar to *in vitro* cell infiltration, it is difficult to quantify any differences in *in vivo* cell infiltration due to the Ar and Ar-NH_3/H_2 plasma treatments. Nevertheless, the results of the present study demonstrate that surface chemical modification of PLLA microfibrous scaffolds with Ar and Ar-NH_3/H_2 plasma treatments not only increases cell affinity and growth *in vitro*, but also improves scaffold biocompatibility *in vivo* and enhances cell ingrowth, which is critical in tissue engineering.

7.4 Conclusions

In this chapter, the effect of surface chemical modification of PLLA microfibrous scaffolds fabricated by elecrtospinning by inert (Ar) and reactive (Ar-NH_3/H_2) plasmas on cell attachment, growth, and infiltration was examined in this study. Measurements of the surface morphology and chemical composition demonstrated that the scaffold surface chemistry was successfully modified without affecting the fiber surface morphology. BAEC and BSMC culture studies showed that both plasma treatments were effective in improving cell spreading and growth, with Ar-NH_3/H_2 plasma treatment enhancing more cell spreading and Ar plasma treatment increasing more the cell proliferation rate. *In vitro* and *in vivo* cell infiltration experiments showed that, in addition to enhancing cell affinity and growth, both plasma treatments promoted cell in-growth in the microfibrous scaffold structure significantly, which is of high importance in tissue engineering.

Table 7.1 Contact angle of untreated and plasma-treated PLLA microfibrous scaffolds and PLLA membranes fabricated by thermal molding.

PLLA material	Untreated	plasma treated	
		Ar	Ar-NH_3/H_2
thermal molded membrane	67.7 ± 2.6	53.6 ± 0.6	48.8 ± 0.8
electrospun microfibrous membrane	116.2 ± 3.6	85.0 ± 4.3	~0

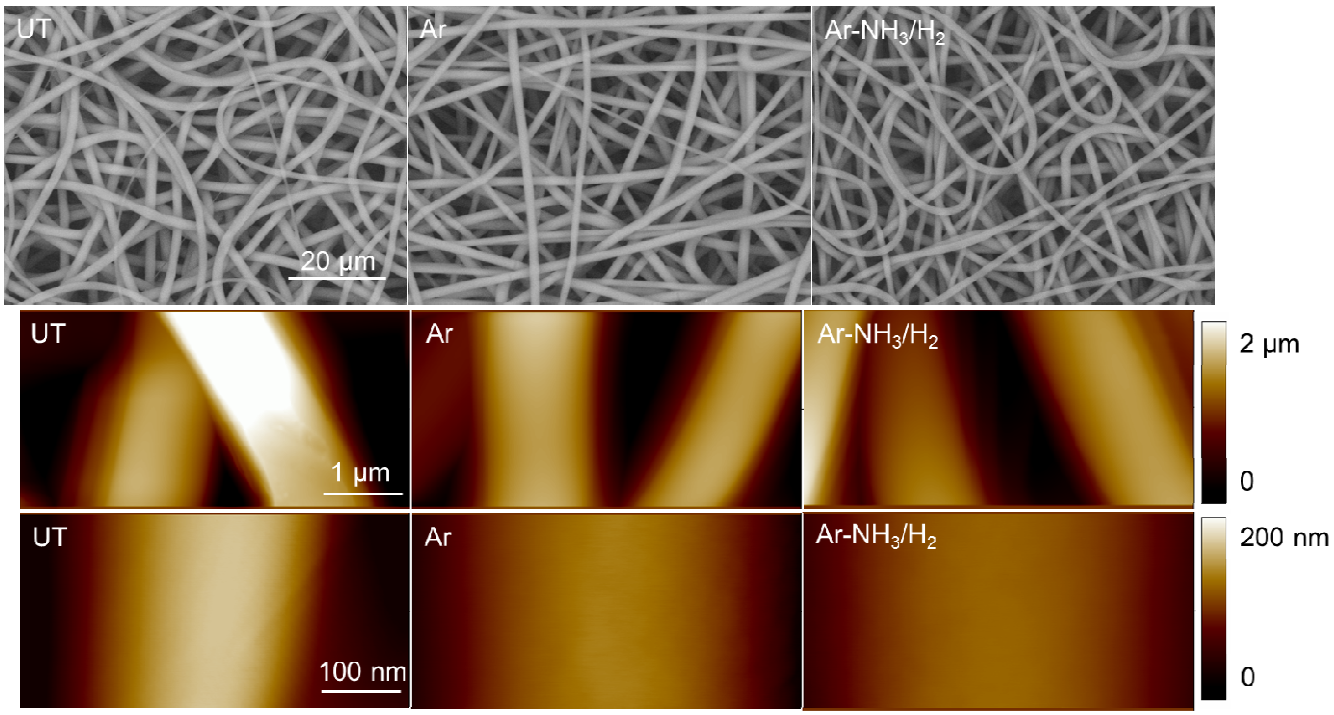

Figure 7.1. SEM (first row) and AFM second and third rows) images of untreated and plasma-treated PLLA microfibrous scaffolds.

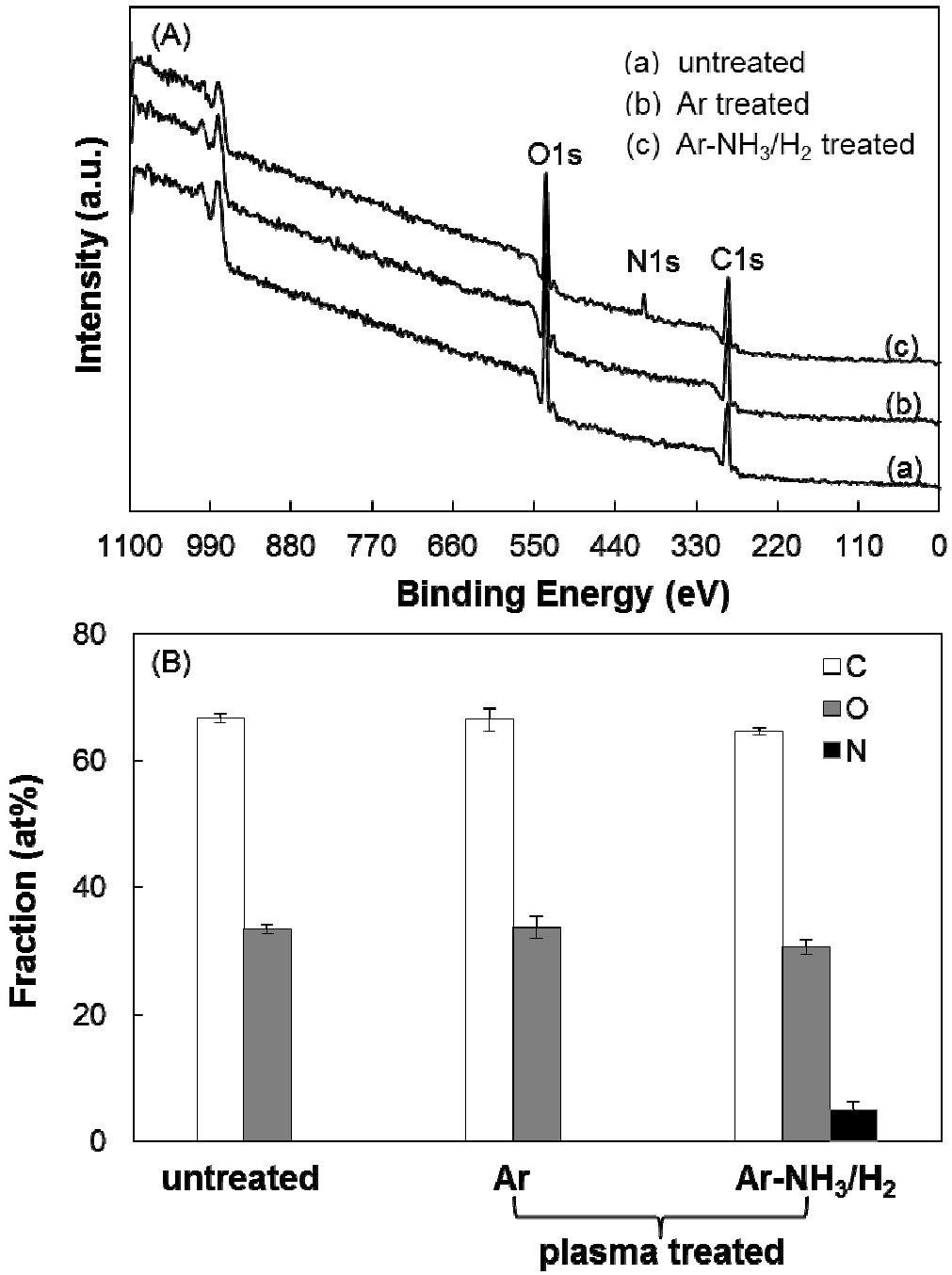

Figure 7.2. (A) XPS spectra and (B) surface concentration of C, O, and N of untreated and plasma-treated PLLA microfibrous scaffolds.

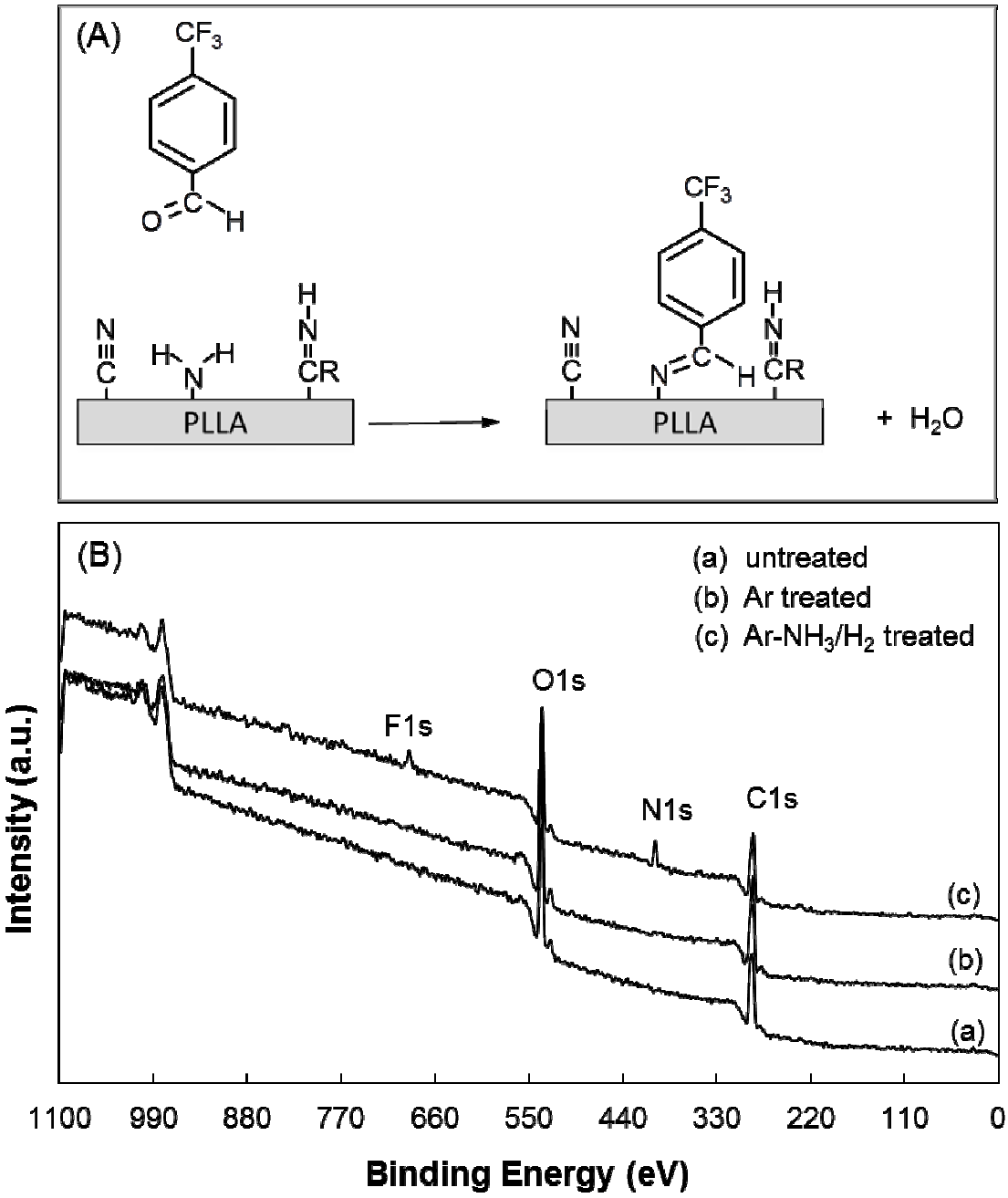

Figure 7.3. (A) Schematic of TFBA labeling of $-NH_2$ groups on Ar-NH_3/H_2 plasma-treated PLLA microfibrous scaffolds, and (B) XPS survey spectra of untreated and plasma-treated PLLA microfibrous scaffolds treated with TFBA.

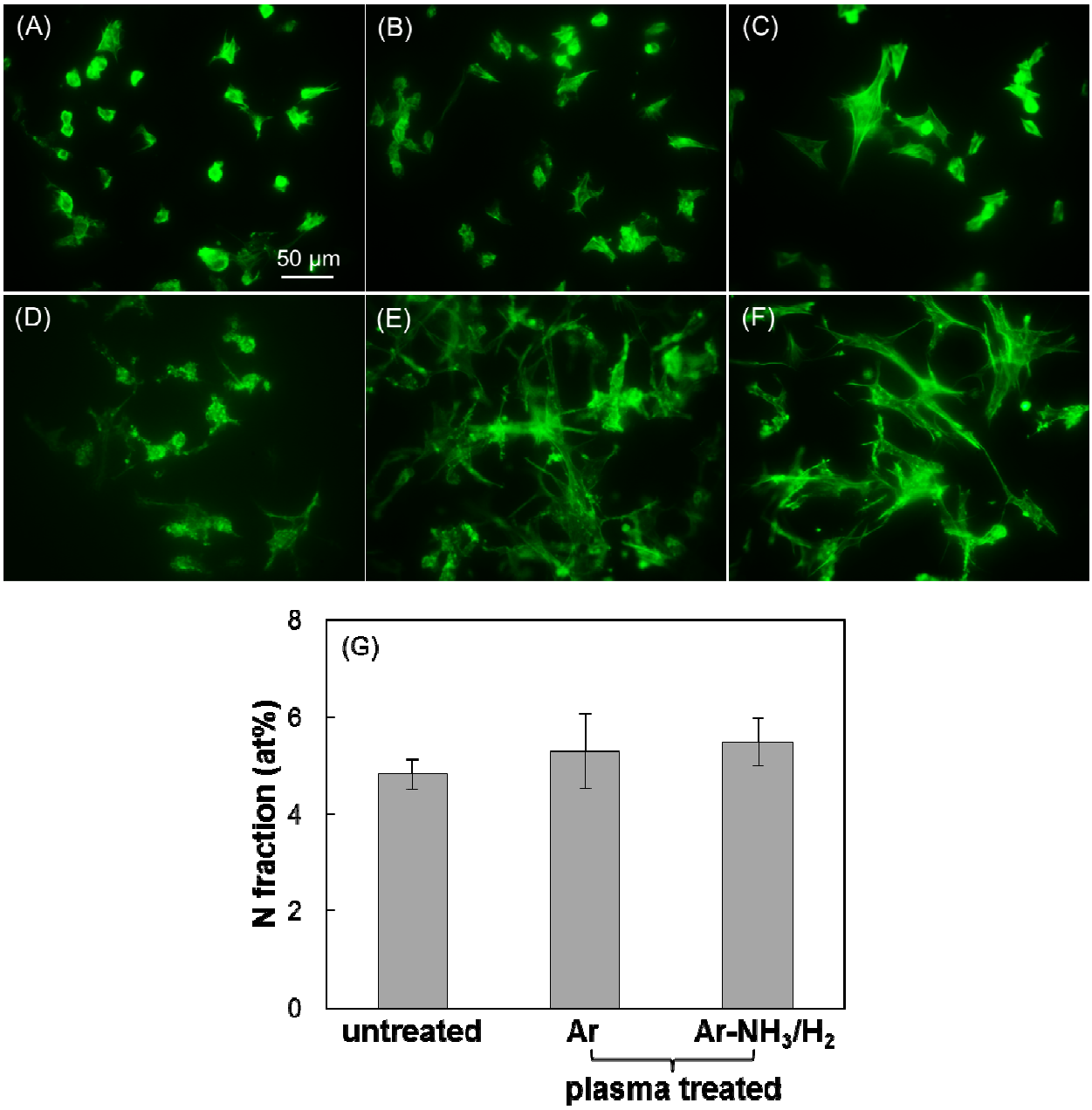

Figure 7.4. BAEC and BSMC morphologies on untreated and plasma-treated PLLA microfibrous scaffolds obtained after incubation in serum medium for 5 h. BAECs cultured on (A) untreated, (B) Ar plasma-treated, and (C) Ar-NH_3/H_2 plasma-treated scaffold surfaces. BSMCs cultured on (D) untreated, (E) Ar plasma-treated, and (F) Ar-NH_3/H_2 plasma-treated scaffold surfaces. (G) Atomic percentage of N indicating the amount of serum protein adsorption on untreated and plasma-treated PLLA microfibrous scaffolds after 5 h incubation in 10% FBS medium.

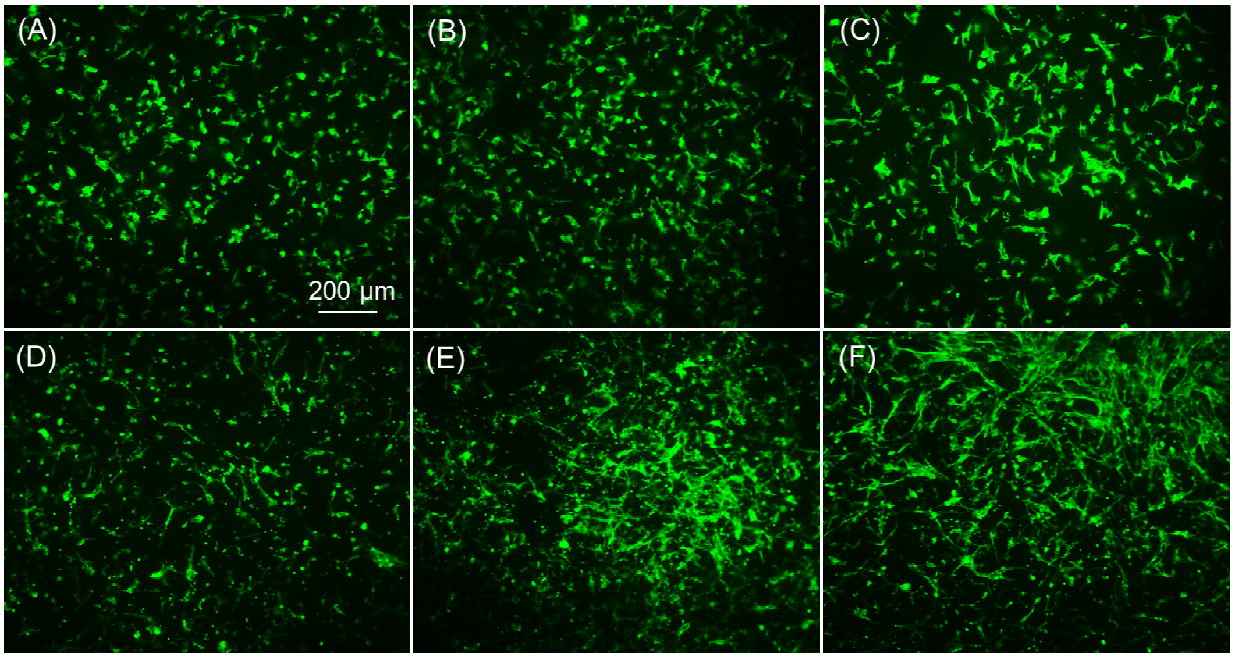

Figure 7.5. BAEC and BSMC morphology on untreated and plasma-treated PLLA microfibrous scaffolds after 24 h incubation in serum medium. BAECs cultured on (A) untreated, (B) Ar plasma-treated, and (C) Ar-NH_3/H_2 plasma-treated scaffold surfaces. BSMCs cultured on (D) untreated, (E) Ar plasma-treated, and (F) Ar-NH_3/H_2 plasma-treated scaffold surfaces.

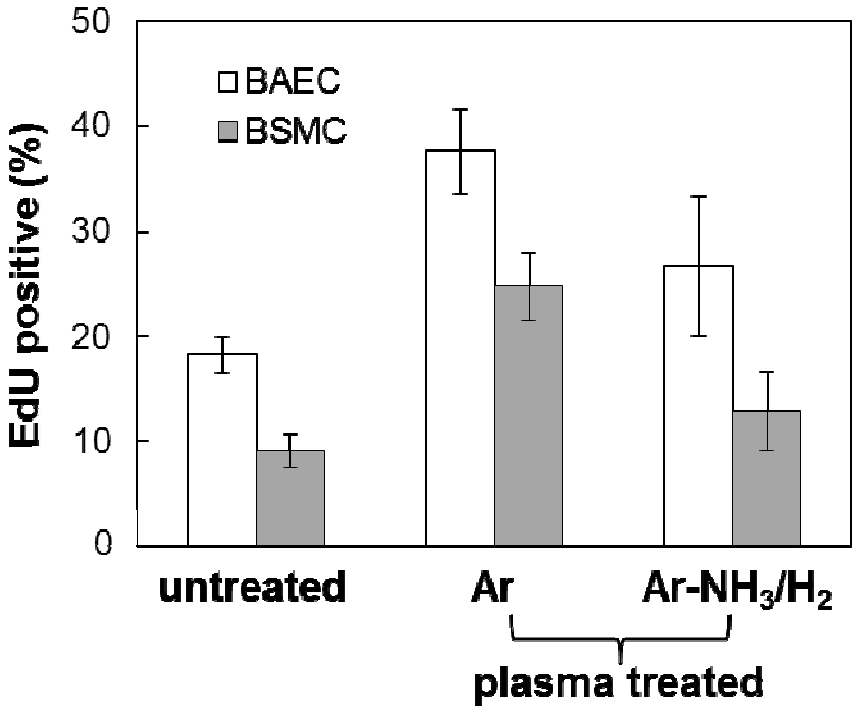

Figure 7.6. BAEC and BSMC proliferation rates after in vivo incubation on untreated and plasma-treated scaffold surfaces in serum medium for 24 h. The proliferation rate of each treatment is differs statistically from the other two treatments for the same cell type. ($P<0.05$, repeated 3 times)

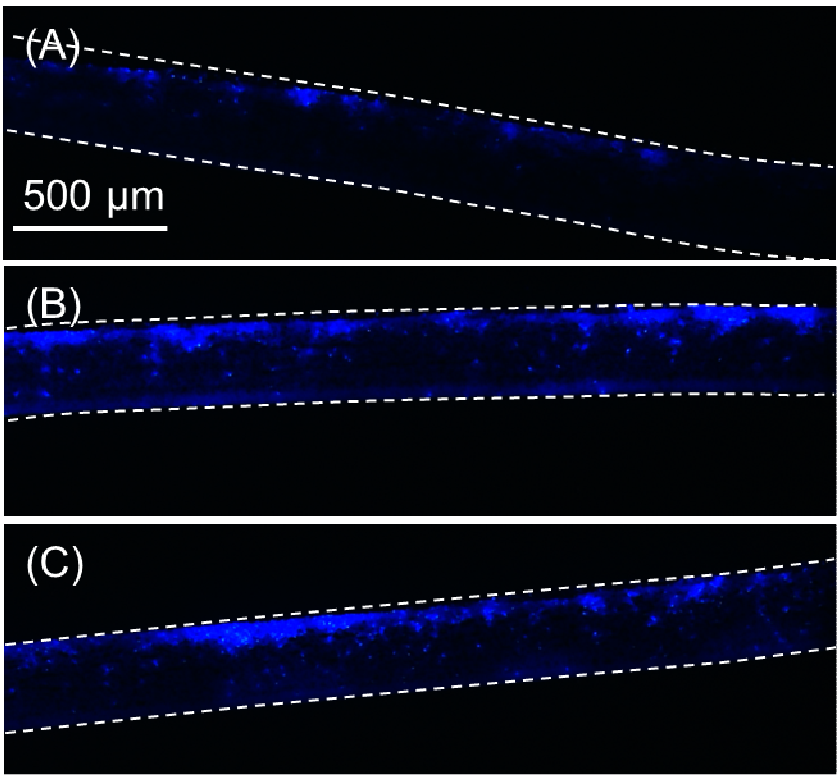

Figure 7.7. Cross-section images of (A) untreated, (B) Ar plasma-treated, and (C) Ar-NH_3/H_2 plasma-treated scaffolds obtained after *in vitro* culture with BAECs in serum medium for 5 days. Cells were stained by DAPI.

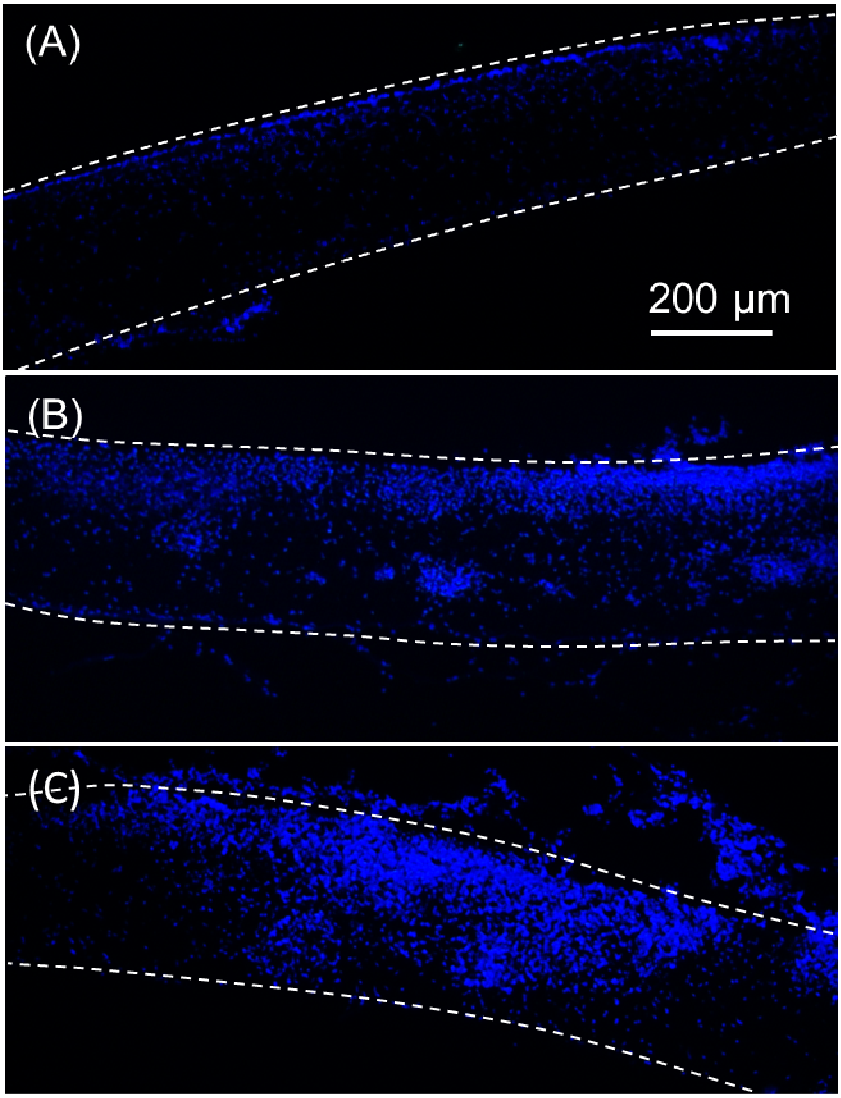

Figure 7.8. Cross-section images of (A) untreated, (B) Ar plasma-treated, and (C) Ar-NH_3/H_2 plasma-treated scaffolds obtained after 5 days of *in vitro* implantation under the skin of Sprague-Dawley rats. Cells were stained by DAPI.

Chapter 8

Plasma Assisted Heparin Conjugation on Poly(L-lactide) Microfibrous Membrane

8.1 Introduction

Electrospinning of poly(L-lactide) (PLLA) nano/micro fibers are getting more and more attention in the fields of tissue engineering and drug delivery. Polymer scaffolds with fibrous structure can mimic the structure of external cell matrix, making them ideal for cell culture and tissue engineering; while the high surface to volume ratio of these fibrous structures make them perfect candidate for drug delivery (Yoo et al.(2009)). While various polymer fibrous structures have been studied extensively for different applications, surface modification of the polymer fiber surfaces is usually required to improve its hydrophilicity, biocompatibility, or increase surface density of functional groups (e.g. $–NH_2$, –COOH) for further biomolecules immobilization. Although coelectrospinning of biopolymers with biomolecules (e.g. collagen, heparin, and lamella) (He et al. (2005), Luong-Vana et al. (2006), Koh et al. (2008)) and physical adsorption of biomolecules on modified polymer fibrous structure surfaces (He et al. (2005)) are widely used for numerous applications, covalent immobilization of biomolecules is critical for many cases where long term functionality of the biomolecules is critical. For example, the heparin molecules grafted on synthetic polymer vascular graft inner wall should be stable enough to resist thrombosis and insure blood circulation before the regeneration of new vascular tissue. For successful functionality, surface density of the covalently immobilized biomolecules is also critical. Therefore increasing the surface density of functional groups on the polymer fiber surfaces becomes extremely important. Currently the most commonly used method to increase polymer surface density of functional groups is wet chemical methods, such as NaOH solution hydrolysis and aminolysis, which are used to increase surface density of –COOH and $–NH_2$ groups respectively for various bioactive molecules immobilization (Croll et al. (2004), Zhu et al. (2002, 2007)), or UV induced grafting of acrylic acid to increase surface density of –COOH group (Cheng et al. (2004)). Besides, plasma treatment or plasma polymerization have also been widely used to introduce functional groups onto various biomaterial surfaces for biomolecules immobilization, and comprehensive reviews can be found elsewhere (Desmet et al. (2009), Siow et al. (2006)). Compared to wet chemical methods, plasma treatment and plasma polymerization are really versatile due to their simple treatment process upon optimizing the processing condition, and it's also an environmental friendly sterile process which can realize surface modification without modifying material bulk property.

Similarly, the objective of plasma treatment or plasma polymerization for biomolecules immobilization is to introduce –COOH and $–NH_2$ groups onto the surface. Many studies have been conducted to introduce these functional groups onto biomaterial surfaces. Plasma polymerization of allyamine has been applied to deposit plasma polymer film onto metal or polymer surface to increase surface density of $–NH_2$ group (Yang et al. (2010), Barry et al. (2005), Dai et al. (2009)), while plasma polymerization of acrylic acid is representative process

to introduce –COOH group (Park et al. (2007), Guptaa et al. (2002), Ju et al. (2008)). Besides, plasma treatment with NH_3 plasma is the most commonly used method to introduce $–NH_2$ groups onto biopolymer surfaces (Favia et al. (1996)). However, most of these studies focused on bulk polymers surface modifications, and surface functionalization for biomolecule immobilization on porous microfibrous structures is still limited. While plasma polymerization has the advantage of coating various substrates successfully, the precursors used are usually extremely toxic and can't be integrated into common plasma processing systems directly. Therefore, plasma treatment with NH_3 is suggested since it's a much less toxic gas which can be equipped on most plasma systems. In this chapter, NH_3 plasma was mixed with Ar plasma and combined with H_2 plasma to directly introduce $–NH_2$ groups onto PLLA surface to increase density of surface conjugation sites and enable immobilization of heparin molecules. The process condition was optimized by varying the plasma power, treatment time, gas composition and post treatment condition. The efficiency of using plasma treatment to increase surface density of $–NH_2$ groups was confirmed with X-ray photoelectron spectroscopy (XPS) measurement, heparin conjugation and quantification, as well as platelets attachment on the heparin conjugated surface. The effect of heparin conjugation for in vitro bovine aorta endothelial cell (BAEC) infiltration on the PLLA scaffold was also investigated.

8.2 Experimental procedures

8.2.1 Sample preparation and plasma treatment

Biodegradable PLLA (1.09 dL/g inherent viscosity) (Lactel Absorbable Polymers, Pelham, AL) was used to fabricate microfibrous membranes by electrospinning, as described previously. The PLLA pellets were first dissolved in hexafluoroisopropanol (HFIP) with ultrasonic water bath (19% w/v), then the solution was delivered by a programmable pump to an electrically charged needle connected to high voltage (12 kV), which ejected polymer fibers with diameter ~ 1μm at the tip. The electrostatically charged fiber were driven to fly towards a grounded collecting drum which was kept at a certain distance away, resulting in a nonwoven microfibrous membrane collected on the drum. During electerospinning, the alignment of the microfibers was controlled by adjusting the rotational speed of the collecting drum and the thickness of the membrane was controlled by collecting time. For microfiber membranes used in this study, a low speed of rotation (150 rpm) was used, which resulted in randomly oriented fibers. For surface chemistry characterization and platelets attachment on the scaffold surface, microfibrous membranes with thickness ~ 100 um were used, while for heparin conjugation and toluidine blue detection, and in vitro cell infiltration, membranes with thickness ~250 um were used. Film thickness was measured with a thickness gage (Mitutoyo America, Aurora, IL).

Surface modification of the PLLA microfibrous membranes was performed in a radio-frequency capacitively coupled plasma reactor (Plasmalab 80plus, Oxford Instruments, Tubney Woods, Abingdon, Oxfordshire, OX13 5QX, UK) with a plate diameter of 20 cm and plate-to-plate distance equal to 2 cm. Before processing, the chamber was cleaned with Ar plasma (300 W power; 100 sccm Ar gas flow rate; 0.9 Torr pressure) for 5 min. Ar plasma treatment was performed under the condition of 30 W power, 100 sccm Ar gas flow and 0.5 Torr pressure for 2min to prepare plasma treated control sample. To incorporate primary amine ($–NH_2$) groups onto PLLA microfibrous membrane surface, Ar and NH_3 mixture plasma was performed (50-

200W power; 0.5 Torr pressure; 100 sccm gas flow; treatment time 2-10 min) with a post treatment of H_2 plasma (10 W power; 50 sccm H_2 gas flow rate; 0.5 Torr pressure, treatment time 10-60 s) to maximize the surface density of $–NH_2$ groups. This treatment will be denoted as Ar-NH_3/H_2 plasma treatments in the following texts.

8.2.2 Surface chemistry characterization

Scaffold surface chemical composition analysis was carried out with an XPS system (Perkin-Elmer PHI 5400 ESCA) without charge neutralization or monochromator, equipped with an Al-Kα X-ray source of photon energy equal to 1486.6 eV. A take-off angle of 54.7º relative to the analyzer axis was used throughout the XPS analysis. During spectral acquisition, the pressure in the main chamber was maintained at ~10^{-7} Torr. Survey spectra were acquired in the binding energy range of 0–1100 eV with pass energy of 178.95 eV. XPS results were deduced from at least three measurements obtained from different surface regions. For detection of $–NH_2$ on PLLA scaffolds surface, chemical derivatization method as described in previous study has been used (Favia et al. (1996)). Briefly, untreated and plasma treated PLLA microfibrous samples were exposed to trifluoromethyl benzaldehyde (TFBA) vapor (Fisher Scientific, Pittsburgh, PA) for 45 min and degased for 1hr with a mechanical pump at ~2 Torr vacuum before XPS detection. The schematic of the chemical derivatization method and the formula used to determine the NH_2/C ratio is shown in Figure 8.1.

8.2.3 Heparin conjugation and quantification

Heparin was conjugated to microfibers by using 1-ethyl-3-(3-dimethylaminopropyl) carbodiimide hydrochloride (EDC) and N-hydroxysulfosuccinimide (sulfo-NHS) (Pierce Biotechnology, Rockford, IL). Briefly, the heparin solution was prepared by first dissolving EDC (20 mg/ml) and sulfo-NHS (10 mg/ml) in 0.5M MES buffer (pH = 5.5), and then adding in heparin into the mixture solution (20 mg/ml). After incubation of the whole solution for 45 min on a shaker, the solution was neutralized with 1N NaOH (110 µL 1N NaOH per 1ml of EDC/sulfo-NHS/heparin solution) and then incubated with the untreated, plasma treated PLLA microfibrous membrane and a control sample on a shaker for 2hrs for complete conjugation. To prepare the control sample, PLLA microfibrous membrane was first hydrolyzed in 0.01N NaOH for 10 min to increase surface -COOH density, and then conjugated with di-amino-poly(ethylene glycol) via EDC/sulfo-NHS method, which is denoted as PEG control sample in the following texts. The presence of heparin on microfibers was verified by toluidine blue staining. Briefly, PLLA microfibrous membranes with and without heparin conjugation were incubated in 2ml toluidine blue solution (0.0005%) in 0.001N hydrochloric acid with 0.02% (w/v) sodium chloride on a shaker for 10 min, then 1.0 ml hexane was added to each solution and the solutions were vortexed for 30 s and allowed for a phase separation, finally aqueous layer of free toluidine blue was extracted. The absorbance of the aqueous layers was determined at 631 nm on a UV spectrophotometer to calculate the amount of heparin conjugated to PLLA microfibrous membrane, and the value measured from samples without heparin conjugation was used for background subtraction.

8.2.4 Platelets attachment and cell infiltration

To examine the effect of heparin conjugation on the platelets attachment, whole blood from Sprague-Dawley rats (Charles River Laboratories, Wilmington, MA) was used for the in vitro platelets activation test. PLLA samples with and without heparin conjugation are incubated with rat whole blood for 2 hr at 37 ºC, and then washed with PBS 3 times, fixed with 2% gluteraldehyde overnight. Then the samples with attached platelets are gradually dehydrated with ethanol of different concentrations: 50% for 5 min, 70% for 5min, 80% for 5 min, 90% for 10 min, 100% for 10 min, and 100% for 10 min, and finally dried in hood overnight and examined with a field emission scanning electron microscope (SEM) (TM-1000, Hitachi, Pleasanton, CA) to check the density of attached platelets. Three sets of samples were examined to confirm the trend of platelets attachment on the PLLA microfibrous membrane surfaces was consistent.

To check the effect of heparin conjugation on cell growth on the PLLA microfibrous membrane, bovine endothelial cells was seeded on untreated and plasma treated PLLA microfibrous membrane with or without heparin conjugation. Untreated control membranes were sterilized in 70% ethanol under ultraviolet light for 30 min and subsequently washed five times with sterile phosphate buffered saline (PBS). Three microfibrous membranes representing each group were then attached to non-tissue-culture-treated polystyrene dishes via sterile double-sided tape. BAECs were seeded at 100% confluency onto the membranes with serum medium consisting of Dulbecco's Modified Eagle's Medium (DMEM), 10% fetal bovine serum (FBS), and 1% penicillin streptomycin (PS) and subsequently kept for 5 days in a humidified incubator (37 °C, 5%CO_2). Sufficient media was used in each dish as to avoid the need to change the medium before the end of 5 days. At Day 5, the whole membrane was fixed and then stained with 4',6-diamidino-2-phenylindole (DAPI) before put in optimal cutting temperature (OCT) compound (TissueTek, Elkhart, IN) on dry ice. Cross-sections of 20-µm thickness were taken in the transverse plane in a -20 ºC cryosectioner. The DAPI fluorescent signals from the cells within these cryosections were viewed with an upright fluorescence microscope (Zeiss HAL 100, Carl Zeiss MicroImaging, Thornwood, NY). A minimum of 30 cryosections were observed for each membrane to confirm consistency between sections.

8.3 Results and discussion

With the chemical derivatization technique and XPS detection method, the ratios of N/C, NH_2/N and NH_2/N on the PLLA microfibrous membrane surface for different plasma conditions can be determined. N/C ratio indicates the efficiency of N incorporation onto the PLLA microfibrous membrane surface, NH_2/N ratio indicates the selectivity of incorporating -NH_2 group over other N containing chemical groups via the plasma treatment, and NH_2/C shows the overall efficiency of introducing -NH_2 groups onto the material surface. The effects of different plasma conditions on these ratios are shown in Figure 8.2 and Figure 8.3. Figure 8.2(a)-(c) indicate that plasma power doesn't affect the N incorporation efficiency significantly, but high plasma power is not conducive to selective incorporation of -NH_2 group, maybe due to the over fragmentation of NH_3 molecules under high power. Therefore, relative low plasma power is more beneficial for higher overall -NH_2 density. The effect of plasma treatment time is shown in Figure 8.2(d)-(f). Increasing plasma treatment time resulted steady increase in N/C ratio, but can decrease the ratio of NH_2/N. Since it's well known that longer plasma treatment will induce more structural change on polymer material, a moderate treatment time should be selected. Figure 8.3(a)-(c) shows the effect of Ar gas fraction in the mixture on the surface chemistry. Similar to

the plasma power, it's found that Ar gas fraction doesn't affect much on N/C ratio, but too high Ar gas fraction will decrease the ratio of NH_2/N and therefore the ratio of NH_2/C, due to more interaction with Ar ion and fragmentation of the NH_3 molecules. The effect of H_2 plasma post treatment time is shown in Figure 8.3(d)-(f), it can be seen that the H_2 plasma post treatment can effectively convert other N containing chemical groups into -NH_2, but the effect saturate after 30s for the given plasma condition. From the above results, it's decided that Ar fraction of 30%, plasma power of 50 W, treatment time of 5 min, with 30 s H_2 plasma post treatment seems to be a the best plasma condition to introduce -NH_2 groups while maintaining the structure of the PLLA microfibrous membrane. It's observed by SEM that for all the plasma condition examined, no noticeable surface structural change on the PLLA microfibers was observed.

The amount of immobilized heparin on the untreated, plasma treated and PEG control PLLA microfibrous membranes are shown in Figure 8.4. It can be seen that very minimal heparin conjugation was detected on untreated and Ar plasma treated PLLA microfibrous membrane samples, which is expected, since the available conjugation sites on untreated and Ar plasma treated PLLA surfaces are limited, and it also confirmed that the detected heparin on the Ar-NH_3/H_2 plasma treated sample is not from the nonspecific adsorption of heparin due to surface activation by plasma treatment. The significantly higher amount of heparin measured on the Ar-NH_3/H_2 plasma treated sample compared to the PEG control sample indicated that plasma treatment can be more efficient than NaOH hydrolysis and aminolysis method to incorporate –NH_2 groups onto PLLA microfibrous membrane surface for biomolecule immobilization.

The efficiency of using Ar-NH_3/H_2 plasma treatment to enhance heparin conjugation on PLLA microfibrous membrane surface is also confirmed by the platelets attachment test on the microfibrous membrane surfaces, as shown in Figure 8.5. It can be seen that without heparin conjugation, lots of platelet attached on untreated and plasma treated PLLA microfibrous membrane surfaces (Figure 8.5(a)-(c)). After heparin conjugation, no significant difference was observed for untreated (Figure 8.5(d)) and Ar plasma treated samples (Figure 8.5(e)), while significantly less attached platelets were found on the heparin conjugated Ar-NH_3/H_2 plasma treated sample (Figure 8.5(f)), indicating more heparin immobilized on the surface, which is in consistent with the toluidine blue test results shown in Figure 8.4.

The effect of heparin conjugation on in vitro BAECs infiltration on PLLA microfibrous membrane was shown in Figure 8.6. It's found that while plasma treatments seem to be able to enhance cell infiltration on samples without heparin conjugation (Figure 8.6(a)-(c)), heparin conjugation can enhance cell attachment and infiltration on all samples (Figure 8.6(d)-(f)), independent on the amount of conjugated heparin. It's speculated that for in vitro cell culture, heparin on the PLLA microfibrous membrane surface can contribute to cell attachment and growth, and when the amount of heparin exceeds a critical value, the effect on cell growth is saturated, which is the case examined in this study. Therefore the improved cell attachment on the heparin conjugated untreated PLLA microfibrous membrane is contributed to the minimal amount of heparin on the surface, while the cell attachment on heparin conjugated Ar and Ar-NH_3/H_2 plasma treated surface can be contributed to surface chemical modification by plasma treatment, heparin adsorption as well as heparin conjugation.

Since surface $–NH_2$ groups are universal conjugation sites for various biomolecules, the plasma method for incorporating $–NH_2$ groups on PLLA surface described in this study is not only useful for heparin conjugation, but can also be used for conjugation of other biomolecules of interest. Besides, with a plasma treatment of commonly used gases (NH_3, Ar, H_2), the density of incorporated conjugations sites was found to be significantly higher than wet chemical methods. Therefore, this study also provides an efficient alternative method to increase functional groups on biopolymer surfaces.

8.4 Conclusions

In this chapter, Ar-NH_3/H_2 plasma treatment was used to incorporate $–NH_2$ groups onto PLLA microfibrous membrane surface for heparin conjugation. It's found that plasma power, plasma treatment time, gas composition and H_2 plasma post treatment time all affect the efficiency of incorporating $–NH_2$ groups onto PLLA surface, and moderate power, treatment time, gas composition and post treatment are conducive to increase surface $–NH_2$ group density. The surface functionalized PLLA microfibrous membrane was found being able to increase the amount of covalently immobilized heparin significantly, as well as decreasing platelets attachment in blood test. It's also found that heparin conjugation can improve in vitro BAEC infiltration on the PLLA microfibrous membrane surfaces independent on the amount of heparin immobilized for the range examined by this study.

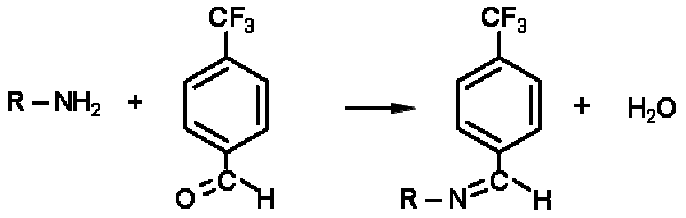

$$\frac{[NH_2]}{[C]} = \frac{[F]/3}{[C]-8[F]/3}$$

Figure 8.1. Schematic of chemical derivatization of $–NH_2$ group with TFBA on Ar-NH_3/H_2 plasma treated PLLA microfibrous membrane surface and the formula used for determination of NH_2/C ratio.

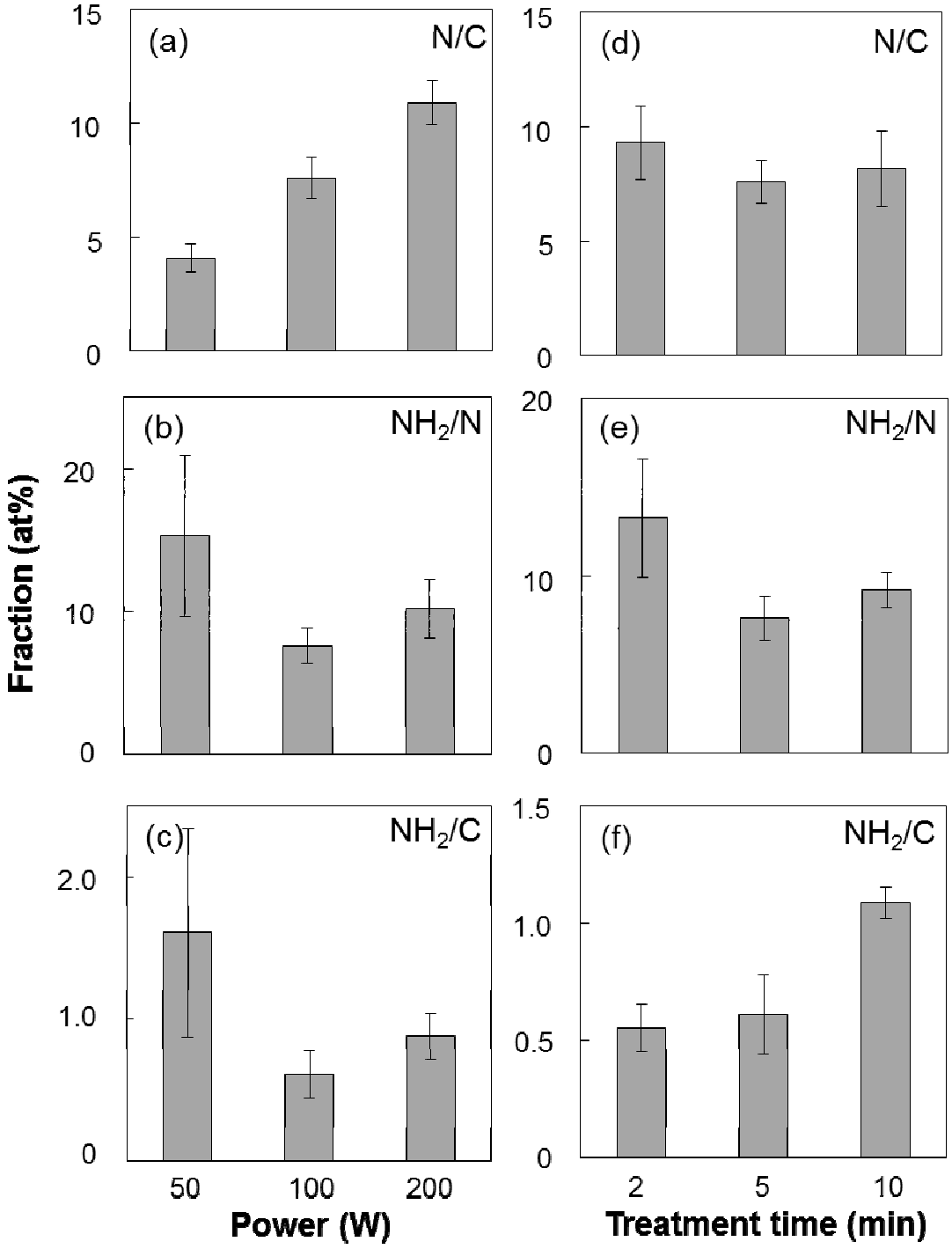

Figure 8.2. (a)-(c), effect of Ar-NH_3 plasma power on N/C, NH_2/N and NH_2/C for plasma treated PLLA microfibrous membrane; (d)-(f), effect of Ar-NH_3 plasma treatment time on N/C, NH_2/C and NH_2/C for plasma treated PLLA microfibrous membrane.

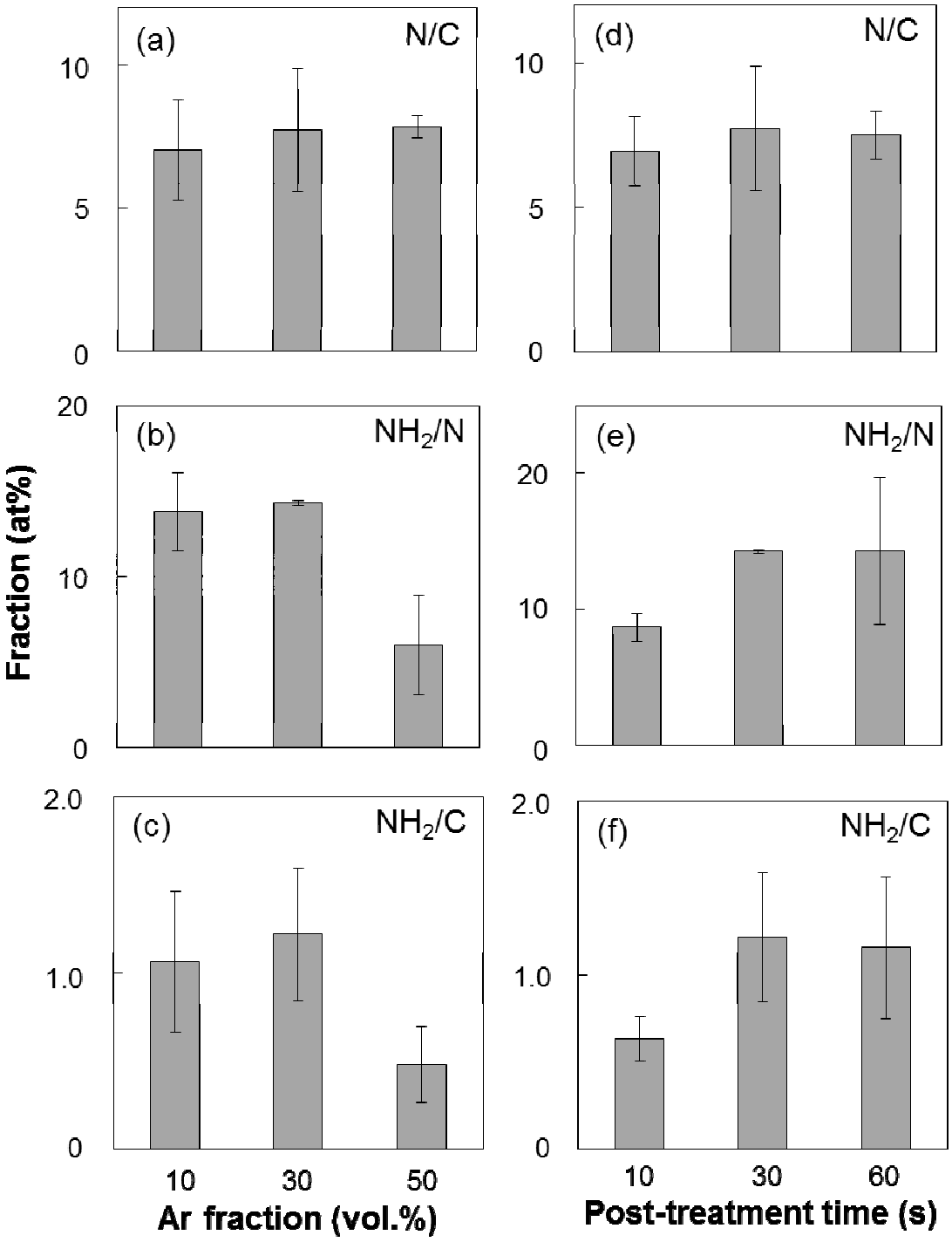

Figure 8.3. (a)-(c), effect of gas composition on N/C, NH_2/N and NH_2/C for plasma treated PLLA microfibrous membrane; (d)-(f), effect of H_2 plasma post-treatment time on N/C, NH_2/N and NH_2/C for plasma treated PLLA microfibrous membrane.

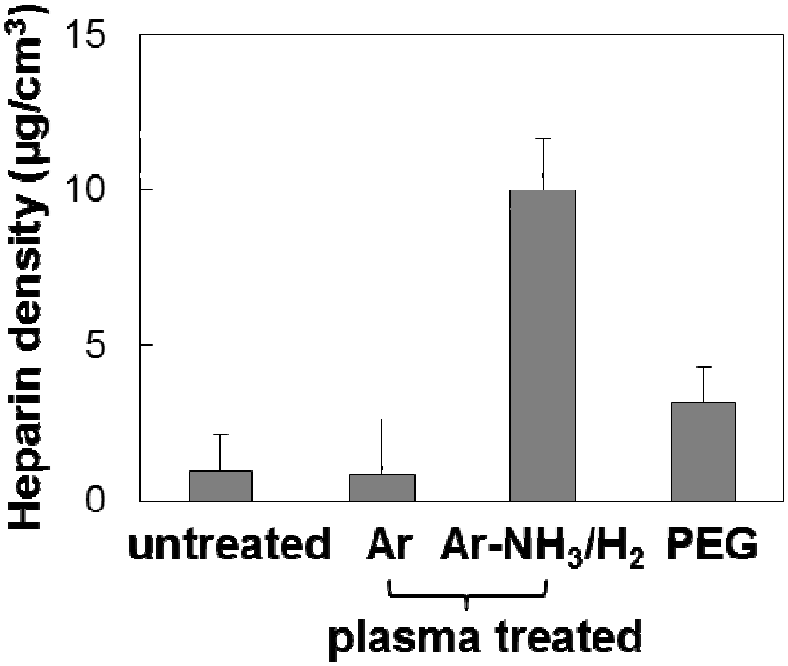

Figure 8.4. Heparin conjugation density on untreated, Ar plasma treated, Ar-NH_3/H_2 plasma treated and PEG conjugated PLLA microfibrous membrane detected with toluidine blue staining assay.

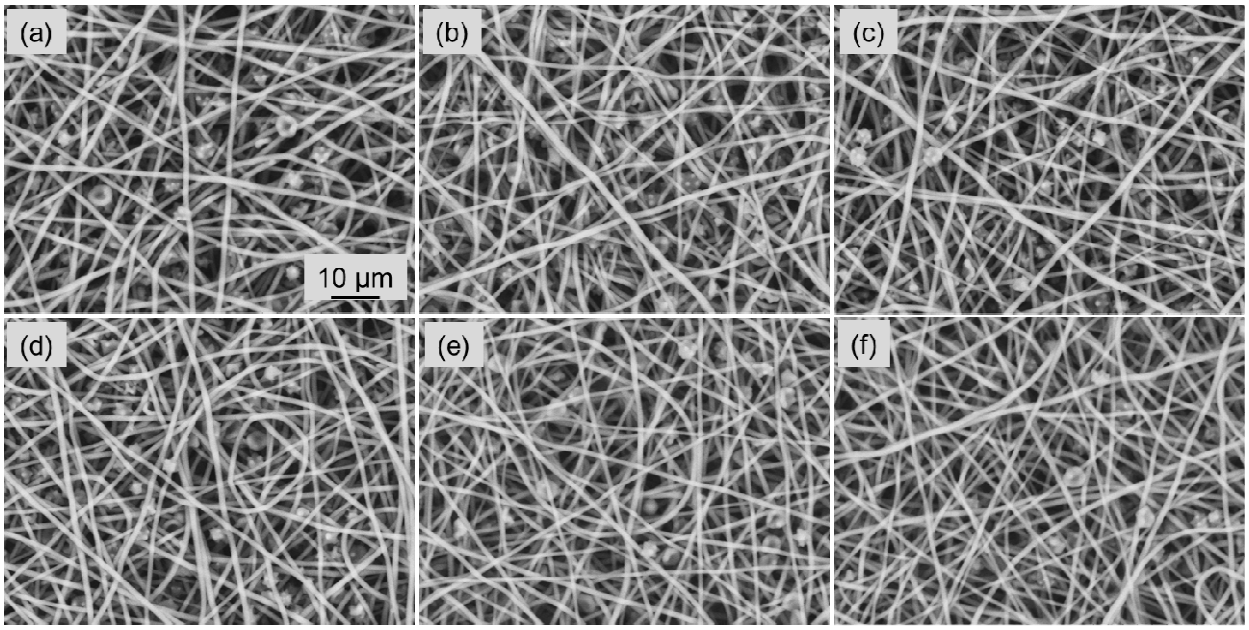

Figure 8.5. Platelets attachment on PLLA microfibrous membrane before heparin conjugation: (a) untreated, (b) Ar plasma treated, (c) Ar-NH_3/H_2 plasma treated; and after heparin conjugation: (d) untreated, (e) Ar plasma treated, (f) Ar-NH_3/H_2 plasma treated .

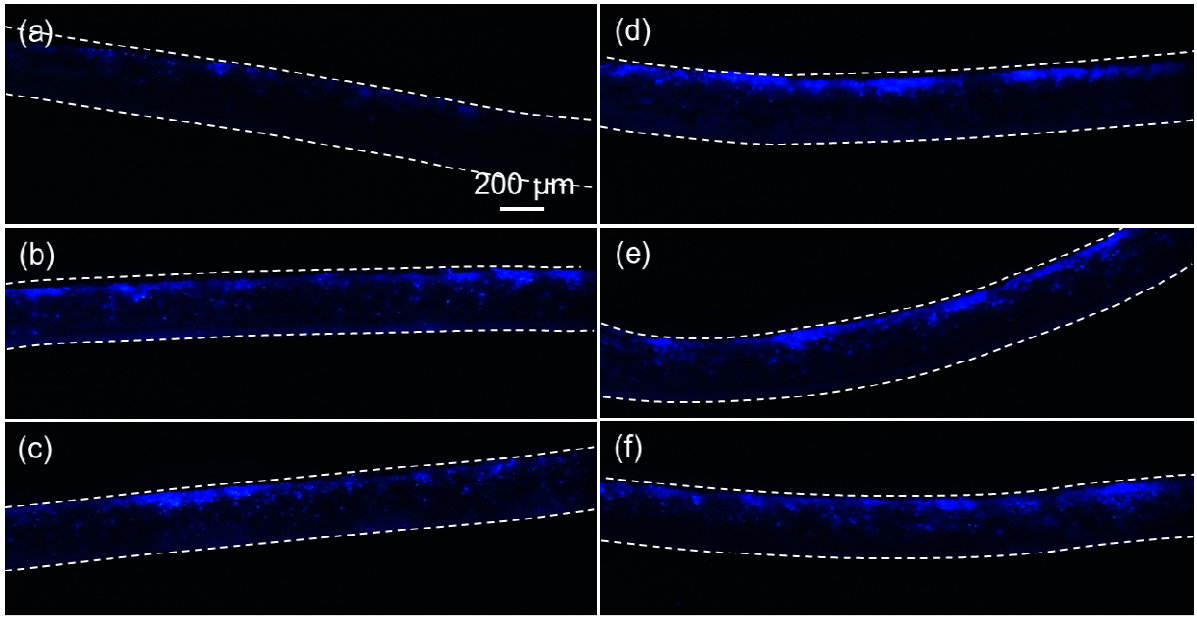

Figure 8.6. In vivo BAECs infiltration on PLLA microfibrous membrane before heparin conjugation: (a) untreated, (b) Ar plasma treated, (c) Ar-NH_3/H_2 plasma treated; and after heparin conjugation: (d) untreated, (e) Ar plasma treated, (f) Ar-NH_3/H_2 plasma treated .

Chapter 9

Control of Nanofiber Conformity and Scaffold Structure by Micropattern Geometry and Electrospinning Condition for Cell Regulation

9.1 Introduction

Electrospinning of polymer micro/nanofibers is a simple, cost-effective method for fabricating fibrous structures (Huang et al. (2003), Li et al. (2004)). Electrospinning of polymer fibrous scaffolds mimicking the structure and function of extracellular matrix has been explored for various biomedical applications (Jang et al. (2009), Lutolf et al. (2009), Wang et al. (2009), Murgan et al. (2007)), such as wound healing, drug delivery, and tissue engineering. Fibrous scaffolds with well-controlled patterned structures are of particular significance in cell biology and scaffold engineering. For example, scaffolds with aligned fibers have been reported to affect the cell behavior, such as migration, organization, and differentiation (Huang et al. (2006), Patel et al. (2007), Kurpinski et al. (2010), Zhu et al. (2011), Xie et al. (2009, 2010), Chew et al. (2008)). Scaffolds with microwell arrays are also of importance in the fabrication of uniform cell arrays (Hwang et al. (2009), Xie et al. (2011)). Moreover, fibrous structures of sufficient porosity are desirable in scaffold engineering, because porosity plays an important role in cell infiltration and tissue remodeling (Nam et al. (2007), Blakeney et al. (2011), Vaquette et al. (2011)).

Various methods have been developed to control fiber alignment (Li et al. (2004), Murugan et al. (2007)) and other types of structure. Traditionally, structures with microwell arrays have been produced by polymer molding (Hwang et al. (2009)). Despite attempts to fabricate microwells by electrospinning on templates consisting of metal spheres, controlling the size and shape of microwells has been problematic (Xie et al. (2011)). A common approach to increase the porosity of electrospun fibrous scaffolds is to incorporate sacrificial structures, such as salt grains or other porogens, which can be easily removed at a later stage; however, leaching of the sacrificial structure is often accompanied by the collapse of pores (Nam et al. (2007)).

Polymer fiber electrospinning onto special templates has been proven to be a more effective method of fabricating porous fibrous constructs with defined fiber organization (Wang et al. (2009), Blakeney et al. (2011), Vaquette et al. (2011), Li et al. (2005), Zhang et al. (2007, 2008), Li et al. (2010)). Templates with two- and three-dimensional (3D) micropatterns produced from machining metal and ice substrates (Vaquette et al. (2011), (Zhang et al. (2007, 2008), Li et al. (2010)) or metal wire networks (Wang et al. (2009), Zhang et al. (2007)) have been used to control the density and alignment of the fibers in the construct. However, these methods are slow, costly, difficult to control, and do not yield a wide range of scalable pattern geometries. To overcome these drawbacks, attempts have been made to fabricate polydimethylsiloxane (PDMS)

templates with surface micropatterns generated by photolithography (Ding et al. (2009)), but with limited success in controlling the fiber density and orientation. Controlling the fiber conformity on micropatterned surfaces is not well understood. In this chapter, a versatile method of fabricating PDMS templates with 3D micropatterns was developed, and applied to explore whether the micropattern geometry and electrospinning condition can be used to regulate fiber conformity and alignment to produce scaffolds with distinct structures that can affect the morphology, migration, and infiltration of cells.

9.2 Materials and experimental methods

9.2.1 Fabrication of nanofibrous scaffolds

Nanofibrous scaffolds were fabricated from biodegradable poly (L-lactide) (PLLA) (Lactel Absorbable Polymers, Pelham, AL) of inherent viscosity equal to 1.09 dL/g (Lactel Absorbable Polymers, Pelham, AL). PLLA pellets were first dissolved in hexafluoroisopropanol (19% w/v) in an ultrasonic water bath. The polymer solution was then delivered through a stainless steel 23G dispensing needle by a syringe pump (Huang et al. (2006), Patel et al. (2007), Kurpinski et al. (2010)).By applying a voltage of 12 kV to the needle with a high-voltage generator, electrostatically charged PLLA fibers of diameter in the range of tens of nm to ~2 μm were ejected from the charged needle toward the surface of a grounded template at a feed rate in the range of 0.2–2 mL/h. The construct produced by the polymer fibers deposited onto the template was then lifted off from the PDMS template. A flat PDMS template without any surface features was used to fabricate control samples under the same electrospinning condition. For cell studies, nanofibrous scaffolds were fabricated at a fixed feed rate of 1.0 mL/h.

9.2.2 Microanalysis techniques and sample sterilization

The pattern geometry of PDMS templates, diameter, distribution, and arrangement of the nanofibers on the micropatterned PLLA scaffolds and cross-sections of the fabricated scaffolds were examined with a field emission scanning electron microscope (SEM) (TM-1000, Hitachi, Pleasanton, CA) at an acceleration voltage of 15 kV without depositing a metal coating onto the samples before imaging. The overall nanofiber density distribution was examined with an upright microscope (Zeiss HAL 100, Carl Zeiss MicroImaging, Thornwood, NY). Cross-section samples for SEM imaging were prepared by cutting the PLLA scaffolds with a laser. Before *in vitro* cell or tissue seeding and implantation into the subcutaneous cavity of rats, the scaffolds were sterilized in 70% ethanol under ultraviolet light for 30 min and then washed 5 times with sterile phosphate buffered saline (PBS).

9.2.3 Cell culture and in vitro experiments

Human mesenchymal stem cells (hMSCs) (Lonza Walkersville, Walkersville, MD) were cultured in hMSC maintenance medium (MSCGM, Cambrex, East Rutherford, NJ) and maintained in a humidified incubator at 37ºC with 5% CO_2. Before cell seeding, scaffolds sterilized as described above were washed with sterile deionized water, coated with 1% fibronectin (Sigma-Aldrich, St. Louis, MO) for 30 min at 37ºC, and washed once with PBS.

hMSCs of density equal to ~3,000 cells/cm^2 were seeded with hMSC maintenance medium and cultured for 24 h. Then, the cells were fixed with 4% paraformaldehyde (PFA) and permeabilized with 0.5% Triton X-100. The actin structure and nuclei of hMSCs were stained with Alexa-Phalloidin 488 and 4',6-diamidino-2-phenylindole (DAPI), respectively. Fluorescence images of stained hMSCs were obtained with a confocal microscope (Zeiss LSM710, Carl Zeiss MicroImaging, Thornwood, NY) at 20X magnification and *z*-distance between cross-sections of 3□5 μm. Fluorescence signals from the entire stack were then projected onto a single plane to construct an overall image.

To examine the proliferation rate of hMSCs, scaffolds prepared as described above were seeded with a density of ~10,000 hMSCs/cm^2 in Dulbecco's modified Eagle medium (DMEM) (Invitrogen, Carlsbad, CA) supplemented with 10% fetal bovine serum (Thermo Fisher Scientific, Waltham, MA) and 1% penicillin/streptomycin antibiotic mixture. After seeding for 24 h, the cells were fixed with 4% PFA, permeabilized with 0.5% Triton X-100, blocked with 3 mg/mL bovine serum albumin (BSA) + 0.1% Triton X-100, and stained with the proliferation marker Ki67 (Abcam, Cambridge, MA) along with DAPI nuclear counterstain. Fluorescent signals were obtained with the Zeiss LSM710 confocal microscope, and positive stained hMSCs were quantified with Scion Image software (Scion, Fredrick, MD). The percentage of hMSCs that were in the active phase of the cell cycle was correlated to the proliferation rate.

For the cell migration studies, dorsal root ganglion (DRG) tissues were harvested from P4 rats and briefly maintained in neurobasal (NB) medium supplemented with B27 and 0.5 mM of L-glutamine (Invitrogen, Carlsbad, CA) prior to seeding onto the micropatterned scaffolds. The scaffolds were first sterilized and then coated with laminin (5 μg/cm^2) (Invitrogen, Carlsbad, CA) for 1 h at 37ºC and washed once with PBS before seeding. After seeding with minimal volume of supplemented NB medium, the DRG tissues were incubated for 2 h and allowed to settle and attach to scaffold surfaces. Sufficient medium was added afterwards to culture the DRG tissues on the nanofibrous scaffolds for 10 days, with the medium partially changed every 3 days. The samples were fixed after a 10-day culture with 4% PFA, permeabilized with 0.5% Triton X-100, blocked with BSA + 0.1% Triton X-100, and, subsequently, stained with anti-S-100 (β-subunit) (Sigma-Aldrich, St. Louis, MO) antibody for Schwann cells and counterstained with DAPI for cell nuclei. Fluorescence signals were obtained with the Zeiss LSM710 confocal microscope at 10X magnification and *z*-distance between cross-sections of 4□6 μm. Fluorescence signals from the entire stack were then projected onto a single plane to construct an overall image.

9.2.4 In vivo cell infiltration

Micropatterned PLLA scaffolds were cut into 0.5 × 0.5 cm^2 samples, and 3 samples of each group were implanted into the subcutaneous cavity of Sprague-Dawley rats (Charles River Laboratories, Wilmington, MA) for 7 days using the following procedure. First, the rats were anesthetized with isofluorane and the incision sites were marked and disinfected with 70% ethanol. Then, incisions were made on the wall of the lower abdominal region, and PLLA scaffolds with different micropatterns were implanted into the incision sites and tucked subcutaneously away from the incision, with the back side of the scaffolds facing the muscle side. Cuts were sewed with interrupted 5-0 Monocryl (Ethicon, Somerville, NJ) mattress sutures.

All animals were monitored daily, with no adverse incidents observed with any of them. The rats were returned to the operating room on the seventh day, where they were given general anesthesia and an overdose of euthanasia solution. Then, the implants with the attached surrounding tissue were removed and embedded in an optimal-cutting-temperature compound (TissueTek, Elkhart, IN) that was placed on dry ice. Transverse cross-sections of thickness equal to 12 μm were obtained with a cryosectioner at □20ºC, fixed with 4% PFA, stained with DAPI, and examined under a microscope (TE 300, Nikon, Melville, NY).

9.3 Results and discussion

9.3.1 Template fabrication for scaffold micropatterning

Figure 9.1 shows the fabrication process of the conductive PDMS templates used in this study. The back side of a ~525-μm-thick p-type Si(100) wafer having both of its sides coated with a ~0.6-μm-thick SiN layer was spin coated with a 4-μm-thick layer of OCG 825 photoresist (PR) (Figure 9.1a). After exposure to UV light through the windows of a Cr mask (Figure 9.1b) (Karl Suss MA6 Mask Aligner, Karl Suss America, Vermont, USA) and development, the micropattern was transferred to the PR (Figure 9.1c) and then to the SiN layer at the back side of the wafer by reactive ion etching (Figure 9.1d) (Technics PE II-A, Plasma Equipment Technical Services, Livermore, CA). After stripping the PR (Figure 9.1e), the exposed Si was etched to a depth of ~500 μm in 30% KOH at 85^0C (Figures 9.1f1 and 1f2), and the SiN layer was etched away by immersing the wafer into a bath of 49% HF for 2 h (Figure 9.1g). Then, the master wafer was exposed to perfluoro-1,1,2,2-tetrahydrooctyl-trichlorosilane (United Chemical Technology, Bristol, PA) vapor in a desiccator overnight to prevent PDMS adhesion. A mixture (10:1) of Sylgard 184 silicone elastomer components (Dow Corning, Midland, MI) was transferred onto the master wafer (Figure 9.1h) and cured at 65^0C overnight to fabricate a micropatterned PDMS template (Figure 9.1i). To increase the conductivity of the PDMS template, carbon black (Vulcan XC-72R, Fuel Cell Store, Boulder, Colorado) was introduced into the silicone mixture (12.5% w/v). Because the mixture was highly viscous, the master wafer was placed in vacuum for 1h to allow the mixture to completely fill up the features on the wafer surface before curing.

Depending on the width of the SiN layer between adjacent surface features, different structures were produced on the master wafer by KOH wet etching (Figures 9.1f1and 1f2), which were then transferred to the PDMS templates. For relatively wide SiN layer between nearby features, KOH anisotropic etching of Si(100) yielded micropatterns of rectangular pyramids of sidewall slope equal to 54.7º with respect to the surface plane (Figure 9.1f1). However, in the case of a relatively narrow SiN layer, undercutting during KOH etching in the Si(111) direction and high etching rates in both Si(100) and Si(110) directions produced rectangular pyramids with double-slope sidewalls (Figure 9.1f2). Thus, by varying the width of the SiN layer between micropattern features along each in-plane direction, different micropattern geometries were etched on the Si(100) wafer and then transferred to the molded PDMS templates. The etching mode shown in Figure 9.1f1 produced PDMS templates with taller pyramids (posts) possessing steep single-slope sidewalls, whereas the etching mode shown in Figure 9.1f2 yielded PDMS templates with shorter pyramids of less steep double-slope sidewalls.

In-plane cross-section schematics of PDMS templates with micropatterns of different dimensions are shown in Figures 9.2a–2c, with corresponding SEM micrographs shown in Figures 9.2d–2i. Molds with cross-sections in both in-plane directions similar to those shown in Figures 9.1f1 and 1f2 produced micropatterned templates consisting of rectangular pyramids with steep single-slope sidewalls (Figures 9.2a, 2d, and 2g) and shallow double-slope sidewalls (Figures 9.2b, 2e, and 2h), respectively. However, molds with cross-sections similar to that shown in Figure 9.1f1 in one direction and similar to that shown in Figure 9.1f2 in the other direction produced micropatterned templates with prismatic pyramids having steep single-slope and shallow double-slope sidewalls in corresponding directions (Figures 9.2c, 2f, and 2i).

9.3.2 Surface and through-thickness structure of micropatterned scaffolds

Figure 9.3 shows PLLA scaffolds fabricated from PDMS templates with different micropatterns. Figures 9.3a1, 3b1, and 3c1 show, schematically, how the PLLA nanofibers conformed onto the micropattern features of the PDMS templates, whereas Figures 9.3a2–3c3 and 3a4–3c6 show SEM micrographs of the back side (facing the PDMS templates) and front side of the fabricated scaffolds, respectively. The template with tall pyramids of steep single-slope sidewalls (Figures 9.2d and 2g) produced scaffolds conformal to the template micropattern only at the top of the tall pyramidal posts (Figure 9.3a1). These scaffolds comprised small and shallow microwells with dense nanofibrous structures, surrounded by arrays of less dense and aligned nanofibers (Figures 9.3a2 and 3a3). The template with short pyramidal posts exhibiting shallow double-slope sidewalls (Figures 9.2e and 2h) produced scaffolds conformal to the template features except at the bottom of the microwells (Figure 9.3b1). These scaffolds consisted of uniformly distributed pyramidal microwells of densely packed nanofibers, surrounded by narrow rectangular arrays of relatively less closely-packed nanofibers aligned perpendicular to array sides (Figures 9.3b2 and 3b3). Scaffolds made with the template that had different micropattern geometries along the in-plane directions (Figures 9.2f and 2i) exhibited features that were combinations of those on the scaffolds fabricated from the templates shown in Figures 9.2a and 2b. The nanofibers of these scaffolds were densely packed along the short post/small sidewall slope direction and aligned along the tall post/high sidewall slope direction (Figures 9.3c2 and 3c3). Figures 9.3a4–3c6 show the front sides of PLLA scaffolds fabricated with different templates for different deposition times. Increasing the deposition time from 1 to 4 min had a negative effect on the micropattern transfer to the front side of the scaffolds, resulting in more randomly oriented nanofibers than those at the back side, especially for thicker scaffolds, i.e., 4 min deposition time (Figures 9.3a6, 3b6, and 3c6). Thus, scaffolds fabricated with the present method possessed heterogeneous through-thickness structures.

Fiber electrospinning on an electrically conductive template containing post structures results in preferential fiber deposition over the posts due to the higher electrostatic forces applied to the nanofibers at the tops of the posts than in any other region of the template surface (Zhang et al. (2007)). Both nanofiber deposition and alignment were found to depend on the overall post geometry (i.e., post height and sidewall slope) and, presumably, the distance between posts. However, because the feature distance was similar in all templates, nanofiber deposition and alignment demonstrated a dependence only on post height and sidewall slope (Figures 9.2a–2c). In particular, nanofiber deposition at the tops of the posts and alignment in the areas between posts was only observed with relatively tall posts of large sidewall slope (Figure 9.3a1), whereas

for short posts with shallow double-slope sidewalls, nanofiber deposition occurred in dense configurations over the entire post surface, closely following the surface micropattern of the template (Figure 9.3b1).

Nanofiber deposition and conformity strongly depend on the magnitude of the electrostatic force between the nanofibers and the template. The scaffolds shown in Figure 9.3 indicate that low posts with small sidewall slopes resulted in high electrostatic forces that enhanced the nanofiber conformity with the micropatterned template surface. Under these conditions, conformal nanofiber deformation resulted in full coverage of the entire post structure by densely packed nanofibers, except at the bottom of microwells where less dense nanofibrous structure was obtained. Alternatively, for templates having tall posts with steep sidewalls, the pattern geometry could not be fully accommodated by nanofiber deformation between the posts due to the significant changes in feature dimensions as well as the weaker electrostatic force in those regions, resulting in nanofiber bridging and, in turn, alignment in areas between the posts. For the template features examined in this study, the critical post height for full coverage of the posts by the nanofibers was found to be between 325 and 375 μm. Moreover, because the overall electrostatic force exerted to the nanofibers decreases with the increase of the scaffold thickness due to the repulsive force exerted by deposited nanofibers carrying the same type of charge, more random and dense nanofibers were obtained with thicker scaffolds, as evidenced by the progressive decrease in contrast of the nanofiber structures shown in Figures 9.3a4-3c6.

Figure 9.4 shows optical microscopy photographs of PLLA nanofibrous scaffolds fabricated from PDMS templates with different micropatterns. Back and front sides of these scaffolds are shown in Figures 9.4a–4c and Figures 9.4d–4f, respectively. Differences in brightness may be associated with local variations in nanofiber density. Tall posts with steep single-slope sidewalls produced dense nanofibrous structures only over the posts, and less dense structures consisting of aligned nanofibers between the posts (Figures 9.4a and 4d). However, low posts with shallow double-slope sidewalls were fully covered by dense nanofibrous structures (Figures 9.4b and 4e), while posts with different post heights and sidewall slopes in the in-plane directions produced hybrid scaffolds (Figures 9.4c and 4f).

The scaffold cross-sections shown in Figure 9.5 provide further insight into the effect of surface micropatterning on the through-thickness scaffold structure. While the structure of the flat (control) scaffold does not show significant variation through the thickness (Figure 9.5a), micropatterned scaffolds show significant spatial variation in nanofiber density. Specifically, posts with steep sidewalls demonstrate densely deposited nanofibers over the posts and nanofiber bridging between the posts (Figures 9.5b and 5c), while posts with small sidewall slopes show dense nanofiber deposition over the whole posts except at the bottom of the scaffold (Figure 9.5c). In addition, the increase of the scaffold thickness produced gradual changes in nanofiber organization through the scaffold thickness (Figures 9.5b–5d). As shown in Figures 9.5b and 5d, the scaffolds comprise heterogeneous porous structures of nanofibers loosely aligned at the back side and densely packed and randomly oriented nanofibers at the front side. A comparison of the nanofibrous structures shown in Figure 9.5 shows that micropatterned PLLA scaffolds may exhibit higher porosity (Figure 9.5c) or both higher porosity and nanofiber alignment (Figures 9.5b and 5d) compared to flat PLLA scaffolds (Figure 9.5a).

To examine the dependence of scaffold structure on nanofiber deformability, for a given template, nanofiber electrospinning on the template with tall posts and steep single-slope sidewalls was carried out at different solution feed rates and voltage fixed at 12 kV. High-resolution SEM images of nanofibers electrospun onto a flat region of this template at a feed rate of 0.2, 0.5, and 2.0 mL/h are shown in Figures 9.6a, 6b, and 6c, respectively. The observed gradual increase in average nanofiber diameter with increasing feed rate is consistent with a previous study (Fridrikh et al. (2003)). Figures 9.6d–6f show that the increase in nanofiber diameter resulted in less post area coverage by the nanofibers and shallower microwells. The depths of the microwells shown in Figures 9.6g, 6h, and 6i are approximately equal to 270, 230, and 190 μm, respectively. This trend can be attributed to the increase of the solution volume charge with the decrease of the feed rate (Fridrikh et al. (2003)), resulting in thinner nanofibers that deformed easily to conform to the micropattern features and a higher attractive force between charged nanofibers and the grounded template. Therefore, the decrease in feed rate enhanced the nanofiber conformity with the micropatterned template surface, leading to more post area coverage by a dense nanofiber structure and deeper microwells (Figures 9.6g–6i).

9.3.3 Effect of scaffold micropattern on cell morphology and organization

Figure 9.7 shows the effect of scaffold micropattern on the actin morphology and alignment and the proliferation rate of hMSCs. The control sample (Figure 9.7a) and the micropatterned scaffold with microwell arrays characterized by randomly oriented nanofibers (Figure 9.7c) do not show actin alignment with the nanofibers. In contrast, actin alignment along the nanofiber direction is observed on scaffolds demonstrating nanofiber alignment at specific surface regions (Figures 9.7b and 7d). However, these scaffolds did not yield significant differences in the proliferation rate of hMSCs (Figure 9.7e). Differentiation of hMSCs into osteogenic and adipogenic lineages also showed insignificant differences (data not shown).

In addition to demonstrating that the PLLA scaffolds with different topographic structures affected the morphology of hMSCs, the effect on cell migration was examined by using isolated DRG tissues (Figure 9.8). On the flat (control) scaffold, Schwann cell migration was confined mainly within the immediate region surrounding the DRG tissue, not showing any particular directionality due to the random orientation of nanofibers and the high nanofiber density (Figure 9.8a). In contrast, Schwann cell migration from the DRG tissue was significantly enhanced on micropatterned scaffolds possessing 3D structures, with a much larger area around the DRG tissue covered by Schwann cells (Figures 9.8b–8d). Since the density and alignment of the nanofibers in the microwell scaffold shown in Figure 9.8c was not significantly different from that of the control scaffold, it may be inferred that the 3D structure was conducive to Schwann cell migration out of the DRG tissue. Although cells were more closely concentrated around the DRG tissue in the case of the scaffold with microwell structures and random dense nanofiber structure (Figure 9.8c), cells on the scaffolds with aligned and more porous structures exhibited more uniform distribution over the regions consisting of aligned and less dense nanofibers (Figures 9.8b and 8d), suggesting that low-density micropatterned scaffolds with nanofiber alignment are conducive to cell migration.

9.3.4 Effect of scaffold micropattern on cell infiltration

Figure 9.9 shows cross-sections revealing *in vivo* cell infiltration in different PLLA nanofibrous scaffolds. Images of characteristic cross-sections are shown for each micropatterned scaffold. In the case of the control sample consisting of a dense structure of randomly oriented nanofibers, cell infiltration through the scaffold thickness was limited, with the cells mostly confined within the near-surface region (Figure 9.9a). However, the micropatterned scaffold shown in Figure 9.9b shows increased cell infiltration from both sides in less dense regions exhibiting nanofiber alignment (Figure 9.9b(A-A)), as opposed to limited cell infiltration in the small microwells possessing a dense nanofiber structure at the back side of the scaffold (Figure 9.9b(B-B)). For the micropatterned scaffold shown in Figure 9.7c, back-side cell infiltration through the cross-section of the microwells (Figure 9.9c(A-A)) is as low as in the control sample, whereas cell infiltration through the cross-section of the regions between microwells (Figure 9.9c(B-B)) is higher; however, these regions represent a very small fraction of the total scaffold surface area. Similar results were obtained with the scaffold shown in Figure 9.7d. High cell infiltration in less dense regions with aligned nanofibers (Figure 9.9d(A-A)), similar to what is shown in Figure 9.9b(A-A), and low cell infiltration in regions of randomly oriented dense nanofibers, especially at the back side of the scaffold (Figure 9.9d(B-B)), similar to what is shown in Figure 9.9c(A-A). In general, more uniform and deeper cell infiltration occurred in scaffold regions characterized by less dense and aligned nanofibers (Figures 9.9b(A-A), 9c(B-B), and 9d(A-A)), while regions of densely packed and randomly oriented nanofibers confined the cells at the surface (Figures 9.9a, 9b(B-B), 9c(A-A), and 9d(B-B)). Despite the higher nanofiber density at the front side of the micropatterned scaffolds than at the region with aligned nanofibers at the back side (Figure 9.5), the cell infiltration results shown in Figures 9.9(b)–9(c) indicate an enhancement of cell infiltration *in vivo*.

9.4 Conclusions

In this chapter, silicon wet etching and PDMS molding techniques were combined to produce micropatterned templates, which were subsequently used to fabricate nanofibrous PLLA scaffolds by electrospinning. To control the nanofiber conformity, scaffolds with significantly different nanofibrous structures were obtained by varying the geometry of micropattern features on the PDMS templates and the electrospinning parameter. Because silicon wet etching and PDMS molding are versatile fabrication techniques, PDMS templates with a wide range of micropatterns can be fabricated with the present method. The results of this study indicate that the present method can easily be used to fabricate nanofibrous structures with different characteristics, including nanofiber alignment, locally high/low porosity (density), and microwells of different dimensions for a variety of biological applications. It was also shown that the fabricated micropatterned nanofibrous scaffolds can significantly affect the cell morphology and enhance cell migration *in vitro* and cell infiltration *in vivo* for potential cell and tissue engineering applications.

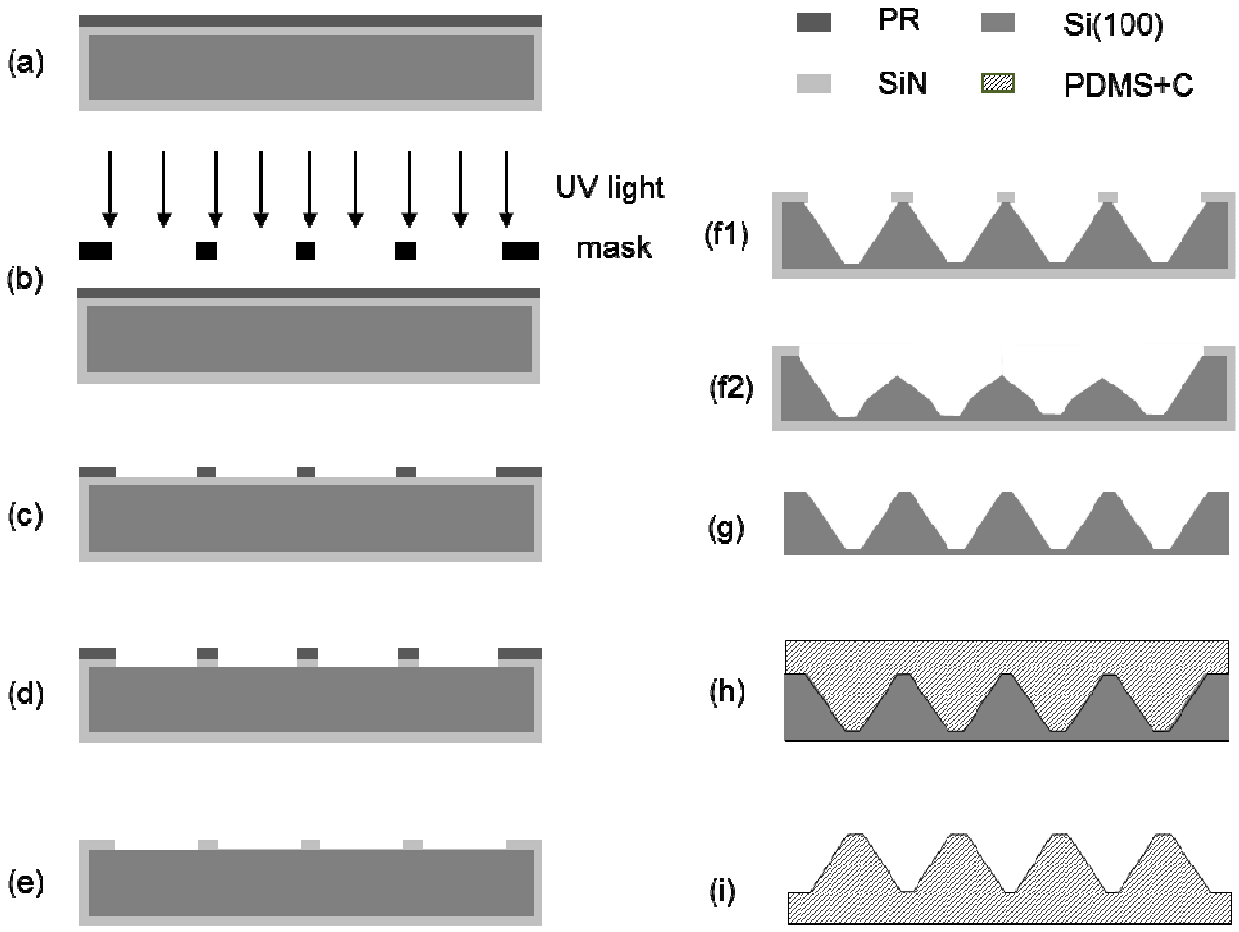

Figure 9.1. Schematic of the PDMS template fabrication process: (a) spin coating of the back side of a SiN-coated Si(100) wafer with PR, (b) PR exposure to UV light, (c) PR development, (d) removal of the exposed SiN layer by RIE, (e) PR stripping, (f1,f2) wet etching with 30% KOH, (g) removal of the SiN layer in (f1) by wet etching with 49% HF, (h) molding of the conductive (12.5% w/v carbon black in silicon mixture) PDMS template using the master wafer shown in (g), and (i) lift-off of the PDMS template produced from the master wafer shown in (g).

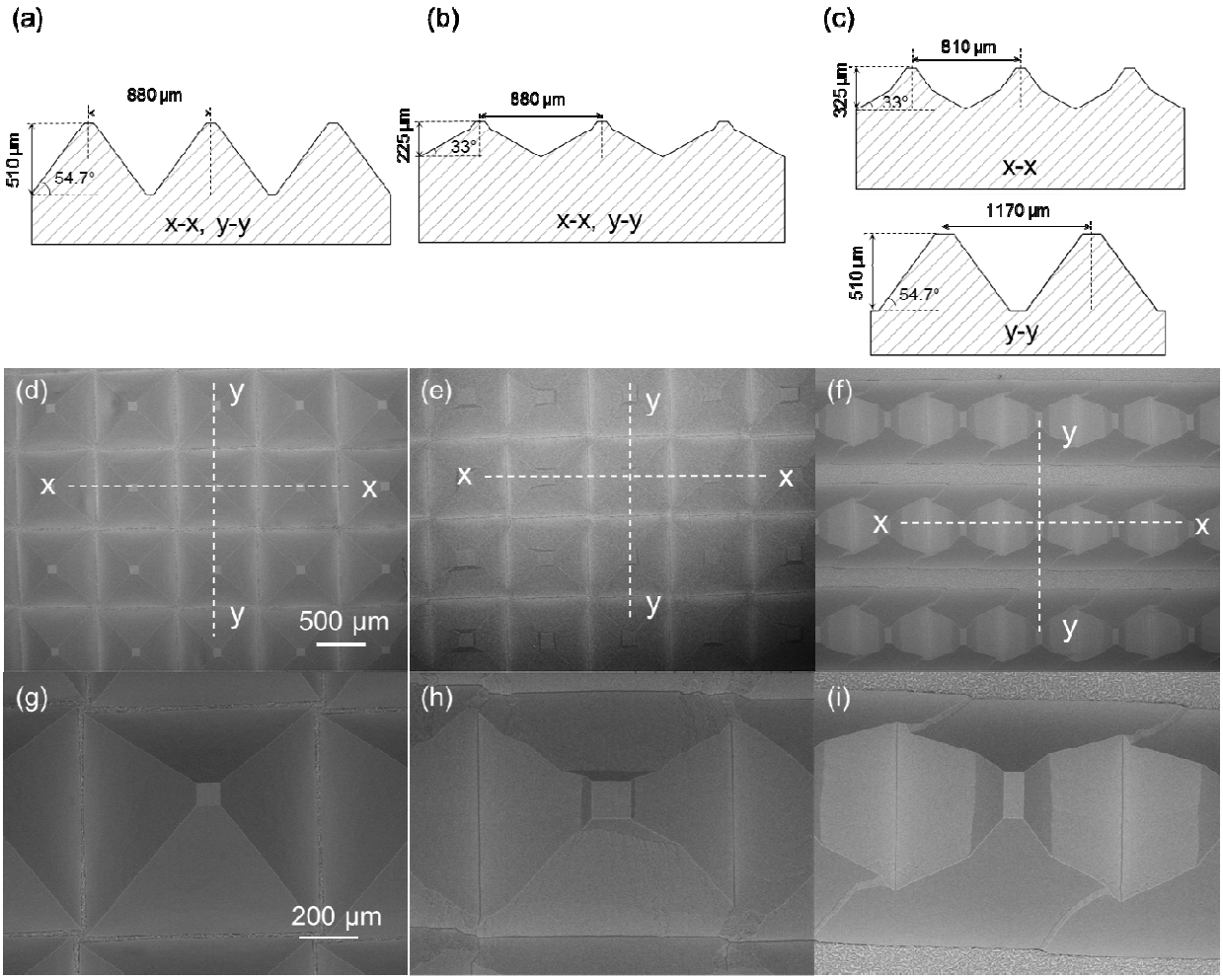

Figure 9.2. (a–c) Schematics and dimensions of PDMS templates with single- and double-slope pyramidal features, and (d–i) SEM micrographs of templates with different surface micropatterns.

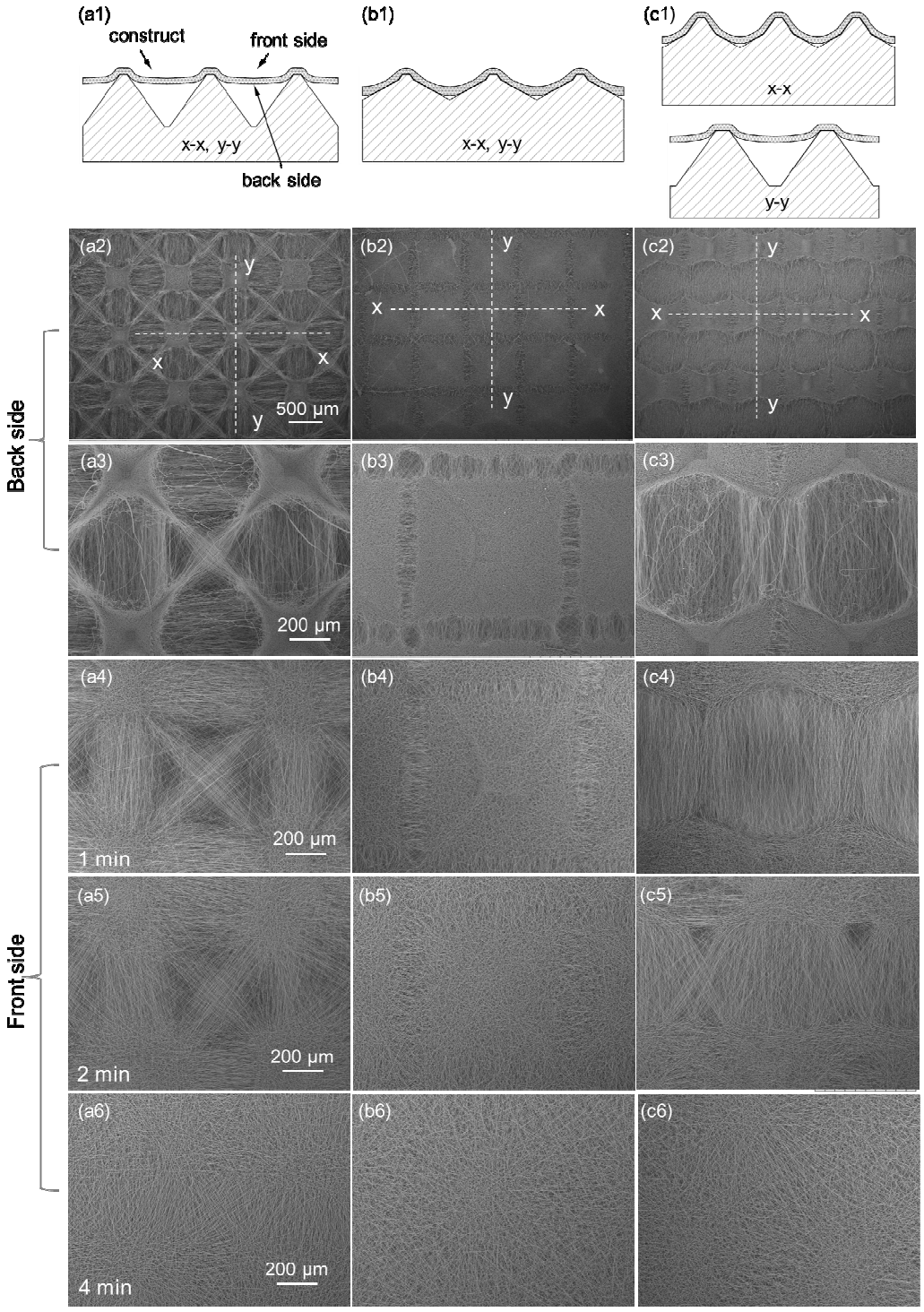

Figure 9.3. Effects of the template micropattern and deposition time on nanofiber surface coverage and alignment: (a1, b1, and c1) schematics of PLLA nanofiber deposition on PDMS templates with different micropatterns, and SEM micrographs of the (a2–c3) back side and (a4–c6) front side of PLLA nanofibrous scaffolds.

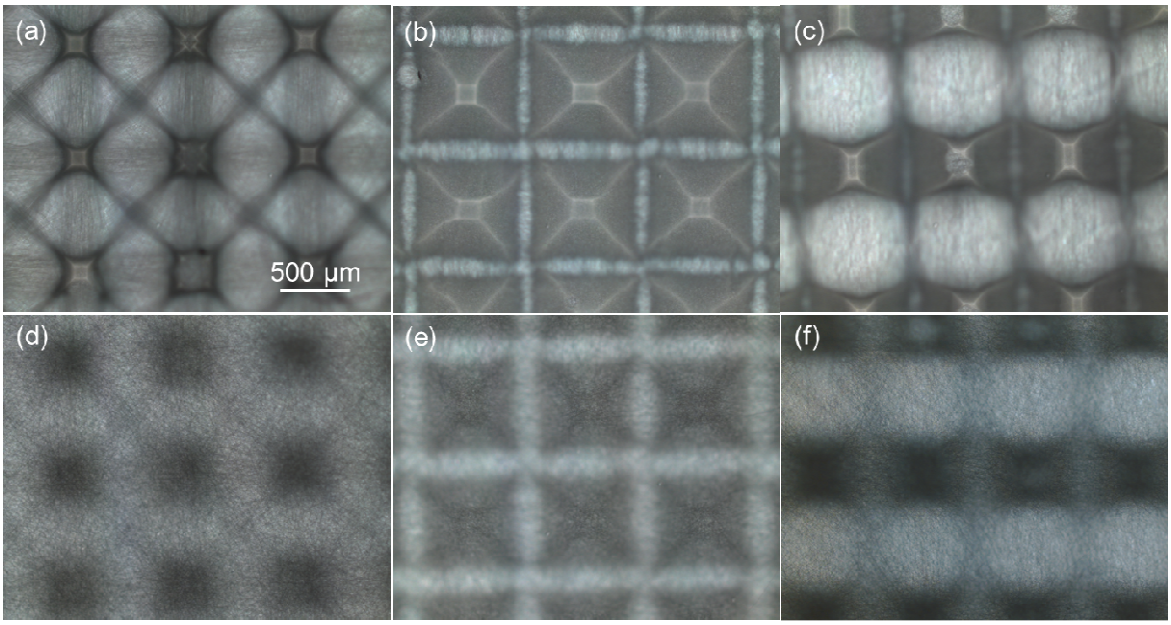

Figure 9.4. Optical photographs of PLLA nanofibrous scaffolds produced from PDMS templates with different micropatterns: (a–c) back side and (d–f) front side of micropatterned scaffolds.

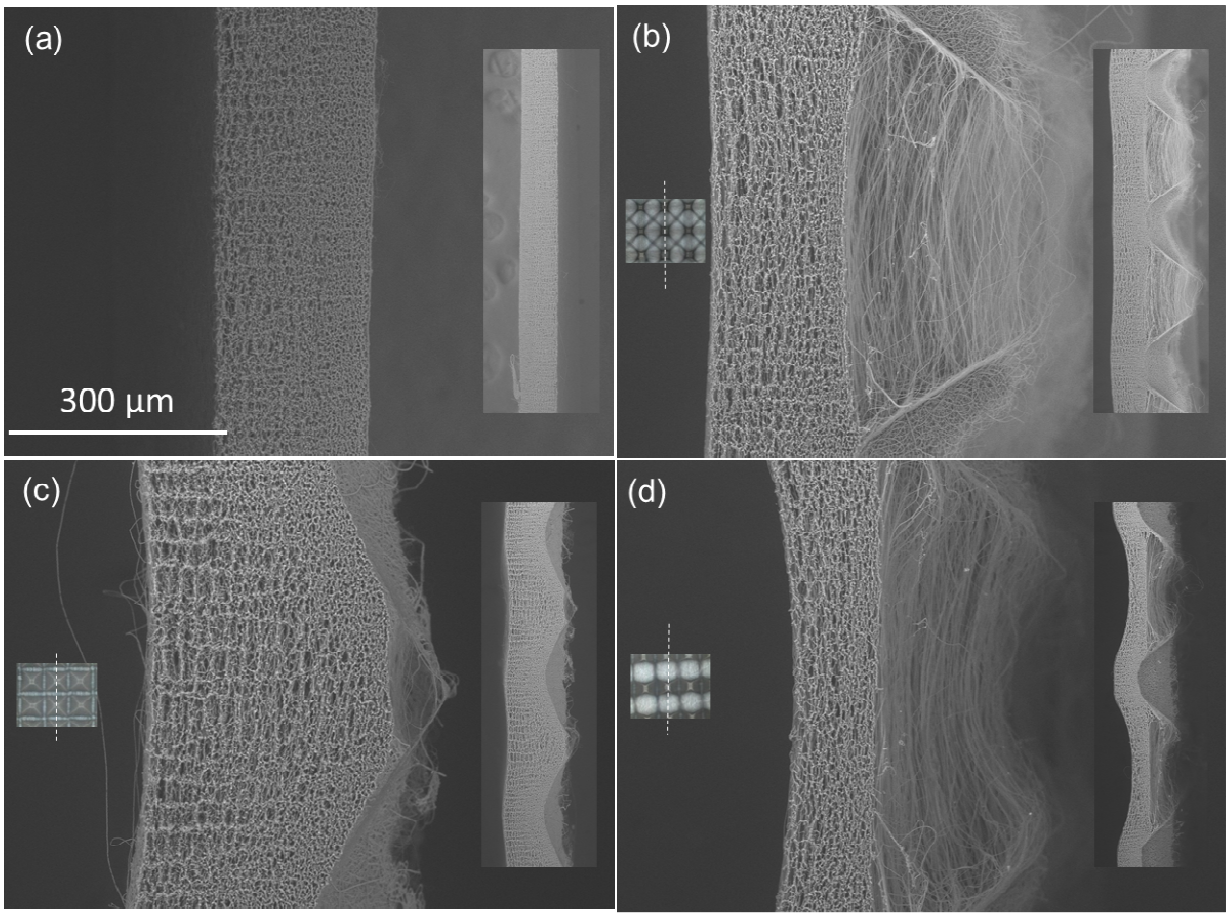

Figure 9.5. Cross-section SEM images of PLLA nanofibrous scaffolds fabricated from (a) flat (control) and (b–d) patterned PDMS templates. Insets on the left show corresponding optical images of the scaffolds and the laser cutting line (dot line in the images), whereas insets on the right show lower magnification images of scaffold cross-sections. The right side of the scaffolds was in contact with the PDMS template.

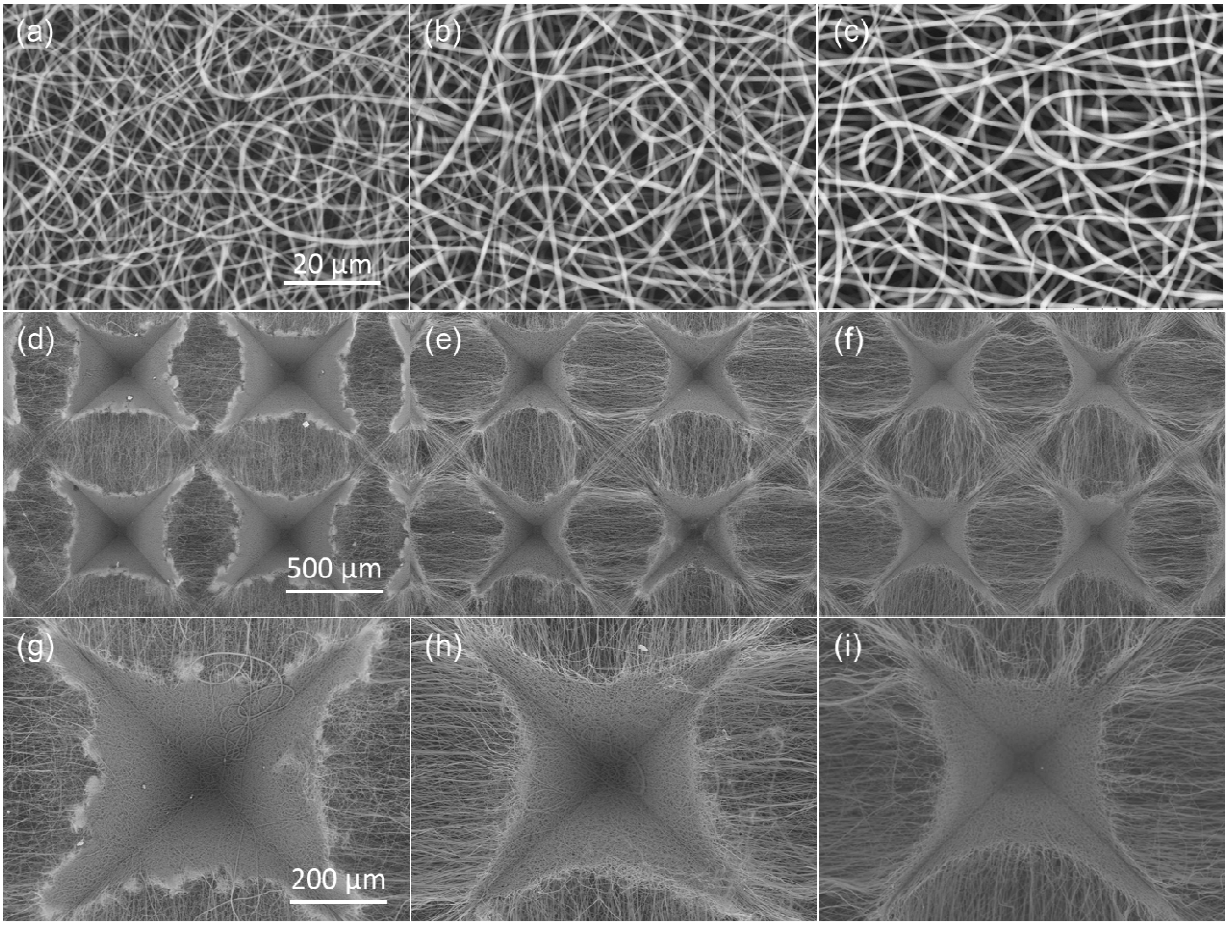

Figure 9.6. Effects of the feeding rate of PLLA solution on the micropattern of electrospun PLLA scaffolds: (a–c) PLLA nanofibers deposited on flat PDMS templates, (d–f) SEM images of PLLA nanofibrous scaffolds fabricated from templates with single-slope pyramidal posts, and (g–i) high-magnification SEM images of the scaffolds shown in (d–f) illustrating the formation of individual microwells. Nanofiber electrospinning was carried out at a feed rate of (a,d,g) 0.2, (b,e,h) 0.5, and (c,f,i) 2 mL/h.

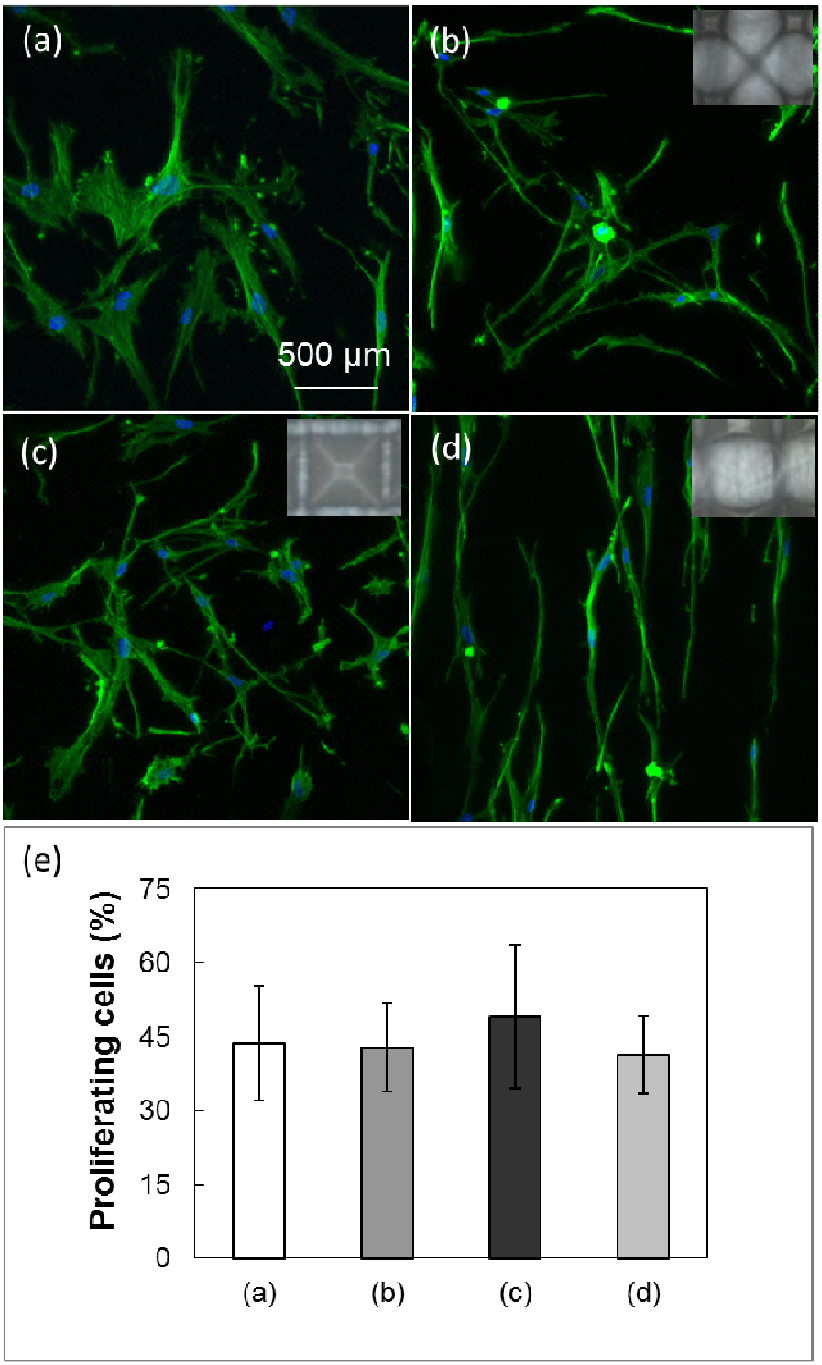

Figure 9.7. (a–d) Morphology and (e) proliferation rate of hMSCs after *in vitro* culture on PLLA nanofibrous scaffolds for 24 h: (a) flat (control) scaffold with dense randomly oriented nanofibers and (b–d) scaffolds micropatterned with different PDMS templates. The inset in (b–d) shows an image of the corresponding micropatterned scaffold surface. Letter symbols on the horizontal axis of the figure shown in (e) correspond to hMSCs shown in (a) through (d), respectively.

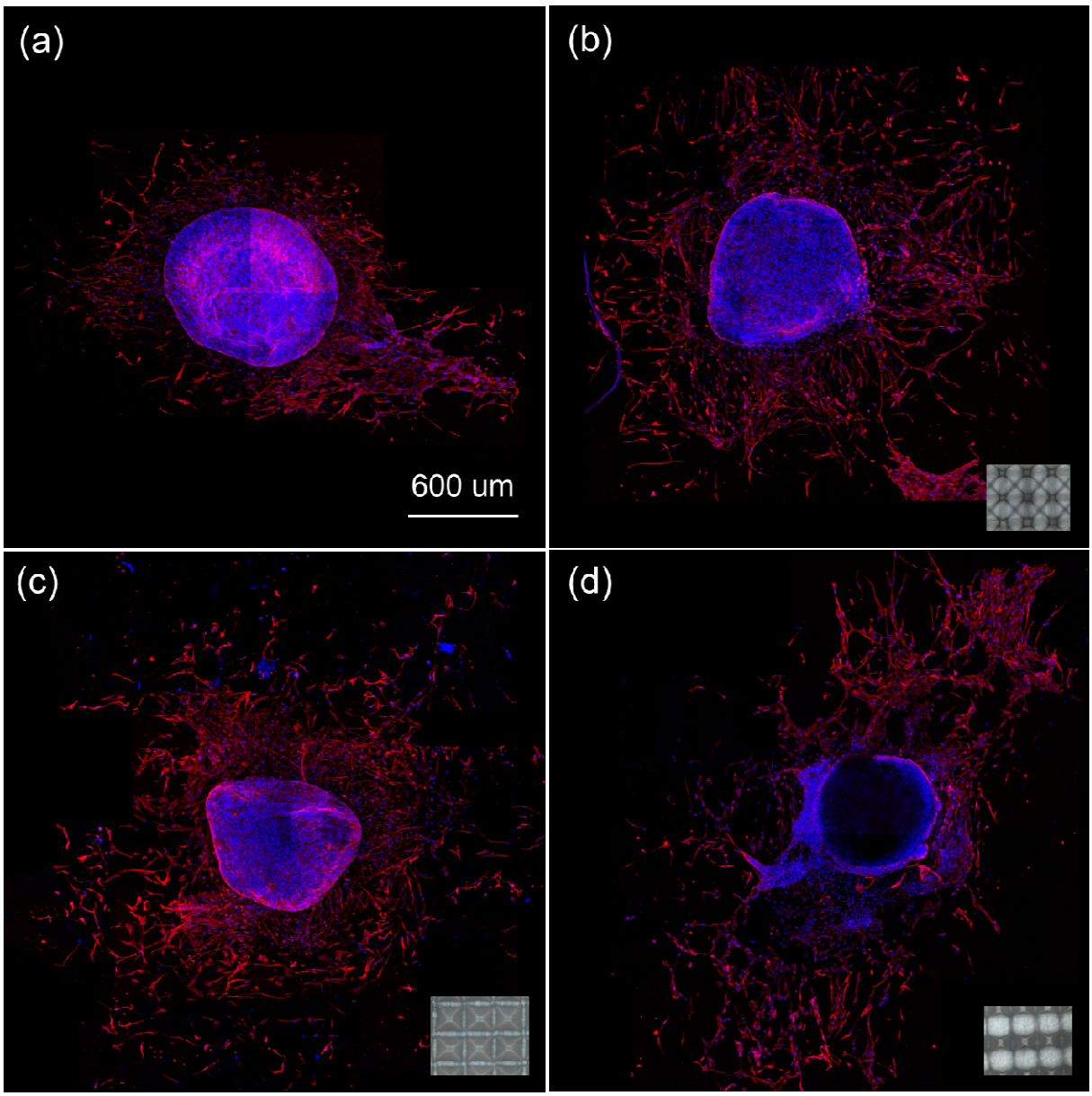

Figure 9.8. In vitro migration of Schwann cells (red staining for S100β) on (a) a flat (control) PLLA scaffold and (b–d) PLLA nanofibrous scaffolds fabricated from PDMS templates with different micropatterns. Insets show corresponding optical images of micropatterned scaffolds.

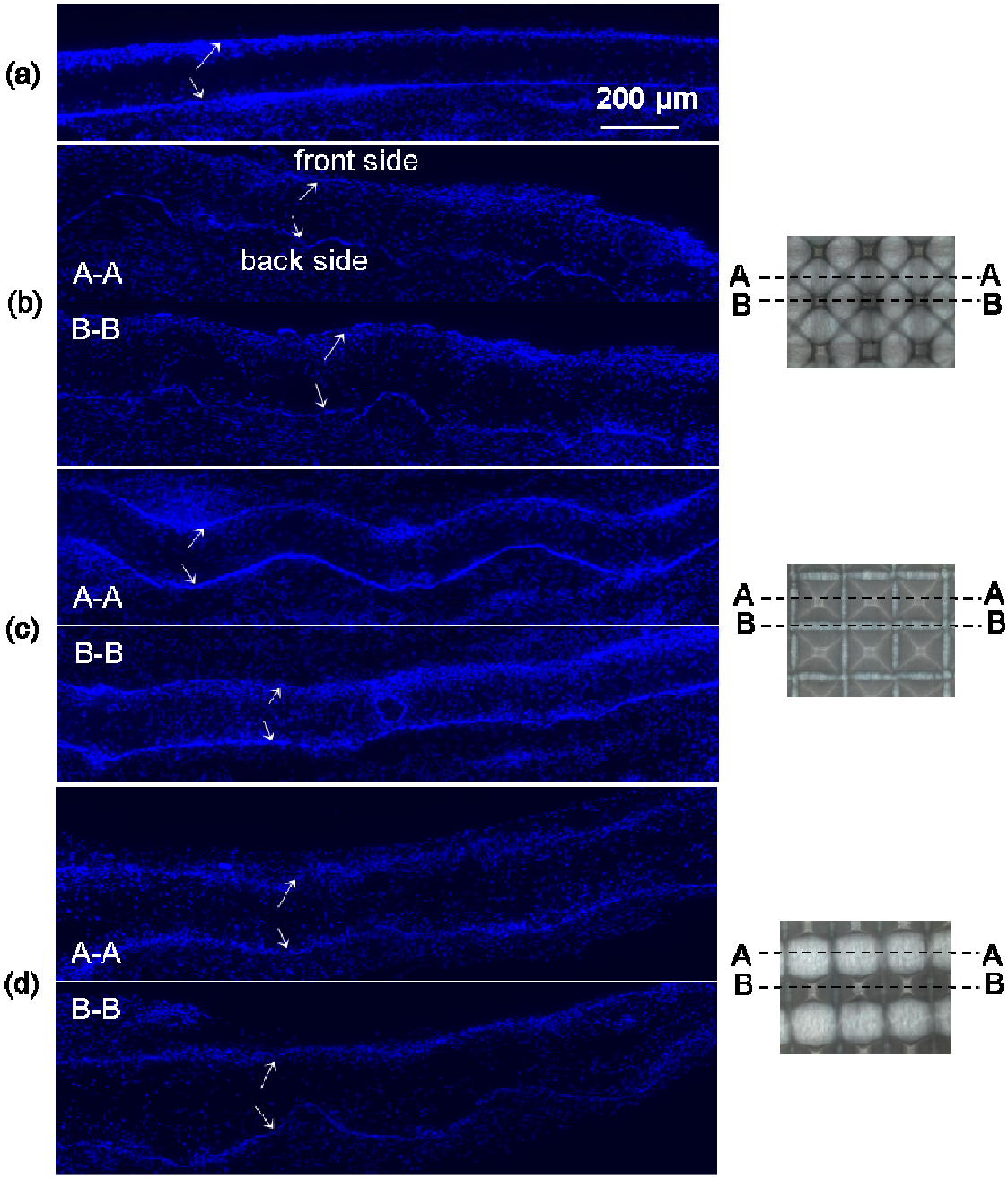

Figure 9.9. Cross-sections of PLLA nanofibrous scaffolds showing in vivo cell infiltration after implantation in the subcutaneous cavity of rats for 7 days: (a) flat (control) scaffold with dense randomly oriented nanofibers and (b–d) scaffolds micropatterned with different PDMS templates. Arrows point to the top (front side) and bottom (back side) boundaries of scaffolds. Images on the right show cross-sections A-A and B-B corresponding to the fluorescence images of each micropatterned scaffold in (b–d).

Chapter 10

Conclusions and Future Directions

10.1 Conclusions

10.1.1 Plasma assisted polymer surface modification

In this thesis, different plasma treatments for biopolymer surface modifications were investigated for various applications. Plasma polymerization and deposition of fluorocarbon (FC) films (Chapter 3) and polyethylene glycol (PEG)-like films (Chapter 4) were considered for bulk biopolymers. FC film deposition on Ar plasma-treated low-density polyethylene (LDPE) and physical/mechanical property studies showed that plasma treatments can modify the surface topography and mechanical properties of LDPE significantly and, therefore, provide a method to increase the surface shear strength while maintaining a low friction coefficient. Plasma deposition of PEG-like films using diethylene glycol dimethyl ether (diglyme) monomer was proven an effective means of functionalizing different substrate surfaces to become bio-nonfouling, as evidenced by the significant decrease in protein adsorption and cell attachment on substrates coated by this film. Detailed studies of the plasma film deposition process revealed that the effect of the substrate pretreatment condition on the wettability and thickness of the films deposited on LDPE was significant, while that of the diglyme plasma treatment time on the film composition was secondary. Film chemical functionalities demonstrated a dependence on both diglyme plasma power and substrate material. Activation of the LDPE surface by bombarding Ar^+ ions followed by a low-power treatment with diglyme plasma was shown to be conducive to the formation of films with chemical characteristics similar to those of PEG. These studies indicated that plasma polymerization is an effective and convenient method for depositing functional polymer films.

Plasma treatments were also applied on electrospun poly(L-lactide) (PLLA) microfibrous scaffolds for biocompatibility enhancement as well as surface functionalization for biomolecule immobilization. Mild Ar and Ar-NH_3/H_2 plasma treatments of PLLA microfibrous scaffolds (Chapter 7) revealed the effect of different plasma treatments on cell attachment and growth on the scaffold surface as well as cell infiltration into the scaffold. Culture of bovine aorta endothelial cells (BAECs) and bovine smooth muscle cells (BSMCs) on treated PLLA microfibrous scaffolds showed that both Ar and Ar-NH_3/H_2 plasma treatments improved cell spreading during the initial stage of attachment and enhanced cell growth rate, especially in the case of Ar plasma treatment. *In vitro* cell infiltration experiments with BAECS and *in vivo* implantation of PLLA scaffolds under the skin of rats showed that both plasma treatments enhanced cell in-growth through the scaffold thickness. Therefore, mild plasma treatments with Ar and Ar-NH_3/H_2 plasma are identified as effective methods to improve the biocompatibility of microfibrous scaffolds while maintaining the mechanical integrity of the scaffolds, which is of high importance in tissue engineering. In addition to improving the biocompatibility enhancement, Ar-NH_3/H_2 plasma treatment was also effective in incorporating $–NH_2$ groups onto the surface of the PLLA scaffolds for heparin conjugation (Chapter 8). It was found that plasma

power, gas composition, and H_2 plasma post treatment time do not affect the N/C ratio significantly; however, they affect the $–NH_2$/N ratio and, in turn, the $–NH_2$/C ratio. On the other hand, plasma treatment time affects both N/C and $–NH_2$/N ratios. Scaffold treatment with optimized Ar-NH_3/H_2 plasma increased the amount of covalently immobilized heparin significantly compared to a hydrolysis method. Heparin immobilization was confirmed by the decrease in platelet attachment after blood testing, showing that Ar-NH_3/H_2 plasma treatment is an effective method of incorporating functional groups into the scaffold microfibrous structure for biomolecule immobilization.

10.1.2 Plasma assisted surface chemical patterning

Surface chemical patterning for controlled cell culture has found various bioengineering applications in recent years. Different methods of surface chemical patterning for single cell culture were explored in this thesis. The first method is based on PEG-like film deposition and plasma surface activation through the windows of a shadow mask (Chapter 5). Using silicon or polydimethylsiloxane (PDMS) membrane shadow masks fabricated by photolithography and simple one-step plasma etch process, different chemical patterns were produced on substrates with grafted PEG-like films. Culture of single human mesenchymal stem cells (hMSCs) on chemically patterned polystyrene dishes demonstrated a strong dependence of the actin structure and nuclear morphology on hMSC shape and spreading area. Moreover, the method was utilized to study the effect of shape regulation on BSMC proliferation. Both cell shape and size were found to affect the cell proliferation rate. A correlation between the shape and volume of the nuclei with the cell proliferation rate was found by analyzing changes in the nucleus morphology (shape and volume) with cell geometry, suggesting that changes in the nucleus morphology (either shape or volume) may modulate DNA synthesis and, in turn, BSMC proliferation.

Another surface chemical patterning method was developed for long-term single cell culture on polystyrene (PS) and parylene C surfaces (Chapter 6). Surface chemical patterning of polystyrene dishes for long-term single-cell culture was accomplished by oxygen plasma treatment through the windows of a PDMS membrane mask that produced hydrophilic surface areas of different shapes and sizes, followed by overnight incubation with either Pluronic F108 solution or a mixture of Pluronic F108 solution and fibronectin. Selective cell attachment on the pattern areas of PS dishes was characterized by cell seeding experiments and XPS measurements, and activation of the hydrophilic areas of patterned PS surfaces by serum proteins from cell culture medium was found conducive to cell attachment on the pattern areas of dishes incubated with only Pluronic solution. It was also found that preferential adsorption of fibronectin on hydrophilic pattern areas promoted selective cell attachment on patterned dishes incubated with a mixture of Pluronic solution and fibronectin. Long-term (two weeks) cell culture experiments elucidated the effect of surface patterning on the shape of cells and nuclei and demonstrated the stability of the produced single-cell patterns in serum medium. Surface chemical patterning for single-cell culture was also realized on Parylene C surfaces, extending the range of substrate materials for patterning. Hydrophilic patterns were produced on parylene C films deposited on glass substrates by oxygen plasma treatment through the windows of a PDMS shadow masks. After incubation first with Pluronic F108 solution and then serum medium overnight, surface seeding with hMSCs in serum medium resulted in single-cell patterning that was stable for two weeks. Both methods provide a means of surface patterning with direct

implications in single-cell culture. Compared to other methods, the presented methods do not require precise control of the patterning process and are effective in producing a wide range of pattern shapes and sizes for single-cell culture.

10.1.3 Patterned templates for eletrospinning of scaffolds with various structures

While surface chemistry of biopolymers is critical for biocompatibility, the biopolymer structure also plays an important role in many applications, especially for scaffolds used in tissue engineering. In this thesis, microfabrication and elelctrospinning were combined to control the structure of microfibrous scaffolds (Chapter 9). PDMS templates with different patterns were fabricated by combining photolithography, silicon wet etching, and PDMS molding techniques. Electrospinning of PLLA microfibers on PDMS templates with different geometries produced microfibrous scaffolds with different topographic patterns. Fibrous structures with different characteristics, including fiber alignment, increased porosity, and microwells of varying dimensions were obtained by varying the pattern geometry of the PDMS templates and the electrospinning parameters. The effects of microfiber arrangement and porosity of the patterned scaffolds on cell morphology, migration, and infiltration were also examined in light of *in vitro* and *in vivo* experiments. The obtained results revealed a dependence of cell morphology, migration, and infiltration on scaffold pattern. This method demonstrates a powerful approach to engineering the microstructure of electrospun scaffolds and materials, and has direct implications in the fabrication of scaffold materials for tissue engineering.

10.2 Future directions

As a widely applied method for surface modification, plasma treatment of biopolymer surfaces with different plasma gases has been studied extensively, especially for bulk biopolymers. Current research aims at developing different plasma processes for new forms of biomaterials, including micro/nanofibrous scaffolds and various porous biomaterials, for both cell growth enhancement and surface functionalization. Due to the 3D structure and small features of the treated material, plasma-induced surface modification may differ significantly from bulk material, leading to new challenges for characterizing the plasma treatment. Moreover, because fibrous/porous scaffolds have high surface area-to-volume ratio, the effectiveness of plasma modification can be strongly enhanced compared to bulk materials, for which the modification is confined to the outermost surface layer. Therefore, the plasma treatment effect on cell behavior may also be very different, which is still open to further study. Regarding the PLLA microfibrous scaffolds investigated in this thesis, it was shown that Ar plasma can enhance cell growth more than NH_3 plasma. The reason for this is still unclear. Plasma treatment was also found to enhance *in vivo* cell infiltration into the scaffold. However, whether different plasma treatments induce incorporation of exactly the same type of cells requires further research.

While control of the surface chemical properties of biopolymers is critical, creating fibrous scaffolds with controlled structure is also equally important in tissue engineering. With the micropatterned PDMS template studied in this thesis as an example, manipulating the collector is an effective means of controlling fiber organization and scaffold porosity. Therefore, further studies are needed to develop new templates with patterns for controlling the structure of

electrospun fibrous scaffolds. For PDMS templates specifically, because Si wet etching and PDMS molding are both very versatile methods for fabricating structures, the effects of the geometry and dimensions of the surface pattern on fiber deposition and organization can also be further studied through careful design of the microstructure.

Currently most studies focus on the effect of either surface chemistry modification or structural modification. Since both surface chemistry modification and scaffold structure modification can be conducive for specific functionality (e.g., cell in-growth), eventually the optimized plasma treatment of biopolymers and optimized scaffold structures should be combined to maximize the impact on cell incorporation, ingrowth, and tissue formation.

As shown in this thesis, plasma treatment can be very useful in surface chemical patterning for controlled protein adsorption and cell growth. Applying plasma treatment combined with microfabrication methods (e.g., selective change from hydrophobic to hydrophilic surface areas achieved by plasma treatment through the windows of a PDMS membrane mask) allows for selective surface property modification. Using Pluronic as an example, many molecules demonstrate different behaviors when absorbed onto different substrates. Therefore, it is desirable to introduce new plasma surface treatments and new molecules of interest to create surface patterns with different properties for bioengineering applications. For example, PLL-g-PEG is a molecule with high affinity for hydrophilic surfaces which can also be used as a nonfouling material. With the same method of plasma treatment through a PDMS mask, it is possible to explore a new method of surface patterning for single-cell culture with PLL-g-PEG as a background nonfouling layer. Therefore, new studies must focus on geometry effects on single cells or organization effects on cell clusters.

Bibliography

Adarnczyk, N. M., Dameron, A. A., and George, S. M., 2008, Molecular layer deposition of poly(p-phenylene terephthalamide) films using terephthaloyl chloride and p-phenylenediamine. *Langmuir*, vol. 24 (5), pp. 2081–2089.

Ademovic, Z., Wei, J., Winther-Jensen, B., Hou, X., and Kingshott, P., 2005, Surface Modification of PET Films Using Pulsed AC Plasma Polymerisation Aimed at Preventing Protein Adsorption. *Plasma Process. Polym.* vol. 2, pp. 53.

Agraharam, S., Hess, D. W., Kohl, P. A., and Bidstrup Allen, S. A., 1999, Plasma chemistry in fluorocarbon film deposition from pentafluoroethane/argon mixtures. *J. Vac. Sci. Technol. A* vol. 17, pp. 3265–3271.

Agraharam, S., Hess, D. W., Kohl, P. A., and Bidstrup Allen, S. A., 2000, Thermal Stability of Fluorocarbon Films Deposited from Pentafluoroethane/Argon Plasmas. *J. Electrochem. Soc.* vol. 47, pp. 2665–2670.

Alcantar, N. A., Aydil, E. S., and Israelachvili, J. N., 2000, Polyethylene glycol–coated biocompatible surfaces. *J. Biomed. Mater. Res.* vol. 51, pp. 343.

Andreas Goessl, A., Bowen-Pope, D. F., and Hoffman, A. S., 2001, Control of shape and size of vascular smooth muscle cells in vitro by plasma lithography. *J Biomed Mater Res*, vol. 57, pp. 15–24.

Azioune, A., Storch, M., Bornens, M., Théry, and M., Pie, M., 2009, Simple and rapid process for single cell micro-patterning, *Lab Chip*, vol. 9, pp. 1640–1642.

Baek H. S., Park Y. H., Ki C. S., Park J. C., Rah D. K., 2008, Enhanced chondrogenic responses of articular chondrocytes onto porous silk fibroin scaffolds treated with microwave-induced argon plasma, *Surf. Coat. Technol.* vol. 202, pp. 5794–5797.

Barry J. J. A., Silva M. M. C. G., Shakesheff K. M., Howdle S. M., and Alexander M. R., 2005, Using plasma depostits to promote cell population of the porous interior of the three-dimensional PLLA tissue engineering scaffolds. *Adv. Funct. Mater.* vol. 15, pp. 1134-1140.

Bernard, A., Delamarche, E., Schmid, H., Michel, B., Bosshard, H. R., Biebuyck, H., 1998, Printing patterns of proteins. *Langmuir*, vol. 14, pp. 2225–2229.

Bhadriraju, K., and L. K. Hansen., 2002, Extracellular matrix- and cytoskeleton-dependent changes in cell shape and stiffness. *Exp Cell Res*, vol. 278(1), pp. 92-100.

Blakeney, B. A., Tambralli, A., Anderson, J. M., Andukuri, A., Lim, D. J., Dean, D. R., and Jun, H.-W., 2011, Cell infiltration and growth in a low density, uncompressed three-dimensional electrospun nanofibrous scaffold. *Biomaterials.* vol. 32, pp. 1583-1590.

Brétagnol, F., Kylián, O., Hasiwa, M., Ceriotti, L., Rauscher, H., Ceccone, G., et al., 2007, Micro-patterned surfaces based on plasma modification of PEO-like coating for biological applications. *Sens Actuat B: Chem.* vol. 123, pp. 283–292.

Brétagnol, F., Lejeune, M., Papadopoulou-Bouraoui, A., Hasiwa, M., Rauscher, H., Ceccone, G., Colpo, P., and Rossi, F., 2006, Fouling and non-fouling surfaces produced by plasma polymerization of ethylene oxide monomer. *Acta Biomater.* vol. 2, pp. 165-172.

Bulychev, S. I., and Alekhin, V. P., 1987, Method of kinetic hardness and microhardness in testing impression by an indenter. J. Zav. Lab. vol. 53(11), pp. 76-80.

Castner, D. G., and Ratner, B. D., 2002, Biomedical surface science: Foundations to frontiers. *Surf Sci.* vol. 500, pp. 28–60.

Chen J.-P. and Su C.-H., 2011, Surface modification of electrospun PLLA microfibers by plasma treatment and cationized gelatin immobilization for cartilage tissue engineering. *Acta Biomaterialia.* vol. 7(1), pp. 234-243.

Chen, C. S., Mrksich, M., Huang, S., Whitesides, G. M., and Ingber, D. E., 1997, Geometric control of cell life and death. *Science.* vol. 276, pp. 1425–1428.

Cheng Q., Komvopoulos K., 2009, Synthesis of polyethylene glycol-like films from capacitively coupled plasma of diethylene glycol dimethyl ether monomer. *J Phys Chem C* vol. 113, pp. 213–219.

Cheng Q., Yan Z.Q., Li S. and K. Komvopoulos, Plasma treatment of PLLA microfibrous membrane to improve cell adhesion, growth and infiltration, in preparation.

Cheng Z. Y., Teoh S. H., 2004, Surface modification of ultra thin poly (e-caprolactone) films using acrylic acid and collagen. *Biomaterials,* vol. 25, pp. 1991–2001

Cheng, Q., Komvopoulos, K., 2009, Synthesis of polyethylene glycol-like films from capacitively coupled plasma of diethylene glycol dimethyl ether monomer. *J Phys Chem C,* vol. 113, pp. 213–219.

Cheng, Q., Li, S., and Komvopoulos, K., 2009, Plasma-assisted surface chemical patterning for single-cell culture. *Biomaterials,* vol. 30, pp. 4203–4210.

Chew, S. Y., Mi, R., Hoke, A., and Leong, K. W., 2008, The Effect of the Alignment of Electrospun Fibrous Scaffolds on Schwann Cell Maturation. *Biomaterials,* vol. 29, pp. 653-661.

Chim H., Ong J. L., Schantz J.-T., Hutmacher D. W., Agrawal C. M., 2003, Efficacy of glow discharge gas plasma treatment as a surface modification process for three-dimensional poly (D,L-lactide) scaffolds. *J Biomed Mater Res A.* vol. 65 (3), pp. 327-35.

Cho, E. H., Lee, S. G., and Kim, J. K., 2005, Surface modification of UHMWPE with gamma-ray radiation for improving interfacial bonding strength with bone cement (II). *Curr. Appl. Phys.* vol. 5 (5), pp. 475–479.

Choi, I., Yang, Y. I., Kim, Y.-J., Kim, Y., Hahn, J.-S., Choi, K., et al., 2008, Directed positioning of single cells in microwells fabricated by scanning probe lithography and wet etching methods. *Langmuir*, vol. 24, pp. 2597–2602.

Croll T. I., O'Connor A. J., Stevens G. W., Cooper-White J. J., 2004, Controllable surface modification of poly(lactic-co-glycolic acid) (PLGA) by hydrolysis or aminolysis I: Physical, chemical, and theoretical aspects, *Biomacromolecules.* vol. 5, pp. 463–473.

Cunge, G., and Booth, J. P., 1999, CF_2 production and loss mechanisms in fluorocarbon discharges: Fluorine-poor conditions and polymerization. *J. Appl. Phys.* vol. 85, pp. 3952–3959.

Dai X. J., Plessis J. D., Kyratzis I. L., Maurdev G., Huson M. G., Coombs C., 2009, Controlled amine functionalization and hydrophilicity of a poly(lactic acid) fabric. *Plasma Process. Polym.* vol. 6, pp. 490–497.

Deng, J., Wang, L., Liu, L., and Yang, W., 2009, Developments and new applications of UV-induced surface graft polymerizations. *Prog. Polym. Sci.* vol. 34 (2), pp. 156–193.

Desmet, T., Morent, R., Geyter, N. D., Leys, C., Schacht, E., and Dubruel, P., 2009, Nonthermal Plasma Technology as a Versatile Strategy for Polymeric Biomaterials Surface Modification, A Review. *Biomacromolecules.* vol. 10 (9), pp. 2351-2377.

Detrait, E., Lhoest, J. B., Bertrand, P., and van den Bosch de Aguilar, Ph., 1999, Fibronectin-pluronic coadsorption on a polystyrene surface with increasing hydrophobicity: Relationship to cell adhesion. *J Biomed Mater Res,* vol. 45(4), pp. 404–413.

Detrait, E., Lhoest, J. B., Knoops, B., Bertrand, P., and van den Bosch de Aguilar, Ph., 1998, Orientation of cell adhesion and growth on patterned heterogeneous polystyrene surface. *J Eurosci Meth,* vol. 84, pp. 193–204.

Dewez, J. L., Berger, V., Schneider, Y. J., and Rouxhet, P. G., 1997, Influence of substrate hydrophobicity on the adsorption of collagen in the presence of Pluronic F68, albumin, or calf serum. *J Colloid Interface Sci*. vol. 191, pp. 1–10.

Digital Instruments Veeco Metrology Group, MultiMode^{TM} Scanning Probe Microscope Instruction Manual Version 4.31ce, 1997.

Dilley, R. J., J. K. McGeachie, and F. J. Prendergast., 1987, A review of the proliferative behaviour, morphology and phenotypes of vascular smooth muscle. *Atherosclerosis*, vol. 63(2-3), pp. 99-107.

Ding, Z., Salim, A., and Ziaie, B., 2009, Selective Nanofiber Deposition through Field-Enhanced Electrospinning. *Langmuir*, vol. 25, pp. 9648-9652.

Dong, B., Jiang, H., Manolache, S., Wong, A. C. L., and Denes, F. S., 2007, Plasma-Mediated Grafting of Poly(ethylene glycol) on Polyamide and Polyester Surfaces and Evaluation of Antifouling Ability of Modified Substrates. *Langmuir*, vol. 23, pp. 7306.

Falconnet, D., Csucs, G., Grandin, H. M., and Textor, M., 2006, Surface engineering approaches to micropattern surfaces for cell-based assays. *Biomaterials*. vol. 27, pp. 3044–3063.

Falconnet, D., Koenig, A., Assi, F., and Textor, M., 2004, Combined photolithographic and molecular-assembly approach to produce functional micropatterns for applications in the biosciences. *Adv Functional Mater*. vol. 14, pp. 749-756.

Fan, C. Y., Tung, Y. C., Takayama, S., Meyhofer, E., and Kurabayashi, K., 2008, Electrically programmable surfaces for configurable patterning of cells. *Adv. Mater.* vol. 20, pp. 1418.

Favia P., Stendardo M. V., and d'Agostino R., 1996, Selective Grafting of Amine Groups on Polyethylene by Means of NH_3-H_2 RF Glow Discharges. *Plasmas and Polymers.* vol. 1(2), pp. 91-112.

Favia, P., and d'Agostino, R., 1998, Plasma treatments and plasma deposition of polymers for biomedical applications. *Surf. Coat. Technol.* vol. 98, pp. 1102–1106.

Favia, P., Perez-Luna, V. H., Boland, T., Castner, D. G., and Ratner, B. D., 1996, Surface Chemical Composition and Fibrinogen Adsorption-Retention of Fluoropolymer Films Deposited from an RF Glow Discharge. *Plasmas and Polymers*, vol. 1, pp. 299–326.

Feng Z.-Q., Lu H.-J., Leach M. K., Huang N.-P., Wang Y.-C., Liu C.-J. and Gu Z.-Z., 2010, The influence of type-I collagen-coated PLLA aligned microfibers on growth of blood outgrowth endothelial cells. *Biomed. Mater.* vol. 5, pp. 065011.

Folkman, J., and A. Moscona., 1978, Role of cell shape in growth control. *Nature*, vol. 273(5661), pp. 345-349.

Freshney, R. I., 2000, Culture of animal cells, a manual of basic technique, 4th ed. Wiley, New York, NY, pp.309-312.

Fridrikh, S. V., Yu, J. H., Brenner, M. P., and Rutledge, G. C., 2003, Controlling the Fiber Diameter during Electrospinning. *Phys. Rev. Lett.* vol. 90, pp. 144502(1)-144502(4).

Gao, J. M., Niklason, L., and Langer, R., 1998, Surface hydrolysis of poly(glycolicacid) meshes increases the seeding density of vascular smooth muscle cells. *J. Biomed. Mater. Res.* vol. 42 (3), pp. 417–424.

Gatenholm, P., Ashida, T., and Hoffman, A. S., 1997, Hybrid biomaterials prepared by ozone-induced polymerization. I. Ozonation of microporous polypropylene. *J. Polym. Sci., Part A: Polym. Chem.* vol. 35 (8), pp. 1461–1467.

Goessl, A., Bowen-Pope, D. F., and Hoffman, A. S., 2001, Control of shape and size of vascular smooth muscle cells in vitro by plasma lithography. *J Biomed Mater Res.* vol. 57, pp. 15–24.

Guerin, D. C., Hinshelwood, D. D., Monolache, S., Denes, F. S., and Shamamian, V. A., 2002, Plasma polymerization of thin films: Correlations between plasma chemistry and thin film character. *Langmuir.* vol. 18 (10), pp. 4118–4123.

Gugala Z., and Gogolewski S., 2006, Attachment, growth, and activity of rat osteoblasts on polylactide membranes treated with various low-temperature radiofrequency plasmas. *J Biomed Mater Res A.* vol. 76(2), pp. 288-299.

Guptaa B., Plummera C., Bissonb I., Freyb P., Hilborn J., 2002, Plasma-induced graft polymerization of acrylic acid onto poly(ethylene terephthalate) films: characterization and human smooth muscle cell growth on grafted films. Biomaterials. vol. 23, pp. 863–871.

Hao, H., P. Ropraz, V. Verin, E. Camenzind, A. Geinoz, M. S. Pepper, G. Gabbiani, and M. L. Bochaton-Piallat., 2002, Heterogeneity of smooth muscle cell populations cultured from pig coronary artery. *Arterioscler Thromb Vasc Biol*, vol. 22(7), pp. 1093-1099.

Harris, J. M., 1992, Poly (ethylene glycol) Chemistry: Biotechnical and Biomedical Application. Plenum Press: New York.

He W., Ma Z. W., Yong T., Teo W. E., Ramakrishna S., 2005, Fabrication of collagen-coated biodegradable polymer nanofiber mesh and its potential for endothelial cells growth, Biomaterials. vol. 26, pp. 7606–7615.

He W., Yong T., Teo W. E., Ma Z. W., Ramakrishna S., 2005, Fabrication and endothelialization of collagen-blended biodegradable polymer nanofibers: potential vascular graft for blood vessel tissue engineering. *Tissue Eng.* vol. 11, pp. 1574–1588.

Holmberg, K., 2002, *Handbook of Applied Surface and Colloid Chemistry*, John Wiley & Sons: New York, pp. 130–131.

Holvoet, S., Chevallier, P., Turgeon, S., and Mantovani, D., 2010, Toward High-Performance Coatings for Biomedical Devices: Study on Plasma-Deposited Fluorocarbon Films and Ageing in PBS. *Materials*, vol. 3, pp. 1515–1532.

Hopp, B., Smausz, T., Papdi, B., Bor, Z., Szabó, A., Kolozsvári, L., et al., 2008, Laser-based techniques for living cell pattern formation. *Appl Phys A: Mater Sci Proces*, vol. 93, pp. 45–49.

http://en.wikipedia.org/wiki/Fourier_transform_infrared_spectroscopy

http://en.wikipedia.org/wiki/Scanning_electron_microscope

http://www.oxfordplasma.de/layouts/dp_fm_s.htm

Huang, N. F., Patel, S., Thakar, R. G., Wu, J., Hsiao, B. S., Chu, B., Lee, R. J., and Li, S., 2006, Myotube Assembly on Nanofibrous and Micropatterned Polymers. *Nano Lett,* vol. 6, pp. 537-542.

Huang, Z.-M., Zhang, Y.-Z., Kotaki, M., and Ramakrishna, S., 2003, A Review on Polymer Nanofibers by Electrospinning and Their Applications in Nanocomposites. *Composites Sci. Technol.* vol. 63, pp. 2223-2253.

Hwang, Y.-S., Chung, B. G., Ortmann, D., Hattori, N., Moeller, H.-C., and Khademhosseini, A. , 2009, Microwell-mediated Control of Embryoid Body Size Regulates Embryonic Stem Cell Fate via Differential Expression of WNT5a and WNT11. *Proc. Nat. Acad. Sci.* vol. 106, pp. 16978-16983.

Hysitron Inc., TriboScope® Users Manual, Minneapolis, MN.

Hyuk S. Y., Taek G. K., and Tae G. P., 2009, Surface-functionalized electrospun nanofibers for tissue engineering and drug delivery. *Advanced Drug Delivery Reviews*, vol. 61, pp. 1033–1042.

Jackman, R. J., Duffy, D. C., Cherniavskaya, O., and Whitesides, G. M., 1999, Using elastomeric membranes as dry resists and for dry lift-off. *Langmuir,* vol. 15, pp. 2973–2984.

Jang, J.-H., Castano, O., and Kim, H.-W., 2009, Electrospun Materials as Potential Platforms for Bone Tissue Engineering. *Adv. Drug Deliv. Rev.* vol. 61, pp. 1065-1083.

Jia J., Duan Y. Y., Yu J., Lu J. W., 2008, Preparation and immobilization of soluble eggshell membrane protein on the electrospun nanofibers to enhance cell adhesion and growth, J. Biomed. *Mater. Res. A.* vol. 86A, pp. 364–373.

Joshi, P. P., Pulikollu, R., Higgins, S. R., Hu, X., and Mukhopadhyay, S. M., 2006, Investigation of growth, coverage and effectiveness of plasma assisted nano-films of fluorocarbon. *Appl. Surf. Sci.* vol. 252, pp. 5676–5686.

Ju Y. M., Park K., Son J. S., Kim J. J., Rhie J. W., Han D. K., 2008, Beneficial effect of hydrophilized porous polymer scaffolds in tissue-engineered cartilage formation. *J Biomed Mater Res B Appl Biomater.* vol. 85(1), pp. 252-260.

Katti, D. S., Robinson, K.W., Ko, F.K., et al., 2004, Bioresorbable nanofiber based systems for wound healing and drug delivery: optimization of fabrication parameters. *J Biomed Mater Res.* vol. 70B, pp. 286–296.

Kiaei, D., Hoffman, A. S., and Hansont, S. R., 1992, Ex vivo and in vitro platelet adhesion on RFGD deposited polymers. *Journal of Biomedical Materials Research.* vol. 26, pp. 357-372.

Kiaei, D., Hoffman, A. S., Horbett, T. A., and Lew, K. R., 1995, Platelet and monoclonal antibody binding to fibrinogen adsorbed on glow-discharge-deposited polymers. *Journal of Biomedical Materials Research.* vol. 29, pp. 729-739.

Klapperich, C., Komvopoulos, K., and Pruitt, L., 1999, Wear mechanisms of untreated and Gamma irradiated ultra-high molecular weight polyethylene for total joint replacements. *ASME J. Tribol.* vol. 121, pp. 394–402.

Koh H. S., Yong T., Chan C. K., Ramakrishna S., 2008, Enhancement of neurite outgrowth using nano-structured scaffolds coupled with laminin, Biomaterials. vol. 29, pp. 3574–3582.

Kurpinski, K. T., Stephenson, J. T., Janairo, R. R. R., Lee, H., and Li, S., 2010, The Effect of Fiber Alignment and Heparin Coating on Cell Infiltration into Microfibrous PLLA Scaffolds. *Biomaterials*, vol. 31, pp. 3536-3542.

Latkany R., Tsuk A., Sheu M.-S., Loh I.-H., Trinkaus–Randall V., 1997, Plasma surface modification of artificial corneas for optimal epithelialization. *J Biomed Mater Res.* vol. 36(1), pp. 29-37.

Lau, K. K. S., Pryce Lewis, H. G., Limb, S. J., Kwan, M. C., and Gleason, K. K., 2001, Hot-wire chemical vapor deposition (HWCVD) of fluorocarbon and organosilicon thin films. *Thin Solid Films*, vol. 395, pp. 288–291.

Lee, J. H., Jeong, B. J., and Lee, H. B., 1997, Plasma protein adsorption and platelet adhesion onto comb-like PEO gradient surfaces. *J. Biomed. Mater. Res.* vol. 34, pp. 105.

Lee, J. Y., Shah, S. S., Zimmer, C. C., Liu, G., Revzin, A., 2008, Use of photolithography to encode cell adhesive domains into protein microarrays. *Langmuir*, vol. 24, pp. 2232–2239.

Lewis, F., Horny, P., Hale, P., Turgeon, S., Tatoulian, M., and Mantovani, D., 2008, Study of the adhesion of thin plasma fluorocarbon coatings resisting plastic deformation for stent applications. *J. Phys. D: Appl. Phys.* vol. 41, pp. 045310(1)–045310(7).

Lewis, F., Turgeon, S., Chevallier, P., Pireaux, J. J., Tatoulian, M., and Mantovani, D., 2010, On the Growth of Fluorocarbon Thin Films Deposited on Plasma-Etched 316L Stainless Steel. *Plasma Process. Polym.* vol. 7, pp. 309–317.

Lhoest, J. B., Detrait, E., Dewez, J. L., Van den Bosch de Aguilar, P., and Bertrand, P., 1996, A new plasma-based method to promote cell adhesion on micrometric tracks on polystyrene substrates. *J. Biomater. Sci.: Polym. Edn.* vol. 7 (12), pp. 1039-1054.

Li, D., and Xia, Y., 2004, Electrospinning of Nanofibers: Reinventing the Wheel?. *Adv. Mater.*, vol. 16, pp. 1151-1170.

Li, D., Ouyang, G., McCann, J. T., and Xia, Y., 2005, Collecting Electrospun Nanofibers with Patterned Electrodes. *Nano Lett.* vol. 5, pp. 913-916.

Li, J., and Yi, X., 2010, Woven Structures Produced by Depositing Electrospun Fibers onto Ice Collectors. *Appl. Phys. A*, vol. 98, pp. 757-760.

Lieberman, M. A., and Lichtenberg, A. J., 2005, Principles of Plasma Discharges and Materials Processing. John Wiley & Sons, Hoboken, NJ, pp.7-9.

Liu, D., Gu, J., Feng, Z., Li, D., Niu, J., and Benstetter, G., 2010, Comparison of fluorocarbon film deposition by pulsed/continuous wave and downstream radio frequency plasmas. *Vacuum*, vol. 85, pp. 253–262.

Luo, W., Jones, S. R., Yousaf, M. N., 2008, Geometric control of stem cell differentiation rate on surfaces. *Langmuir*, vol. 24, pp. 12129–12133.

Luong-Vana E., Grøndahla L., Chuad K. N., Leongd K. W., Nurcombeb V., Cool S. M., 2006, Controlled release of heparin from poly(e-caprolactone) electrospun fibers. *Biomaterials*, vol. 27, pp. 2042–2050.

Lussi, J. W., Michel, R., Reviakine, I., Falconnet, D., Goessl, A., Csucs, G., et al., 2004, A novel generic platform for chemical patterning of surfaces. *Prog Surf Sci.* vol. 76, pp. 55–69.

Lutolf, M. P., Gilbert, P. M., and Blau, H. M., 2009, Designing Materials to Direct Stem-cell Fate. *Nature*, vol. 462, pp. 433-441.

Ma Z. W., He W., Yong T., Ramakrishna S., 2005, Grafting of gelatin on electrospun poly (caprolactone) nanofibers to improve endothelial cell spreading and proliferation and to control cell orientation, *Tissue Eng.* vol. 11, pp. 1149–1158.

Martins A., Pinho E. D., Faria S., Pashkuleva I., Marques A. P., Reis R. L., and. Neves N. M., 2009, Surface modification of electrospun polycaprolactone nanofiber meshes by plasma treatment to enhance biological performance. *Small*. vol. 5(10), pp. 1195–1206.

McBeath, R., Pirone, D. M., Nelson, C. M., Bhadriraju, K., and Chen, C. S., 2004, Cell shape, cytoskeletal tension, and RhoA regulate stem cell lineage commitment. *Develop Cell.* vol. 6, pp. 483–495.

Murugan, R., and Ramakrishna, S., 2007, Design Strategies of Tissue Engineering Scaffolds with Controlled Fiber Orientation. *Tissue Eng.* vol. 13, pp. 1845-1866.

Nam, J., Huang, Y., Agarwal, S., and Lannutti, J., 2007, Improved Cellular Infiltration in Electrospun Fiber via Engineered Porosity. *Tissue Engineering*. vol. 13(9), pp. 2249-2257.

Nejadnik, R. M., Olsson, A. L. J., Sharma, P. K., van der Mei, H. C., Norde, W., and Busscher, H. J., 2009, Adsorption of Pluronic F-127 on surfaces with different hydrophobicities probed by quartz crystal microbalance with dissipation. *Langmuir,* vol. 25(11), pp. 6245–6249.

Nelea, V., Holvoet, S., Turgeon, S., and Mantovani. D., 2009, Deposition of fluorocarbon thin films on outer and inner surfaces of stainless steel mini-tubes by pulsed plasma polymerization for stents. *J. Phys. D: Appl. Phys.* vol. 42, pp. 225208(1)–225208(9).

Ohl, A., and SchrÖder, K., 1999, Plasma-induced chemical micropatterning for cell culturing applications: a brief review. *Surface and Coatings Technology*. vol. 116–119, pp. 820–830.

Ohring, M., 2002, *Materials Science of Thin Films: Deposition and Structure*, 2nd ed., Academic Press: San Diego, CA.

Oliver, W. C., and Pharr, G. M., 1992, An improved technique for determining hardness and elastic modulus using load and displacement sensing indentation experiments. J. Mater. Res. vol. 7, pp. 1564-1583.

Oliver, W. C., and Pharr, G. M., 2004, Measurement of hardness and elastic modulus by instrumented indentation: Advances in understanding and refinements to methodology. J. Mater. Res. vol. 19, pp. 3-20.

Ostuni, E., Chen, C. S., Ingber, D. E., Whitesides, G. M., 2001, Selective deposition of proteins and cells in arrays of microwells. *Langmuir*, vol. 17, pp. 2828–2834.

Ostuni, E., Kane, R., Chen, C.S., Ingber, D. E., Whitesides, G. M., 2000, Patterning mammalian cells using elastomeric membranes. *Langmuir*, vol. 16, pp. 7811–7819.

Ostuni, E., Yan, L., Whitesides, G. M., 1999, The interaction of proteins and cells with self-assembled monolayers of alkanethiolates on gold and silver. *Coll Surf B: Biointerfaces*, vol. 15, pp. 3–30.

Owens, G. K., 1995, Regulation of differentiation of vascular smooth muscle cells. *Physiol Rev*, vol. 75(3), pp. 487-517.

Paletta J. R. J., Bockelmann S., s Walz A., Theisen C., Wendorff J. H., Greiner A., 2010, Susanne Fuchs-Winkelmann and Markus Dietmar Schofer. RGD-functionalisation of PLLA microfibers by surface coupling using plasma treatment: influence on stem cell differentiation. *J Mater Sci: Mater Med.* vol. 21, pp. 1363–1369.

Palumbo, F., Favia, P., Vulpio, M., and d'Agostino, R., 2001, RF Plasma Deposition of PEO-Like Films:Diagnostics and Process Control. *Plasmas and Polymers,* vol. 6, pp. 163.

Park H., Lee K. Y., Lee S. J., Park K. E. and Park W. H., 2007, Plasma-treated poly(lactic-co-glycolic acid) microfibers for tissue engineering. *Macromolecular Research*. vol. 15(3), pp. 238-243.

Park K., Ju Y. M., Son J. S., Ahn K. D., Han D. K., 2007, Surface modification of biodegradable electrospun nanofiber scaffolds and their interaction with fibroblasts, *J. Biomater. Sci., Polym. Ed.* vol. 18, pp. 369–382.

Park, J. S., Chu, J. S., Tsou, A .D., Diop, R., Tang, Z., Wang, A., and Li, S., 2011, The Effect of Matrix Stiffness on the Differentiation of Mesenchymal Stem Cells in Response to TGF-beta. *Biomaterials,* vol. 32, pp. 3921-3930.

Patel, S., Kurpinski, K. T., Quigley, R., Gao, H., Hsiao, B. S., Poo, M.-M., and Li, S., 2007, Bioactive Nanofibers: Synergistic Effects of Nanotopography and Chemical Signaling on Cell Guidance. *Nano Lett.* vol. 7, pp. 2122-2128.

PerkinElmer, Technical Note, FT-IR Spectroscopy: Attenuated Total Reflectance (ATR)

Pham, Q. P., Sharma, U. and Mikos, A. G., 2006, Electrospinning of Polymeric Nanofibers for Tissue Engineering Applications: A Review. *Tissue Engineering*. vol. 12(5), pp. 1197-1212.

Popat, K. C., Sharma, S., and Desai, T. A., 2004, Quantitative XPS Analysis of PEG-Modified Silicon Surfaces. *J. Phys. Chem. B,* vol. 108, pp. 5185.

Popelka, S., L. Machova, and F. Rypacek., 2007, Adsorption of poly(ethylene oxide)-block-polylactide copolymers on polylactide as studied by ATR-FTIR spectroscopy. *J. Colloid Interface Sci.* vol. 308 (2), pp. 291– 299.

Prabhakaran M. P., Venugopal J., Chan C. K., Ramakrishna S., 2008, Surface modified electrospun nanofibrous scaffolds for nerve tissue engineering, *Nanotechnology*. vol. 19, pp. 455102.

Prime, K. L., and Whitesides, G. M., 1991, Self-assembled organic monolayers: model systems for studying adsorption of proteins at surfaces. *Science,* vol. 252, pp. 1164.

Ranjan, R., and Brittain, W. J., 2007, Tandem RAFT polymerization and click chemistry: An efficient approach to surface modification. *Macromol. Rapid Commun.* vol. 28 (21), pp. 2084–2089.

Ratner, B. D., Hoffman, A. S., Schoen, F. J., and Lemons, J. E., 1996, Biomaterials Science: An Introduction to Materials in Medicine, Academic press, San Diego CA, pp.57-59.

Roca-Cusachs, P., Alcaraz, J., Sunyer, R., Samitier, J., Farré, R., and Navajas, D., 2008, Micropatterning of single endothelial cell shape reveals a tight coupling between nuclear volume in G1 and proliferation. *Biophys J*. vol. 94, pp. 4984–4995.

Rosato, D. V., and Szycher, M., 1983, Biocompatible Polymers, Metals, and Composites, Technomic Publ. pp.1022.

Sarkar, S., M. Dadhania, P. Rourke, T. A. Desai, and J. Y. Wong., 2005, Vascular tissue engineering: microtextured scaffold templates to control organization of vascular smooth muscle cells and extracellular matrix. *Acta Biomater*, vol. 1(1), pp. 93-100.

Sasaki, K., Takizawa, K., Takada, N., and Kadota, K., 2000, Correlation between CF_2 and C_xF_y densities in C_4F_8 plasmas. *Thin Solid Films,* vol. 374, pp. 249–255.

Shen H., Hu X. X., Yang F., Bei J. Z., Wang S. G., 2007, Combining oxygen plasma treatment with anchorage of cationized gelatin for enhancing cell affinity of poly(lactide-co-glycolide). *Biomaterials*. vol. 28, pp. 4219–4230.

Shirley, D. A., 1972, High-Resolution X-Ray Photoemission Spectrum of the Valence Bands of Gold. Phys Rev. B, vol. 5, pp. 4709-4714.

Singhvi, R., A. Kumar, G. P. Lopez, G. N. Stephanopoulos, D. I. Wang, G. M. Whitesides, and D. E. Ingber., 1994, Engineering cell shape and function. *Science,* vol. 264(5159), pp. 696-698.

Siow, K. S., Britcher, L., Kumar, S., and Griesser, H. J., 2006, Plasma Methods for the Generation of Chemically Reactive Surfaces for Biomolecule Immobilization and Cell Colonization - A Review. *Plasma Process. Polym.* vol. 3, pp. 392–418.

Tajima S., and Komvopoulos K., 2005, Surface Modification of Low-Density Polyethylene by Inductively Coupled Argon Plasma. *J. Phys. Chem. B*, vol. 109, pp. 17623-17629.

Tajima, S., and Komvopoulos, K. Dependence of nanomechanical modification of polymers on plasma-induced cross-linking. *J. Appl. Phys.* 2007, vol. 101, pp. 014307(1)–014307(8).

Tajima, S., and Komvopoulos, K., 2005, Surface Modification of Low-Density Polyethylene by Inductively Coupled Argon Plasma. *J. Phys. Chem. B*. vol. 109, pp. 17623–17629.

Tajima, S., and Komvopoulos, K., 2006, Effect of Ion Energy Fluence on the Topography and Wettability of Low-Density Polyethylene Exposed to Inductively Coupled Argon Plasma. *J. Phys. D: Appl. Phys*. vol. 39, pp. 1084–1094.

Tajima, S., and Komvopoulos, K., 2006, Effect of Reactive Species on Surface Crosslinking of Plasma-Treated Polymers Investigated by Surface Force Microscopy. *Appl. Phys. Lett*., vol. 89, pp. 124102(1)–124102(3).

Tajima, S., and Komvopoulos, K., 2007, Physicochemical properties and morphology of fluorocarbon films synthesized on crosslinked polyethylene by capacitively coupled octafluorocyclobutane plasma, *J. Phys. Chem. C.* vol. 111, pp. 4358–4367.

Tajima, S., 2006, Plasma-assisted surface modification of biopolymers. Ph.D. Thesis, University of California, Berkeley, pp. 39-66. In Dissertations & Theses @ University of California [database on-line]; available from http://www.proquest.com (publication number AAT 3254102; accessed November 27, 2011).

Takahashi, K., Itoh, A., Nakamura, and T., Tachibana, K., 2000, Radical kinetics for polymer film deposition in fluorocarbon (C_4F_8, C_3F_6 and C_5F_8) plasmas. *Thin Solid Films*, vol. 374, pp. 303–310.

Tan, J. L., Liu, W., Nelson, C. M., Raghavan, S., and Chen, C. S., 2004, Simple approach to micropattern cells on common culture substrates by tuning substrate wettability. *Tissue Eng.* vol. 10, pp. 865–872.

Tang, B., and Ngan, A. H. W., 2003, Accurate measurement of tip–sample contact size during nanoindentation of viscoelastic materials. *J. Mater. Res.* vol. 18, pp. 1141–1148.

Tang, G., Ma, X., Sun, M., and Li, X., 2005, Mechanical characterization of ultra-thin fluorocarbon films deposited by R.F. magnetron sputtering. *Carbon*, vol. 43, pp. 345–350.

Thakar, R. G., Cheng, Q., Patel, S., Chu, J., Nasir, M., Liepmann, D., et al., 2009, Cell-shape regulation of smooth muscle cell proliferation. *Biophys J.* vol. 96, pp. 3423–3432.

Thakar, R. G., Cheng, Q., Patel, S., Chu, J., Nasir, M., Liepmann, D., et al., 2009, Cell-shape regulation of smooth muscle cell proliferation. *Biophys J.* vol. 96, pp. 3423–3432.

Thakar, R. G., Ho, F., Huang, N. F., Liepmann, D. and Li, S., 2003, Regulation of vascular smooth muscle cells by micropatterning. *Biochem Biophys Res Commun*, vol. 307(4), pp. 883-890.

Thomas, C. H., Collier, J. H., Sfeir, C. S., and Healy, K. E., 2002, Engineering gene expression and protein synthesis by modulation of nuclear shape. *Proc Natl Acad Sci.* vol. 99, pp. 1972–1977.

Thomas, C. H., Lhoest, J. B., Castner, D. G., McFarland, C. D., and Healy, K. E., 1999, Surfaces designed to control the projected area and shape of individual cells. *J Biomech Eng*. vol. 121(1), pp. 40-48.

Thyberg, J., 1998, Phenotypic modulation of smooth muscle cells during formation of neointimal thickenings following vascular injury. *Histol Histopathol*, vol. 13(3), pp. 871-891.

Tonnis, E. J., Graves, D. B., Vartanian, V. H., Beu, L., Lii, T., and Jewett, R. J., 2000, Inductively coupled, point-of-use plasma abatement of perfluorinated compounds and hydrofluorinated compounds from etch processes utilizing O_2 and H_2O as additive gases. *Vac. Sci. Technol. A*, vol. 18, pp. 393-400.

Tsang, V. L., and Bhatia, S. N., 2004, Three-dimensional tissue fabrication. *Adv Drug Deliv Rev*, vol. 56(11), pp. 1635-1647.

van Os, M.T., Menges, B., Foerch, R., Vancso, G. J., and Knoll, W., 1999, Characterization of plasma-polymerized allylamine using waveguide mode spectroscopy. *Chem. Mater.* vol. 11, pp. 3252.

Vaquette, C., and Cooper-White, J. J., 2011, Increasing Electrospun Scaffold Pore Size with Tailored Collectors for Improved Cell Penetration. *Acta Biomater.* vol. 7, pp. 2544-2557.

Vargo, T. G., Thompson, P. M., Gerenser, L. J., Valentini, R. F., Aebischer, P., Hook, D. J., and Gardella, J. A., 1992, Monolayer Chemical Lithography and Characterization of Flurocarbon films. *Langmuir*. vol. 8, pp. 130-134.

Vasita, R., and Katti, D. S., 2006, Nanofibers and their applications in tissue engineering. *International Journal of Nanomedicine,* vol. 1 (1), pp. 15–30.

Visser, S.A., Hergenrother, R.W., and Cooper, S.L., 1996, Polymers. Biomaterials Science, Academic Press, pp. 50–60.

Wan Y. Q., Yang J., Yang J. L., Bei J. Z., Wang S. G., 2003, Cell adhesion on gaseous plasma modified poly-(l-lactide) surface under shear stress field. *Biomaterials.* vol. 24, pp. 3757–3764.

Wang, N., Ostuni, E., Whitesides, G. M., Ingber, D. E., 2002, Micropatterning tractional forces in living cells. *Cell Motility and the Cytoskeleton*, vol. 52, pp. 97–106.

Wang, P., Tan, K. L., Kang, E. T., and Neoh, K. G., 2001, Surface functionalization of low density polyethylene films with grafted poly(ethylene glycol) derivatives. *J. Mater. Chem.* vol. 11, pp. 2951.

Wang, Y., Wang, G., Chen, L., Li, H., Yin, T., Wang, B., Lee, J. C.-M., and Yu, Q., 2009, Electrospun Nanofiber Meshes with Tailored Architectures and Patterns as Potential Tissue-engineering Scaffolds. *Biofabrication,* vol. 1, pp. 015001(1)-015001(9).

Whitesides, G. M., Ostuni, E., Takayama, S., Jiang, X., and Ingber, D. E., 2001, Soft lithography in biology and biochemistry. *Annu Rev Biomed Eng*, vol. 3, pp. 335-373.

Xie, J., Liu, W., MacEwan, M. R., Yeh, Y.-C., Thomopoulos, S., and Xia, Y., 2011, Nanofiber Membranes with Controllable Microwells and Structural Cues and Their Use in Forming Cell Microarrays and Neuronal Networks. *Small*, vol. 7, pp. 293-297.

Xie, J., MacEwan, M. R., Ray, W. Z., Liu, W., Siewe, D. Y., and Xia, Y., 2010, Radially Aligned Electrospun Nanofibers as Dural Substitutes for Wound Closure and Tissue Regeneration Applications. *ACS Nano*, vol. 4, pp. 5027-5036.

Xie, J., Willerth, S. M., Li, X., Macewan, M. R., Rader, A., Sakiyama-Elbert, S. E., and Xia, Y., 2009, The Differentiation of Embryonic Stem Cells Seeded on Electrospun Nanofibers into Neural Lineages. *Biomaterials*, vol. 30, pp. 354-362.

Yang J., Bei J. Z., Wang S. G., 2002, Enhanced cell affinity of poly (d,l-lactide) by combining plasma treatment with collagen anchorage. *Biomaterials.* vol. 23, pp. 2607–2614.

Yang Z. L., Wang J., Luo R. F., Maitz M. F., Jing F. J., Sun H., Huang N., 2010, The covalent immobilization of heparin to pulsed-plasma polymeric allylamine films on 316L stainless steel and the resulting effects on hemocompatibility. *Biomaterials,* vol. 31, pp. 2072–2083.

Yang, M.-R., Chen, K.-S., and He, J.-L., 1997, The interaction between blood and the surface characteristics of plasma polymerized films. *Mater. Chem. Phys.* vol. 48, pp. 71–75.

Yim, E. K., and Leong, K. W., 2005, Significance of synthetic nanostructures in dictating cellular response. *Nanomedicine*, vol. 1(1), pp. 10-21.

Yoo H. S., Kim T. G., Park T. G., 2009, Surface-functionalized electrospun nanofibers for tissue engineering and drug delivery. *Advanced Drug Delivery Reviews*, vol. 61, pp. 1033–1042.

Zhang, D., and Chang, J., 2007, Patterning of Electrospun Fibers Using Electroconductive Templates. *Adv. Mater*. vol. 19, pp. 3664–3667.

Zhang, D., and Chang, J., 2008, Electrospinning of Three-Dimensional Nanofibrous Tubes with Controllable Architectures. *Nano Lett*. vol. 8(10), pp. 3283-3287.

Zheng, L., Ling, L., Hua, X., Oehrlein, G. S., and Hudson, E. A., 2005, Studies of film deposition in fluorocarbon plasmas employing a small gap structure. *J. Vac. Sci. Technol. A* vol. 23, pp. 634–642.

Zhou, J., and Komvopoulos, K., 2006, Surface and interface viscoelastic behaviors of thin polymer films investigated by nanoindentation. *J. Appl. Phys.* vol. 100, pp. 114329(1)–114329(8).

Zhou, W., Wang. Z. L., 2006, Scanning microscopy for nanotechnology: techniques and applications. Springer Science + Business Media, LLC, pp. 3-10.

Zhu Y. B., Gao C. Y., Liu X. Y., Shen J. C., 2002, Surface modification of polycaprolactone membrane via aminolysis and biomacromolecule immobilization for promoting cytocompatibility of human endothelial cells, *Biomacromolecules*, vol. 3, pp. 1312–1319.

Zhu Y. B., Leong M. F., Ong W. F., Chan-Park M. B., Chian K. S., 2007, Esophageal epithelium regeneration on fibronectin grafted poly(l-lactide-co-caprolactone) (PLLC) nanofiber scaffold, *Biomaterials*, vol. 28, pp. 861–868.

Zhu, Y., Wang, A., Patel, S., Kurpinski, K. T., Diao, E., Bao, X., Kwong, G., Young, W., and Li, S., 2011, Engineering Bi-layer Nanofibrous Conduits for Peripheral Nerve Regeneration. *Tissue Eng., Part C: Methods,* vol. 17, pp. 705–715.